Lehrstuhl für Elektrische Antriebssysteme und Leistungselektronik
der Technischen Universität München

Computational Efficient Optimum Control for 3-Level-Inverters with DC-link Capacitance Balancing

Xinbo Cai

Vollständiger Abdruck der von der Fakultät für Elektrotechnik und Informationstechnik der Technischen Universität München zur Erlangung des akademischen Grades eines

Doktor-Ingenieurs

genehmigten Dissertation.

Vorsitzender:	Prof. Dr.-Ing. Georg Sigl
Prüfer der Dissertation:	
	1. Prof. Dr.-Ing. Dr. h.c. Ralph Kennel
	2. Prof. Dianguo Xu, Ph.D.

Die Dissertation wurde am 18.06.2018 bei der Technischen Universität München eingereicht und durch die Fakultät für Elektrotechnik und Informationstechnik am 07.12.2018 angenommen.

Anhang I

Eidesstattliche Erklärung

Ich erkläre an Eides statt, dass ich die bei der promotionsführenden Einrichtung
Elektrotechnik und Informationstechnik
der TUM zur Promotionsprüfung vorgelegte Arbeit mit dem Titel:
Computational Efficient Optimum Control for 3-Level-Inverters with DC-link Capacitance Balancing
in Lehrstuhl für Elektrische Antriebssysteme und Leistungselektronik

Fakultät, Institut, Lehrstuhl, Klinik, Krankenhaus, Abteilung

unter der Anleitung und Betreuung durch: Prof. Kennel ohne sonstige Hilfe erstellt und bei der Abfassung nur die gemäß § 6 Ab. 6 und 7 Satz 2 angebotenen Hilfsmittel benutzt habe.

- ☒ Ich habe keine Organisation eingeschaltet, die gegen Entgelt Betreuerinnen und Betreuer für die Anfertigung von Dissertationen sucht, oder die mir obliegenden Pflichten hinsichtlich der Prüfungsleistungen für mich ganz oder teilweise erledigt.
- ☒ Ich habe die Dissertation in dieser oder ähnlicher Form in keinem anderen Prüfungsverfahren als Prüfungsleistung vorgelegt.
- ☐ Die vollständige Dissertation wurde in _____ veröffentlicht. Die promotionsführende Einrichtung _____ hat der Veröffentlichung zugestimmt.
- ☒ Ich habe den angestrebten Doktorgrad noch nicht erworben und bin nicht in einem früheren Promotionsverfahren für den angestrebten Doktorgrad endgültig gescheitert.
- ☐ Ich habe bereits am _____ bei der Fakultät für _____ _____ der Hochschule _____ unter Vorlage einer Dissertation mit dem Thema _____ die Zulassung zur Promotion beantragt mit dem Ergebnis: _____ _____

Die öffentlich zugängliche Promotionsordnung der TUM ist mir bekannt, insbesondere habe ich die Bedeutung von § 28 (Nichtigkeit der Promotion) und § 29 (Entzug des Doktorgrades) zur Kenntnis genommen. Ich bin mir der Konsequenzen einer falschen Eidesstattlichen Erklärung bewusst.

Mit der Aufnahme meiner personenbezogenen Daten in die Alumni-Datei bei der TUM bin ich

☒ einverstanden, ☐ nicht einverstanden.

Xinbo Cai

München, 17.04.2018, Unterschrift

I have a personal philosophy in life: If somebody else can do something that I'm doing, they should do it. And what I want to do is find things that would represent a unique contribution to the world - the contribution that only I, and my portfolio of talents, can make happen. Those are my priorities in life.

Neil deGrasse Tyson (1958-)

Acknowledgment

The research work in this dissertation has been carried out during the years 2014-2017 at the Institute for Electrical Drive Systems and Power Electronics (EAL), TUM.

First of all, I would like to thank my supervisor, Prof. Dr-Ing. Ralph Kennel, for all his inspiring guidance, constant encouragement, and support during my study. I really appreciated the freedom during all the stages of my work.

I would also like to thank Prof. Dr.Ing Dianguo Xu, one of the most respectable specialists in the field of power electronics and drives for reviewing and co-examining my dissertation.

An extraordinary gratitude goes out to Shanghai STEP Electric Corporation. In particular, I would like to thank Mr. Defa Ji, the chief executive officer (CEO) of the company, not only for providing the funding which allowed me to undertake this research but also for giving me the opportunity to study abroad.

I also had very fruitful discussions and collaborations with many of my colleagues at EAL, which made my work possible and pleasant. I would especially like to thank Dr.-Ing Zhenbin Zhang with whom I worked closely and published several papers. Many thanks to Mr. Dietmar Schuster for his help in my constructing process of the testbench. Those people, such as Dr.-Ing. Fengxiang Wang, Dr.-Ing. Zhe Chen, Hui Sun, Darshan Manoharan, Guangye Si, Hui Fang, Junxiao Wang, Wei Tian, Xiaonan Gao, Xicai Liu, etc., also deserve thanks for helping me.

The partial financial support of the China scholarship council (CSC) is gratefully acknowledged.

Thanks to all my family for their support.

Munich, Germany
Tuesday 17th April, 2018
Xinbo Cai

Abstract

This work belongs to the optimization of control methods for power converters and electrical drives. Main contributions are as follows: an analytical solution of both continuous and discrete optimum control for power converters and drives is given, focusing on computational efficiency and enhanced performance; a new DC-link voltage balancing method using the deadbeat control concept for three-level neutral point clamped converters is proposed, which is suitable for the control applications using space vector modulation; a simple and effective neutral-point voltage balancing technique is proposed within the model predictive control framework for three-level neutral point clamped converters, which decouples the neutral point voltage balance control and targets current tracking; a fixed gain filter is proposed to estimate the position, velocity, and acceleration in angular motion, with computational efficiency and less tuning effort.

***Index Terms*— Optimum control, predictive control, fixed gain filter, current control, power converters, electrical drives.**

Zusammenfassung

Diese Arbeit befasst sich mit der Optimierung von Regelungsverfahren für Stromrichter und elektrische Antriebe. Die wesentlichen Beiträge der Dissertation sind folgende: Eine analytische Betrachtung von kontinuierlichen als auch diskreten optimalen Regelungen für Stromrichter und Antriebe; dabei wird trotz deutlich reduzierter Rechenleistung ein verbessertes Regelungsergebnis erzielt. Ein neues Konzept zur Regelung der Zwischenkreismittelpunktspannung für Dreipunkt-NPC-Umrichter wird auf Basis eines Deadbeat-Algorithmus vorgeschlagen; dieser Ansatz ist für Regelungen mit Raumzeigemodulation (PWM) geeignet. Weiterhin wird eine einfache und trotzdem wirkungsvolle Regelung der Zwischenkreismittelpunktspannung nach dem Konzept der modelprädiktiven Regelung vorgeschlagen. Dieser Ansatz ermöglicht die Entkopplung von Mittelpunktspannung und Statorströmen. Ein Filter mit konstanten Parametern wird vorgeschlagen, um die Position, die Geschwindigkeit und die Beschleunigung der Rotationsbewegung abzuschätzen. Dieser Ansatz benötigt weniger Rechenleistung und verringert somit den Verarbeitungsaufwand.

***Index Terms*— Optimale Steuerung, prädiktive Regelung, Filter mit konstanter parameter, Aktuelle Kontrolle, Stromrichter, Elektrische Antriebs.**

Contents

Chapter 1

Introduction

This chapter gives an introduction to the research area studied in this thesis. Section 1.1 explains the main problems existing in industry that has motivated the research. In Section 1.2, the main contributions of this thesis are listed and briefly explained. Finally, Section 1.3 contains an outline of this thesis.

1.1 Research motivation

Industry 4.0 is considered as the next industrial revolution since its first presentation at the Hannover Messe (HM), 2014. A key part of industry 4.0 is the ability to convert the electrical energy to mechanical movements where the motion control of industrial electromechanics systems plays an important role. However, the increasing complexity of the design makes it difficult for applying in industry. Thus, the requirements of simple, economical, robustness, and efficient control system have created great enthusiasm to pave the path towards an optimal refined industry.

The components of motion control of industrial electromechanics systems may be split into four parts: the electrical drive, the converter, the real-time system, and motion sensor. Note that, both electrical drive and industry 4.0 require angular motion sensors for collecting essential position, velocity, and acceleration data. For electrical drives, the primary concern is the inner loop design of the controller. More precisely, it is the current tracking problem. For converters, the issue is about how to effectively incorporate the characteristic of the converter into the control algorithm. For real-time systems, a low complexity control algorithm is required. For the motion sensor, a simple and effective filter is required to get the feedback signal for the control algorithm.

Thus, the work presented in this thesis deals with the refinements of control algorithm in these four aspects according to the standard industrial requirements. Only in this way it can be incorporated successfully into a product that is acceptable to customers in the industry and translated into a valuable work.

In the following subsections, the motivations of this work are detailed.

1.1.1 Computational burden

Due to the flexibility, cost, programmability, and adaptability, the micro-controller unit (MCU) is popular to implement various types of controllers. In general, the tasks executed in the MCU are based on interrupt handling to achieve a real-time process. The interrupt service routine (ISR) is executed each control period. Therefore, the MCU must provide the computational capability to finish the ISR before next control period. In other words, due to the limited computational resource, the computation time for solving the control problem should not exceed the sampling interval. However, the MCU selected in the industry is limited due to the cost. In such case, we have to decrease the complexity of the control algorithm in the developments of controller. As an example, considering the case where model predictive control (MPC) is employed, the optimization problems are usually solved by the enumeration of the possible vectors. This leads to computational difficulties as numbers of the vectors increase, in particular for multilevel power converters. Hence it is important to obtain a control law with minimal complexity.

In this work, the complexity of the control system is reduced by explicitly computing (compared with using a numerical solver), taking into account only the feasible vectors (decreasing the enumeration directly), decoupling the control objects (decrease the enumeration indirectly), and translating variable calculation into constant calculation. All these methods are detailed in this work. Therefore, a common character of the presented methods in this work is the reduction of complexity.

1.1.2 Control algorithm

In control theory, the usual control problem is to find an adequate controller so that the output of the plant follows a desired control signal (reference), which may be a fixed or changing value. Generally, there are four means to evaluate the tracking performance in the conventional controller (e.g. proportional–integral–derivative (PID) controller) design.

- The tracking error.
- The rising time.
- The overshoot.
- The settling time.

The controller should be designed to minimize rising time and settling time while keeping an acceptable overshoot and tracking error. Following this guide, the trade-off between the four terms creates great challenges on the control system design. Besides, the controller should be designed under some constraints. Moreover, it is difficult to involve the four evaluate functions in the online calculation.

To solve these problems, the model predictive control has been introduced as a highly successful control method in the process industries. The main reason for this success is

the inherent ability to handle constraints and evaluate the control performance simultaneously. It selects an optimal vector, which is kept for a complete control interval, from a finite control set. This leads to higher control variable ripples than the classical modulator based techniques under a similar sampling interval. Increasing the control frequency would be helpful for reducing the ripples. However, this is not compliant with the requirements of industry. Thus, how to reduce the control variable ripples within reasonable efforts is one of the problems that should be solved. This thesis will solve the problem and form a discrete solution of optimum control which adopts half explicitly computing and half enumeration process.

Additionally, for the algorithms using modulator, linear quadratic regulator (LQR) control has been introduced as one of solutions that can be used for minimizing the control objectives. Although the control law is an explicit equation, the explicit equation depends on a Riccati equation which is normally very difficult to get the explicit solution. Besides, constraints are not involved in the control law. Thus, how to get an explicit solution operating on the constraints is eager to be solved. This thesis will form a continuous solution of optimum control that solves the problem entirely.

1.1.3 Converters

A general problem in the converter is the voltage unbalance of the direct current (DC)-link capacitors. For the two-level converter, the voltages of the DC-link capacitors can be balanced by two voltage-sharing resistors. However, the three-level neutral point clamped (NPC) converters are particularly affected by the neutral-point current. Therefore, only adopting passive voltage-sharing resistors is not enough to balance the voltages.

To avoid increasing the hardware cost, software-based methods to overcome the neutral-point unbalance are usually adopted. They can be mainly classified as carrier-based techniques, which in essence are adjusting the time of the redundant vectors. In this strategy, a proportional-integral (PI) controller is usually employed to generate the duty for redundant voltage vectors. Although the results show that the PI-based strategy is capable of keeping the neutral-point voltage stable, the performance is highly dependent on the PI gain which is hard to be selected. To overcome this problem, this work proposes a deadbeat-based method for decreasing the tuning efforts.

Another control scheme is using direct model predictive control (DMPC), which combines the cost function with weighting factors for voltage balance and the cost function for current tracking together as a new cost function. The drawback of this method is obvious: it has an assumption that the weighting factor for the voltage balance is properly selected. However, one cannot assure this condition in most working cases. In fact, in many cases it may not be possible at all, the component of voltage balance and the component of current tracking are closely coupled. On the other hand, when this method is used, it is difficult to ensure one of the control objects to be well achieved while keeping a good performance of another. this work proposes a decoupled solution to solve the problem while reducing the enumeration complexity.

1.1.4 Observer and filter

A good state observer or filter will improve the system robustness. The Kalman filter (KF) is an optimal observer for linear systems and Gaussian distributions. It does the best (the feedback gain for the innovations is recalculated at each step) within its capability to minimize the expected value of the square of the error between the actual system state and the estimated one. However, it has repeatedly been noted, that one of the difficulties is its computational burden.

The Luenberger observer (LO) requires less computational time due to the fixed feedback gain. The primary challenge in the applications is that the feedback gain design is heavily dependent on the accuracy of the mathematical model of the plant.

This work proposes a fixed gain filter which combines the advantages of KF and LO. In the case of study, position, velocity, and acceleration estimates are obtained from a position measurement only.

1.2 Contributions

The main theoretical contributions of this thesis are on the explicit form of optimum control for both continuous and discrete solution.

In this work, the conventional MPC problem is extended to the frame of optimum control with the explicit solution of the proposed problem. Therefore, it is possible to avoid the complicated calculation of Riccati equation or decrease the complete enumeration of all possible case into an acceptable complexity.

More specifically, within this work the following aspects have been achieved:

- By using a so-called fixed gain filter, excellent dynamics and accuracy of the position, velocity and acceleration estimation in the electrical drives can be achieved. More importantly, there is only one parameter used to tune the performance of the proposed observer, which makes it very easy to put into practice.

- A general optimum control for power converters and drives is proposed. both continuous and discrete solutions are derived and unified in the frame of *optimum control*. The *continuous solution* utilizes the averaged continuous-time model of the system and is capable of dealing with multiple system constraints, showing good performance with fewer calculation efforts. This method is similar as the well-known deadbeat controller. The advantage is that it is capable of dealing with multiple system constraints while the *discrete solution* takes the finite set of the power converter switching vectors into consideration and the state transition of the system can be predicted with a chosen vector. Both methods require fewer calculation efforts compared to the well-known finite control set model predictive control (FCS-MPC) method, which makes it very suitable for practical realization.

- A *new* DC-link voltage balancing method using the deadbeat control (DBC) concept for three-level NPC converters is proposed and experimentally verified. The DC-link balancing control algorithm is designed and incorporated into a space vector modulation (SVM) method, which allows adjusting the neutral point current continuously.
- A decoupled neutral point voltage balancing method for FCS-MPC is also proposed.

1.3 Outline

The outline of this thesis is as follows.

In Chapter 2, the necessary mathematical background for the remaining parts of the thesis is reviewed.

The basic theoretical frame is presented in Chapter 3. In this chapter, both continuous and discrete optimum solution are discussed. The explicit formulation for optimum control is also given. The performance of the proposed controller is compared with other state of the art methods.

In Chapter 4, a detailed application for control of the three level converter is presented. Both SVM based DC-link voltage balance control and DC-link voltage balance control under MPC scheme are demonstrated and analyzed.

In Chapter 5, the necessary observers used in this thesis are presented. Among them, the fixed gain Kalman filter is derived, and the stability is proven.

The thesis finishes with some concluding remarks and thoughts on future work in Chapter 6.

Chapter 2

Background and preliminaries

This chapter introduces the background and mathematical preliminaries. Firstly, the symbols and abbreviations used in this work are discussed. Then, the mathematical models of power electronics and drives are recalled. These models include:

- two-level converter,
- three-level neutral point clamped (NPC) converter,
- permanent magnet synchronous motor (PMSM),
- and alternating current induction motor (ACIM).

Moreover, the basic methods to convert an analog system into a digital system are presented in this chapter. Finally, the classical control schemes of electrical drives are revisited and discussed. These include:

- speed control scheme of indirect field oriented control (IFOC),
- speed control scheme of direct field oriented control (DFOC),
- direct torque flux control (DTFC),
- DTFC with modulator,
- and model predictive control (MPC).

2.1 Nomenclature

In this thesis, the mathematical notation generally follows the guidelines of international organization for standardization (ISO). Thus, matrices are denoted by a bold capital letter; Vectors (column) are indicated by boldface lowercase letters. Scalars and scalar

valued functions are then denoted by non-bolded italic font letters. Some examples are listed in Table 2.1. The identity matrix and null matrix are written as $\mathbf{I}$, $\mathbf{0}$, respectively. However, the dimensions of $\mathbf{I}$ and $\mathbf{0}$ are not stated unless self-evident is impossible. The superscript $^\top$ denotes the transpose of a matrix. Thus, the transpose of a matrix $\mathbf{A}$ is denoted by $\mathbf{A}^\top$ and the inverse of a matrix $\mathbf{A}$ is $\mathbf{A}^{-1}$.

The notions of positive-definite and positive-semidefinite (or nonnegative- definite) matrices are employed in the derivation of optimum control. For such matrices, $\mathbf{A} > \mathbf{B}$ ($\mathbf{A} \geq \mathbf{B}$) means that $\mathbf{A} - \mathbf{B}$ is positive-definite (positive-semidefinite).

Table 2.1: General principle of symbols

Item	**Format**	**Example**
Scalars	Italic font letters	x
Vectors	Bold lowercase letters	$\boldsymbol{x}$
Matrices	Bold capitals	$\mathbf{X}$
References	Star superscript	x^*

The meaning of symbols is usually defined and explained locally. However, a general meaning of symbols is listed in Appendix A.2. .

In addition to that, international system of units (SI) is used unless units are mentioned explicitly in a few places.

2.2 Mathematical basics

2.2.1 Coordinate transformation

The coordinate transformation theory is a public knowledge, so the detailed explanation is not going to be discussed. The conversion from the three-phase coordinate system (abc frame) to an equivalent two-phase orthogonal system ($\alpha\beta$ frame) is called Clark transformation ($\mathbf{T}_{abc}$) [1]. The geometric interpretation can be found in Figure 2.1. Generally, the conversion from $\alpha\beta$ frame to the rotational coordinate (dq frame) is called Park transformation ($\mathbf{T}_{\alpha\beta}$) [2, 3]. The geometric interpretation can be found in Figure 2.2.

The vector $\boldsymbol{v}$ can be expressed in abc frame by

$$\boldsymbol{v} = v_a \cdot e^{j0} + v_b \cdot e^{j\frac{2\pi}{3}} + v_c \cdot e^{j\frac{4\pi}{3}}. \tag{2.1}$$

The vector $\boldsymbol{v}$ can also be expressed in $\alpha\beta$ frame by

$$\boldsymbol{v} = v_\alpha \cdot e^{j0} + v_\beta \cdot e^{j\frac{\pi}{2}} = v_\alpha + j \cdot v_\beta. \tag{2.2}$$

According to Equation (2.1) and (2.2), the $\mathbf{T}_{abc}$ in a balanced system can be derived from

$$\begin{bmatrix} v_\alpha \\ v_\beta \end{bmatrix} = \mathbf{T}_{abc} \cdot \begin{bmatrix} v_a \\ v_b \\ v_c \end{bmatrix} = \frac{2}{3} \begin{bmatrix} 1 & -\frac{1}{2} & -\frac{1}{2} \\ 0 & \frac{\sqrt{3}}{2} & -\frac{\sqrt{3}}{2} \end{bmatrix} \begin{bmatrix} v_a \\ v_b \\ v_c \end{bmatrix}. \tag{2.3}$$

The inverse Clark transformation ($\mathbf{T}_{abc}^{-1}$) can be derived from[1]

$$\begin{bmatrix} v_a \\ v_b \\ v_c \end{bmatrix} = \mathbf{T}_{abc}^{-1} \cdot \begin{bmatrix} v_\alpha \\ v_\beta \end{bmatrix} = \begin{bmatrix} 1 & 0 \\ -\frac{1}{2} & \frac{\sqrt{3}}{2} \\ -\frac{1}{2} & -\frac{\sqrt{3}}{2} \end{bmatrix} \begin{bmatrix} v_\alpha \\ v_\beta \end{bmatrix}. \tag{2.4}$$

In the same way, the vector $\boldsymbol{v}$ can also be expressed in dq frame by

$$v = v_d \cdot e^{j\theta} + v_q \cdot e^{j\left(\theta + \frac{\pi}{2}\right)} = v_\alpha + j \cdot v_\beta \tag{2.5}$$

Thus, the $\mathbf{T}_{\alpha\beta}$ is described by the following equation:

$$\begin{bmatrix} v_d \\ v_q \end{bmatrix} = \mathbf{T}_{\alpha\beta} \cdot \begin{bmatrix} v_\alpha \\ v_\beta \end{bmatrix} = \begin{bmatrix} \cos(\theta) & \sin(\theta) \\ -\sin(\theta) & \cos(\theta) \end{bmatrix} \begin{bmatrix} v_\alpha \\ v_\beta \end{bmatrix}, \tag{2.6}$$

where θ is the angle between the d-axis and α-axis. The inverse Park transformation ($\mathbf{T}_{\alpha\beta}^{-1}$) can be written as

$$\begin{bmatrix} v_\alpha \\ v_\beta \end{bmatrix} = \mathbf{T}_{\alpha\beta}^{-1} \cdot \begin{bmatrix} v_d \\ v_q \end{bmatrix} = \begin{bmatrix} \cos(\theta) & -\sin(\theta) \\ \sin(\theta) & \cos(\theta) \end{bmatrix} \begin{bmatrix} v_d \\ v_q \end{bmatrix}. \tag{2.7}$$

Note that all the transformations above are magnitude invariant. This kind of transformation is useful in the normalized systems which will be discussed in Section 2.2.3.

2.2.2 Discretization of analog systems

Many controllers are developed in the continuous-time domain, and they can provide continuous processing of the feedback signal. They are therefore used for high bandwidth control systems. Many analytical tools have also been developed for many years which make it easy to design an analog controller. However, the analog controllers are usually implemented by hardware. Thus, the analog controllers suffer easily from the component aging and temperature drifts. On the contrary, digital controllers have many advantages. They are not easily influenced by component aging and temperature drift while providing stable performance. Hence, the final controllers should be implemented in digital form. The methods converting existing continuous-time/analog signal to discrete-time/digital signal or from s-domain to z-domain are listed in this section.

[1] This case is derived by adding a third parameter in the framework of the theory of the symmetrical components.

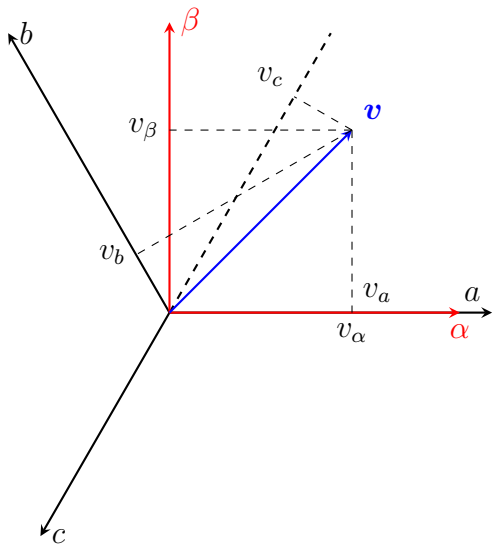

Figure 2.1: Clark transformation.

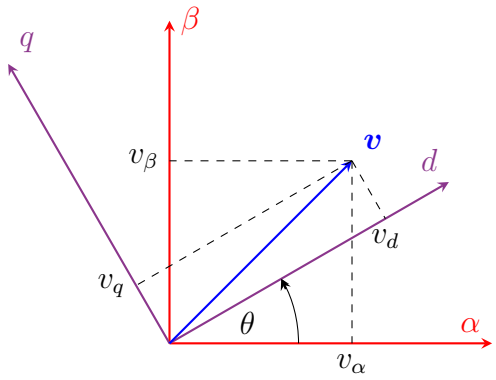

Figure 2.2: Park transformation.

2.2.2.1 Zero-order hold

The most commonly used technique is Zero-order hold (ZOH) which assumes that the controlled object is actuated by a ZOH (e.g. digital-to-analog converter (DAC)). The ZOH describes the effect of converting a discrete-time signal to a continuous-time signal in such a manner that holding each sample value for one sample interval. The conversion from s-domain to z-domain can be described by the following equation:

$$G(z) = \mathcal{Z}\left(\frac{1-e^{-sT_s}}{s}G(s)\right) = \left(1-z^{-1}\right)\mathcal{Z}\left(\frac{G(s)}{s}\right), \tag{2.8}$$

where T_s is the sampling period, $G(s)$ is the transfer function in s-domain.

Another way is found by substituting

$$s = \frac{z-1}{T_s z}. \tag{2.9}$$

2.2.2.2 Pole–zero matching method

This method is also called the matched $\mathcal{Z}$-transform method or the pole–zero mapping. In this technique, all poles and zeros of the s-plane are directly mapped to z-plane with the equation:

$$z = e^{sT_s}. \tag{2.10}$$

This method applies only to single-input and single-output (SISO) systems. Especially, when poles or zeros are located at the origin in s-plane, additional poles or zeros should be added at $z = -1$ in z-plane. The continuous and discretized systems have matching direct current (DC) gains at the critical frequency by choosing an arbitrary gain constant.

2.2.2.3 Bi-linear transform

The bi-linear transform (also known as Tustin or trapezoidal approximation) uses the relationship

$$s = \frac{2\,z-2}{T_s\,(z+1)}. \tag{2.11}$$

to transform a s-domain function to z-domain which yields the best frequency-domain match between the continuous-time and discretized systems.

2.2.3 Normalization values

In former times, most micro-controller units (MCUs) are fixed-point arithmetic processors. So, only a finite amount of word length (i.e. 4, 8, 16 or 32 bit) can be used to represent the physical signals or some parameters. Therefore, the signals and parameters have to be scaled according to the word length of the processor. In this process, quantization noise due to the small scale factor may cause instability of the system. Additionally, if large scale factors are chosen, overflow of registers may occur during the calculation.

Working with poorly scaled models can cause a severe loss of accuracy and puzzling results. To minimize the effects caused by word length, choosing a proper scale factor is critical. The scale factor should support the full range of the physical signals and system parameters. The process of selecting appropriate scale factor is called as normalization. For a fixed point arithmetic processor, normalization is essential to achieve the requirements of accuracy.

One of the ways to avoid normalization is using floating-point number due to the large dynamic range which is enough for most control systems. Meanwhile, using floating-point number can release the burden of identifying the dynamic range of the system. Moreover, the development cost is more significant than the expense of a floating-point arithmetic processor. Therefore, it seems that it is not necessary anymore to use normalized values for the implementation of control algorithms. However, using normalization values (per unit value) has the following advantages:

- A similar apparatus (motors, transformers, generators) will have similar per-unit impedance and losses expressed on their rating, regardless of their absolute size.
- Per-unit data can be checked rapidly for gross errors.
- Both hand and automatic calculations are simplified.
- It improves numerical stability of automatic calculation methods.

which motivate us still using normalization in a floating-point arithmetic processor.

In this thesis, firstly, the normalized power (P_{base}), normalized phase current (I_{base}) , and normalized phase voltage(V_{base}) for the three phase system are defined as follows:

$$V_{base} = \frac{\sqrt{2}V_{rated}}{\sqrt{3}}, \tag{2.12}$$

$$I_{base} = \sqrt{2}I_{rated}, \tag{2.13}$$

$$P_{base} = P_{rated}, \tag{2.14}$$

$$F_{base} = F_{rated}, \tag{2.15}$$

where V_{rated}, I_{rated}, P_{rated}, and F_{rated} are the rated voltage of the line-line voltage, rated current, rated power, and rated frequency, respectively, which can be found on the name-plate of a motor or other apparatus. Then, the following per-unit system formulas for electrical systems are derived:

$$R_{base} = \frac{U_{base}}{I_{base}}, \tag{2.16}$$

$$\omega_{base} = 2\pi F_{base}, \tag{2.17}$$

$$\theta_{base} = 2\pi, \tag{2.18}$$

$$\omega_{mbase} = \frac{\omega_{base}}{p}, \tag{2.19}$$

$$L_{base} = \frac{R_{base}}{\omega_{base}}, \tag{2.20}$$

$$\psi_{base} = \frac{U_{base}}{\omega_{base}}, \tag{2.21}$$

$$T_{base} = \frac{P_{base}}{\frac{\omega_{base}}{\frac{p}{2}}} = \frac{p}{2} \times \frac{P_{base}}{\omega_{base}}, \tag{2.22}$$

$$H = \frac{\frac{1}{2}J\omega_m^2}{P_{base}}, \tag{2.23}$$

$$J_{base} = \frac{P_{base}H}{\frac{\omega_{mbase}}{2}}, \tag{2.24}$$

$$B_{base} = \frac{T_{base}}{\omega_{mbase}}, \tag{2.25}$$

where R_{base}, ω_{base}, θ_{base}, ω_{mbase}, L_{base}, ψ_{base}, T_{base}, J_{base}, and B_{base} are the base value of resistance, electrical angle velocity, mechanical angle velocity, inductance, flux, torque, inertia, and friction, respectively. All used physical quantities are given in SI units.

2.3 Converters

2.3.1 Two-level inverter

The topology of a two-level voltage source power converter is shown in Figure 2.3. There are three legs which are denoted by a, b, c. Each leg has two switches (the upper switch of the leg x in two level inverter ($x \in \{a, b, c\}$) (S_x), the lower switch of the leg x in two level inverter ($x \in \{a, b, c\}$) ($\bar{S}_x$)) and two diodes. S_x and $\bar{S}_x$ are complementary in ideal states. For describing the behavior of the ideal switches, the switch function of the leg x ($x \in \{a, b, c\}$) (s_x) is defined as

$$s_x = \begin{cases} 1 & \Longleftrightarrow \; S_x = 1 \wedge \bar{S}_x = 0 \\ -1 & \Longleftrightarrow \; S_x = 0 \wedge \bar{S}_x = 1 \end{cases}. \tag{2.26}$$

Without considering the dead time of the switches, the universal set of the switching state vector $(s_a, s_b, s_c)^\top$ for two level converter ($\mathcal{U}^2$) has 8 possibilities which is shown in Figure 2.4, where $\mathcal{U}^2$=$\{(0,0,0)^\top, (0,0,1)^\top, (0,1,0)^\top, (0,1,1)^\top, (1,0,0)^\top, (1,0,1)^\top, (1,1,0)^\top, (1,1,1)^\top\}$. The converter switching state is denoted by $\boldsymbol{u_j} \in \mathcal{U}^2$ ($j \in \{0, 1...7\}$).

Additionally, the direction of the phase current of the leg x ($x \in \{a, b, c\}$) ($\boldsymbol{i}_x$) is defined from the converter to load.

Therefore, the pole voltage of phase a (v_{ao}), the pole voltage of phase b (v_{bo}), and the pole voltage of phase c (v_{co}) can be defined by the switch function and given as follows:

$$\begin{aligned} v_{ao} &= \frac{v_{dc}}{2}s_a, \\ v_{bo} &= \frac{v_{dc}}{2}s_b, \\ v_{co} &= \frac{v_{dc}}{2}s_c. \end{aligned} \tag{2.27}$$

To solve the voltage of phase a to neutral point (v_{an}), the voltage of phase b to neutral point (v_{bn}), and the voltage of phase c to neutral point (v_{cn}), consider the following

equations:

$$\begin{aligned} v_{ao} &= v_{an} + v_{no}, \\ v_{bo} &= v_{bn} + v_{no}, \\ v_{co} &= v_{cn} + v_{no}. \end{aligned} \tag{2.28}$$

Due to the absence of a neutral connection in the load, the phase current of the leg a (i_a), the phase current of the leg b (i_b), and the phase current of the leg c (i_c) respect

$$i_a + i_b + i_c = 0. \tag{2.29}$$

For an arbitrary balanced load, v_{an}, v_{bn}, and v_{cn} are constrained by

$$v_{an} + v_{bn} + v_{cn} = 0. \tag{2.30}$$

By combining Equation (2.28) and (2.30), the voltage between O and N is solved as

$$v_{no} = \frac{1}{3}\left(v_{ao} + v_{bo} + v_{co}\right). \tag{2.31}$$

Thus, v_{an}, v_{bn}, and v_{cn} can be modeled as

$$\begin{bmatrix} v_{an} \\ v_{bn} \\ v_{cn} \end{bmatrix} = \frac{1}{3}\begin{bmatrix} 2 & -1 & -1 \\ -1 & 2 & -1 \\ -1 & -1 & 2 \end{bmatrix}\begin{bmatrix} v_{ao} \\ v_{bo} \\ v_{co} \end{bmatrix} = \frac{v_{dc}}{6}\begin{bmatrix} 2 & -1 & -1 \\ -1 & 2 & -1 \\ -1 & -1 & 2 \end{bmatrix}\begin{bmatrix} s_a \\ s_b \\ s_c \end{bmatrix}. \tag{2.32}$$

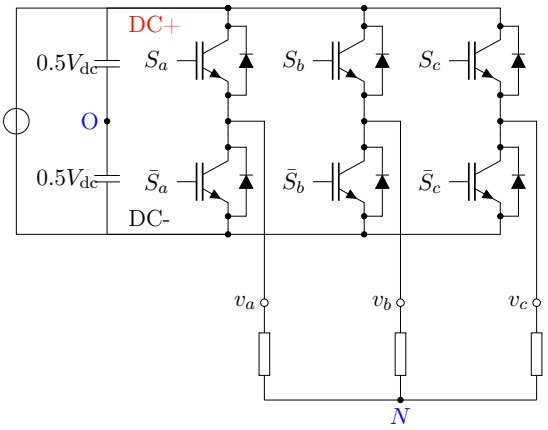

Figure 2.3: Two-level power converter.

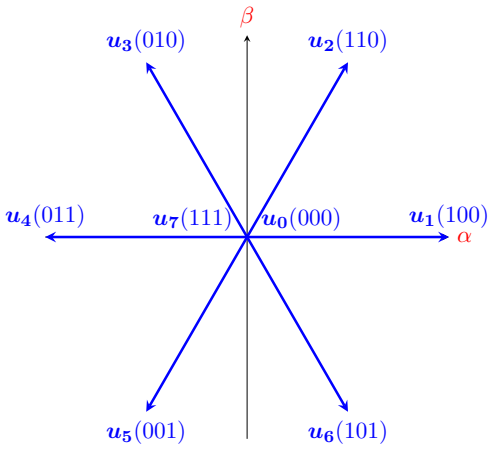

Figure 2.4: Permissible voltage vectors.

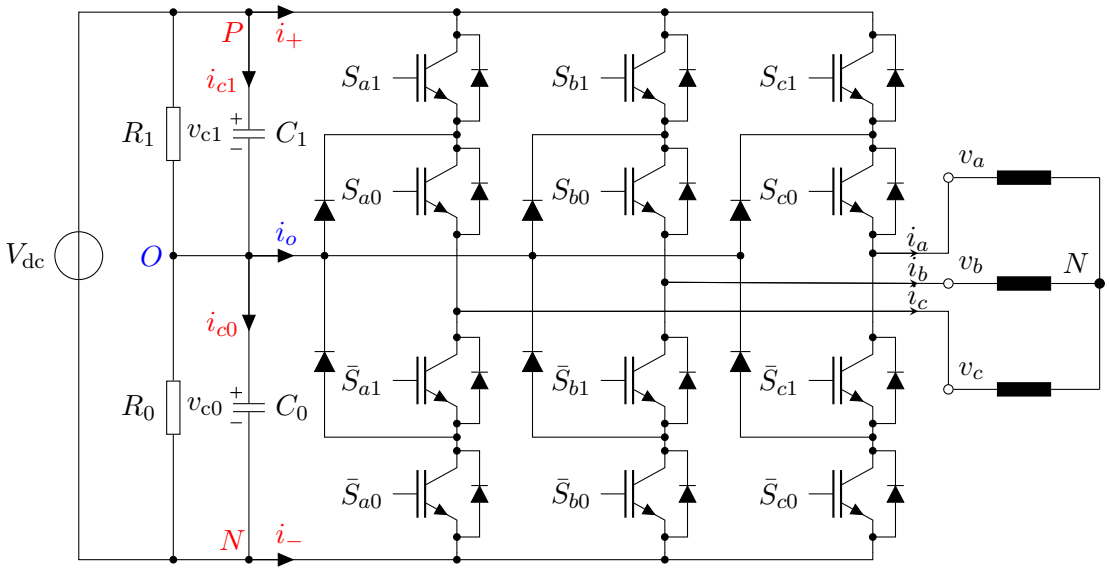

Figure 2.5: Topology of the Three phase Three-level NPC.

2.3.2 Three-level neutral point clamped inverter

Figure 2.5 shows a simple three level NPC converter. As can be seen from Figure 2.5 , there are three legs in the three level NPC converter. Each leg has six devices which are the j^{th} switch of the upper leg x in three level inverter (S_{xj}), the j^{th} switch of the lower leg x in three level inverter ($\bar{S}_{xj}$), and two diodes, where $x \in [a, b, c]$, $j \in [0, 1]$.

To avoid the possible short circuit, the switches S_{xj} and $\bar{S}_{xj}$ are complementary. To avoid the inner switches suffering from high voltage, the outer two switches are not allowed to be in *on* state at the same time. Therefore, three different phase voltage outputs exist (hence, it is called three-level). Table 4.1 lists the pole voltage of phase x ($x \in \{a, b, c\}$) (v_{xo}) under different switch states, accordingly, the switch function of the leg x ($x \in \{a, b, c\}$) for the three-level NPC is defined as

$$s_x = \begin{cases} 1 & \equiv P \iff (S_{x1} = 1 \wedge \bar{S}_{x1} = 0 \wedge S_{x0} = 1 \wedge \bar{S}_{x0} = 0) \\ 0 & \equiv O \iff (S_{x1} = 0 \wedge \bar{S}_{x1} = 1 \wedge S_{x0} = 1 \wedge \bar{S}_{x0} = 0) \\ -1 & \equiv N \iff (S_{x1} = 0 \wedge \bar{S}_{x1} = 1 \wedge S_{x0} = 0 \wedge \bar{S}_{x0} = 1) \end{cases} \tag{2.33}$$

to mathematically describe the switching behavior of such converters.

Thus, the universal set of the switching state vector $(s_a, s_b, s_c)^\top$ for three level converter ($\mathcal{U}^3$) has 27 possibilities which is shown in Figure 2.6. $\mathcal{U}^3$ can be further divided into four categories:

1. the set of zero vector for three level converter ($\mathcal{U}_z^3$), where $\mathcal{U}_z^3 = \{(-1, -1, -1)^\top, (0, 0, 0)^\top, (1, 1, 1)^\top\}$,

2. the set of small vector for three level converter ($\mathcal{U}_s^3$), where $\mathcal{U}_s^3 = \{(0, -1, -1)^\top,$

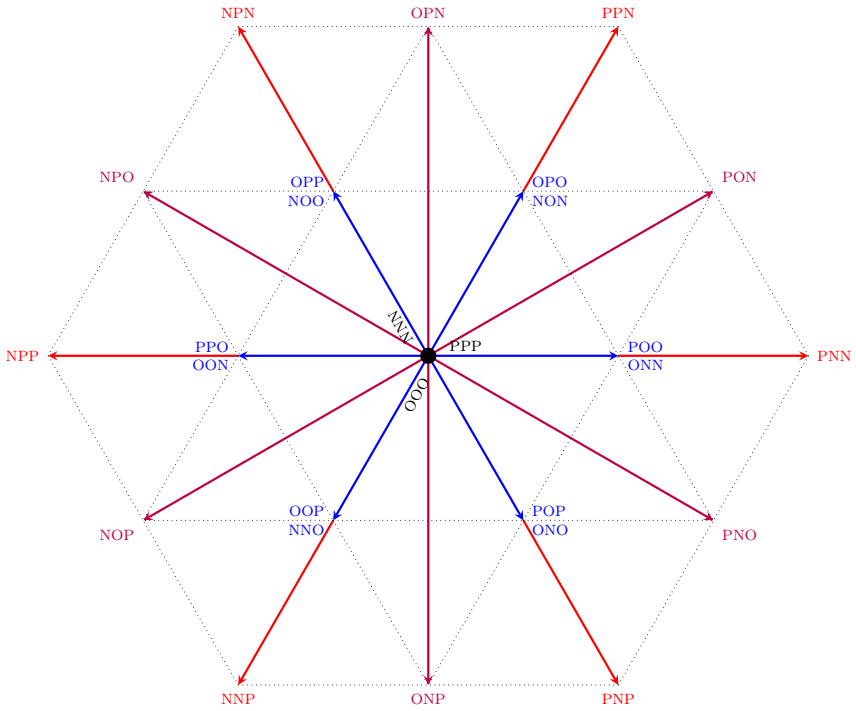

Figure 2.6: Vectors of the NPC.

Table 2.2: Switch function and pole voltages of a three-level NPC inverter leg x

v_{xo}	s_x	**state**	S_{x1}	$\bar{S}_{x1}$	S_{x0}	$\bar{S}_{x0}$
v_{c1}	1	P	1	0	1	0
0	0	O	0	1	1	0
v_{c0}	-1	N	0	1	0	1

$(-1,0,-1)^\top$, $(-1,0,0)^\top$, $(0,0,-1)^\top$, $(-1,-1,0)^\top$, $(0,-1,0)^\top$, $(1,0,0)^\top$, $(0,1,0)^\top$, $(0,1,1)^\top$, $(1,1,0)^\top$, $(0,0,1)^\top$, $(1,0,1)^\top$},

3. the set of medium vector for three level converter ($\mathcal{U}_m^3$), where $\mathcal{U}_z^3 = \{(-1,-1,-1)^\top$, $(0,0,0)^\top$, $(1,1,1)^\top\}$,

4. the set of big vector for three level converter ($\mathcal{U}_b^3$), where $\mathcal{U}_b^3 = \{(1,-1,-1)^\top$, $(1,1,-1)^\top$, $(-1,1,-1)^\top$, $(-1,1,1)^\top$, $(-1,-1,1)^\top$, $(1,-1,1)^\top\}$,

The relationship between these four sets and $\mathcal{U}^3$ is $\mathcal{U}^3 = \mathcal{U}_z^3 \cup \mathcal{U}_s^3 \cup \mathcal{U}_m^3 \cup \mathcal{U}_b^3$.

Furthermore, these sets have the following characters:

1. $\mathcal{U}_z^3$ is redundant, however, it does not cause a neutral point current.

2. $\mathcal{U}_s^3$ has redundant pairs which is controllable to the neutral point current compared with $\mathcal{U}_m^3$.

3. $\mathcal{U}_s^3$ and $\mathcal{U}_m^3$ will contribute to the neutral point current production (to be explained in Section 4.1).

4. $\mathcal{U}_b^3$ is not redundant and it does not cause a neutral point current.

As is shown in Figure 2.6, $\mathcal{U}_s^3$ and $\mathcal{U}_z^3$ are redundant. Besides, $\mathcal{U}_s^3$ can be further divided into two categories: the set of small vector containing P state ($\mathcal{U}_{sp}^3$) and the set of small vector containing N state ($\mathcal{U}_{sn}^3$). In the same way, $\mathcal{U}_z^3$ are further divided into the set of zero vector containing P state ($\mathcal{U}_{zp}^3$), the set of zero vector containing O state ($\mathcal{U}_{zo}^3$), and the set of zero vector containing N state ($\mathcal{U}_{zn}^3$).

By using the voltage between O and N in three-level NPC converter (v_{c0}) and the voltage between P and O in three-level NPC converter (v_{c1}), the pole voltages is described in Table 2.2. Then, v_{xo} can be rewritten by the following equation

$$v_{xo} = \frac{1}{2}\left(v_{c1} + v_{c0}\right) s_x + \frac{1}{2}\left(v_{c1} - v_{c0}\right) |s_x| \,. \tag{2.34}$$

Thus, by combining equations (2.34), (2.30), (2.28), (2.31), v_{an}, v_{bn}, and v_{cn} can be obtained as

$$\begin{aligned}\begin{bmatrix} v_{an} \\ v_{bn} \\ v_{cn} \end{bmatrix} =& \frac{v_{c1}}{6} \begin{bmatrix} 2 & -1 & -1 \\ -1 & 2 & -1 \\ -1 & -1 & 2 \end{bmatrix} \begin{bmatrix} s_a + |s_a| \\ s_b + |s_b| \\ s_c + |s_c| \end{bmatrix} \\ &+ \frac{v_{c0}}{6} \begin{bmatrix} 2 & -1 & -1 \\ -1 & 2 & -1 \\ -1 & -1 & 2 \end{bmatrix} \begin{bmatrix} s_a - |s_a| \\ s_b - |s_b| \\ s_c - |s_c| \end{bmatrix}. \end{aligned} \tag{2.35}$$

This model will be used for estimating the candidate voltage in the model predictive control.

2.4 Induction motor

The induction motors are by far the most popular motor used in industrial drives due to their good characteristics (i.e. They are rugged, reliable and economical). The mathematical model of induction motor has been well explained in the past literature [1,4]. For better understanding and analyzing the relationship of flux, current, and torque, a detailed mathematical model of the induction motor is revisited in this section.

2.4.1 Complex representation of induction motor

An induction machine can be described using a set of complex equations in arbitrary rotating reference frame as:

$$\boldsymbol{v}_s = R_s \boldsymbol{i}_s + s\boldsymbol{\psi}_s + j\omega\boldsymbol{\psi}_s, \tag{2.36a}$$

$$\boldsymbol{v}_r = R_r \boldsymbol{i}_r + s\boldsymbol{\psi}_r + j\left(\omega - \omega_r\right)\boldsymbol{\psi}_r, \tag{2.36b}$$
$$\boldsymbol{\psi}_s = L_s \boldsymbol{i}_s + L_m \boldsymbol{i}_r, \tag{2.36c}$$
$$\boldsymbol{\psi}_r = L_r \boldsymbol{i}_r + L_m \boldsymbol{i}_s, \tag{2.36d}$$

where $\boldsymbol{v}_s$ is the stator voltage, $\boldsymbol{v}_r$ is the rotor voltage, R_s is the stator resistance, R_r is the rotor resistance, L_s is the stator inductance, L_r is the rotor inductance, L_m is the mutual inductance, $\boldsymbol{i}_s$ is the stator current, $\boldsymbol{i}_r$ is the rotor current, ψ_s is the stator flux, ψ_r is the rotor flux, s denotes the differential operator to the vector of variables.

The rotor voltage vector $\boldsymbol{v}_r$ is equal to zero due to the short-circuit of the rotor winding when a squirrel-cage motor is applied. ω is the rotating speed of the reference frame. ω_r is the rotor speed. When a $\alpha\beta$ frame is used, ω is zero.

2.4.2 State space representation in dq frame

By rearranging Equation 2.36 and after some further calculations, the state space model of an induction motor can be described as follows:

$$\begin{bmatrix} \frac{d\boldsymbol{i}_s}{dt} \\ \frac{d\boldsymbol{\psi}_r}{dt} \end{bmatrix} = \begin{bmatrix} -\frac{R_s {L_r}^2 + R_r {L_m}^2}{\sigma L_s {L_r}^2} - j\omega & \frac{L_m R_r}{\sigma L_s L_r^2} - j\frac{L_m \omega_r}{\sigma L_s L_r} \\ \frac{L_m R_r}{L_r} & -\frac{R_r}{L_r} - j\left(\omega - \omega_r\right) \end{bmatrix} \begin{bmatrix} \boldsymbol{i}_s \\ \boldsymbol{\psi}_r \end{bmatrix} + \begin{bmatrix} \frac{1}{\sigma L_s} \\ 0 \end{bmatrix} \boldsymbol{v}_s, \tag{2.37}$$

where $\sigma = 1 - \frac{L_m^2}{L_s L_r}$.

2.4.3 State space representation in $\alpha\beta$ frame

Since the reference frame is $\alpha\beta$ frame, the rotating speed of the reference frame is zero which is $\omega = 0$. By substituting $\omega = 0$ to Equation (2.37), the state space model of an induction motor can be easily obtained as follows:

$$\begin{bmatrix} \frac{d\boldsymbol{i}_s}{dt} \\ \frac{d\boldsymbol{\psi}_r}{dt} \end{bmatrix} = \begin{bmatrix} -\frac{L_m^2 R_r + L_r^2 R_s}{\sigma L_s L_r^2} & \frac{L_m R_r}{\sigma L_s L_r^2} - j\frac{L_m \omega_r}{\sigma L_s L_r} \\ \frac{L_m R_r}{L_r} & -\frac{R_r}{L_r} + j\omega_r \end{bmatrix} \begin{bmatrix} \boldsymbol{i}_s \\ \boldsymbol{\psi}_r \end{bmatrix} + \begin{bmatrix} \frac{1}{\sigma L_s} \\ 0 \end{bmatrix} \boldsymbol{v}_s, \tag{2.38}$$

where $\sigma = 1 - \frac{L_m^2}{L_s L_r}$.

2.4.4 Mechanical model

Finally, the electric torque produced by the induction machine can be expressed in terms of the stator current and stator flux:

$$T_e = \frac{3}{2} p \Im(\boldsymbol{\psi}_s \times \boldsymbol{i}_s), \tag{2.39}$$

where p is the pole pair number, T_e denotes the electromagnetic torque.

The mechanical dynamic equation is given by

$$J\frac{d\omega_m}{dt} + B\omega_m = T_e - T_l, \tag{2.40}$$

where T_l is the load torque, J presents the inertia, B is the friction coefficient. ω_m is the mechanical rotor speed and it is related to the electric rotor speed ω:

$$\omega_m = \frac{\omega}{p}, \tag{2.41}$$

where p is the number of pole pairs.

Due to the using of the encoder, the exact position of the rotor (θ_m) can be obtained easily. The relationship between rotor position and rotor speed is described as:

$$\frac{d\theta_m}{dt} = \omega_m. \tag{2.42}$$

So far, both the electrical model and mechanical model of the induction motor are presented.

2.5 Permanent magnet synchronous motor

The principles of operation of induction machines have been simply described in Section 2.4. The rotor windings of an induction machine are short-circuited. A certain amount of slip is required to balance the induced rotor current and the applied load. The construction of stator windings and stator magnetic circuit of the PMSM is rather similar to that of the induction machine. However, the rotor is built by a permanent magnet. The flux generated by the permanent magnet aligns with the rotor.

If the rotor reference frame is aligned with the permanent flux, an ideal model of PMSM in synchronous reference frame dq is classically modeled by the following equations:

$$\begin{aligned} v_{sd} &= R_s i_{sd} + \tfrac{d\psi_{sd}}{dt} - \omega\psi_{sq}, \\ v_{sq} &= R_s i_{sq} + \tfrac{d\psi_{sq}}{dt} + \omega\psi_{sd}, \\ \psi_{sd} &= L_d i_{sd} + \psi_r, \\ \psi_{sq} &= L_q i_{sq}, \end{aligned} \tag{2.43}$$

where i_{sd} and i_{sq} are the d-axis and q-axis stator currents, R_s and L_s are the stator-phase resistance and inductance, respectively, ω_r is the rotor electrical speed, v_d and v_q are the stator voltages in the dq reference frame, and ψ is the flux established by the permanent magnets of the rotor.

The torque equation is

$$T_e = \frac{3}{2}p\left[\psi_r i_{sq} + (L_d - L_q)\, i_{sd} i_{sq}\right]. \tag{2.44}$$

Equations (2.43) can be described as state-space model

$$\dot{\boldsymbol{x}} = \mathbf{A}\boldsymbol{x} + \mathbf{B}\boldsymbol{u} + \mathbf{W}, \tag{2.45}$$

where $\boldsymbol{x} = \begin{bmatrix} i_{sd} & i_{sq} \end{bmatrix}^\top$, $\boldsymbol{u} = \begin{bmatrix} v_{sd} & v_{sq} \end{bmatrix}^\top$, $\mathbf{A}$, $\mathbf{B}$, $\mathbf{C}$, $\mathbf{W}$ are

$$\mathbf{A} = \begin{bmatrix} -\frac{R_s}{L_d} & \omega_r \\ -\omega_r & -\frac{R_s}{L_q} \end{bmatrix} \qquad \mathbf{B} = \begin{bmatrix} \frac{1}{L_d} & 0 \\ 0 & \frac{1}{L_q} \end{bmatrix} \tag{2.46}$$

$$\mathbf{C} = \begin{bmatrix} 1 & 0 \\ 0 & 1 \end{bmatrix} \qquad \mathbf{W} = \begin{bmatrix} 0 \\ -\frac{\omega_r}{L_d}\psi_r \end{bmatrix}. \tag{2.47}$$

2.6 Classical control techniques

2.6.1 Field oriented control

The field oriented control for alternating current (AC) motor drives are usually referred to the rotor oriented control which makes it possible to allow the decoupled control between the electromagnetic torque and the rotor flux. Thus, the AC motor can be controlled like a dc motor that can control the torque and flux independently. Due to the benefits (i.e. flux and torque current are still decoupled during transient and static conditions) of decoupled control, the field-oriented control is one of the most widely used control schemes in the industrial field.

To achieve the decoupled control, the direction of the flux must be known. Two kinds of field oriented control schemes were developed to get the flux direction. The first one named indirect vector control was proposed by K.Hasse in 1968 [5] by using the slip relation to instead the flux estimation. The second one named direct vector control was applied by F. Blaschke in 1971 [6] by using flux sensors or flux observer.

2.6.1.1 Indirect field oriented control

The nature of the so-called IFOC is that the rotating speed of the reference frame is identical to the rotor flux angular speed ω when using a model of the induction machine in dq frame described in Equation (2.37). Thus, in fact, this method is not really rotor flux oriented. However, the reference frame will finally converge to the rotor flux angle due to the dynamics of the induction motor and the control scheme. The condition for aligning the rotor flux to the d-axis of the dq rotating reference frame is to make the imaginary part of the rotor flux be equal to zero. i.e. $\psi_{rq} = 0$ and $\frac{d\psi_{rq}}{dt} = 0$. By substituting the two conditions to Equation (2.37), the following equations can be obtained:

$$\omega_s = \omega - \omega_r = \frac{L_m R_r}{L_r \psi_{rd}} i_{sq}, \tag{2.48}$$

$$\psi_{rd} = \frac{L_m}{\frac{L_r}{R_r}s + 1} i_{sd}, \tag{2.49}$$

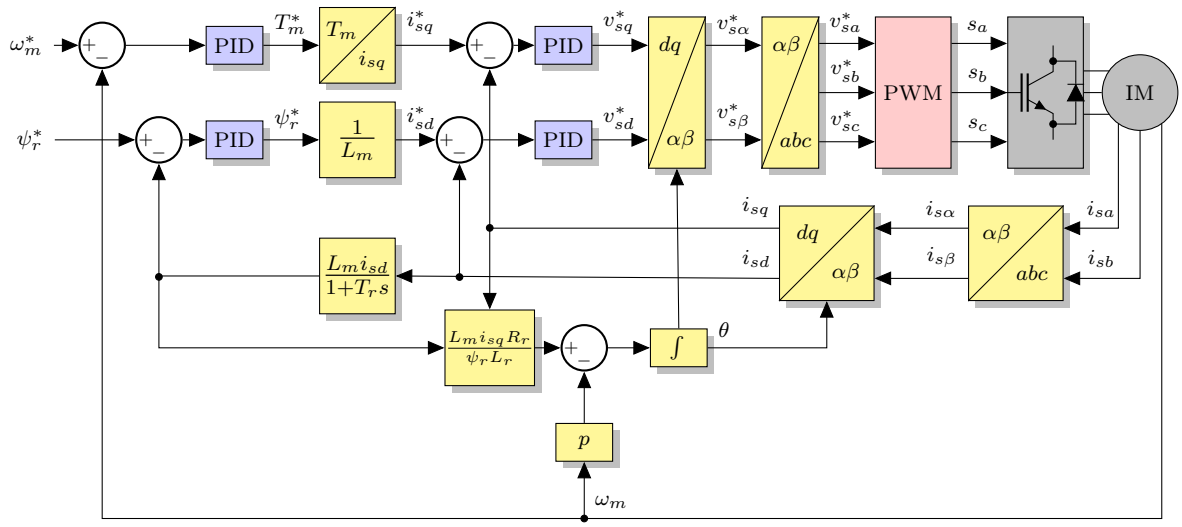

Figure 2.7: Speed control scheme of IFOC.

where ω_s is the slip speed which is the angular speed of the induced current in the rotor. The rotor speed (ω_r) can get from the encoder. Thus, the angular speed (ω) of the dq frame can be obtained by adding the slip speed and rotor speed. It is, therefore, the angle of the dq frame are getting from the integral of ω.

A speed control scheme of IFOC is shown in Figure 2.7.

The position of the dq frame is determined by the integration of the sum of slip and rotor speed. On the dq frame, a torque current control loop and a flux current loop is applied to give the voltage command. Additionally, the speed loop is used for determining the torque current reference while the flux loop is used for giving the flux current command.

2.6.1.2 Direct field oriented control

Another method for obtaining the rotor flux is based on the direct measurement or rotor flux observer. Thus, it is called DFOC when using such kind of technologies to get the rotor flux. The cascaded speed control scheme of DFOC is shown in Figure 2.8. Unlike the IFOC, the position of the dq frame is obtained directly from the flux observer. From the literature, many kinds of methods can be used as the flux observer, such as Kalman filter (KF) [7–9], Luenberger observer (LO) [10,11], sliding mode observer (SMO) [12–14], and adaptive flux observer [15].

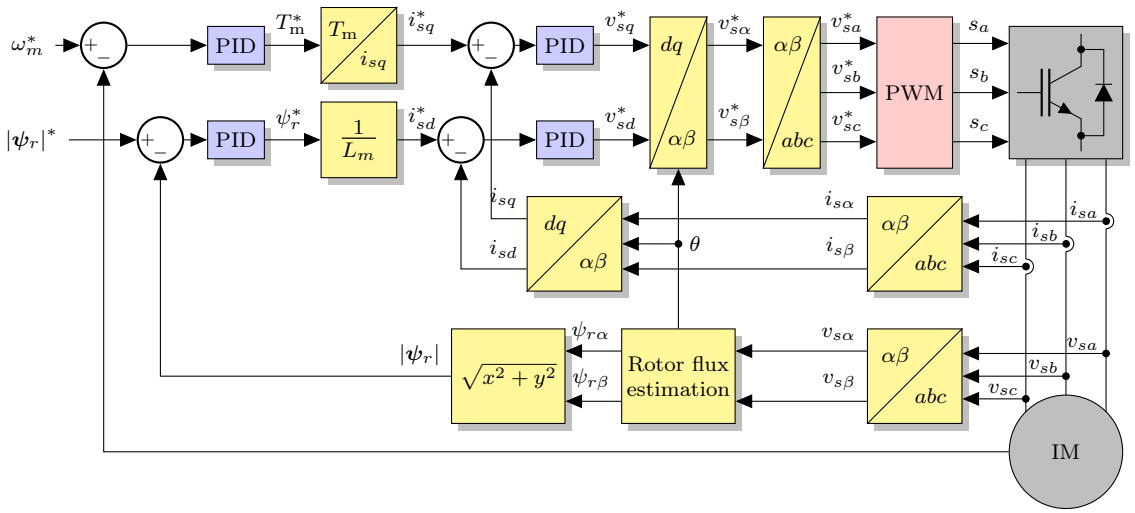

Figure 2.8: Speed control scheme of direct field oriented control.

2.6.2 Direct torque flux control

Another commonly used control scheme for AC drives is the direct torque control (DTC). It was presented by Isao Takahashi and Toshihiko Noguchi in an IEEJ paper in September 1984 [16] and in an IEEE paper published in 1986 [17]. Additionally, it was also patented by Manfred Depenbrock in October 1984 [18] and later published in [19].

Different from the field oriented control (FOC) which requires the rotor flux observer, the DTC requires stator flux observer. Thus, the dq frame and park transformation are not involved in DTC. All the calculations are done in the $\alpha\beta$ frame. To achieve very fast control response, the torque and flux are controlled by hysteresis controllers which define the switch control signals directly.

Due to its simplicity and very fast torque and flux control response, it is also widely used in the applications that requiring high performance.

A speed control scheme of DTC is shown in Figure 2.9.

The effectiveness of DTC, in particular, the fast control dynamics, have been illustrated by many research efforts. However, every control method has its advantages and disadvantages. Due to the hysteresis controller, switching frequency is unfixed, big noise/vibrations and big current ripples are observed, which are regarded as some of their drawbacks. For most cases, control techniques with fast control dynamics but fixed switching frequency are highly desirable.

Therefore, DTC with modulator [20, 21] was developed to compute the required average voltage vector and generates responding vector combination during each switching period. Thus, it is a good alternative candidate who achieves better control dynamics, less tuning efforts (in comparison with the conventional FOC) and more importantly fixed switching frequency. Therefore, less noise/vibrations and smaller control variable ripples are seen compared to the hysteresis based DTC. A speed control scheme of space vector

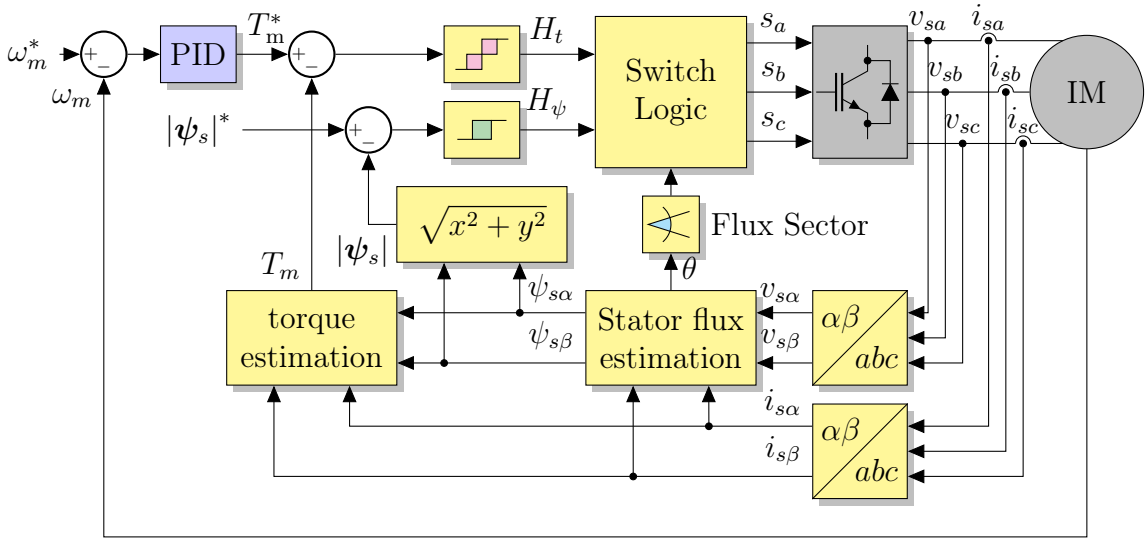

Figure 2.9: Speed control scheme of DTC.

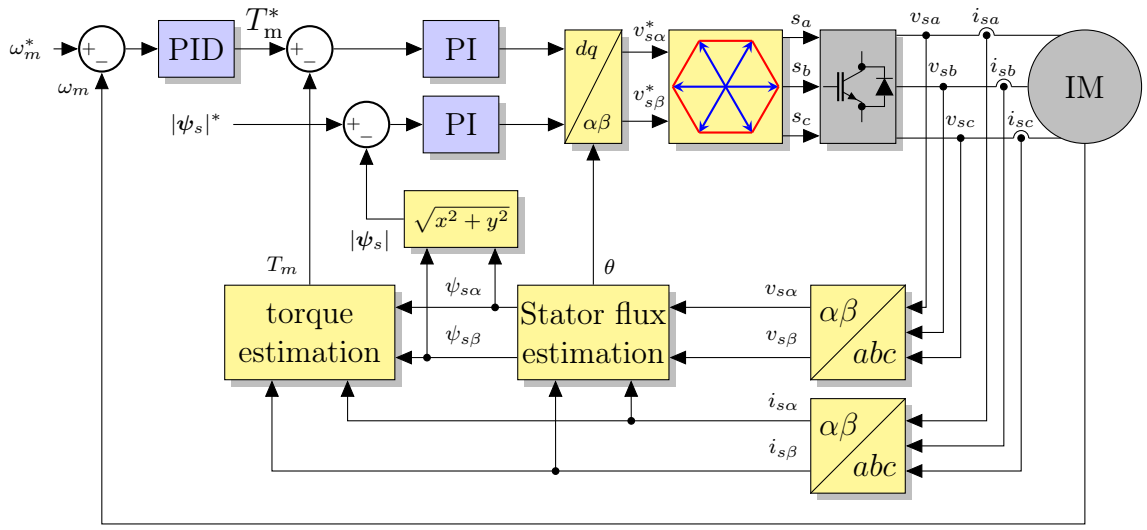

Figure 2.10: Speed control scheme of DTC-SVM.

modulation (SVM)-based DTC is shown in Figure 2.10.

2.6.3 Model predictive control

The MPC research originated in the early 1960's with the work of Propoi [22], however, after that, much of the applications came from the process control in industry. A big leap in the area of power electronics and electrical drives was started in the 1980's [23], [24], due to the fast development of microprocessors. Now, finite control set model predictive control (FCS-MPC) gains plenty of applications in power drives field which requires no space vector pulse width modulation (SVPWM) technology. Moreover, MPC is considered as an effective solution where control constraints and non-linearities [25–27] can be

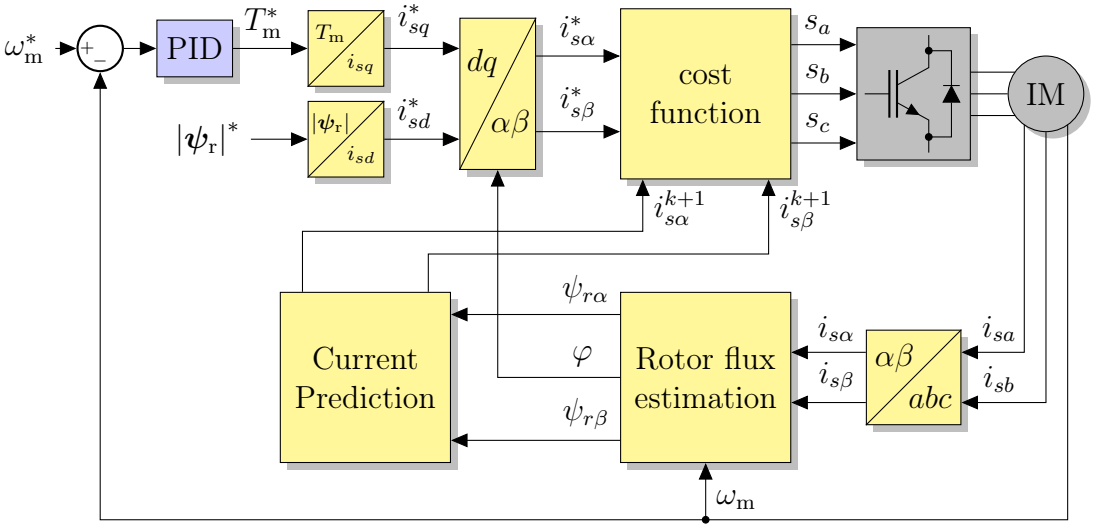

Figure 2.11: Speed control scheme of MPC-PCC.

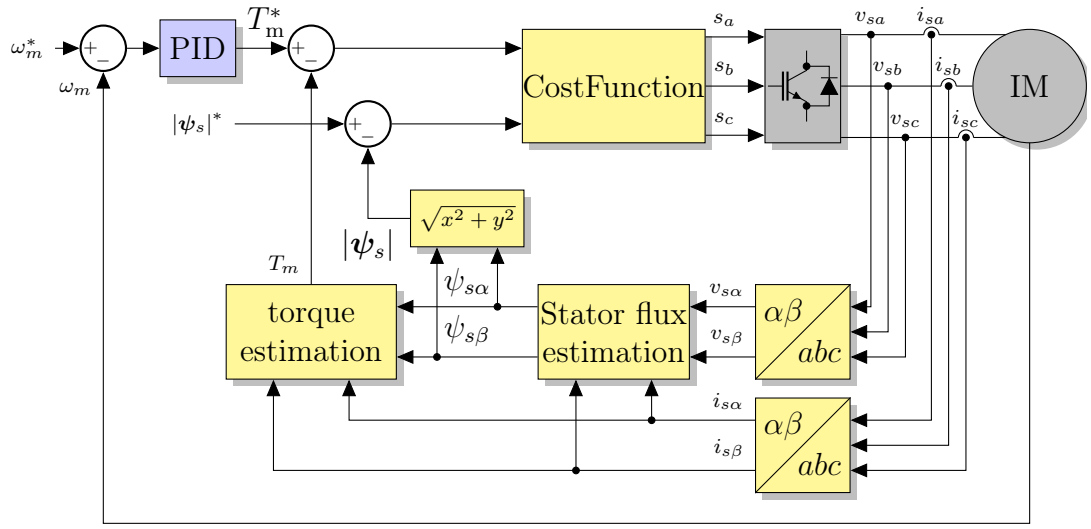

Figure 2.12: Speed control scheme of MPC-PTC.

included easily into the control law.

By including the non-linearities and constraints of the system, it is possible to choose an optimal solution from permissible switching states through minimizing a predefined cost function (i.e., the performance index). In MPC, the actuating variables are selected as the one that is minimizing the designed cost function in every sampling instant. A speed control scheme of the model predictive current control and model predictive torque control for induction motor is shown in Figure 2.11 and Figure 2.12 .

Chapter 3

Optimum control

In this chapter, a general optimum control for power converters and drives is proposed. The proposed optimum control will select an optimum voltage vector from the whole hexagonal plane, leading to the best control performance fulfilling a predefined performance index. With the proposed concept, two sub-solutions, i.e., both continuous and discrete solutions are derived and unified in the frame of *optimum control*. The *continuous solution* utilizes the averaged continuous-time model of the system and is capable of dealing with multiple system constraints, showing good performance with fewer calculation efforts, which is similar to the well-known deadbeat controller, but is capable of dealing with multiple system constraints. While the *discrete solution* takes the finite set of the power converter switching vectors into consideration and the state transition of the system can be predicted with a chosen vector. The second solution directly selects the switching position(s), which achieves better steady state performances meanwhile maintains a fast control dynamics as the well-known finite control set model predictive control (FCS-MPC) method, Both methods require fewer calculation efforts compared to the well-known FCS-MPC method, which makes it very suitable for practical realizations. Finally, as a case of study, the proposed concept is tested at a current controlled 3 kW surface mounted permanent magnet synchronous motor (SPMSM) drive under different scenarios. Experimental results validate the effectiveness of both solutions.

3.1 Motivation

Power converters play a key role in the electrical energy conversion system, in particular as the energy demands keep increasing. Utilization of switching mode power converters has been seen in many applications, such as motor drives [28, 29], active power filters [30], energy management system [31], renewable energy applications [32, 33], etc.. The performances of the power converter system highly depend on the design of the control methods, which motivates the research of effective control strategies. Based on the recent reports, the mostly used control strategies, which have been proved to be very useful and attractive, can be divided into two categories, i.e., the linear and nonlinear controller based

methods [34, 35].

One of the most well-known linear control methods is the proportional-integral (PI) controller, which outputs a continuous reference and then decoded by a pulse width modulation (PWM) [36]. Besides, the deadbeat control (DBC) and state feedback control [37,38] are also popular solutions. General similarity of these methods is that a PWM is required. With a PWM, advantages of constant switching frequency, well-defined harmonic spectrum, optimum switching pattern, etc., can be achieved. Also, the compensation of current error is separated from the voltage modulation which allows for an independent design process for both the controller and modulator. However, system performances greatly rely on the fine tuning of the parameters, which can be very tedious. Constraints and multiple control objectives are difficult to be included. Meanwhile, most of the linear controllers are designed assuming the system is situated in linear area. Many additional constraints and nonlinear characters in the real power electronics and drive systems, (e.g., the output voltage of the inverter has a hexagonal limitation due to the possible vectors and the available direct current (DC)-link voltage, the power converter is, in essence, a switched, discrete plant, etc.), were not taken into account. Therefore, few of the existed linear controllers can provide an effective solution, in general, to deal with such kinds of nonlinear problems.

The reported nonlinear control strategies aiming to treat such non-linearities including hysteresis, sliding mode, direct model predictive control (DMPC) [39–42], etc. Recently, DMPC has become a highly established research front. By including the non-linearities and constraints of the system, it is possible to choose an optimal solution from permissible switching states through minimizing a predefined cost function (i.e., the performance index). However, although DMPC has a talent for solving the above-mentioned nonlinear problems, it selects an optimal vector from a finite control set which is kept for a whole control interval. This leads to higher control variable ripples than modulator based techniques under a similar sampling interval.

Thinking in a deeper view, the control of a power system and drives is, in essence, a multiple objective optimization problems under system constraints. For such problems, the optimal control is the most suitable philosophy. Therefore, this work tries to build a bridge between the classical optimum control theory and power electronic drive control issues, which make it possible to combine the capability of handling nonlinear problems in predictive control and the advantages of using PWM in linear control. Instead of selecting one optimum vector from the basic vectors as the conventional DMPC, the proposed optimum control will select an optimum vector in the hexagonal plane composed of the original vectors. Considering whether the solution is continuous or not, the proposed concept will result in two control variants. The first will lead to a continuous solution and use a modulator to decode the switching positions for the drive, and it is named as continuous optimum control (COC) in the following sections. The second solution takes the finite set of the power converter switching vectors into consideration, which is named as discontinuous optimum control (DOC) in the following. Additionally, the relation between COC and deadbeat-like predictive control is clarified. Meanwhile, the relationship between the DOC and conventional DMPC is investigated as well.

As a case of study, a SPMSM drive system with current control as the primary targets, using both the proposed COC and DOC solutions is verified. Performances are experimentally validated and theoretically interpreted.

3.2 Optimization formulation and solution

The primary purpose of this section is to formulate the general optimum control problem without constraints and give its solution.

3.2.1 Linear system dynamics

From the modern control theory, a linear system can be described by a set of first-order differential equations , which may be expressed in the form of state space model

$$\begin{aligned} \dot{\boldsymbol{x}} &= \mathbf{A}(t)\boldsymbol{x} + \mathbf{B}(t)\boldsymbol{u}(t), \\ \boldsymbol{y} &= \mathbf{C}(t)\boldsymbol{x}, \end{aligned} \tag{3.1}$$

where $\boldsymbol{x}$ is a n-vector, representing the system states; $\boldsymbol{u}$ is a m-vector ($m \leq n$) which represents the inputs of the system; $\boldsymbol{y}$ is a p-vector ($p \leq n$) denoting the system outputs; $\mathbf{A}(\mathbf{t})$, $\mathbf{B}(\mathbf{t})$ and $\mathbf{C}(\mathbf{t})$ are respectively system transition matrices $n \times n$, input matrices $n \times m$, output matrices $p \times n$. If the coefficients of $\mathbf{A}(\mathbf{t})$, $\mathbf{B}(\mathbf{t})$ and $\mathbf{C}(\mathbf{t})$ are constants, the system (3.1) is regarded as time invariant or stationary.

The solution of (3.1) can be described in terms of a matrix function $\boldsymbol{\Phi}(t,\tau)$ that has the following properties

$$\begin{aligned} \dot{\boldsymbol{\Phi}}(t,\tau) &= \mathbf{A}(t)\,\boldsymbol{\Phi}(t,\tau), \\ \boldsymbol{\Phi}(\tau,\tau) &= \mathbf{I}, \end{aligned} \tag{3.2}$$

where $\mathbf{I}$ is the identity matrix. This matrix function $\boldsymbol{\Phi}(t,\tau)$ is referred to as the state transition matrix which is an unique solution to equation (3.2). In general, the transition matrix has no explicit form, unless the following commutativity property is satisfied

$$\mathbf{A}(t)\int_{t_0}^{t}\mathbf{A}(\tau)d\tau = \int_{t_0}^{t}\mathbf{A}(\tau)d\tau\mathbf{A}(t). \tag{3.3}$$

Then the transition matrix can be and only be written by

$$\boldsymbol{\Phi}(t,t_0) = e^{\int_{t_0}^{t}\mathbf{A}(\tau)d\tau\mathbf{A}(t)}. \tag{3.4}$$

It is easy to verify that the solution of system (3.1) is

$$\boldsymbol{x}(t) = \boldsymbol{\Phi}(t,t_0)\,\boldsymbol{x}_0 + \int_{t_0}^{t}\boldsymbol{\Phi}(t,\tau)\left[\mathbf{B}(\tau)\,\boldsymbol{u}(\tau)\right]d\tau, \tag{3.5}$$

where $\boldsymbol{x}_0 = \boldsymbol{x}(t_0)$.

3.2.2 Principle problem

Define the principle problem as follows: Consider the system (3.1), given the measurable values $\boldsymbol{y}$, an optimization problem is seeking an optimal control input variable $\boldsymbol{u}$ such that

$$V = \min J\left(\boldsymbol{x}, \boldsymbol{u}, t\right), \tag{3.6}$$

where $J\left(\boldsymbol{x}, \boldsymbol{u}, t\right)$ is performance index (or cost functional) which is usually defined as

$$J = J_f + J_e + J_u, \tag{3.7}$$

where J_f represents final error which is defined as

$$J_f = \frac{1}{2}\boldsymbol{e}^\top\left(t_f\right)\mathbf{L}\boldsymbol{e}\left(t_f\right), \tag{3.8}$$

where t_f is the final time of the optimization window, $\mathbf{L}$ is a positive definite symmetric matrix (i.e., $\mathbf{L}^\top = \mathbf{L} > \mathbf{0}$). $\boldsymbol{e}$ is defined as the error vector satisfies $\boldsymbol{e} = \boldsymbol{y}^* - \boldsymbol{y}$, and $\boldsymbol{y}^*$ is the ideal output or desired output, J_e represents the tracking error, i.e., the difference between the desired states and real ones. It is defined as

$$J_e = \frac{1}{2}\int_{t_0}^{t_f} \boldsymbol{e}^\top\mathbf{Q}\boldsymbol{e}dt, \tag{3.9}$$

where $\mathbf{Q}$ is a positive semi-definite symmetric matrix (i.e., $\mathbf{Q}^\top = \mathbf{Q} \geq 0$). J_u represents the energy cost. The desired final state will be attained with minimum effort. It is defined as

$$J_u = \frac{1}{2}\int_{t_0}^{t_f} \boldsymbol{u}^\top\mathbf{R}\boldsymbol{u}dt, \tag{3.10}$$

where $\mathbf{R}$ is a positive semi-definite symmetric matrix (i.e, $\mathbf{R}^\top = \mathbf{R} \geq 0$).

3.2.3 Solution of the principle problem

According to the Pontryagin's Maximum Principle [43], the optimum control law can be derived as

$$\boldsymbol{u}^* = -\mathbf{R}^{-1}\mathbf{B}^\top\mathbf{P}(t)\boldsymbol{x}, \tag{3.11}$$

where $\mathbf{P}(t)$ is given by solving the continuous time Riccati differential equation:

$$\dot{\mathbf{P}}(t) = -\mathbf{P}(t)\mathbf{A} - \mathbf{A}^\top\mathbf{P}(t) + \mathbf{P}(t)\mathbf{B}\mathbf{R}^{-1}\mathbf{B}^\top\mathbf{P}(t) - \mathbf{Q}, \tag{3.12}$$

where $\mathbf{P}(t)$ is time-variant. For a finite horizon problem, $\mathbf{P}(t)$ satisfies $\mathbf{P}(t_f) = \mathbf{L}$.

This solution is one of the modern control system design techniques that called linear quadratic regulator (LQR).

In a very few special cases, the solution to the problem 3.12 can be solved analytically, Unfortunately, in almost all cases, problems that can be solved analytically have no real

physical meaning. So, usually, the problem has to be solved by an iterative algorithm. This will dramatically increase the calculation time.

Usually, the Riccati equation can be solved offline. However, what we are targeting to, are:

1. To include the system parameter variation into the optimal control law, due to the matter of fact, parameters involved in the controller are highly *time-varying*, and the variations of the parameters will affect the control performances. Therefore, an online parameter estimation solution shall be ultimately included in the control methods, which requires (definitely) online calculations of the required system matrices;

2. To control *multiple* machines with big ranges of parameter values, are one of our targets and if of great necessity in reality. For instance, in a rubber-tired cranes used for moving integrated container, multiple motors are used for *both* horizontal/vertical *and* other movements. However, these motors share the same drive due to cost. Thus, the drive should have the capability to control motors with entirely different parameters.

Based on the above consideration, solving the Riccati equations offline (e.g., via matrix laboratory (MATLAB), etc.) is not proper. Therefore, the control law should be solved online (i.e., through the real-time controller). However, real-time systems used for the motor control have only a few hundred megahertz (MHz) clock frequency (e.g., in our system, the clock frequency is 168 MHz). Meanwhile, taking the optimization problem of multiple objectives under multiple system constraints into account, the traditional control law (3.11) is computationally not possible.

To cope with this, we newly developed the control law with simplified solutions in Section 3.3 and Section 3.4. The intermediate expression ((3.18), (3.21), (3.23)) in the derivation of our simplified solutions can be directly used to calculate the partial derivative of J, which saves computational time.

3.3 Continuous-control solution of optimum control

Using modulation techniques like PWM, the inverter can be approximated as a linear system. Therefore, the control variable $\boldsymbol{u}$ can be an *arbitrary* vector in the hexagonal plane composed of the eight basic vectors. This section will discuss the situation when *control variable* is continuous. Certainly, the solution without constraints can be solved by the existing continuous-time LQR or discrete-time LQR [44]. Taking the aspects mentioned in section 3.2.3 into consideration, we newly developed a simplified solution with constraints, which are detailed as follows.

3.3.1 Solution of the state transition

To reuse the existing modulation algorithm, the average model of the $\boldsymbol{u}$ should be used. The optimization window will be selected as T_s, which is the switching period. At the initial time $t_0 = 0$, the state variable is $\boldsymbol{x_0}$. If a constant input (usually, for a power converter this assumption holds) $\boldsymbol{u}$ is employed on system (3.1), according to equation (3.5), the state transition equation from initial time to time t is

$$\boldsymbol{x}\left(t\right) = e^{\mathbf{A}t}\boldsymbol{x}_0 + \int_0^t e^{\mathbf{A}(t-\tau)}\mathbf{B}\boldsymbol{u}d\tau. \tag{3.13}$$

Within a small interval $[0, T]$, thus $e^{\mathbf{A}t} \approx \mathbf{I} + \mathbf{A}t$, $\int_0^t e^{\mathbf{A}(t-\tau)}d\tau \approx \mathbf{I}t$, Equation (3.13) is simplified as

$$\boldsymbol{x}\left(t\right) = (\mathbf{I} + \mathbf{A}t)\boldsymbol{x_0} + \mathbf{B}\boldsymbol{u}t. \tag{3.14}$$

So, the error vector can be calculated as

$$\boldsymbol{e}\left(t\right) = \mathbf{C}\left(\boldsymbol{x}^* - \boldsymbol{x}\right) = \mathbf{C}\left[\boldsymbol{x}^* - (\mathbf{I} + \mathbf{A}t)\boldsymbol{x}_0 - \mathbf{B}\boldsymbol{u}t\right]. \tag{3.15}$$

3.3.2 Solution of continuous optimum control

By defining two matrices as follows:

$$\begin{aligned} J_{f0} &= \mathbf{C}\boldsymbol{x}^* - \mathbf{C}(\mathbf{I} + \mathbf{A}T_s)\boldsymbol{x_0}, \\ J_{f1} &= -\mathbf{C}\mathbf{B}T_s, \end{aligned} \tag{3.16}$$

Equation (3.8) can be rewritten to:

$$J_f = \frac{1}{2}(J_{f1}\boldsymbol{u} + J_{f0})^\top \mathbf{L}\left(J_{f1}\boldsymbol{u} + J_{f0}\right). \tag{3.17}$$

Taking partial derivative of J_f with respect to $\boldsymbol{u}$ gives:

$$\frac{\partial J_f}{\partial \boldsymbol{u}} = J_{f1}^\top \mathbf{L}\left(J_{f1}\boldsymbol{u} + J_{f0}\right). \tag{3.18}$$

By introducing three matrices as follows:

$$\begin{aligned} J_{e0} &= \mathbf{C}\boldsymbol{x}^* - \mathbf{C}\boldsymbol{x_0}, \\ J_{e1} &= -\mathbf{C}\mathbf{A}\boldsymbol{x_0}, \\ J_{e2} &= -\mathbf{C}\mathbf{B}, \end{aligned} \tag{3.19}$$

Then, with the introduced (3.19), J_e can be rewritten to:

$$\frac{1}{2}\int_0^{T_s} \left(J_{e0} + J_{e1}t + J_{e2}\boldsymbol{u}t\right)^\top \mathbf{Q}\left(J_{e0} + J_{e1}t + J_{e2}\boldsymbol{u}t\right)dt. \tag{3.20}$$

Taking partial derivative of J_e with respect to $\boldsymbol{u}$ gives:

$$\frac{\partial J_e}{\partial \boldsymbol{u}} = \frac{1}{2}J_{e2}^\top \mathbf{Q} J_{e0} T_s^2 + \frac{T_s^3}{3}J_{e2}^\top \mathbf{Q}\left(J_{e1} + J_{e2}\boldsymbol{u}\right). \tag{3.21}$$

Additionally, because of control variable $\boldsymbol{u}$ is constant in the optimize window, J_u has the following simple form

$$J_u = \frac{1}{2}\boldsymbol{u}^\top \mathbf{R}\boldsymbol{u}T_s. \tag{3.22}$$

Taking partial derivative of J_u with respect to $\boldsymbol{u}$ gives:

$$\frac{\partial J_u}{\partial \boldsymbol{u}} = \mathbf{R}\boldsymbol{u}T_s. \tag{3.23}$$

Therefore, the three parts of performance index are all functions with respect to $\boldsymbol{u}$. According to extremal principle, J achieves extremal when

$$\frac{\partial J}{\partial \boldsymbol{u}} = \frac{\partial J_f}{\partial \boldsymbol{u}} + \frac{\partial J_e}{\partial \boldsymbol{u}} + \frac{\partial J_u}{\partial \boldsymbol{u}} = 0. \tag{3.24}$$

The sufficient condition for minimization J is that J is convex. Thereby, J should satisfy

$$\frac{\partial^2 J}{\partial \boldsymbol{u}^2} = J_{f1}^\top \mathbf{L} J_{f1} + \frac{1}{2} J_{e2}^\top \mathbf{Q} J_{e2} T_s^2 + \mathbf{R} > 0. \tag{3.25}$$

Since $\mathbf{L}$ is a positive definite symmetric matrix, $\mathbf{Q}$ and $\mathbf{R}$ are positive semi-definite symmetric matrix. Equation (3.25) indeed holds, the solution of continuous optimum control is thereby obtained from equation (3.24):

$$\boldsymbol{u} = -\mathbf{M}^{-\mathbf{1}}\mathbf{N}, \tag{3.26}$$

where $\mathbf{M}$ and $\mathbf{N}$ are expressed as

$$\mathbf{M} = J_{f1}^\top \mathbf{L} J_{f1} + \frac{1}{3} J_{e2}^\top \mathbf{Q} J_{e2} T_s^3 + \mathbf{R}T_s, \tag{3.27}$$

$$\mathbf{N} = J_{f1}^\top \mathbf{L} J_{f0} + \frac{1}{3} J_{e2}^\top \mathbf{Q} J_{e1} T_s^3 + \frac{1}{2} J_{e2}^\top \mathbf{Q} J_{e0} T_s. \tag{3.28}$$

So far the continuous solution without constraints is presented.

3.3.3 Continuous optimum control within constraints

In a real system, the control variables usually have some constraints. Taking the two-level converter for example, the output voltage is subjected to constraints on its magnitude. The output voltage vector can not exceed the hexagon. This will lead to that the obtained final states are restricted.

Generally, defining the constraints as

$$\boldsymbol{\varphi}(\boldsymbol{u}) = 0, \tag{3.29}$$

where $\boldsymbol{\varphi}$ is a q-vector functions explicitly depends on $\boldsymbol{u}$. It describes the constraints for the control variable $\boldsymbol{u}$. In order to solve the extremal of J, a co-vector function Lagrange multipliers is introduced as

$$\boldsymbol{\lambda} = [\lambda_1 \ \lambda_2 \ ... \ \lambda_q], \tag{3.30}$$

A Hamiltonian function is defined by

$$H = J + \boldsymbol{\lambda}\boldsymbol{\varphi}. \tag{3.31}$$

A necessary condition for J to be an extremal is

$$\frac{\partial H}{\partial \boldsymbol{u}} = \frac{\partial H}{\partial \boldsymbol{\lambda}} = \boldsymbol{\varphi} = 0. \tag{3.32}$$

After solving the equation set (3.32), the solution for optimum control within constraints can be obtained.

3.3.4 Relationship between COC and DBC

The deadbeat-like predictive control technique is usually proposed as a SVM-based model predictive control method. As an alternate method of conventional predictive control, it can employ a moderately voltage vector to eliminate the high current ripple existing in the conventional direct model predictive control.

With deadbeat predictive control, the desired control variable which allows the output to reach the reference output after one calculation period is computed using the model (3.14). If J_e and J_u are ignored ($\mathbf{Q} = \mathbf{R} = \mathbf{0}$), the solution of the continuous optimum control without constraints is identical to the solution of deadbeat control. The detailed theoretical proof can be found in [45]. So dead-beat control is still an optimal control problem. The performance index (cost function) for dead-beat control is quadratic and only the final state is considered. However, one cannot get the solution with constraints from the original concept of deadbeat control. From this point, the optimum control provides a more practical method for control systems with constraints.

3.4 Discrete-control solution of optimum control

Considering about the real situation of power electronics, e.g. a two-level inverter, has *only eight possible* output vectors. That means traversing all the possible control variables to get the minimum performance index can be an efficient way. This section will discuss the situation when control variable is *discrete/finite*. The optimization window will be selected as T_c which is the control interval.

3.4.1 Single vector optimum

In such case, the control variable $\boldsymbol{u}$ will always be a constant. The duration time of $\boldsymbol{u}$ to system (3.1) is T_c. With the condition $t_f = T_c$, the performance index J is computed when the control variable $\boldsymbol{u}$ is employed separately (for a power converter, $\boldsymbol{u}$ is a finite space. In a two-level inverter, only eight vectors can be used for output). After the computation, the performance index with minimum value can be found. Thus the responding control variable $\boldsymbol{u}$ is the discrete-control solution with single vector.

Specially, when neglecting the energy performance part (J_u) and the whole process tracking error part (J_e), the performance index will have the same form with the original predictive control which is well known in literature [39, 40].

3.4.2 Two vectors optimum

The optimization window will also be selected as control interval T_c. However, we will employ two vectors in the optimization window. For a simplistic demonstration of this solution, a zero vector and another vector are selected in one optimization window [46]. Using vectors $\boldsymbol{u_0}$, $\boldsymbol{u_1}$ for example, the order of two vectors is shown in Figure 3.1 when using sawtooth carrier based modulator. The duration time is respectively t_0, t_1. So, the J_u part of the performance index has the following form

$$J_u = \frac{1}{2}\int_0^{t_1} \boldsymbol{u_1}^\top \mathbf{R}\boldsymbol{u_1} dt. \tag{3.33}$$

After taking the partial derivative of J_u, we can obtain

$$\frac{\partial J_u}{\partial m} = \frac{1}{2}\left(\boldsymbol{u_1}^\top \mathbf{R}\boldsymbol{u_1}\right) T_c. \tag{3.34}$$

For the purpose of reusing carrier based modulation to generate PWM signals, the during time t_0, t_1 are expressed by modulation index m ($0 \le m \le 1$) and sample time T_c. The initial state at the beginning of $\boldsymbol{u_1}$ is $\boldsymbol{x_0}$ that can be measured. The state transition in the optimum window is calculated as (3.35) according equation (3.14).

$$\boldsymbol{x}(t) = \begin{cases} (\mathbf{I} + \mathbf{A}t)\boldsymbol{x}_0 + \mathbf{B}\boldsymbol{u}_1 t & 0 \le t \le mT_c \\ (\mathbf{I} + \mathbf{A}\,(t - mT_c))\,\boldsymbol{x}(mT_c) & mT_c < t \le T_c \end{cases}. \tag{3.35}$$

Therefore, the final error performance J_f has the following form

$$J_f = \frac{1}{2}(\boldsymbol{x}^* - \boldsymbol{x_f})^\top \mathbf{C}^\top \mathbf{L}\mathbf{C}\,(\boldsymbol{x}^* - \boldsymbol{x_f})\,. \tag{3.36}$$

In order to avoid the complex calculation about discussing the distribution of solutions of a cubic equation, some simplicity should be considered.

1. J_e is ignored.
2. For a discrete solution of optimum control, the calculation interval T_c is very small. Thus, $T_c^2 \approx 0$ holds.

Based on the above simplicity, $\boldsymbol{x_f}$ can be revised as:

$$\boldsymbol{x_f} = \boldsymbol{x_0} + \mathbf{A}T_c\boldsymbol{x_0} + \mathbf{B}\boldsymbol{u_1}T_c m. \tag{3.37}$$

Taking partial derivative of J_f with respect to m gives

$$\frac{\partial J_f}{\partial m} = \boldsymbol{u_1}^\top \mathbf{B}^\top \mathbf{C}^\top \mathbf{L}\mathbf{C}\left(\boldsymbol{x}^* - \boldsymbol{x_f}\right). \tag{3.38}$$

Thereby, the solution of two-vector optimum control is obtained from $\frac{\partial J_f}{\partial m} + \frac{\partial J_u}{\partial m} = 0$, as

$$m = \mathbf{P}^{-1}\mathbf{O}, \tag{3.39}$$

where

$$\mathbf{P} = \boldsymbol{u_1}^\top \mathbf{B}^\top \mathbf{C}^\top \mathbf{L}\mathbf{C}\mathbf{B}\boldsymbol{u_1} T_c, \tag{3.40}$$

$$\mathbf{O} = \boldsymbol{u_1}^\top \mathbf{B}^\top \mathbf{C}^\top \mathbf{L}\mathbf{C}\left(\boldsymbol{x}^* - \boldsymbol{x_0} - \mathbf{A}T_c\boldsymbol{x_0}\right) + \frac{1}{2}\boldsymbol{u_1}^\top \mathbf{R}\boldsymbol{u_1} T_c. \tag{3.41}$$

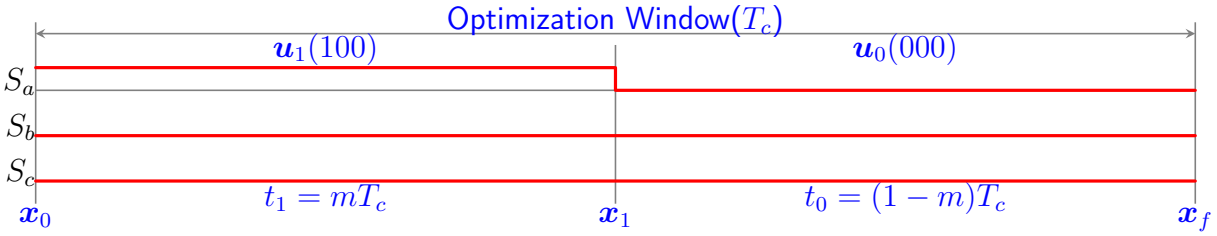

Figure 3.1: Vector pattern during time.

3.4.3 Multiple vectors optimum

It should be noted that in two control intervals the selected two non-zero vectors and zero vector in aforementioned method can form an equivalent vector which will cover the whole hexagonal plane [47]. According to the principle of dynamic programming (also known as dynamic optimization), for the optimization problem of multiple vectors can be broken down into two or more optimization processes of two vectors optimization problem. Thus, it is still a problem about optimization of two vectors.

So far the DOC solutions are thoroughly discussed. In the following, current control of an SPMSM drive system using the proposed COC and DOC solutions will be demonstrated as a case of study.

3.5 Optimum current control for SPMSM

3.5.1 Unconstrained solution with COC

Because the state variable and control variable for SPMSM are given in dq reference frame, its also more straightforward to apply the optimum control in dq reference frame.

By comparing the permanent magnet synchronous motor (PMSM) state-equation form (2.45) with the predefined system (3.1), it is apparent that an extra constant structure $\mathbf{W}$ is added to the normal state-equation. So, J_{f0}, J_{e1} should be revised as

$$J_{f0} = -\mathbf{CB}T_s - \mathbf{W}T_s, \tag{3.42}$$
$$J_{e1} = -\mathbf{CA}\boldsymbol{x_0} - \mathbf{W}. \tag{3.43}$$

The optimum control strategy can be performed in the following steps:

1. At the beginning of the current sampling-calculation period, measuring the stator currents i_a, i_b, i_c and rotor position θ_r, and transform the stator current to system state $\boldsymbol{x_0} = [\ i_d \quad i_q\ ]^\top$;
2. According to the speed controller and flux controller, The future reference current value can be obtained; The future reference current is considered as final state which is denoted as $\boldsymbol{x}^* = [\ I_d \quad I_q\ ]^\top$;
3. Select one positive definite symmetric matrix $\mathbf{L}$ and two semi-positive definite symmetric matrix $\mathbf{Q}$, $\mathbf{R}$;
4. Now, the optimum control variable can be obtained by substituting $\boldsymbol{x_0}$, $\boldsymbol{x}^*$, $\mathbf{L}$, $\mathbf{R}$, $\mathbf{Q}$, $\mathbf{A}$, $\mathbf{B}$, $\mathbf{C}$ into the equations that are needed in equation (3.26);
5. Apply the obtained optimum control variable $\boldsymbol{u}$ through inverse park transformation and space-vector modulation;
6. Go to step 1 and do the next iterator;

In such case, with $\mathbf{L} = \mathrm{diag}\left[\ L_1 \quad L_2\ \right]$, $\mathbf{R} = \mathrm{diag}\left[\ R_1 \quad R_2\ \right]$, $\mathbf{Q} = \mathrm{diag}\left[\ Q_1 \quad Q_2\ \right]$, the solution is

$$v_d = \frac{N_{d1} + N_{d2}}{D_d}, \qquad v_q = \frac{N_{q1} + N_{q2} + N_{q3}}{D_q}, \tag{3.44}$$

where N_{d1}, N_{d2}, N_{q1}, N_{q2}, N_{q3}, D_{dq} are collected as follows:

$$N_{d1} = 6L_1\left(R_sT_si_d - L_si_d - L_sT_si_q\omega_r\right), \tag{3.45}$$
$$N_{d2} = Q_1\left(2R_sT_s^2i_d - 3L_sT_si_d - 2L_sT_s^2i_q\omega_r\right), \tag{3.46}$$
$$N_{q1} = Q_2T_s^2\left(2R_si_q + 2\omega_r\psi + 2L_si_d\omega_r\right), \tag{3.47}$$
$$N_{q2} = 6L_2\left(I_qL_s - L_si_q + R_sT_si_q + T_s\omega_r\psi + L_sT_si_d\omega_r\right), \tag{3.48}$$
$$N_{q3} = 3L_sQ_2T_s\left(I_q - i_q\right), \tag{3.49}$$
$$D_d = 6R_1L_s^2 + 2Q_1T_s^2 + 6L_1T_s, \tag{3.50}$$
$$D_q = 6L_s^2R_2 + 6L_2T_s + 2Q_2T_s^2. \tag{3.51}$$

$\boldsymbol{v}_{d,q}$ is then assigned to a space vector modulation (SVM) after transferred into $\alpha\beta$ frame, invoking the Park transformation.

3.5.2 Constrained solution

From the solution of optimum control, it can be seen that when the rotor speed goes up or there is a big current demand, the voltage can easily exceed the maximum voltage output of the inverter. So, the aforementioned optimum control can not be guaranteed in such case, and the response of the system will deteriorate. Therefore, the problem is how to ensure the optimum control of current with a restricted magnitude voltage output.

To formulate the problem, the output voltage is constrained with the following constraint, as

$$\boldsymbol{u}^\top \boldsymbol{u} = v_d^2 + v_q^2 \leq r^2, \tag{3.52}$$

where r is the radius of the voltage limit circle. Thus, the co-function can be defined as

$$\varphi(\boldsymbol{u}) = \boldsymbol{u}^\top \boldsymbol{u} - r^2 = v_d^2 + v_q^2 - r^2. \tag{3.53}$$

The Hamiltonian function is further rewritten as

$$H = J + \lambda\varphi(\boldsymbol{u}) = J + \lambda(v_d^2 + v_q^2 - r^2). \tag{3.54}$$

The necessary conditions for J to be an extremal are

$$\begin{aligned} \frac{\partial H}{\partial v_d} &= \frac{\partial J}{\partial v_d} + 2\lambda v_d = 0, \\ \frac{\partial H}{\partial v_q} &= \frac{\partial J}{\partial v_q} + 2\lambda v_q = 0, \\ \varphi(\boldsymbol{u}) &= v_d^2 + v_q^2 - r^2 = 0. \end{aligned} \tag{3.55}$$

After solving the equation set (3.55), v_d and v_q are now obtained in the following compact form:

$$\begin{aligned} v_d &= \frac{(N_{d1} + N_{d2})\, T_s}{D_d T_s + 12\lambda {L_s}^2}, \\ v_q &= \frac{(N_{q1} + N_{q2} + N_{q3})\, T_s}{D_q T_s + 12\lambda {L_s}^2}. \end{aligned} \tag{3.56}$$

For simplicity, assuming the condition $R_1 = R_2$, $Q_1 = Q_2$, $L_1 = L_2$, λ is expressed as:

$$\lambda = \frac{T_s \sqrt{(N_{d1} + N_{d2})^2 + (N_{q1} + N_{q2} + N_{q3})^2}}{12 {L_s}^2 r} - \frac{D_q T_s}{12 {L_s}^2}. \tag{3.57}$$

Substituting equation (3.57) to (3.56), Equation (3.56) can be rewritten as

$$\begin{aligned} v_d &= \frac{(N_{d1} + N_{d2})\, r}{\sqrt{(N_{d1} + N_{d2})^2 + (N_{q1} + N_{q2} + N_{q3})^2}}, \\ v_q &= \frac{(N_{q1} + N_{q2} + N_{q3})\, r}{\sqrt{(N_{d1} + N_{d2})^2 + (N_{q1} + N_{q2} + N_{q3})^2}}. \end{aligned} \tag{3.58}$$

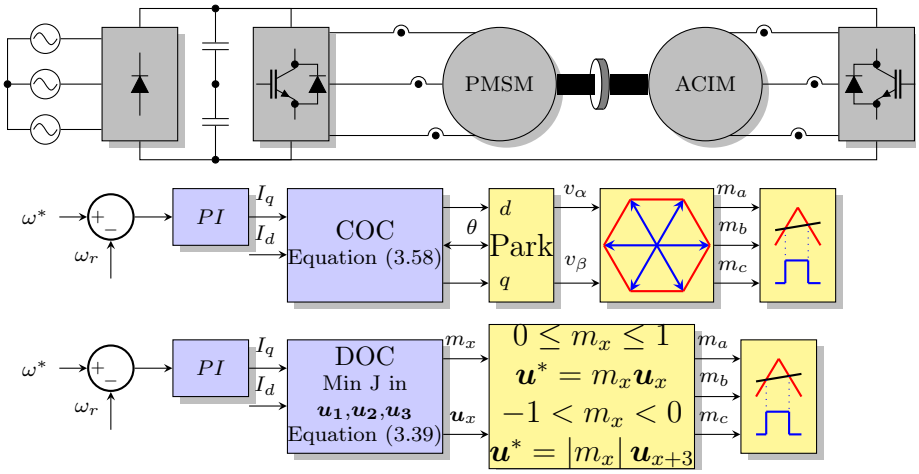

Figure 3.2: Structure of the test-bench for experimental verification.

Compared with the unconstrained solution (3.44), we can conclude that in case of exceeding the limit of voltage magnitude, the voltage vector should be kept in the same direction as the unlimited condition. However, one cannot guarantee this with the original field oriented control (FOC) concept.

3.5.3 Two vectors optimum solution

The main purpose of this method is to reduce the current ripple with a reasonable time calculation cost. Due to the fact that the candidate vectors have three pairs of vectors with opposite directions, the exploration of the optimization process can be significantly reduced by adopting only three candidate vectors ($\boldsymbol{u_1}$,$\boldsymbol{u_2}$,$\boldsymbol{u_3}$) that have different directions.

The exploration algorithm is listed in Algorithm 1:

3.6 Experimental results and analysis

To assess the performance of the proposed control methods, various experimental scenarios are tested. In the following, we first introduce the hardware setup and the configuration. Then, both transient and steady state control performances of the proposed control system are assessed and compared with that of the well-known FOC and DMPC methods. Meanwhile, the robustness of the proposed control system is also carried out and then compared with that of the FOC and DMPC under the same condition.

3.6.1 Experimental setup

All the control schemes in this work are implemented on the same test bench shown in Figure B.1. For more details, please refer to Appendix B.

Function *Calculation()*
  Collect the stator currents i_d, i_q and the future reference current I_d, I_q;
  Calculate the modulation indexes m_1, m_2, m_3 for the three candidate vectors ($\boldsymbol{u} \in \{\boldsymbol{u_1}, \boldsymbol{u_2}, \boldsymbol{u_3}\}$) using equation (3.39);
  if $m_j > 1$ **then**
    $m_j = 1$;
  end
  else if $m_j < -1$ **then**
    $m_j = -1$;
  end
  Calculate three performance indexes with m_1, m_2, m_3 with the corresponding vectors;
  Find the minimum performance index and the corresponding $\boldsymbol{u}_x$ and m_x ;
  if $m_x \geq 0$ **then**
    apply the vector $m_x \boldsymbol{u}_x$;
  end
  else if $m_x < 0$ **then**
    apply the opposite vector $|m_x| \, \boldsymbol{u}_{x+3}$;
  end

Algorithm 1: Algorithm of two vectors optimum solution.

Table 3.1: System Configuration and Parameters.

Symbol	**Parameter**	**Value**
R_s	Stator Resistance	$0.95\,\Omega$
$L_d = L_q = L$	d-axis Inductance	9.6 mH
ψ	Flux	0.26 Wb
$T_s = T_c = T$	Control interval for COC and DOC	83.3 µs
ω_r^b	Base value of rotor speed	$314\,\mathrm{rad\,s^{-1}}$
i^b	Base value of current	8.9 A
v^b	Base value of voltage	311 V
t_d	Dead time	8 µs
P	Number of pole Pairs	3
L_1, L_2	Final value matrix parameter	1
Q_1, Q_2	Tracking error matrix parameter	0.1
R_1, R_2	Energy cost matrix parameter	0.1

An overview control scheme for the proposed control methods is depicted in Figure 3.2. It should be noted that the control frequency for both methods is 12 kHz to achieve a fair comparison[1], the switching frequency for COC and FOC is 6 kHz.

[1]In this work, the comparison is carried out under the same control frequency, rather than the same switching frequency so to ease the implementation and assure a fair comparison.

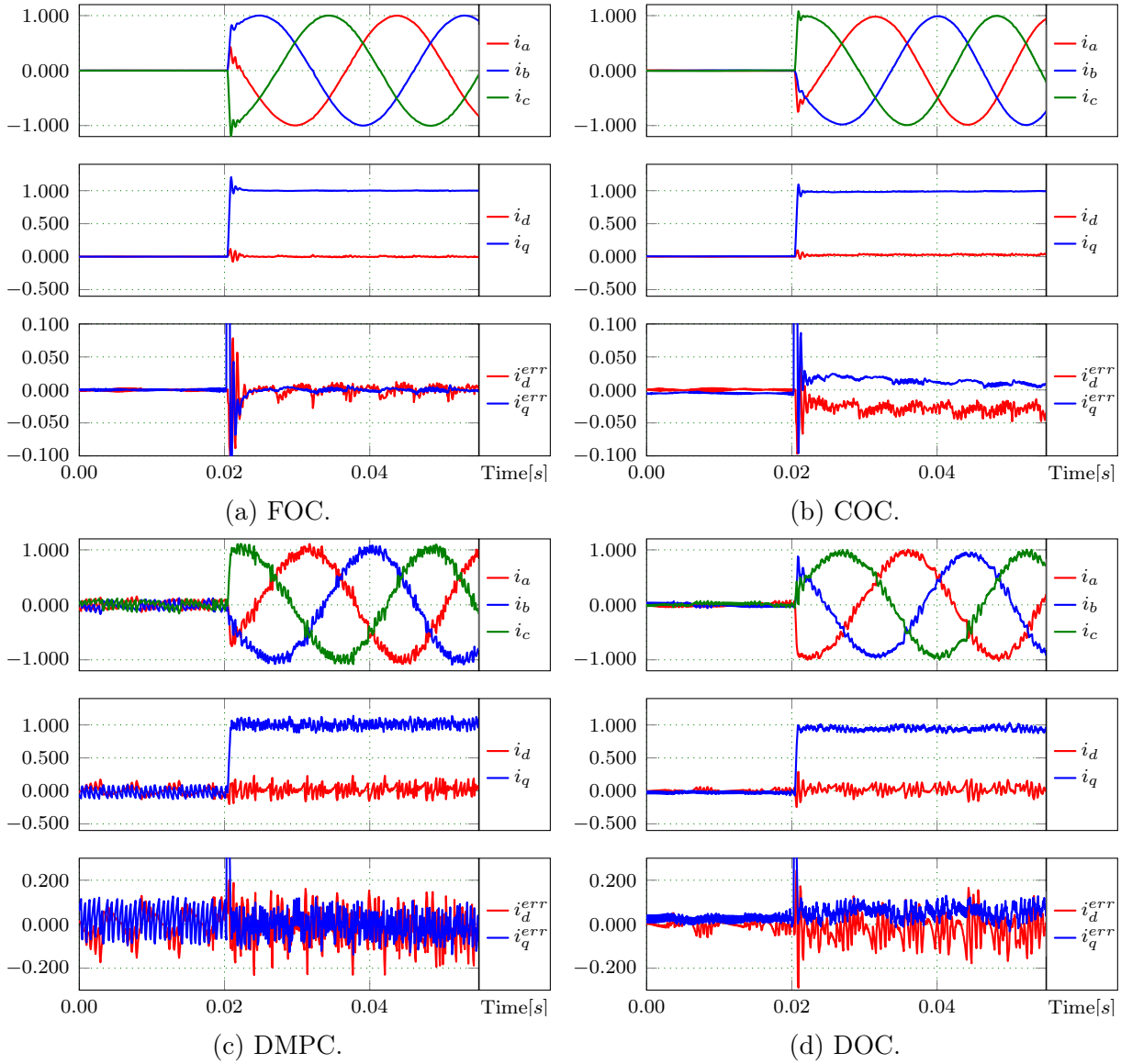

(a) FOC. (b) COC.

(c) DMPC. (d) DOC.

Figure 3.3: Transient phase performance evaluation in *torque* mode.

3.6.2 Assessment of control dynamics and steady-state performance

Fast inner loop control dynamics and steady-state performance are very desirable for a drive system. To test this, the scenarios are set as follows: the system is set to run in "torque control mode" (i.e., the torque command is directly set to the inner control loop of all the four control schemes under consideration (i.e., the COC, DOC, FOC, and DMPC), without using the outer speed control loops, to omit its bandwidth effect), while the load-side machine is at the "speed control mode". A rated torque current command is set to the control methods under consideration. Note that, the parameters used in PI controller for FOC are optimized individually according to [48] so as to ensure a high

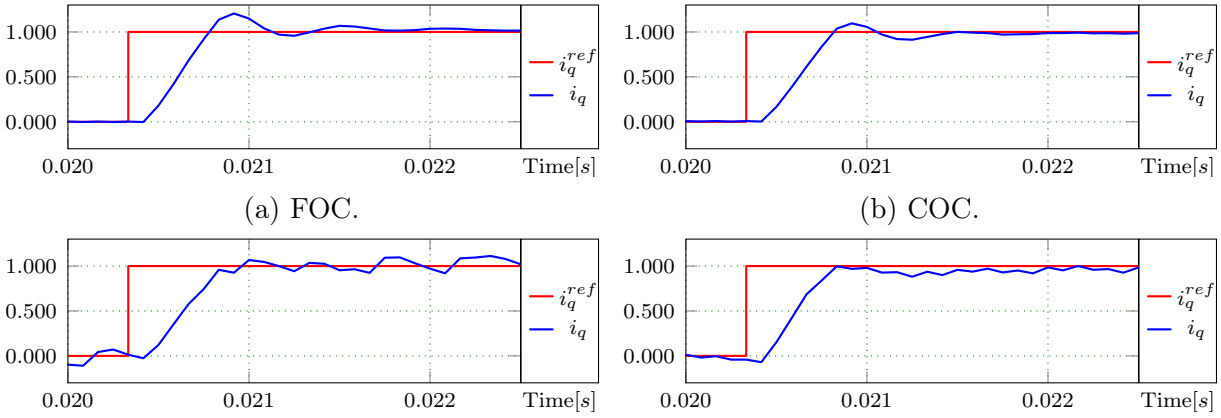

(a) FOC. (b) COC.

(c) DMPC. (d) DOC.

Figure 3.4: Transient phase performance evaluation in *torque* mode.

bandwidth of the current loop. The basic parameters used in other control schemes are listed in Table 3.1. At such configuration, the stator currents (in both *abc*- and *dq*-frames) and current tracking errors are recorded, and the results are in Figure 3.3. As can be seen: The current ripples of the FOC and COC are significantly lower than that of the DMPC and DOC due to the existence of a modulator. The current ripples of the DOC are less than that of the DMPC due to the employing of two vectors in the control interval. Similar results are obtained when the motor rotates without load. In steady states, FOC has nearly zero error between the reference and feedback. On the contrary, the COC has static errors.

To directly depict the transient phase performances during the test, the torque current and its reference are zoomed-in in Figure 3.4. As is observed, (less than) 1ms is required to finish a rated torque change tracking, for all the methods[2]. The dynamic response of the four methods is nearly identical. However, COC and FOC show a slight overshoot in comparison with the DOC and DMPC solutions. Note that, for all solutions, the torque current starts to follow its reference after one control cycle, which is, the delay effect of the operating voltage.

3.6.3 Assessment of disturbance rejection capabilities

Good rejection capabilities to abruptly changing load disturbances are one of the key requirements for a drive system. To examine the disturbance rejection capabilities, testing scenarios are identically set for both the proposed solutions and the classical FOC and DMPC methods, as follows: the system operates under "speed control mode" (i.e., the constant speed command is set to both methods with the same outer speed control loop configurations), the rated load is abruptly dismounted[3] at around 0.06 s (See Figure 3.5) at a given speed command. This generates a "step-like" load torque disturbance (to test the

[2]The transient time can be calculated roughly using Equation (2.43).

[3]The method that generates a rated torque step using another inverter which works on torque mode is not reasonable. Because the generated torque step highly depends on the performance of the inverter.

harshest situation). Figure 3.5a to 3.5d show the performances with FOC, COC, DMPC, DOC solutions, respectively, where the stator current ($i_{a,b,c}$), excitation and torque current ($i_{d,q}$), tracking error of excitation and torque current ($i_{d,q}^{err}$) and rotor speed (ω_r) responses are shown. As can be seen, both the FOC and COC have much smaller ripples while a second order phenomenon is seen during the transient phase. The largest ripple is seen with the DMPC solution.

3.6.4 Assessment of parameter robustness

As fully model-based solutions, the proposed concept requires all the system parameters. To investigate the influences of parameter variations to the system performances, i.e., parameter robustness, the parameter sensitivity of both the proposed solutions are verified. In this section, three experimental testing scenarios are carried out to examine their performances under variations of motor inductance. All tests were carried out with a rated load torque change applied to the SPMSM. To investigate the influence of *dq*-axis inductance variations, the controller employs various inductance values ($\hat{L}_d$, $\hat{L}_q$) which are set to 80%, 100%, and 120% of the nominal motor values (real parameters) respectively[4]. At such configurations, the motor speed and the tracking error of the *dq*-axis currents (i_d^{err}, i_q^{err}) are shown for all methods at 20% of the nominal speed, with an abruptly changed load (between 0 and 100% of its rated value). As can be seen from Figure 3.6, all methods work well during the test, i.e., all are robust within such parameter changing range, and nearly identical performances of the speed response (overshoot and the setting time) are seen with all methods during these three tests. However, quite small transient tracking error for both the *dq*-axis currents are seen with the DOC solution, while the tracking biases are relatively big with the COC method under these tests, which can be explained by that, the dynamics of the DOC is much faster and also robust to parameter variations during transient phases. The FOC and DMPC solutions were (almost) not affected (no obvious biases are seen) by these parameter variations, demonstrating the highest robustness.

3.6.5 Assessment of performance under constraint

For certain cases, e.g., e-cars, the capabilities of the controller to reject the influences of the DC-link voltage changes (mainly reductions) are very important. In this section, this capability of all the afore-mentioned schemes is tested. The experimental scenarios are as follows:

- The DC-link voltage is set as 420 V (the nominal value is 540 V). Thus, the DC-link voltage is not enough when the motor runs at high speed (above 0.77 p.u.);

On the contrary, dismounting from rated value abruptly to zero loads through the PWM lock of the load side inverter is reasonable.

[4]This testing range is chosen due to that, our measurements show, the estimated values of the system is in (0.8, 1.2) times of the actual values.

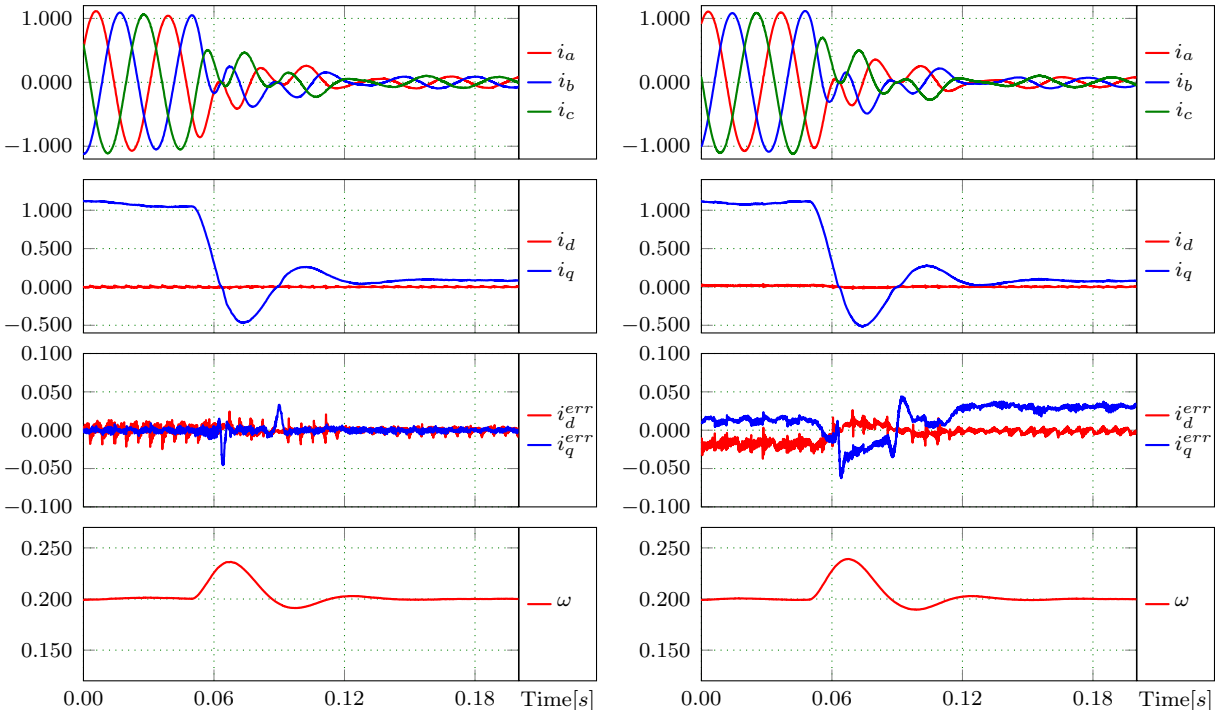

(a) FOC.

(b) COC.

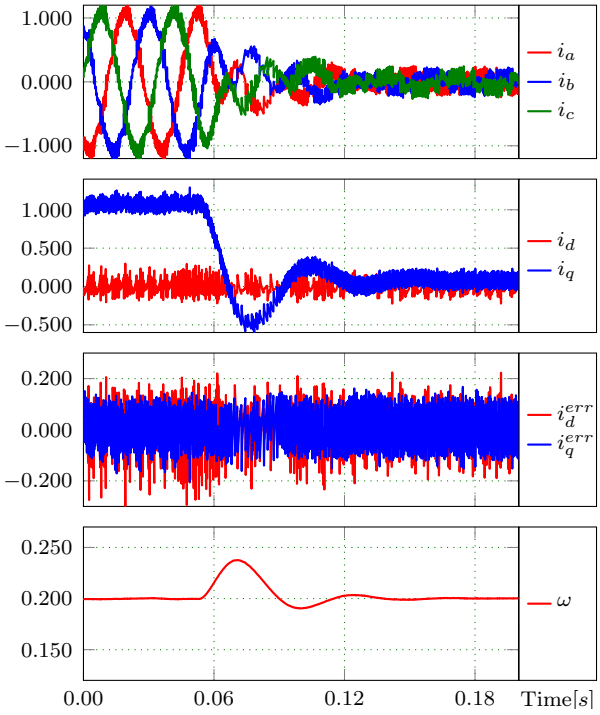

(c) DMPC.

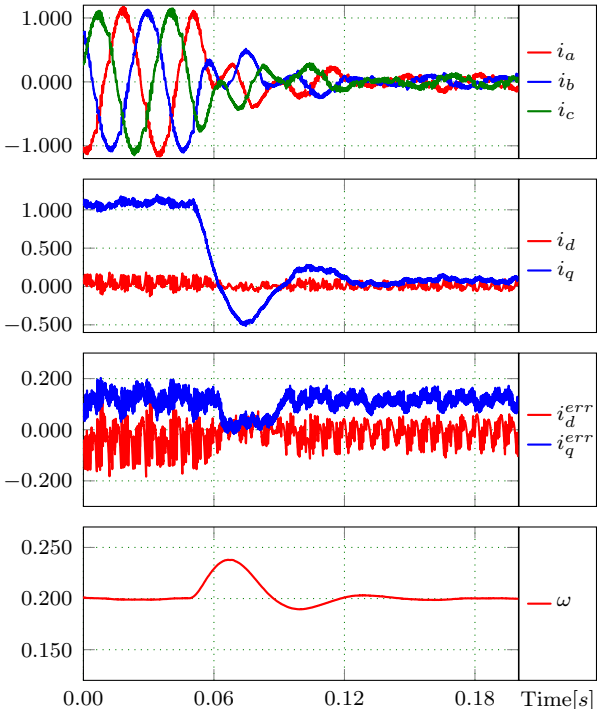

(d) DOC.

Figure 3.5: Transient phase performance evaluation in *speed mode* (at 0.2 of its nominal speed).

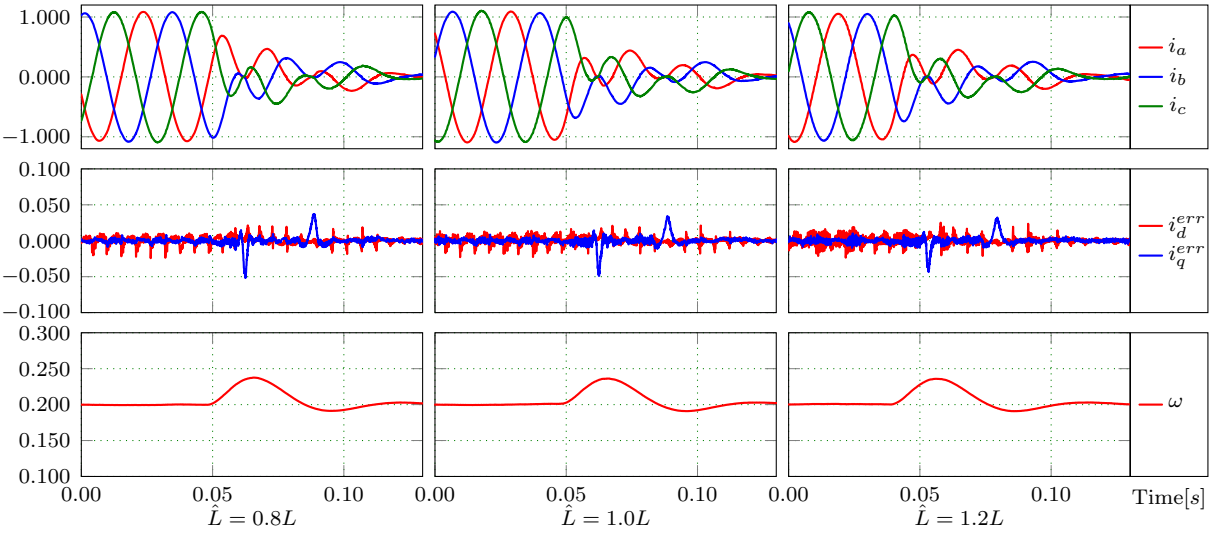

(a) FOC.

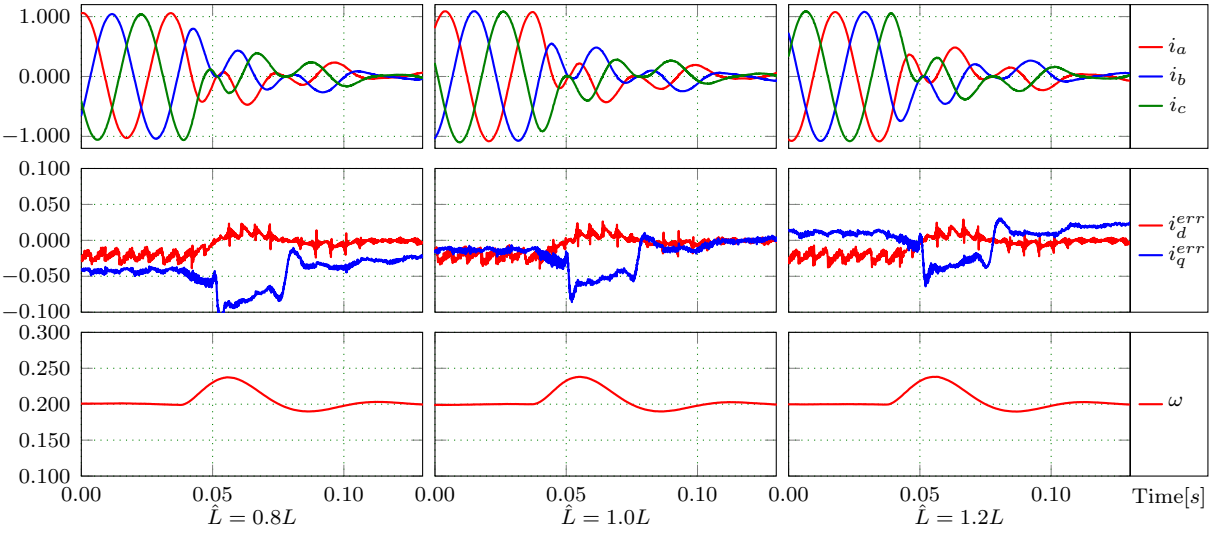

(b) COC.

- There is no field-weaken algorithm, i.e., no other aspects may influence the results when DC-link voltage is lower;

- The speed reference is set to 0.9 p.u..

With the above configuration, a rated load is applied to the equipment under test (EUT). The results are shown in Figure 3.7. As can be seen, at the condition of that, the DC-link voltage is not enough to output the desired output voltages, good speed tracking performances are achieved with FOC and DMPC, and then is DOC. However, the current waveform and quality of using COC out-performs all the other solutions.

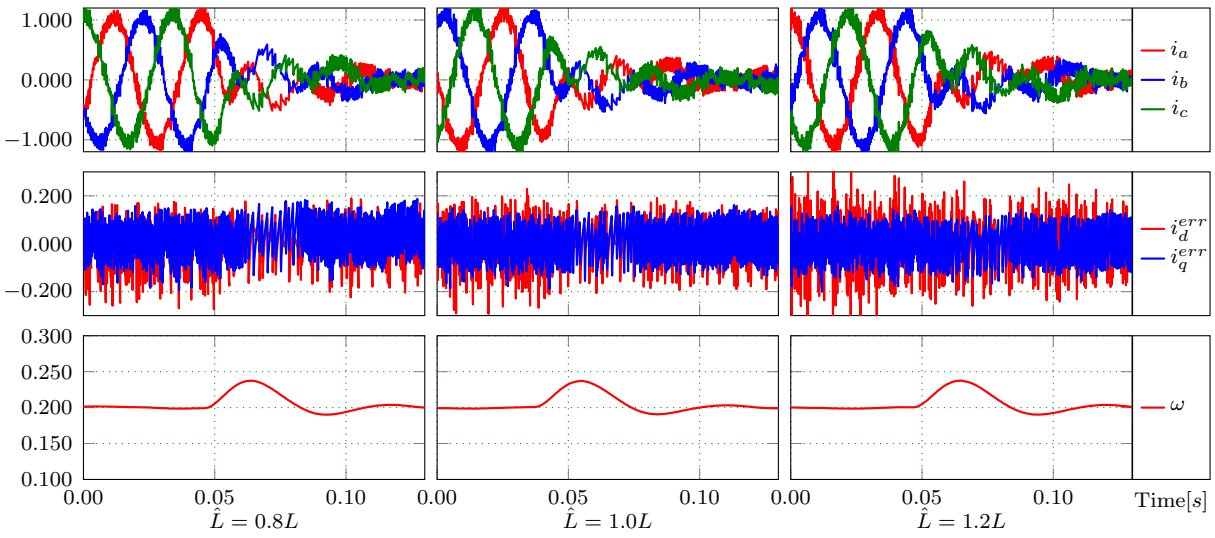

(c) DMPC.

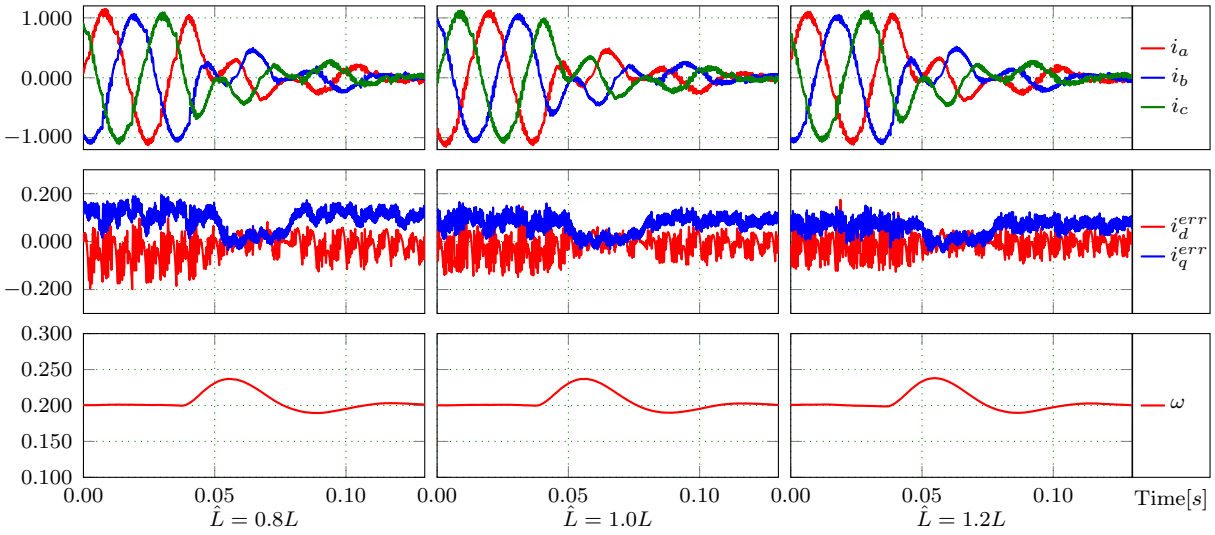

(d) DOC.

Figure 3.6: Parameter sensitivity investigation results.

3.6.6 Assessment of computation burden

As is already mentioned in Section 3.2.3, small computational time is one of the advantages of the proposed control schemes. To assess the computational time, the time duration required for calculating the algorithm of each method in one sampling/control cycle is determined by instrumentation trace macro (ITM) cell which is integrated into Cortex™-M4 processor. The timestamps are recorded at the entrance of the function and recorded again at the exit of the function. The elapsed time is obtained from the difference of the two timestamps. Detailed results are collected in the first row of Table 3.2. The DMPC takes the longest time, 22.1 µs, to execute, while the COC takes the shortest time, only 10.3 µs. The results confirm that COC can achieve better overall performance

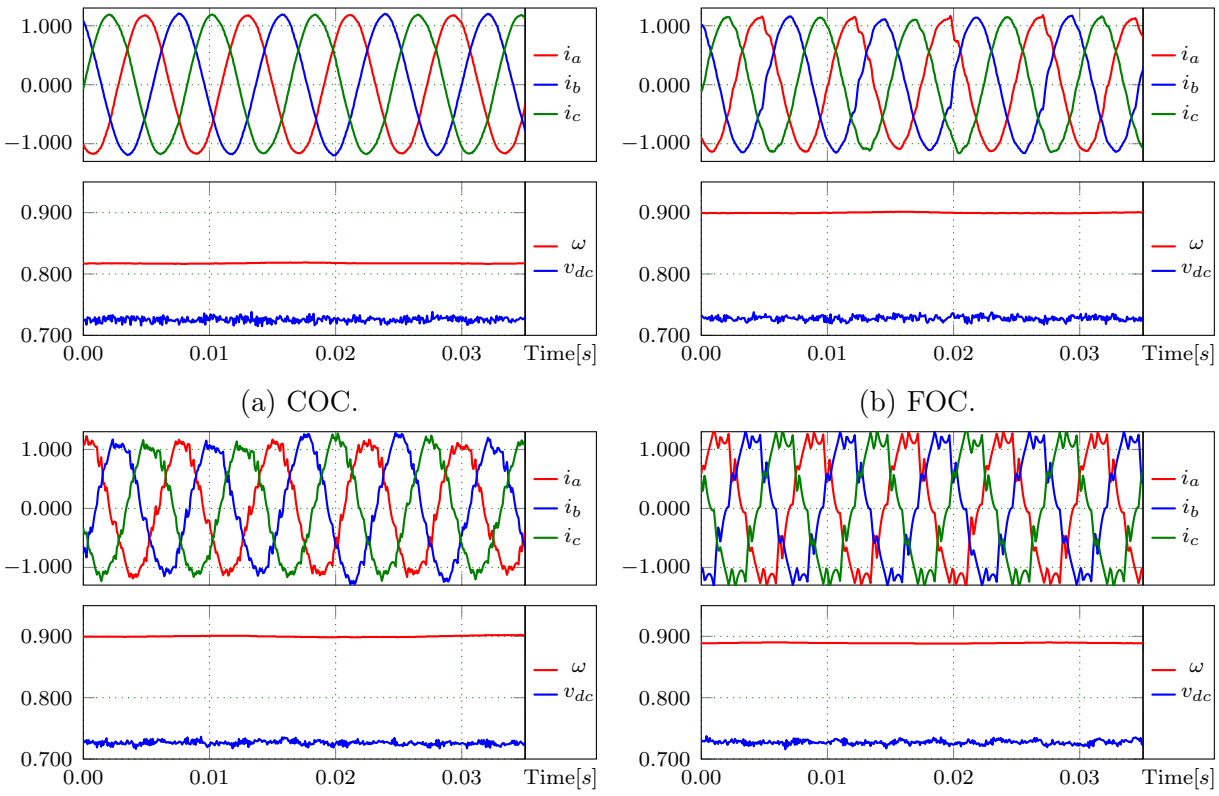

(a) COC. (b) FOC.

(c) DMPC. (d) DOC.

Figure 3.7: Working under low voltage limit.

with similar control complexity and computational burden, which is practical for real-time implementation.

To ease an overall assessment of the experimental output, the performances (including, execution time, switching frequency, steady and transient status performances, disturbance rejection capabilities, and the robustness to parameter variations) of each method are summarized in Table 3.2.

Table 3.2: Overall assessment results of afore-discussed control schemes.

Methods	**FOC**	**COC**	**DMPC**	**DOC**
Execution time	12.3 µs	10.3 µs	22.1 µs	19.1 µs
Switching frequency	constant	constant	variable	variable
Steady performances	good	good	bad	moderate
Dynamics[5]	fast	fast	fast	fast
Disturbance rejection	moderate	moderate	moderate	moderate
Robustness	strong	moderate	moderate	moderate

[5]This test result is obtained based on that, all schemes are assessed at the same *control interval*. When assessing with similar switching frequency, then the conclusion can be different.

3.7 Summary

Optimal control has been investigated theoretically since many years. However, its applications in power electronics and electric drives have rarely been reported. In this work, both the continuous and discrete solutions of the optimal control concept were proposed and experimentally validated. As a case of study, current control problems of a two-level power converter fed surface mounted permanent magnet synchronous motor drives are evaluated with both the proposed continuous and discrete solutions using optimal control concept. The experimental results showed outstanding performances of the proposed methods, which indicates that the optimal control is another effective strategy for the control of power electronics and drives. Although both the classical proportional-integral and standard non-linear controls (e.g., hysteresis, sliding mode control, etc.) are also capable of controlling an electronic drive system, the introduced method based on the optimal control concept can optimize multiple objectives with multiple system constraints of the similar drive system.

Note that, the proposed concept is not limited to the current control of surface mounted permanent magnet synchronous motor drives. It can be applied to all model based control problems with or without constraints (e.g., grid-connected renewable energy systems or alternating current-drives with multilevel power converters). Future work will focus on extending the proposed scheme to more advanced topologies. The author believes that, with the demanding of effective and practical control methods, the presented optimum control concepts will represent a new powerful and interesting perspective for the area of control of power electronics and drives.

Chapter 4

Voltage balance of NPC

This chapter presents two neutral-point voltage balance control strategies for three-level neutral point clamped (NPC) converter. For the space vector pulse width modulation (SVPWM)-based control scheme, the deadbeat control concept for neutral-point voltage balancing is detailed in Section 4.2. In the case of using model predictive control (MPC) algorithm, the decoupled method is presented in Section 4.3.

4.1 Neutral Point Current

In most applications, there are two direct current (DC) capacitors connected in series between P and N. However, the DC-link is usually powered by one DC voltage source in most cases, such as powered by a three-phase diode bridge rectifier. The current equation of the capacitors is $i_{cj} = C\frac{dv_{cj}}{dt}$. By applying Kirchoff's current law (KCL) at the neutral point O

$$i_o = i_{c1} - i_{c0} = C\frac{d}{dt}\left(v_{c1} - v_{c0}\right) \tag{4.1}$$

where v_{c1} is the voltage between DC-link plus (P) and neutral point (O), v_{c0} is the voltage between neutral point (O) and DC-link minus (N), i_{c0} is the current flowing through C_0, i_{c1} is the current flowing through C_1, i_o is the neutral point current.

As can be seen form Equation (4.1), the voltage drift is totally caused by the i_o. Once the i_o is known, the voltage drift of the two capacitors can be controlled precisely. Fortunately, the neutral point current i_o can also be expressed as a function of the switches state and the phase current. Considering the dead time of the switches, the typical switches state timing of each leg can be seen in Figure 4.1. There are five different switches states.

From Table 4.1, the neutral point current caused by one phase(i_{ox}) can be expressed as:

$$i_{ox} = \begin{pmatrix} \overline{S_{x1}}\overline{\bar{S}_{x0}}\overline{S_{x0}}\bar{S}_{x1}GE\left(-i_x\right) + \\ \overline{S_{x1}}\overline{\bar{S}_{x0}}S_{x0}\bar{S}_{x1} + \\ \overline{S_{x1}}\overline{\bar{S}_{x0}}S_{x0}\overline{\bar{S}_{x1}}GE\left(i_x\right) \end{pmatrix} i_x \tag{4.2}$$

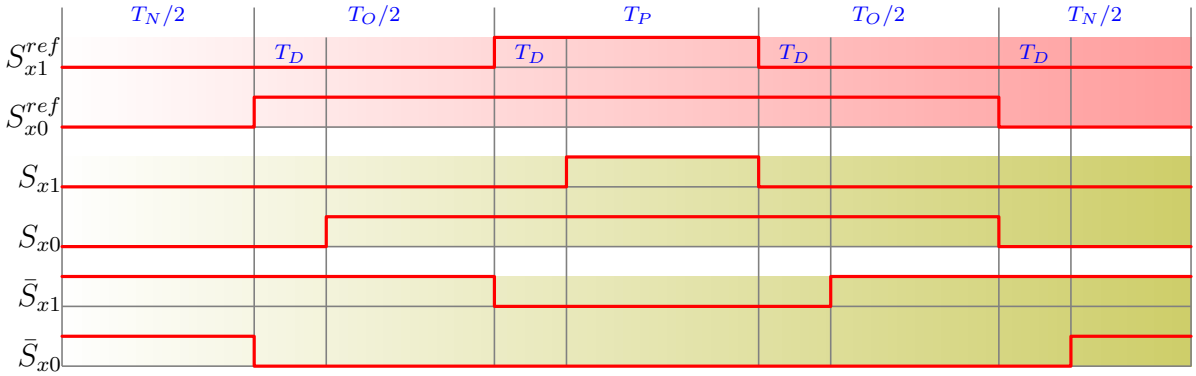

Figure 4.1: Switch state timing signals of each phase.

S_{x1}	S_{x0}	$\bar{S}_{x1}$	$\bar{S}_{x0}$	i_x	v_{xo}	i_{ox}
0	0	1	1		$-v_{c0}$	0
0	0	1	0	≥ 0	$-v_{c0}$	0
0	0	1	0	< 0	0	i_x
0	1	1	0		0	i_x
0	1	0	0	≥ 0	0	i_x
0	1	0	0	< 0	v_{c1}	0
1	1	0	0		v_{c1}	0

Table 4.1: switch states of a leg

where $\overline{S_{xj}}$ is the negation of S_{xj}, $\overline{\bar{S}_{xj}}$ is the negation of $\bar{S}_{xj}$, i_x is the corresponding phase current. The function $GE\,(x)$ is defined as:

$$GE\,(x) = \begin{cases} 1 & x \geq 0 \\ 0 & x < 0 \end{cases} \tag{4.3}$$

With the assumption that the output phase currents are not varying during one sample time. According to Figure 4.1 and Equation (4.2), the averaged neutral-point current of one leg in one switching period can be expressed as

$$\frac{1}{T_s}\int_t^{t+T_s} i_{ox}dt = \frac{1}{T_s}\begin{pmatrix} T_D GE\,(-i_x) + \\ (T_{Ox} - T_D) + \\ T_D GE\,(i_x) \end{pmatrix} i_x = \frac{1}{T_s} T_{Ox} i_x \tag{4.4}$$

where T_D is the dead time, T_{Ox} is the duration time in such state: $S_{x1} = 0$ and $S_{x0} = 1$ which is called O state.

So the average neutral-point current is :

$$i_o = \sum_{x=a}^{c} \frac{1}{T_s} T_{Ox} i_x = \frac{1}{T_s}\left(T_{Oa} i_a + T_{Ob} i_b + T_{Oc} i_c\right) \tag{4.5}$$

If the switching state has no change in one sampling time, the equation that describes the logic which has O state can be drawn with $1-|s_x|$ where s_x is defined in Equation (2.33). In such situation, the averaged neutral-point current is

$$i_o = \sum_{x=a}^{c} (1-|s_x|)\, i_x = \sum_{x=a}^{c} (-|s_x|)\, i_x = -\left(|s_a|\, i_a + |s_b|\, i_b + |s_c|\, i_c\right) \tag{4.6}$$

4.2 DBC of neutral-point voltage balance for SVM

A *new* DC-link voltage balancing method using the deadbeat control concept for three level NPC converters is proposed and experimentally verified in this chapter. Within this chapter, a model of the *instant* neutral point current is firstly derived, which is relevant to the real switch states and the output phase currents. Additionally, the *average* model of the neutral point current is also obtained. This *average* model allows us to calculate neutral point current within *one sample interval*. Based on a well-known model of the DC-link voltage and the developed *average* neutral point current model, a deadbeat controller dealing with the DC-link balancing control is designed and incorporated into a space vector modulation (SVM), which allows adjusting the neutral point current continuously. The novelty of the proposed method is that a good DC-link voltage balancing control can be assured, at an any load condition and any output voltage of the converter, while the normal functionality (phase voltage and current output) of a three level NPC converter remains, which has been proofed with both simulation and experimental data. The experimental data also shows that good dynamics of the DC-link voltage adjusting and low neutral point voltage ripples can be achieved with such solution.

4.2.1 Motivation

In recent years, the demands of high power converters increase rapidly. Compared to two level converters, the three level NPC converter, as shown in Figure 2.5 have been drawing great interests in the industry field [29, 49]. Because of its increased voltage levels, three level NPC converters can be used for high voltage and high power levels applications. Also, a three level NPC converter is economically visible in high energy-cost markets due to the substantial reductions in filter size/weight and cost (30%) [50]. Low harmonic current distortion is another benefit [51, 52].

Although three level NPC converter has been studied for several decades after its introduction in 1981 [53]. There are still many issues requiring further research efforts. Among them, the DC-link voltage balancing is eager to be solved with reasonable cost. When the voltage of the two capacitors has a significant drift, the output voltage of the inverter will be distorted. Furthermore, long time high voltage pressure may cause failure of the capacitor and switches.

To the best of the authors' knowledge, the following methods can be used to solve the voltage balancing problem in the NPC power converters:

1. One is to use two isolated transformers or equivalent circuits which provide energy separately for the two capacitors [54, 55]. Usually, it is done through diode bridge rectifiers. Apparently, this method requires extra hardware and will increase the cost of the whole system.

2. The second method is using an extra current source to inject current in the neutral point.

3. The other method is based on pulse width modulation(PWM) strategy [56,57]. This approach requires modification for the switching pattern. Thus, the modulation algorithm is more sophisticated compared to the general SVPWM. This method provides an economical way to solve the unbalance issue in the NPC. However, the existing balance methods based on PWM have the following shortcomings:

   (a) Lacking a strategy that adjusts the neutral point voltage continuously.

   (b) Can not work well in fully ranged operation point with the same parameter.

   (c) Big ripple of the neutral point voltage.

Therefore, a *new* DC-link voltage balancing method using the deadbeat control concept for three level NPC converters is proposed and experimentally verified. Based on a well-known model of the DC-link voltage and the developed *average* neutral-point current model, a deadbeat controller dealing with the DC-link balancing control is designed and incorporated into a SVM method, which allows adjusting the neutral-point current continuously. The novelty of the proposed method is that a good DC-link voltage balancing control can be assured, at an any load condition and any output voltage of the converter, while the normal functionality (phase voltage and current output) of a three level NPC converter remains, which has been proofed with both simulation and experimental data. The experimental data also shows that good dynamics of the DC-link voltage adjusting and low neutral point voltage ripples can be achieved with such solution.

4.2.2 Space vector based modulation of the three-level NPC

The space vector based modulation methods of three-level NPC are well explained in [51,57,58]. To solve the unbalance issue, an efficient way is to control the neutral point current. So, in this section, a special SVPWM which can generate the demanded neutral point current is proposed.

Figure 2.6 shows a space vector diagram for the three-level NPC converter. There are 19 possible space vectors, which corresponds to a total of 27 switching states which are also shown in the figure. The calculation for the triangles are similar, so only the operation in triangle 1 of the first sector(see Figure 4.2) is analyzed.

Additionally, there are many approaches to design the switch sequence. The present work shows only the general design of SVPWM sequences which is possible to get symmetrical waveforms. The design for switch sequence is detailed in Section 4.2.2.2.

4.2.2.1 Voltage second balance

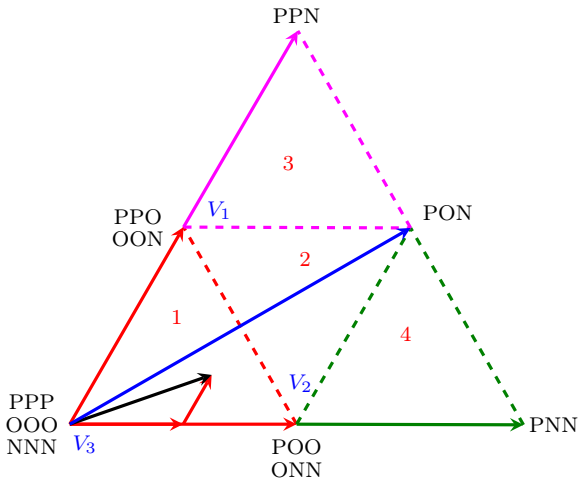

Figure 4.2: Vectors in Sector I.

Based on voltage second balance, the reference voltage(V^*) can be expressed by the adjacent three vectors(V_1, V_2, V_3).

$$T_s V^* = V_1 T_1 + V_2 T_2 + V_3 T_3 \tag{4.7}$$

where T_1, T_2, T_3 are the duration times of the V_1, V_2 and V_3 respectively. T_s is the sample period. So the time balance is given by

$$T_s = T_1 + T_2 + T_3 \tag{4.8}$$

Figure 4.2 also illustrates the basic relationship of V_1 and V_2 in the $\alpha\beta$ plane.

$$V_2 = \left(\cos\frac{\pi}{3} + j\sin\frac{\pi}{3}\right) \times V_1 \tag{4.9}$$

$$V_1 = \frac{1}{2} \tag{4.10}$$

Rewritten (4.7) in the $\alpha\beta$ plane, we obtain

$$(V_\alpha + jV_\beta)\, T_s = V_1 T_1 + V_2 T_2 \tag{4.11}$$

$$\frac{1}{2}(\cos 0 + j\sin 0)\, T_1 + \frac{1}{2}(\cos 60 + j\sin 60) \times T_2 = (\alpha + \beta j) \times T_s \tag{4.12}$$

$$\begin{bmatrix} \frac{1}{2}\cos x & \frac{1}{2}\cos\left(x+\frac{\pi}{3}\right) & 0 \\ \frac{1}{2}\sin x & \frac{1}{2}\sin\left(x+\frac{\pi}{3}\right) & 0 \\ 1 & 1 & 1 \end{bmatrix} \begin{bmatrix} T_a \\ T_b \\ T_o \end{bmatrix} = \begin{bmatrix} \alpha \\ \beta \\ 1 \end{bmatrix} T_s \tag{4.13}$$

In order to use the per unit system, select the circle as the base value 1 so,

$$\begin{bmatrix} \frac{\cos x}{2} & \frac{1}{2}\cos\left(x+\frac{\pi}{3}\right) & 0 \\ \frac{\sin x}{2} & \frac{1}{2}\sin\left(x+\frac{\pi}{3}\right) & 0 \\ 1 & 1 & 1 \end{bmatrix} \begin{bmatrix} T_a \\ T_b \\ T_o \end{bmatrix} = \begin{bmatrix} \frac{\sqrt{3}\alpha}{2} \\ \frac{\sqrt{3}\beta}{2} \\ 1 \end{bmatrix} T_s \tag{4.14}$$

4.2.2.2 switch timing of IGBT

The determination of switching sequence is done as conventional two-level SVPWM method which is based on the following consideration:

- Each of the phases is switched at least once in each sampling interval.
- Only one switch is allowed to switch during the state transition.
- The final switch state of the current sample and the initial state of next sample are same.

Figure 4.3 shows the demanded switch timing of the IGBTS. This figure will be helpful in calculating the duty cycle of each switch.

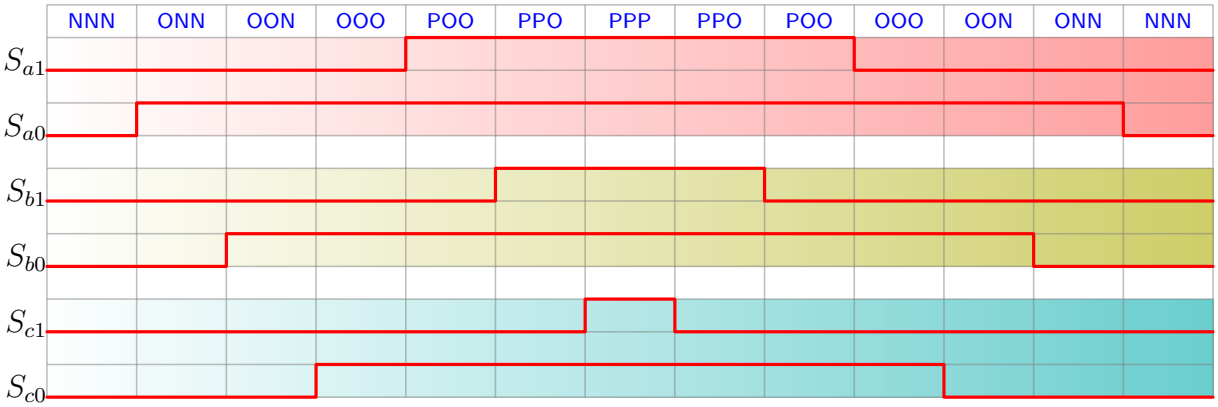

Figure 4.3: IGBT switch timing in triangle 1 of Sector I.

So the duty of each insulated gate bipolar transistor (IGBT) is

$$\begin{aligned} m_{a1} &= \frac{T_{POO} + T_{PPO} + T_{PPP}}{T_s} \\ m_{a0} &= 1 - \frac{T_{NNN}}{T_s} \\ m_{b1} &= \frac{T_{PPO} + T_{PPP}}{T_s} \\ m_{b0} &= 1 - \frac{T_{NNN} + T_{ONN}}{T_s} \\ m_{c1} &= \frac{T_{PPP}}{T_s} \\ m_{c0} &= 1 - \frac{T_{NNN} + T_{ONN} + T_{OON}}{T_s} \end{aligned} \tag{4.15}$$

From Figure 4.2 we can get

$$\begin{aligned} T_{ONN} + T_{POO} &= T_1 \\ T_{PPO} + T_{OON} &= T_2 \\ T_{NNN} + T_{PPP} + T_{OOO} &= T_3 \end{aligned} \tag{4.16}$$

In order to provide more flexibility, the time distribution of zero vectors is using index μ and γ which satisfy:

$$\begin{aligned} T_{PPP} &= \gamma T_3 \\ T_{OOO} &= \mu T_3 \end{aligned} \tag{4.17}$$

So that if the dwelling time of zero vector is calculated, the switching sequence can be determined according to the indexes μ and γ. As the voltage vector PPP, OOO and NNN are all zero vectors, changing the dwelling times of the two vectors has no influence to the desired voltage vector if the following conditions hold.

$$\begin{aligned} 0 \le \gamma \le 1 \\ 0 \le \mu \le 1 \\ 0 \le 1 - \mu - \gamma \le 1 \end{aligned} \tag{4.18}$$

Due to the vectors ONN, POO, OON and PPO are related to the voltage balance, the distribution of these vectors is discussed in Section 4.2.2.3.

4.2.2.3 Rearranging time distribution of the redundant voltage vectors

From Equation (4.5), the averaged neutral point currents is $-\frac{T_{POO}}{T_s} i_{\mathrm{a}}$ when vector POO is applied. Meanwhile, the averaged neutral point currents is $\frac{T_{ONN}}{T_s} i_{\mathrm{a}}$ when vector ONN is applied. Additionally, to quantitative analyze the relationship between neutral point current and dwelling time of the redundant vector, a coefficient λ is introduced which is defined as follows:

$$\lambda = \begin{cases} \frac{T_{POO}}{T_{POO}+T_{ONN}} = \frac{T_{POO}}{T_1} & i_a \le 0 \\ \frac{T_{ONN}}{T_{POO}+T_{ONN}} = \frac{T_{ONN}}{T_1} & i_a > 0 \end{cases} \tag{4.19}$$

So $0 \le \lambda \le 1$, and it will increase more voltage of $C1$ as λ becomes bigger. When applying vector V_2, from Equation (4.5), the averaged neutral point current is $\frac{T_{PPO}}{T_s} i_{\mathrm{c}}$ when using vector PPO. Meanwhile, the averaged neutral point currents is $-\frac{T_{OON}}{T_s} i_{\mathrm{c}}$ when using vector OON. In the same way, in order to make it increase more voltage of $C1$ as λ becomes bigger, λ is defined as follows in such case:

$$\lambda = \begin{cases} \frac{T_{PPO}}{T_{PPO}+T_{OON}} = \frac{T_{PPO}}{T_2} & i_c \le 0 \\ \frac{T_{OON}}{T_{PPO}+T_{OON}} = \frac{T_{OON}}{T_2} & i_c > 0 \end{cases} \tag{4.20}$$

When the reference voltage vector is located in other triangles or triangles in other sectors, λ can be defined using similar means. Considering one condition $i_a > 0, i_c > 0$ in sector I triangle 1 and with all the redundant vectors used, the averaged neutral point current is expressed as:

$$i_o = \frac{1}{T_s} \begin{pmatrix} (T_{ONN} - T_{POO})\, i_a + \\ (T_{PPO} - T_{OON})\, i_c \end{pmatrix} = \frac{1}{T_s} \left((2\lambda - 1)\, T_1 i_a + (1 - 2\lambda)\, T_2 i_c \right) \tag{4.21}$$

So the duty of each IGBT in sector I triangle 1 is[1]:

$$\begin{aligned}
m_{a1} &= (\lambda - 1) \left(\beta - \sqrt{3}\, \alpha \right) + 2\, \beta\, \lambda - \gamma \left(\beta + \sqrt{3}\, \alpha - 1 \right) \\
m_{a0} &= (-\gamma - \mu) \left(\beta + \sqrt{3}\, \alpha - 1 \right) + \left(\beta + \sqrt{3}\, \alpha \right) \\
m_{b1} &= 2\, \beta\, \lambda - \gamma \left(\beta + \sqrt{3}\, \alpha - 1 \right) \\
m_{b0} &= (-\gamma - \mu) \left(\beta + \sqrt{3}\, \alpha - 1 \right) + \lambda \left(\beta - \sqrt{3}\, \alpha \right) + \left(\beta + \sqrt{3}\, \alpha \right) \\
m_{c1} &= -\gamma \left(\beta + \sqrt{3}\, \alpha - 1 \right) \\
m_{c0} &= (-\gamma - \mu) \left(\beta + \sqrt{3}\, \alpha - 1 \right) + \lambda \left(\beta - \sqrt{3}\, \alpha \right) + \left(\beta + \sqrt{3}\, \alpha + 2\, \beta\, (\lambda - 1) \right)
\end{aligned} \tag{4.22}$$

With a series of Equation (4.21), adjusting the neutral point current continuously can be achieved by changing λ. Once the neutral point current is controlled, the neutral point voltage drift can be controlled. Certainly, the control capability of the neutral point current is related to the modulation index and the output current which can't be modified freely.

4.2.3 Conventional deadbeat controller design

For a control system, the settling time is one of the most important characteristics. Deadbeat controller aims to reach the stable state after a minimum number of sampling periods, which equal to the order of the system to be controlled. Therefore, if there is a demanding of quick setting time, the deadbeat controller is probably used.

For an nth-order linear system, the minimum number of sampling periods will be at most equal to n. That is to say, it is possible to reduce the final error to zero by applying an appropriate control input. It turns out that the minimum number of sampling periods setting time can be possible without the limitation of the control input. This is, in fact, meaningless in practice. For example, for nth-order system, in a real world, to achieving minimum number step settling time, the control signal may exceed the possibilities of the usual actuator. So we have to find a solution which would make the control signal under-excitation with the cost of increasing the settling time while the tracking performance can take care of as well.

[1] All the equations are listed in Appendix C.

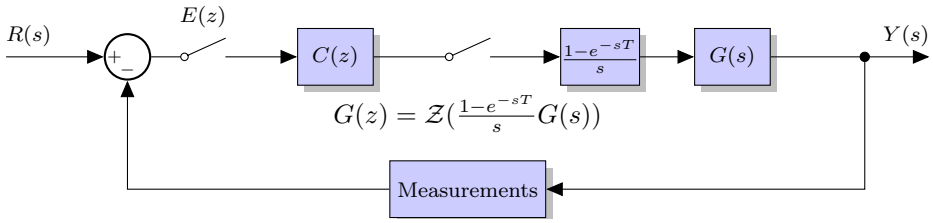

Figure 4.4: Digital control system.

Figure 4.4 depicts a general digital control system, where $G(s)$ is the transfer function of the plant, $G(z)$ is the transfer function of the plant in discrete domain, $C(z)$ is the transfer function of the digital controller, $R(z)$ is reference input , $E(z)$ is tracking error, $Y(z)$ is the system output. In this figure, there is a zero order hold circuit used for data reconstruction. The formulation problem can be stated in the following behavior.

Find a digitial controller $C(z)$ such that the output of the system $G(s)$ equals to the reference input $R(z)$ after a certain time (nT_s).

The closed loop transfer function is therefore

$$N(z) = \frac{Y(z)}{R\,(z)} = \frac{C(z)G(z)}{1 + C(z)G(z)} \tag{4.23}$$

For designing the dead-beat controller with fastest setting time, the transfer function of the closed loop between the output signal and the input signal should be equal to the order of the system. Specially, for one order system, the condition is $N(z) = z^{-1}$ provide the system is stable which means the poles of the system should not have poles outside or in the vicinity of the unit circle in the z-plane. Hence the transfer function of digital controller can be calculated as

$$C(z) = \frac{z^{-1}}{G(z)\,(1 - z^{-1})} \tag{4.24}$$

However, in a real world, to achieving this one step settling time, the control signal would exceed the possibilities of a usual actuator. Thus, one has to find a solution which would make the control signal under-excitation with the cost of increasing the settling time. One method is divide the reference signal into more sub-levels and reach the desired reference in more steps. That is in For example choosing the transfer function of the closed loop as

$$N(z) = \sum_{j=1}^{n} w_j z^{-j} \tag{4.25}$$

which satisfy $N(1) = 1$, so that the design will not affect the final value. w_j are weighting factors which are used for each error sequence. The weighting factors w_j should satisfy $\sum_{j=0}^{n-1} w_j = 1$ and $w_j \in [0; 1]$. In such case, the practical realization of the control law is

given by

$$C(z) = \frac{\sum_{j=1}^{n} w_j z^{-j}}{G(z)\left(1 - \sum_{j=1}^{n} w_j z^{-j}\right)} \tag{4.26}$$

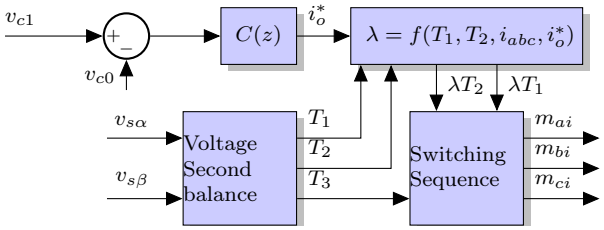

Figure 4.5: Control scheme of proposed method.

4.2.4 Case application: Deadbeat controller for neutral-Point voltage balance

Transferring equations (4.1) into Laplace (frequency) domain, yields the transfer function of voltage drift is:

$$G(s) = \frac{v_{c1} - v_{c0}}{i_o} = \frac{1}{sC} \tag{4.27}$$

Applying equation(4.26), the deadbeat controller for the voltage drift is designed as

$$C(z) = \frac{z^{-1}}{\mathcal{Z}(G(s))(1 - z^{-1})} \tag{4.28}$$

The proposed control scheme is shown in Figure 4.5. The neutral point current command i_o is the output of the deadbeat controller. From Equation (4.21), λ can be solved. Then the duration time of the redundant vectors is determined.

4.2.5 Simulation Results

The three-level space vector modulator with the neutral point balance algorithm was simulated in Matlab. Figures 4.6-4.7 show the performance of the proposed control strategy under different modulation index. In the simulation, the output line-line voltage of phase A (v_a), the filtered output line-line voltage (v_{af}), two modulation signals (m_{aj},m_{bj},m_{cj}), two capacitor voltages(v_{cj}), filtered neutral point current (i_{of}), the external current (i_{ex}) applied between node O and N and the control variable (λ) are shown.

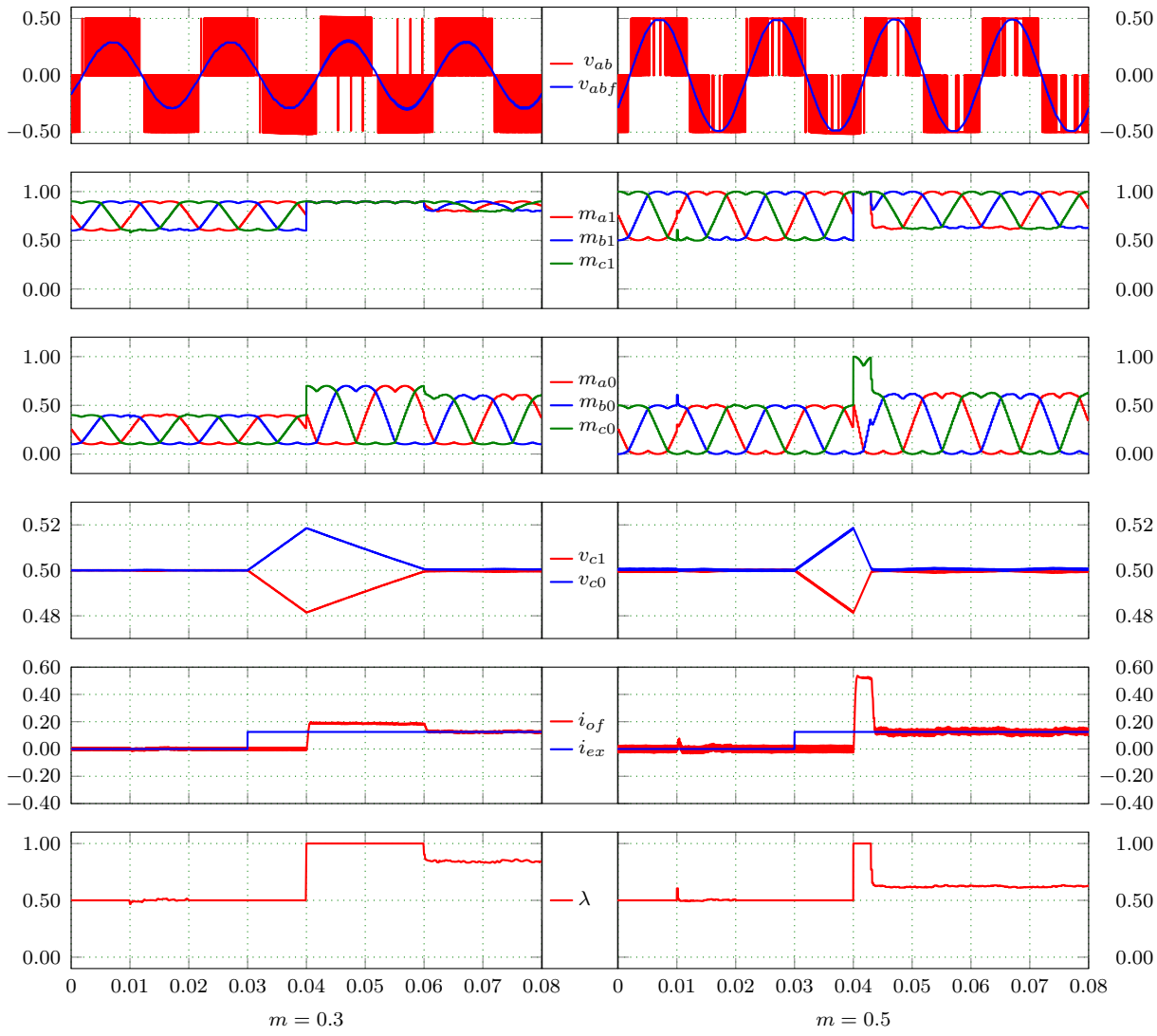

Figure 4.6: Waveforms of the simulation result with modulation index 0.3 and 0.5.

The units of voltage and current are per unit. The base value of voltage is 537 V. The base value of current is 16 A. The value of the DC-link capacitance is 1100 µF. The carriers frequency is 5 kHz. The filters for the line-line voltage and neutral point current are both second order low pass filters with 1 kHz natural frequency. The load for the converter is wye–connected RL, with R =15 Ω ,L =15 mH .

The whole simulation process is divided into five phases:

1. 0 s to 0.01 s: the steady state without neutral point voltage balance algorithm applied.

2. 0.01 s to 0.02 s: neutral point voltage balance algorithm is applied to verify the effectiveness of voltage drift control without obvious high neutral point current disturbance.

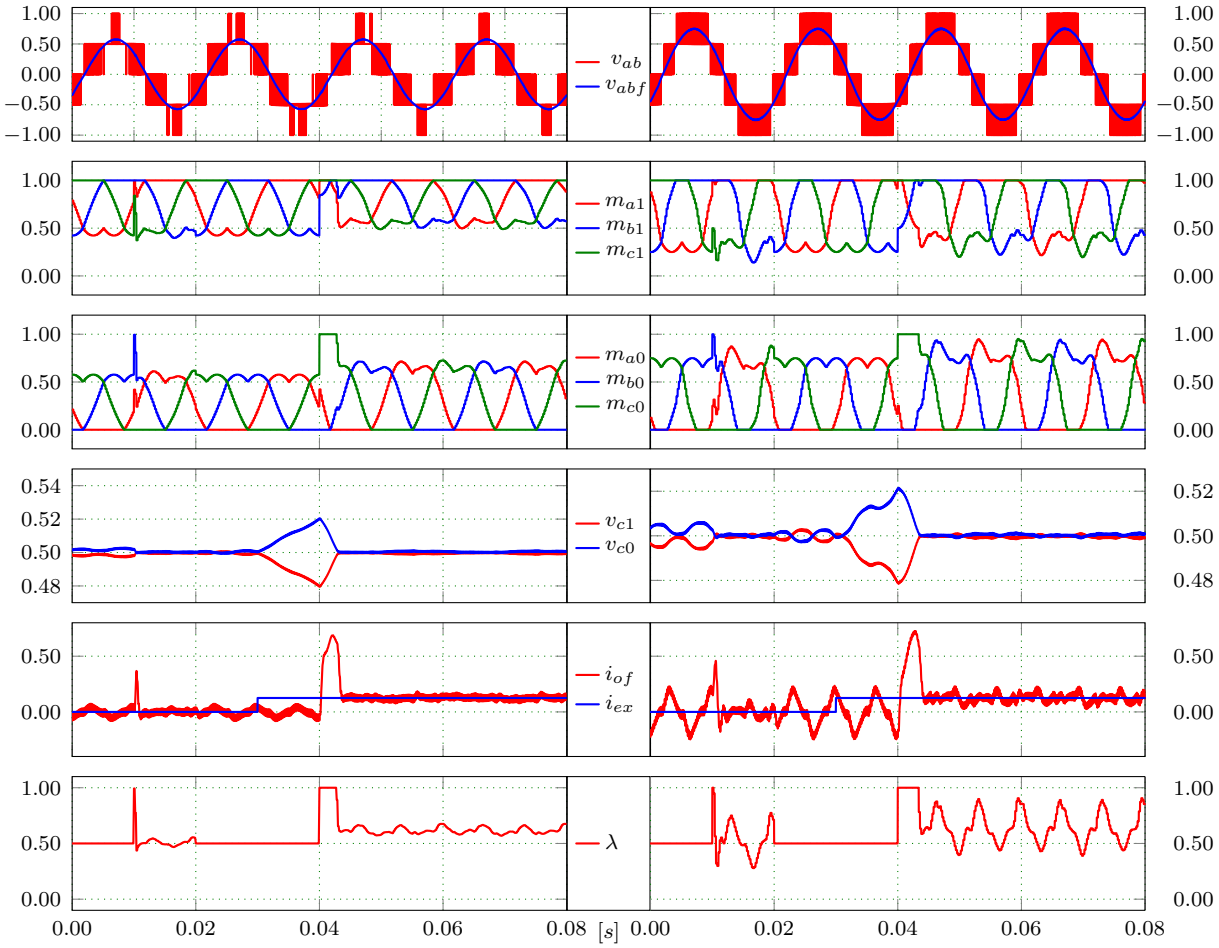

Figure 4.7: Simulation Results with modulation index $1/\sqrt{3}$ and 0.75

3. 0.02 s to 0.03 s: neutral point voltage balance algorithm is not used. Together with phases 1-2, it shows the performance in a steady state.

4. 0.03 s to 0.04 s: A high external current source is applied between node O and node N without balance algorithm.

5. 0.04 s to 0.08 s: A strong external current source is used between node O and node N with balance algorithm.

As can be seen from the v_{abf} curves of Figures 4.6-4.7, there is no obvious distortion of output line-line voltage when the balance algorithm applied or not. The balancing processes are shown in phase 5 of the two figures in which the initial voltages of the two capacitors is unbalanced very much. The voltage becomes equal quickly with the control variable $\lambda = 1$. Also, the neutral point voltage drift is suppressed significantly in phase 2 of Figure 4.7 when the strategy is carried out. It is noticeable that the neutral point voltage drift seems to become bigger in phase 2 than phase 1 of Figure 4.6. This is

because the neutral current in one sample period is varying while the algorithm has the assumption that the output phase currents are not changing.

The waveforms of λ show the fast dynamics of the controller. After the balance algorithm applied, λ goes to 1 immediately which demonstrates the deadbeat behavior. Meanwhile, the neutral point current behaves the same with λ except a little bit phase delay due to the second order filter. Also, there is no overshoot or adjusting the time in the response curve of neutral point current.

4.2.6 Experimental Results

The proposed algorithm was coded in C++ and implemented in a drive system which drives a permanent magnet synchronous motor (PMSM). The drive is controlled using vector control. V_{dc} is a six-pulse rectifier. Compared to the simulation configuration, it's difficult to inject current between neutral point O and N for a real system. So the experimental process is designed to make the neutral-point voltage drift tracking a reference. Because of the neutral-point is related to the modulation index and the output current, the performance under different modulation index has been investigated through simulation. So in this section, two kinds of an experiment are designed under no load or half load which has the similar modulation index. The modulation index is around 0.5 at no load and 0.6 at half load.

The system configuration parameters and PMSM parameters used in the experimental verification are listed in Table 4.2.

The test results under no load are shown in Figure 4.8b. It can be seen from the curve of λ that the proposed algorithm provides a fast response to the neutral-point voltage drift reference. Due to the small phase current, the contribution to the neutral point current is also very small even under the condition $\lambda = 1$. So it will cost a long time for the neutral-point voltage drift tracking the reference. In this set-up, λ vibrates from 0 to 1 severely in the steady state. This is due to the less contribution of the phase current. Little voltage unbalance can cause big variation of λ to generate same neutral point current. Figure 4.8a shows the test results at half load. Compared with the adjusting time(0.2 s) at no load, the DC-link voltage balance is achieved within 0.03 s. The experimental results show that the controller can track desired capacitor voltages quickly. Additionally, there is no 300 Hz ripple voltage caused by a six-pulse rectifier.

4.2.7 Summary

The modified space vector pulse width modulation with the proposed algorithm in this section is straightforward and is still based on two carrier waveforms. This method ensures the entirely using standard pulse width modulation of three-level inverters. Therefore, its very easy to be implemented with no more extra efforts. The modulation algorithm neither increases the switching frequencies of the devices nor influences the output voltage. Based on the proposed solution, an efficient deadbeat controller which is used to control

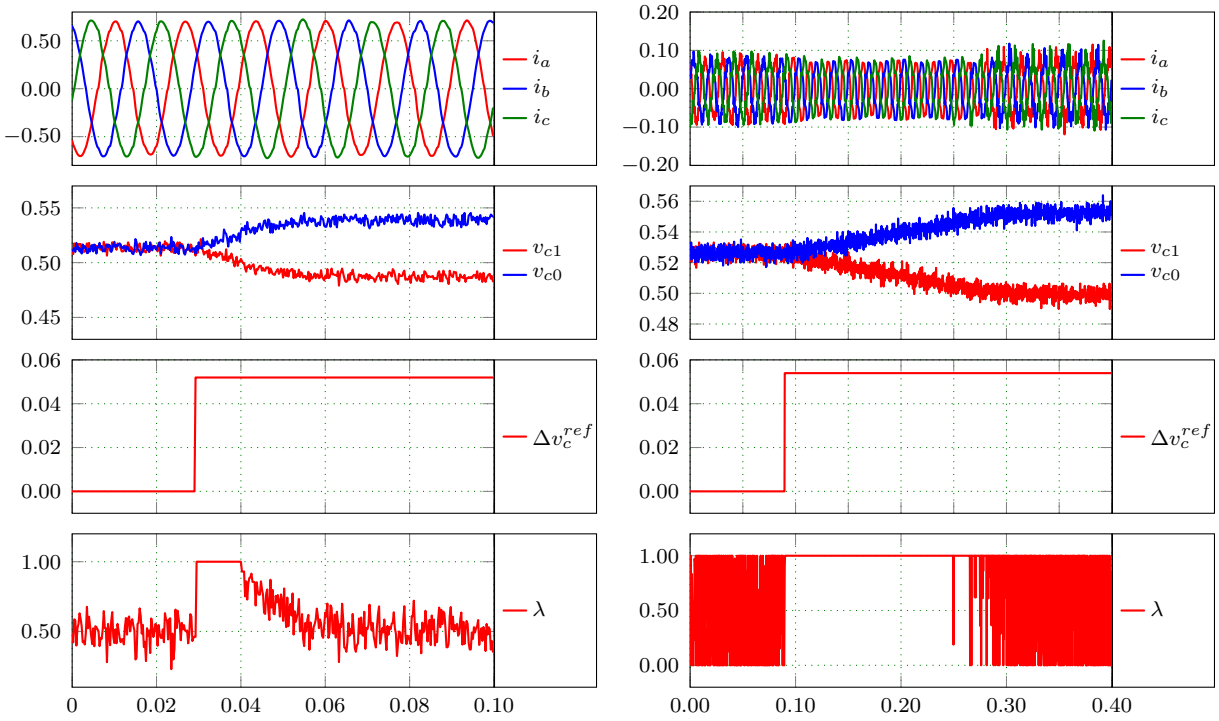

(a) half load. (b) no load.

Figure 4.8: Experiment Results. From up to down: three phase currents (i_a,i_b,i_c); DC-link voltage(v_{c0},v_{c1}); DC-link voltage drift reference(v_c^{ref}); Corresponding adjusting coefficient(λ) all in per-unit values.

Symbols	**Parameter**	**Value**
C_0	DC-link capacitor 0	1462.5 µF
C_1	DC-link capacitor 1	1462.5 µF
f_s	Switch Frequency	4000 Hz
ω_r^b	Base value of rotor speed	314 rad s^{-1}
i^b	Base value of current	8.9 A
v^b	Base value of DC-link voltage	539 V
t_d	Dead time	8 µs
F_e	PMSM rated frequency	150 Hz
I_e	PMSM rated current(rms)	6.3 A

Table 4.2: System Configuration and Parameters

the neutral point voltage is proposed. This controller just uses the output phase current to determine how the modulation works. There is no parameter to tune like traditional proportional-integral controller in the full operating range. As a conclusion, the strategy proposed can be implemented without extra sensors and will help to extend the using of the neutral point clamped converter.

Future work will focus on the experimental investigation/comparison of the proposed

solution with the already existing methods, and the improvement of its steady state errors inherent with the model based deadbeat control nature.

4.3 Decoupled neutral-point voltage balance for MPC

In this section, we propose a simple and effective neutral-point voltage balance technique within the MPC framework for three-level NPC converters. The novelty lies in that, unlike the conventional MPC methods, for which an extra weighting factor is required to adjust the tradeoff between the *neutral point voltage balance* and *targeting current* tracking, the proposed solution decouples these two objects and improves the performance of current tracking, without using any weighting factor(s). *Additionally*, the switching states to assess decrease from 27 to 19, the prediction for the DC-link voltage is not necessary. Both have considerably reduced the calculation efforts. The effectiveness of the proposed method is validated by *both* simulation *and* experimental data. Compared to the conventional MPC method, the proposed method has evidently enhanced control performances, such as faster DC-link voltage control dynamic, low total harmonic distortion (THD) in both the phase current and voltage, and better neutral voltage balancing capabilities, which have been confirmed by the experimental data obtained at a lab-constructed prototype.

This section is organized as follows: Section 4.3.1 introduce the background and motivation for this topic; Following, in Section 4.3.2, the conventional MPC method is briefly introduced. In Section 4.3.3, the proposed method is introduced and developed in detail. Section 4.3.4 and Section 4.3.5 presents the simulation results and the experiment results, which validate the effectiveness and enhancements of the proposed solution. Finally, conclusions are drawn in Section 4.3.6.

4.3.1 Motivation

In the former sections, a neutral-point voltage balance method based on SVPWM technology was proposed and verified. So, this method can be used in all the traditional occasions where SVPWM is employed. However, Predictive control applied to power converters has gained very much attention, since its introduction in the 1980s [23, 24]. Due to the fast development of microprocessors, recently, finite control set model predictive control (FCS-MPC) has been employed in plenty of applications in the power drives field, which does not require modulator. Moreover, MPC is considered as an effective solution where multiple control constraints and non-linearities [25, 59] have to be dealt with. A common used method in the literature (e.g., [60–63]) to deal with three level NPC converter control with neutral point balancing, is to combine the cost function with weighting factor for voltage balance and the cost function for current tracking (same as for the conventional two-level current control case) together as a new cost function. The drawback of this method is obvious: it has an assumption that the weighting factor for the voltage balance is properly selected. However, one cannot assure this condition in

most working cases. In fact, the component of voltage balance and the component of current tracking are closely coupled. It is difficult to ensure one of the control objects to be well achieved while keeping a good performance of another when using such method. Although in reference [64] the authors have proposed some guidelines regarding how to obtain appropriate weighting factors for getting better performances, the tuning process is still an open issue for the systems having different kinds of control objectives with different units. In reference [65], the authors proposed a modified solution that allows the unbalance voltage in the capacitors within a band: when the predicted value for the unbalance voltage is within the band, the cost function is selected as the conventional one (cost function without covering the DC-link voltage balancing), whilst when the unbalance voltage is out of the band, the cost function becomes a function of the unbalanced voltage and other control objectives, where the voltage balancing control is highly weighted. However, for a three level NPC converter, to achieve a similar current quality as the conventional linear controller with modulator, the control the interval of FCS-MPC should be much shorter. The FCS-MPC algorithm requires 27 times calculation in one sampling period for the state prediction and cost function for a three level NPC converter, which requires a much more powerful micro-controller than what is used in the conventional linear controllers. The calculation time optimizing remained untouched in the method proposed in reference [65]. Meanwhile, the cost function has no corrections to achieve current tracking when the unbalanced voltage is out of the band. Therefore the control performance of the currents gets deteriorated during this case. Additionally, how to deal with the voltage balance when the phase current is very small (at such case, the neutral point current is very small, which may lead to the failure of the neutral point voltage balance) is untraceable.

Inspired by the above analysis, an improved FCS-MPC method with decoupled DC-link voltage balancing control is proposed to solve the mentioned problems. In the proposed solution, an average neutral point current model is derived, which is used to decouple the control target of neutral point voltage control form the conventional approaches. Thereby, a reduced set of candidate vectors is considered to reduce the computational burden, without affecting the control performances. As a case study, a three level NPC converter fed induction motor drive system, with the phase current control, for the induction motor, and voltage balancing control, for the three level NPC converter, being the control objectives, is considered to demonstrate the proposed *improved predictive control solution with decoupled neutral-point voltage balancing*. The major contributions of this work include: with the proposed solution,

1. current tracking and voltage balance are controlled independently, which greatly decrease the influence of the existing coupling effects;

2. the candidate switching vectors decrease from 27 to 19, which effectively reduces the computational burden; prediction for the DC-link voltage is not necessary, which further saves the calculation time;

3. weighting factors are not required, which eases the tuning efforts;

4. the maximum balancing capability of the system is extended, with the proposed increasing flux current.

4.3.2 Conventional FCS-MPC controller

In the classical current control using FCS-MPC for three level NPC converter, the control objectives of FCS-MPC for current control of three level NPC converter fed induction motor include

1. Regulation of i_α and i_β, and
2. DC-link capacitor voltage balancing control.

These objectives are achieved by the following cost function

$$\begin{aligned} J\left(k+1\right) = &\left[\boldsymbol{i}_s^*\left(k\right) - \hat{\boldsymbol{i}}_s\left(k+2\right)\right]\overline{\left[\boldsymbol{i}_s^*\left(k\right) - \hat{\boldsymbol{i}}_s\left(k+2\right)\right]} \\ &+ \lambda\left[\hat{V}_{c0}\left(k+2\right) - \hat{V}_{c1}\left(k+2\right)\right]^2, \end{aligned} \tag{4.29}$$

where λ is the weighting factor, allowing us to determine which part is more important. The control algorithm for FCS-MPC can be designed either in the $\alpha\beta$ frame or the dq frame. For saving the computational time, the algorithm is implemented in the $\alpha\beta$ frame. The discrete-time equations (sampling time T_s) at time $k+1$ and $k+2$ can be easily obtained by applying the Euler-forward transformation from Equation (2.37), which are

$$\begin{aligned} \hat{\boldsymbol{i}}_s\left(k+1\right) = &\left(1 - \frac{L_m^2 R_r + L_r^2 R_s}{\sigma L_s L_r^2} T_s\right)\boldsymbol{i}_s\left(k\right) \\ &+ \left(\frac{L_m R_r}{\sigma L_s L_r^2} - j\frac{L_m \omega_r}{\sigma L_s L_r}\right) T_s \boldsymbol{\psi}_r\left(k\right) \\ &+ \frac{T_s}{\sigma L_s}\boldsymbol{v}_s\left(k\right), \end{aligned} \tag{4.30}$$

$$\begin{aligned} \hat{\boldsymbol{\psi}}_r\left(k+1\right) = &\left(1 - \frac{R_r}{L_r}T_s + j\omega_r T_s\right)\boldsymbol{\psi}_r\left(k\right) \\ &+ \frac{L_m R_r}{L_r} T_s \boldsymbol{i}_s\left(k\right), \end{aligned} \tag{4.31}$$

$$\begin{aligned} \hat{\boldsymbol{i}}_s\left(k+2\right) = &\left(1 - \frac{L_m^2 R_r + L_r^2 R_s}{\sigma L_s L_r^2} T_s\right)\hat{\boldsymbol{i}}_s\left(k+1\right) \\ &+ \left(\frac{L_m R_r}{\sigma L_s L_r^2} - j\frac{L_m \omega_r}{\sigma L_s L_r}\right) T_s \hat{\boldsymbol{\psi}}_r\left(k+1\right) \\ &+ \frac{T_s}{\sigma L_s}\boldsymbol{v}_s\left(k+1\right), \end{aligned} \tag{4.32}$$

where $\hat{\boldsymbol{i}}_s\left(k\right)$ is the real current at time k which can be measured by the current sensor, $\boldsymbol{\psi}_r\left(k\right)$ can be estimated using Equation (2.49). $\boldsymbol{v}_s\left(k\right)$ is the voltage applied at time k

which is also the calculation results at time $k-1$. $\boldsymbol{v}_s(k+1)$ is the candidate voltage in $\alpha\beta$ frame, which can be obtained by invoking Clark transformation to the line-to-neutral voltages estimated using Equation (2.35). The switch vectors in Equation (2.35) belong to $\mathbb{U}^3$.

The difference voltage of the two capacitors can be obtained, taking Equation (4.1) and 4.6 into account. The voltage difference at time $k+1$ and $k+2$ are given by

$$\Delta\hat{V}(k+1) = \Delta V(k) - \frac{T_s}{C}\sum_{x=a}^{c}|s_x(k)|\, i_x(k), \tag{4.33}$$

$$\Delta\hat{V}(k+2) = \hat{\Delta}V(k+1) - \frac{T_s}{C}\sum_{x=a}^{c}|s_x(k+1)|\,\hat{i}_x(k+1). \tag{4.34}$$

4.3.3 Proposed decoupled FCS-MPC controller

Unlike the traditional FCS-MPC, the primary control objective of the decoupled FCS-MPC is selected as the current control, which is to ensure the higher level priority for current performance. The cost function is defined as

$$J(k+1) = \left[\boldsymbol{i}_s^*(k) - \hat{\boldsymbol{i}}_s(k+2)\right]\overline{\left[\boldsymbol{i}_s^*(k) - \hat{\boldsymbol{i}}_s(k+2)\right]}. \tag{4.35}$$

Instead of combining the cost function of voltage balance to the current control together, the voltage balance control objective is to ensure that the difference of the two voltages is within a symmetrical bounds defined by the references (usually set to zero). Two bounds are defined to achieve the tradeoff between the voltage balance and the current tracking performance. The first bound (δ_1) is defined to distinguish whether the voltage difference is big enough to influence the current tracking performance. The second bound (δ_2) is defined to distinguish whether the phase current is big enough to adjust the voltage difference that can influence the current tracking performance. Thus, the following constraints are defined:

$$\begin{aligned}\left|\hat{V}_{c0}(k+2) - \hat{V}_{c1}(k+2)\right| &\le \delta_1\\ \left|\hat{V}_{c0}(k+2) - \hat{V}_{c1}(k+2)\right| &\le \delta_2,\end{aligned} \tag{4.36}$$

where $\delta_1 \le \delta_2$.

The two control objectives must be tuned according to a strategy to achieve the optimal current tracking performance. In this work, the strategy is designed as follows:

1. When the voltage difference is within the first bound, the candidate vectors are selected from the 19 effective vectors which are the set of zero vector containing P state ($\mathcal{U}_{zp}^3$), the set of small vector containing P state ($\mathcal{U}_{sp}^3$), the set of medium vector

for three level converter ($\mathcal{U}_m^3$), and the set of big vector for three level converter ($\mathcal{U}_b^3$). In such case, the current tracking performance can be guaranteed to the greatest extent possible.

2. When the voltage difference is out of the first bound and within the second bound, the voltage difference is big enough to influence the current performance. Thus, the candidate vectors are selected from the 12 effective vectors that can provide contribution to the neutral point current, which are $\mathcal{U}_{sp}^3$ and $\mathcal{U}_m^3$. So that, the voltage difference can be decreased quickly.

3. When the voltage difference is out of the second bound, the voltage difference exceeds the capability of the adjustment with the small phase current. Thus, only selecting candidate vectors from $\mathcal{U}_{sp}^3$ and $\mathcal{U}_m^3$ is not enough. Under such situation, the current reference should be increased. The method used in this work is increasing the flux reference for the induction motor.

After the selection of the effective vector, the rest is to decide which redundant vector should be applied. There are two kinds of redundant vectors; the first one is the zero vector that can be used to adjust the switching frequency: If the last switching states in two of the three phase are same, then the switching states are selected as that one. The second one is the small vectors that will be used for balancing the voltage. According to Equation (4.6), the rule for selecting $\mathcal{U}_{sp}^3$ or the set of small vector containing N state ($\mathcal{U}_{sn}^3$) is listed in Table 4.3.

To further explain the whole process and ease its realization, the main steps of the proposed solution is summarized in Algorithm 2.

4.3.4 Simulation verification

It will be damaging dangerous to provide a huge unbalance in the available hardware testbench. However, an effective balancing control capability of a predictive control solution during very small phase current is very desirable. Therefore, in this section, the maximum balancing capability of the proposed solution under *small phase current* situations is tested in simulation using matrix laboratory (MATLAB)/Simulink in this work, for the sake of safety concerns. All the other tests and performance comparisons are carried out experimentally.

The simulation scenario is constructed to verify the effectiveness of the DC-link voltage balancing ability under a small phase current. Since the control plant is induction motor which means the phase current should be maintained in the range of 25%∼50% of the nominal current to provide the excitation current. Thus, it is hard to make the phase current in a low amplitude for the normal work condition.

In this work, the condition is satisfied in the process of excitation for the induction motor, with a zero speed command. Since the flux is the integration of the voltage

[2]The symbol "✖" indicates that, the relevant case has no influences to the output switching vector.

Function *Initial ()*
  $S_{abc} = \mathcal{U}^3_{zo} \cup \mathcal{U}^3_{sp} \cup \mathcal{U}^3_m \cup \mathcal{U}^3_b$;
  $S_{abcmid} = \mathcal{U}^3_{sp} \cup \mathcal{U}^3_m$;
Function *Subfunc($\boldsymbol{S}_{in}$)*
  input : The candidate set $\boldsymbol{S}_{in}$
  output: The selected voltage output $\boldsymbol{S}_{out}$
  $J_{min} = inf$;
  for $n = 1 : sizeof(\boldsymbol{S}_{in})$ **do**
    Estimate the line-to-neutral voltage v_{xn}
    using Equation (2.35) with candidate vector $\boldsymbol{S}_{in}$
    $\boldsymbol{v}_s = \mathbf{T}_{abc} \cdot v_{xn}$
    Estimate $\hat{\boldsymbol{i}}_s(k+2)$ using Equation (4.32)
    Calc cost J using Equation (4.35)
    if $J < J_{min}$ **then**
      $J_{min} = J$;
      $\boldsymbol{v}_s(k+1) = \boldsymbol{v}_s$;
      $S_{abc} = \boldsymbol{S}_{in}[n]$;
    end
  end
Function *Calculation()*
  output: The selected voltage output $\boldsymbol{S}_{out}$
  Estimate $\hat{\boldsymbol{i}}_s(k+1)$ using Equation (4.30)
  Estimate $\hat{\boldsymbol{\psi}}_s(k+1)$ using Equation (4.31)
  $V^{err}_{dc}(k) = V_{c1}(k) - V_{c0}(k)$
  if $V^{err}_{dc}(k) > \delta_2$ **then**
    Increase flux current reference;
    $\boldsymbol{S}_{out}$=Subfunc(S_{abcmid});
  else
    if $V^{err}_{dc}(k-1) > \delta_1$ **then**
      $\boldsymbol{S}_{out}$=Subfunc(S_{abcmid});
    else
      $\boldsymbol{S}_{out}$=Subfunc(S_{abc});
    end
  end
  Apply rules defined in Table 4.3;

Algorithm 2: Algorithm of the proposed *improved predictive control solution with decoupled neutral-point voltage balancing.*

Table 4.3: Rules for selecting redundant vectors.

$\mathcal{U}_{sp}^3$	$\hat{\Delta}V\,(k+1)$	i_a	i_b	i_c	**vector output**
POO	≥ 0	≥ 0	✖[2]	✖	POO
		< 0	✖	✖	ONN
	< 0	≥ 0	✖	✖	ONN
		< 0	✖	✖	POO
PPO	≥ 0	✖	✖	≥ 0	OON
		✖	✖	< 0	PPO
	< 0	✖	✖	≥ 0	PPO
		✖	✖	< 0	OON
OPO	≥ 0	✖	≥ 0	✖	OPO
		✖	< 0	✖	NON
	< 0	✖	≥ 0	✖	NON
		✖	< 0	✖	OPO
OPP	≥ 0	≥ 0	✖	✖	NOO
		< 0	✖	✖	OPP
	< 0	≥ 0	✖	✖	OPP
		< 0	✖	✖	NOO
OOP	≥ 0	✖	✖	≥ 0	OOP
		✖	✖	< 0	NNO
	< 0	✖	✖	≥ 0	NNO
		✖	✖	< 0	OOP
POP	≥ 0	✖	≥ 0	✖	ONO
		✖	< 0	✖	POP
	< 0	✖	≥ 0	✖	POP
		✖	< 0	✖	ONO

applied to the winding, if a PI controller is used to control the flux, there should be a process that the current is small enough leading to the failure of the DC-link voltage balancing when no extra method is adopted. From Figure 4.9, the process is obvious in the post-excitation (within $[0.02, 0.06]$ s).

The simulation parameters are listed in Table 4.5. The simulation scenario is set and analyzed as follows:

1. For $t \in [0, 0.1]$ s, a PI based excitation process is applied with a maximum current limitation at 1.5 pu. Meanwhile, the two balancing resistances are set as $R_0 = 60\Omega$ and $R_1 = 100\Omega$. Due to this unbalance, the neutral-point current is about 0.25 p.u. This setup was designed to provide a strong unbalance of the neutral point. As expected, the voltage difference diverges when the phase current is not enough to provide a proper neutral current in the original FCS-MPC. However, in the proposed FCS-MPC, the voltage difference is limited in a boundary which is set as $\delta_1 = 0.01pu$. This is caused by the increasing flux current in the algorithm.

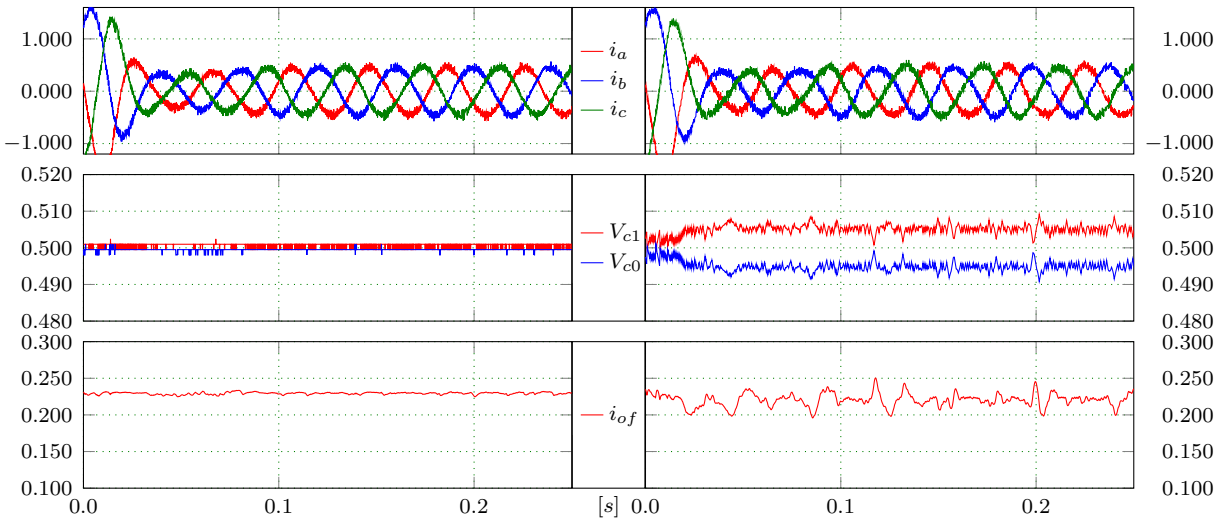

Figure 4.9: Performance comparison at excitation time and zero speed. For each figure, from up to down are: the phase currents of the stator (i_a, i_b, i_c), voltages of the two capacitor (V_{c1}, V_{c0}), neutral current filtered (i_{of}) by a second order filter (cutoff frequency is 50Hz), respectively, all are per-unit values.

2. For $t \in [0.1, 0.3]$ s: The motor is accelerating up in consequence with a bigger current generated to test the balancing ability under a big current state. As can be seen, both the two methods achieve nearly the same response. Thus, the decoupled scheme has no obvious difference with the conventional method in case of the current is big enough.

4.3.5 Experimental verification

4.3.5.1 Experimental setup

All the control schemes in this work are implemented on the same test bench shown in Figure B.1. For more details, please refer to Appendix B.

The detailed configuration of the controller is collected in Table 4.5. In the following sections, based on the test-bench afore-described, different testing are carried out experimentally, including *the DC-link voltage control dynamics*, *the THD* of the phase currents and the phase voltages, and the *computational burdens* (in terms of the calculation time) of both the classical and the proposed solutions.

4.3.5.2 DC-link voltage control dynamic performance test

Compared to the simulation configuration, it's difficult to make an unbalanced neutral point voltage for a real system. Thus, the experimental process is designed to make the neutral-point voltage drift tracking a reference. The process is shown in Figure 4.10.

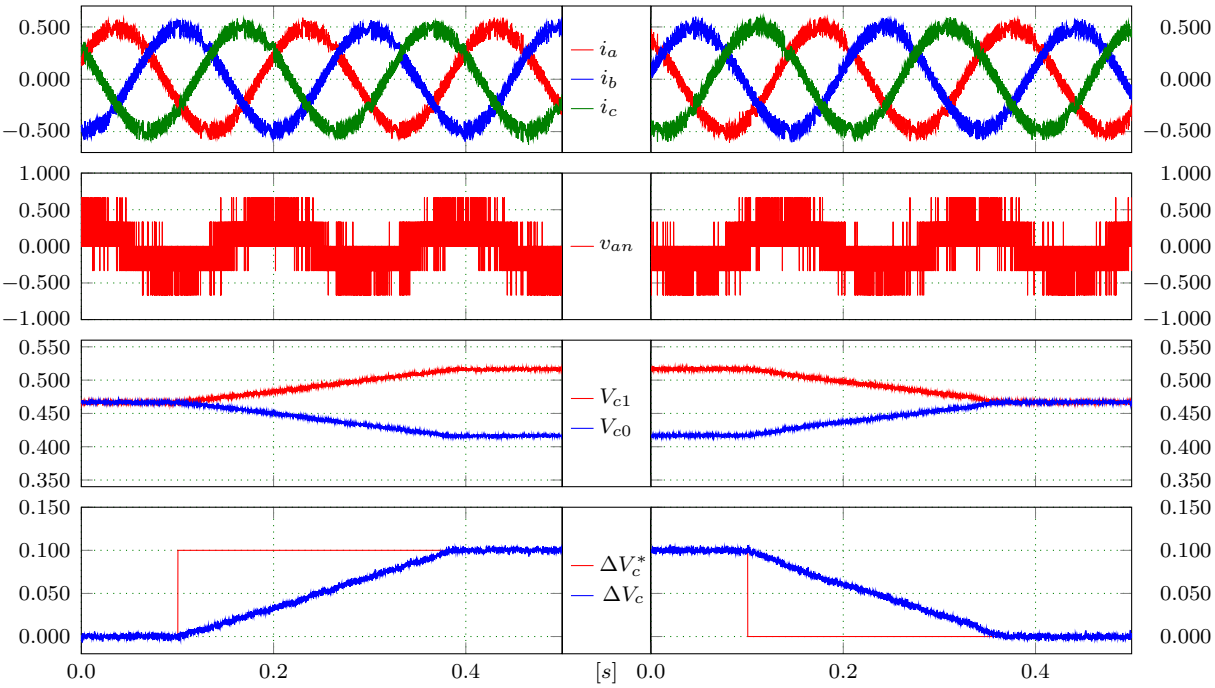

(a) Proposed solution.

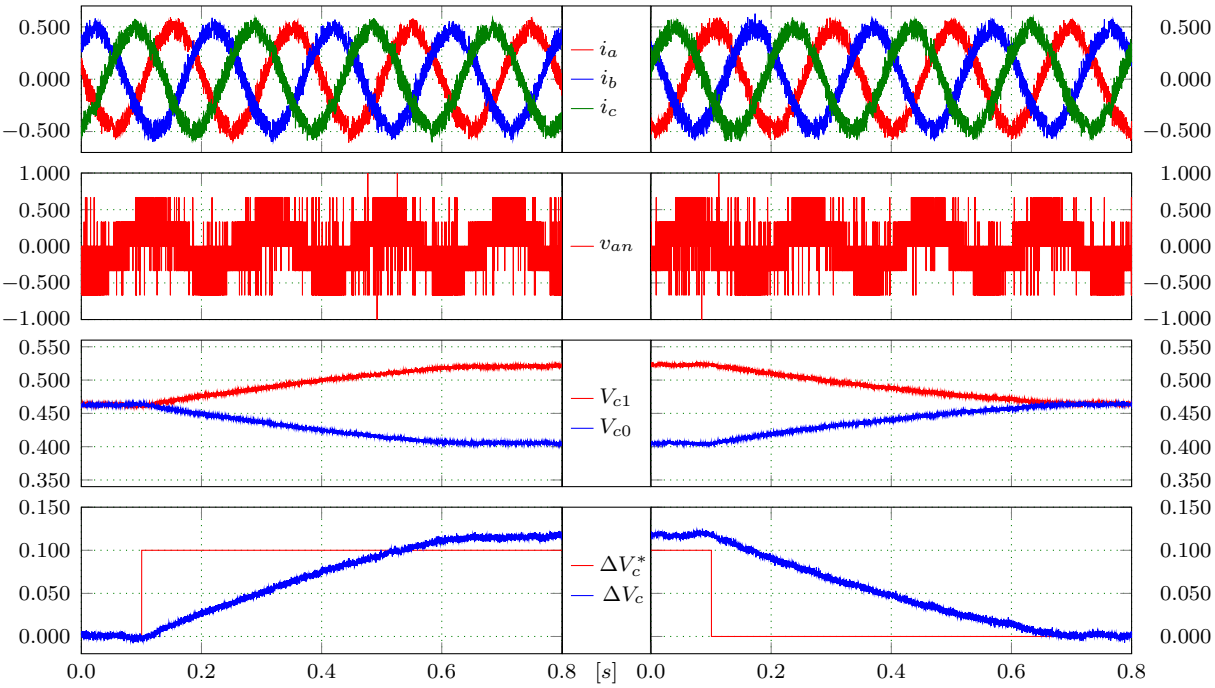

(b) Conventional solution ($\lambda = 0.007$).

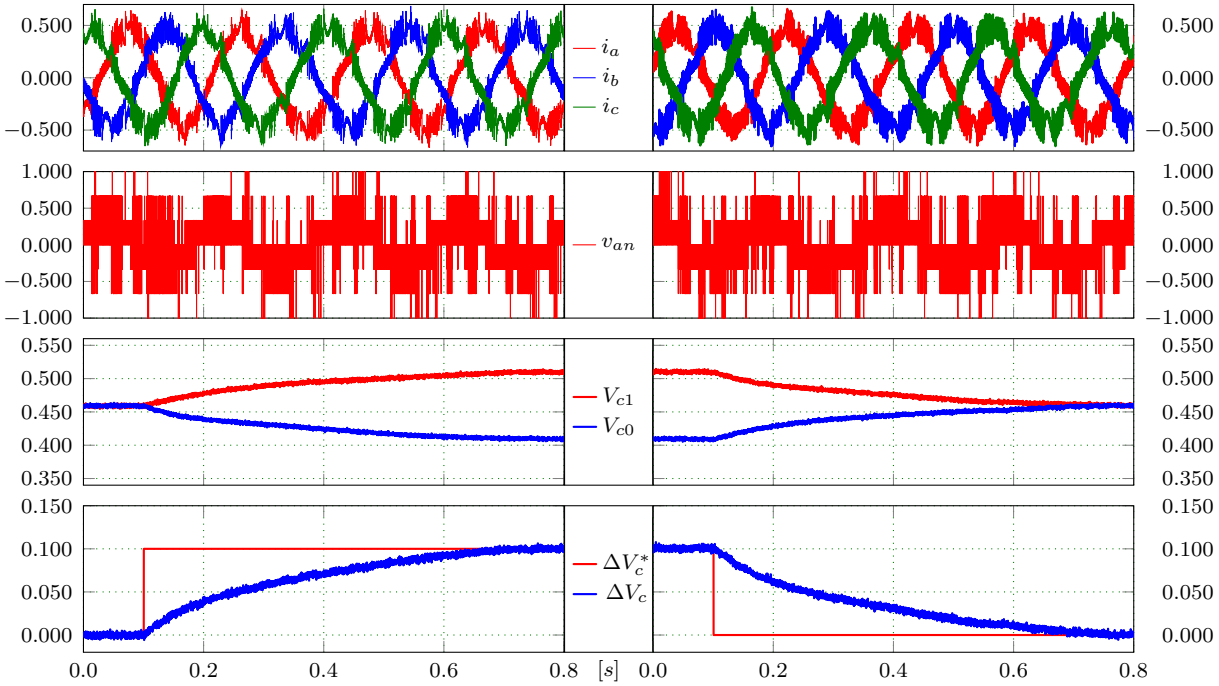

(c) Conventional solution ($\lambda = 0.07$).

Figure 4.10: Performance of neutral-point voltage balance. The left side is a converge process, and the right side is a diverge process. For each figure, from up to down are: the phase currents of the stator (i_a, i_b, i_c), the phase voltages of the stator (v_{an}, v_{bn}, v_{cn}), voltages of the two capacitors (V_{c1}, V_{c0}), DC-link voltage drift reference (ΔV_c^*) and feedback (ΔV_c), respectively, all are per-unit values.

Two processes are designed, the left side is the converging process. At instant $t = 0.1$ s, the reference of the voltage drift is set to 10% of the nominal DC-link voltage. We see that the DC-link voltage drift achieve its reference after about 0.3 s with the proposed method. However, with the conventional method (see Figure 4.10b and Figure 4.10c), the time is around 0.5 s. So, in this case, the proposed method outperforms the conventional one. Similar results can also be seen in the diverge process (right side of the figure). Additionally, the static error of the DC-link voltage drift tracking exist in the conventional MPC method when the weighing factor is small (see Figure 4.10b). Note that as the weighting factor becomes bigger, the dynamic performance of the conventional MPC may become better with the cost of high THD of current (see Figure 4.10b and Figure 4.10c).

4.3.5.3 Steady state quality assessment: THDs

The THD of a signal V is computed according to

$$\mathrm{THD} = \sqrt{\sum_{\mathrm{i}=2}^{\mathrm{n}} \mathrm{V_i^2}} \Big/ \mathrm{V_1}, \tag{4.37}$$

where V_i is the root-mean square value of the i-th harmonic of the signal and V_1 is the fundamental component. V_i are obtained with discrete Fourier transform (DFT), at the identical setting. In this work, n is selected as the maximum order of the harmonic[3].

Comparison of experimental THD results, for the proposed and conventional strategies, for the phase current and voltage THD(s) is given in Figure 4.11 and Figure 4.12, respectively. During these experiments, the capacitor voltages of the converter were always balanced which is not present in the figure.

Current THD analysis[4], Illustrated in Figure 4.11, shows that in general, somewhat higher current THD of the conventional method than the proposed method. This is caused by the weighting factor in the conventional method, which cannot ensure the controller concentrated on the current tracking. Contrary to the conventional method, the proposed method selects the current tracking as the control object, which is in reality decoupled with the neutral point voltage balance, making it better.

Figure 4.12 shows the detailed experimental results of the output phase voltage when 50% of the nominal current is applied. The phase voltage during the experiments presented a THD of about 139.67% with the conventional MPC method, and the THD of phase voltage with the proposed method is 131.69%. This illustrates that the proposed method is also better in decreasing the phase output voltage THDs.

4.3.5.4 Assessment of computation burden: calculation time

As is already mentioned in Section 4.3.1, small computational time is one of the advantages of the proposed control schemes. To assess the computational time, the time duration required for calculating the algorithm of each method in one sampling/control cycle is determined by instrumentation trace macro (ITM) cell which is integrated into Cortex-M4 processor. The timestamps and central processing unit (CPU) ticks are recorded at the entrance of the function and recorded again at the exit of the function. The elapsed time is obtained from the difference of the two timestamps. Detailed results are collected in the first row of Table 4.4.

4.3.5.5 An overall assessment: summarized results and evaluations

To ease an overall assessment of the experimental output, the performances (including, execution time, current THD, voltage THD and DC-link voltage control dynamic performance) of each method are summarized in Table 4.4.

[3]For example, if the sample rate is 8000 Hz and the fundamental frequency is 48 Hz, then n is selected as $\text{int}\left(\frac{8000}{2\times 48}\right) = 83$.

[4]All the THD analysis were tested under a 537 V DC-link voltage and 0.5pu current. Meanwhile, the control interval is 125 µs, That is why a little bit high current THDs were seen.

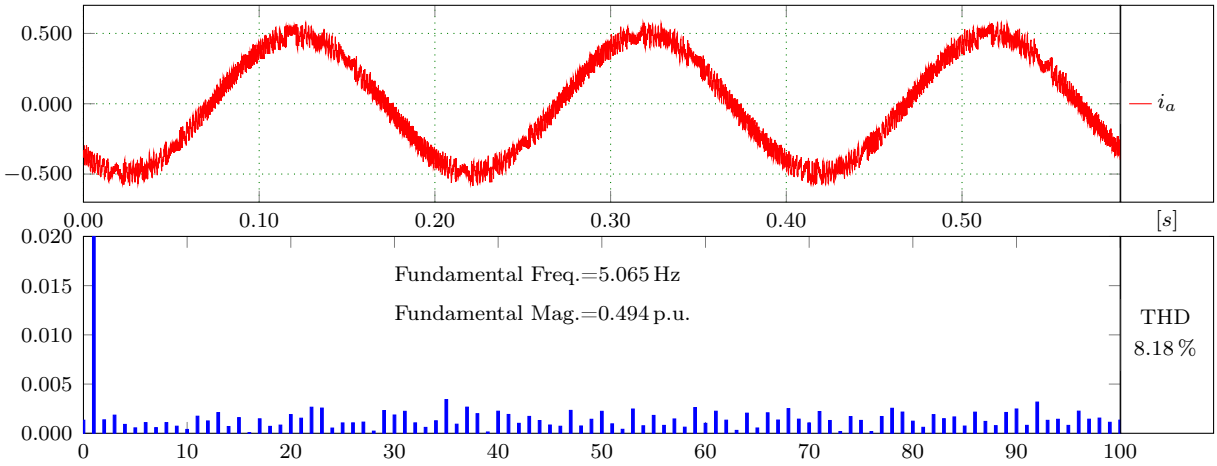

(a) Proposed solution.

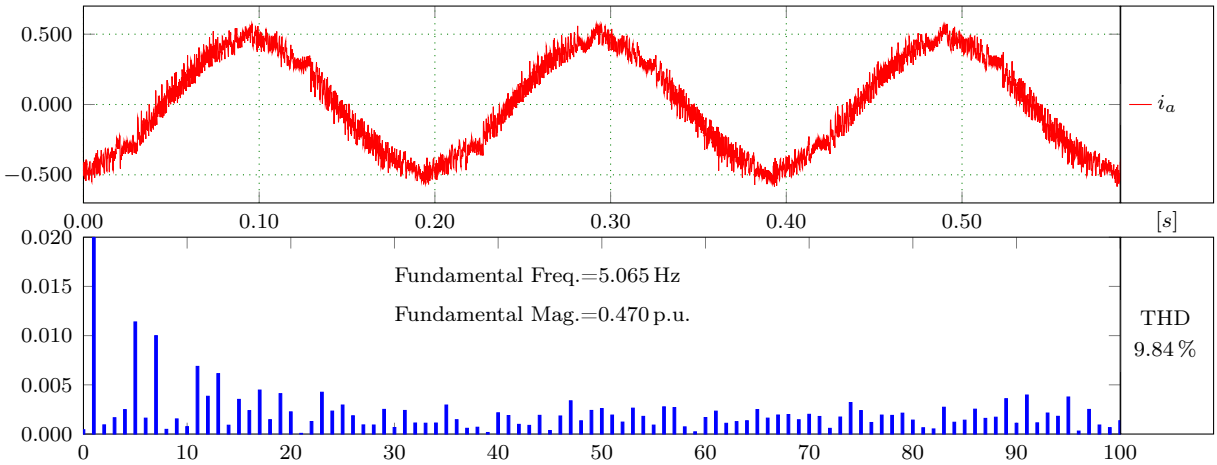

(b) Conventional solution ($\lambda = 0.007$).

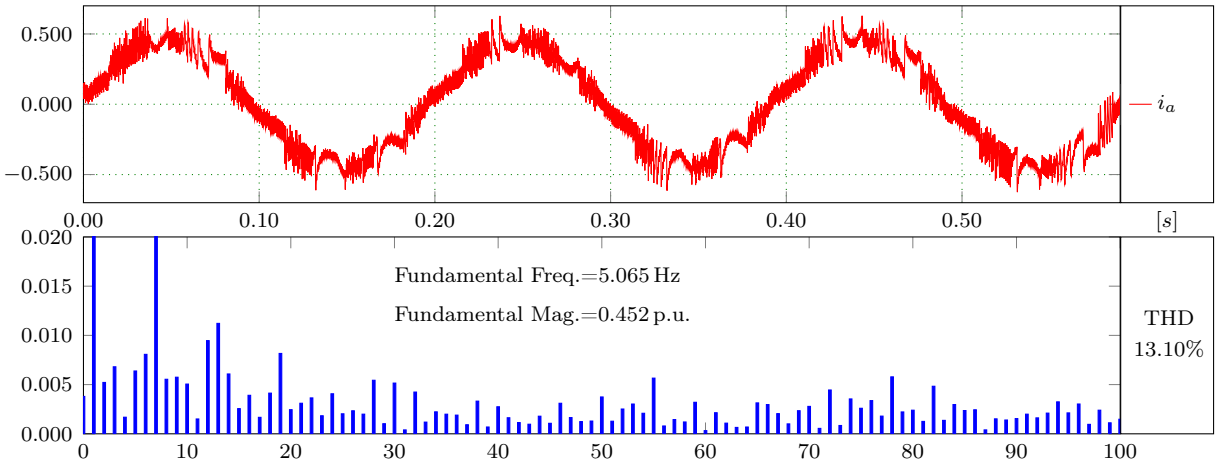

(c) Conventional solution ($\lambda = 0.07$).

Figure 4.11: Phase current spectrum and THDs.

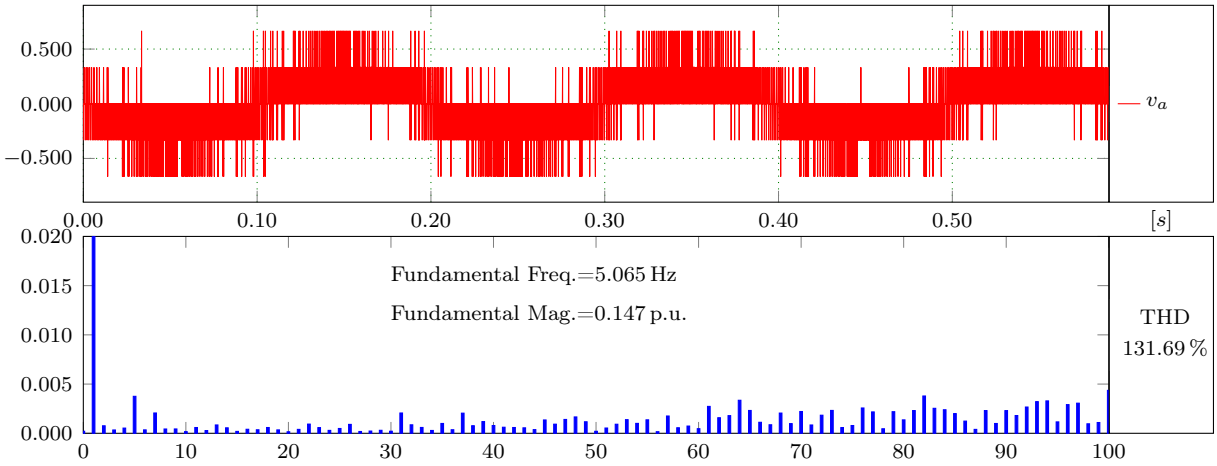

(a) Proposed solution.

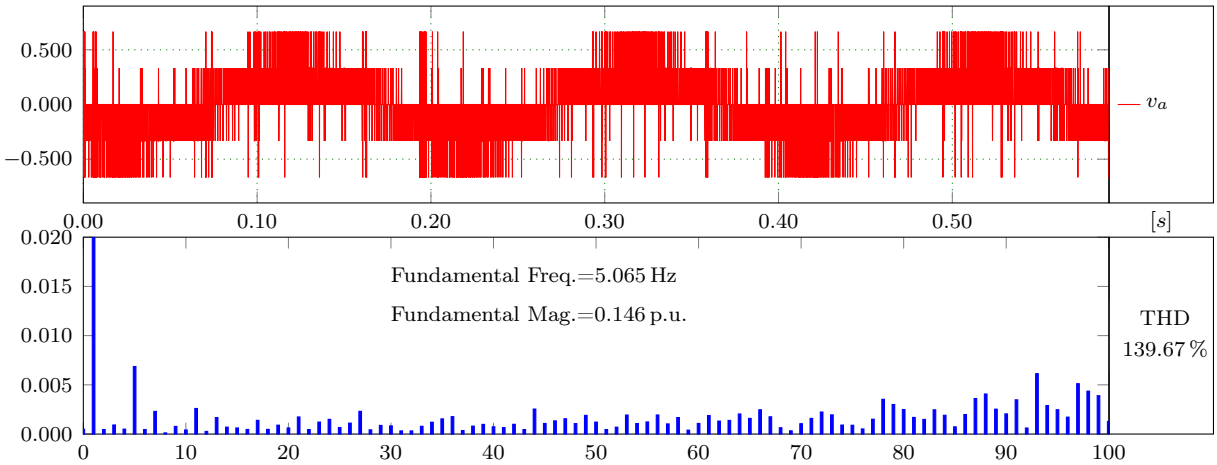

(b) Conventional solution ($\lambda = 0.007$).

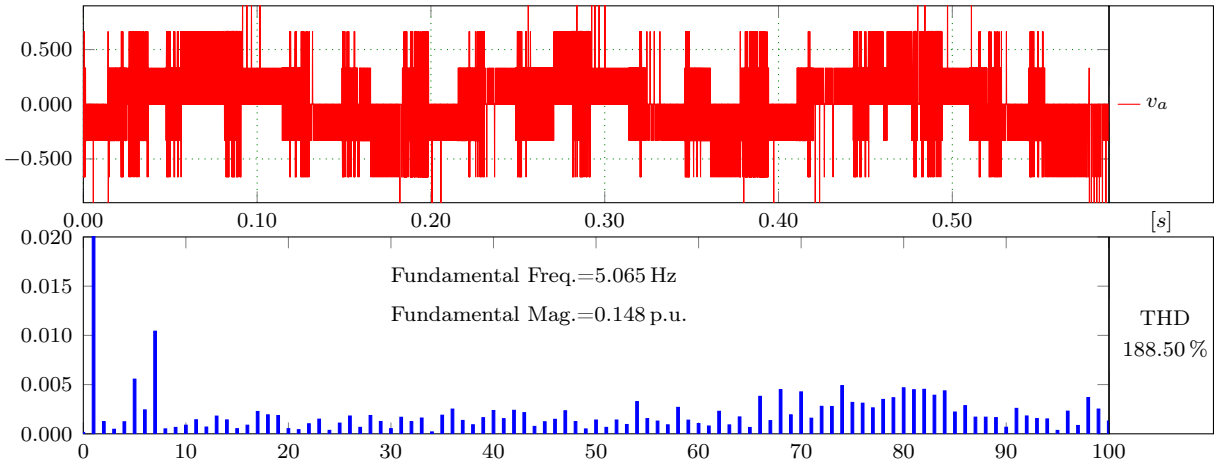

(c) Conventional solution ($\lambda = 0.07$).

Figure 4.12: Phase voltage spectrum and THDs.

Table 4.4: Overall assessment results.

	Conventional	**Proposed**
Execution time	68.0 µs	38.9 µs
CPU ticks	11431	6541
Balancing ability	Weak	Strong
Current THD	9.84%	8.18%
Voltage THD	139.67%	131.69%
Dynamic	Slow	Fast

Table 4.5: System parameters and configuration.

Symbol	**Parameter**	**Value**
C_0	the DC-link capacitor 0	1462.5 µF
C_1	the DC-link capacitor 1	1462.5 µF
R_s	Stator Resistance	1.509 Ω
R_r	Rotor Resistance	1.235 Ω
L_m	Mutual Inductance	232.5 mH
L_s	Stator Inductance	239.5 mH
L_r	Rotor Inductance	239.5 mH
i^b	Base value of current	8.1 A
v^b	Base value of phase voltage	311 V
V_{dc}^b	Base value of DC-link voltage	537 V
t_d	Dead time	8 µs
T_s	Control interval	125 µs

4.3.6 Summary

In this work, an improved predictive control solution with decoupled neutral-point voltage balancing for three-level neutral point clamped converter systems has been proposed and verified. With the proposed method, the current tracking and the neutral point balancing requirement can be controlled independently, which provides extra advantages in computational efforts, current total harmonic distortion, voltage total harmonic distortion and direct current-link voltage control dynamic performance.

As a case of study, current control problems of induction motor drives are evaluated with both the proposed and conventional solutions. The experimental results confirmed that better performances had been achieved with the proposed methods. Considerably enhanced neutral point voltage balancing control is obtained, with reduced current harmonic distortions at fast control dynamics of direct current-link voltage drift tracking. This validates that the proposed method is an effective strategy for the control of neutral point voltage within the model predictive control framework for three-level neutral point clamped converters. Note that, the proposed solution, in particular, the same concept for the average current modeling, can be extended into all neutral point clamped based

converter topologies.

Chapter 5

Observers and filters

The former chapters present the controllers for the system. Some of the controllers are based on the state variables. If all the state variables can be measured by physical sensors, the feedback of the controller can be easily accessed.

If, however, some of the state variables can not be measured by physical sensors, or it is not practical to measure all of them, or the physical sensors are too expensive to measure all of the state variables, the implementation of the controller is hard to complete. In such case, either the control method has to be discarded, or an alternative state vector must be found. A feasible solution is to introduce an observer which would reconstruct the state variables with the help of existing measurable variables and system model.

In this chapter, the observers used in the design of the controller are summarized. Then a method for designing speed observer is proposed. In more details, the proposed method can greatly decrease the parameters of the observer and optimize the observer characteristics to some extent.

5.1 Luenberger observer

The Luenberger observer (LO) was well explained in the early papers of Luenberger [66–68]. For a well understanding of LO, it is useful to recall the basic concepts.

Consider a linear system described by

$$\begin{aligned} \dot{\boldsymbol{x}} &= \mathbf{A}(t)\boldsymbol{x} + \mathbf{B}(t)\boldsymbol{u}(t), \\ \boldsymbol{y} &= \mathbf{C}(t)\boldsymbol{x} \end{aligned} \tag{5.1}$$

where the symbols are well explained in equation 3.1.

The LO is designed as

$$\begin{aligned} \hat{\dot{\boldsymbol{x}}} &= \mathbf{A}\hat{\boldsymbol{x}} + \mathbf{B}\boldsymbol{u} + \mathbf{L}\left(\boldsymbol{y} - \hat{\boldsymbol{y}}\right) \\ \hat{\boldsymbol{y}} &= \mathbf{C}\hat{\boldsymbol{x}} \end{aligned} \tag{5.2}$$

where $\mathbf{L}$ is an observer gain that places the eigenvalues of matrix $\mathbf{A}-\mathbf{LC}$ within the unit circle to make sure the stability of the system.

the discrete domain equations can be written as

$$\hat{\boldsymbol{x}}(k+1)=\mathbf{F}\hat{\boldsymbol{x}}(k)+\mathbf{G}\boldsymbol{u}(k)+\mathbf{LC}(\boldsymbol{x}(k)-\hat{\boldsymbol{x}}(k)) \tag{5.3}$$

where

$$\begin{aligned}\mathbf{F}&=e^{\mathbf{A}T_s}\\ \mathbf{G}&=\left(e^{\mathbf{A}T_s}-I\right)\mathbf{A}^{-1}\mathbf{B}\end{aligned} \tag{5.4}$$

.

The structure of LO is depicted in Fig. 5.1.

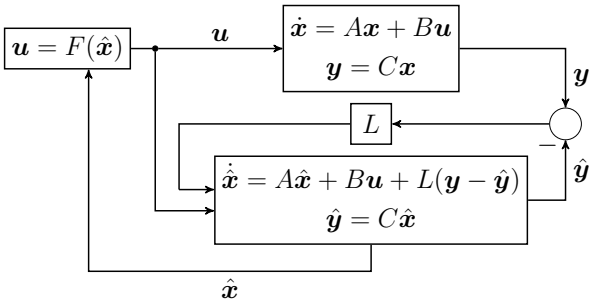

Figure 5.1: Luenberger Observer.

5.2 Kalman filter

5.2.1 Introduction

The performance of the LO greatly depends on the exact system parameters and the exact measurement of the output. However, in a real physical system, none of these conditions can be granted. Additionally, there is no universal theory for determining the best observer gain terms, and the gains are usually adjusted by experiment. Although the gain of the LO can be calculated by some methods like pole placement while certain performance can also be met, we do not know whether the gain is optimal in most case.

So, a method that can optimize the gain is desired. Kalman filter (KF) was first introduced by [69], which provides an alternative method that can optimize the feed back gain based on the presence of process noise and measurement errors. It provides an optimal method to get the state variable based on the filtering of the noises existed in measurement and the system. The drift of the system parameters can be regarded as noise.

In this section, a short introduction of the theory for KF will be presented.

Suppose the discrete plant model is described as

$$\boldsymbol{x}_{k+1} = \mathbf{F}\boldsymbol{x}_k + \mathbf{G}\boldsymbol{u}_k + \boldsymbol{\Gamma}\boldsymbol{w}_k \tag{5.5}$$

where $\boldsymbol{x}$ and $\boldsymbol{u}$ are the state variable and system input; $\mathbf{F}$ is the state transition matrix; $\mathbf{G}$ is the control-input matrix; $\boldsymbol{\Gamma}$ is the process noise transition matrix. The measurement model is given by

$$\boldsymbol{y}_{k+1} = \mathbf{H}\boldsymbol{x}_k + \mathbf{D}\boldsymbol{v}_k \tag{5.6}$$

where $\boldsymbol{y}$ is the measurement output; $\mathbf{H}$ is the observation matrix which maps the state variable into observed variable; $\mathbf{D}$ is the observation noise transition matrix.

The process noise $\boldsymbol{w}_k$ and measurement noise $\boldsymbol{v}_k$ are white Gaussian random sequences having zero mean. Thus, the equations

$$\mathbb{E}\{\boldsymbol{w}_k\} = 0,\ \mathbb{E}\{\boldsymbol{v}_k\} = 0 \tag{5.7}$$

hold, where $\mathbb{E}\{\}$ denotes the expected value. Since both the two sequences are random variables without dependency on each other, that is

$$\mathbb{E}\left\{\boldsymbol{w}_i\boldsymbol{w}_j^\top\right\} = 0,\ \mathbb{E}\left\{\boldsymbol{v}_i\boldsymbol{v}_j^\top\right\} = 0 \tag{5.8}$$

where $i \neq j$ and the covariances are defined by

$$\mathbb{E}\left\{\boldsymbol{w}_k\boldsymbol{w}_k^\top\right\} = \sigma_w^2,\ \mathbb{E}\left\{\boldsymbol{v}_k\boldsymbol{v}_k^\top\right\} = \sigma_v^2. \tag{5.9}$$

Function *Initial ()*
  $\hat{\boldsymbol{x}}_0 = 0$;
  $\mathbf{P}_0 = diag$;
  $k = 1$;
Function *Calculation()*
  input : $\boldsymbol{u}_{k-1}, \boldsymbol{y}_k$
  output: $\hat{\boldsymbol{x}}_k$
  Prediction:
  $\hat{\boldsymbol{x}}_k^- = \mathbf{F}\hat{\boldsymbol{x}}_{k-1} + \mathbf{G}\boldsymbol{u}_{k-1}$;
  $\mathbf{P}_k^- = \mathbf{F}\mathbf{P}_{k-1}\mathbf{F}^\top + \boldsymbol{\Gamma}\sigma_w^2\boldsymbol{\Gamma}^\top$;
  Correction:
  $\mathbf{K}_k = \mathbf{P}_k^-\mathbf{H}^\top\left(\mathbf{H}\mathbf{P}_k^-\mathbf{H}^\top + \mathbf{D}\sigma_v^2\mathbf{D}^\top\right)^{-1}$;
  $\hat{\boldsymbol{x}}_k = \left(\mathbf{I} - \mathbf{K}_k\mathbf{H}\right)\hat{\boldsymbol{x}}_k^- + \mathbf{K}_k\boldsymbol{y}_k$;
  $\mathbf{P}_k = \left(\mathbf{I} - \mathbf{K}_k\mathbf{H}\right)\mathbf{P}_k^-$;
  $k = k + 1$;

Algorithm 3: Recursive algorithm for the KF.

The structure of the KF is the same as that of the LO in Fig.5.1. As a case study, An angular motion system is introduced in the following sections.

5.2.2 case study: angular motion system

Position control and speed control are the most common function in modern electric drives. The sensors mounted to the shaft have different principles(e.g., optical encoder, sinusoidal encoders, magnetic devices, and resolvers). However, most of the sensors can directly or indirectly output the position of the motor with a digital format. So, to control the position and speed precisely and smoothly, the method of estimating speed and position should be investigated.

Since the position error of the encoder can be considered as Gaussian white noise, this coincides with the nature of KF. Additionally, the KF reduces the usage of external timers or captures used in the conventional M/T method [70]. So, KF is widely used to estimate the motor speed and position. As a result, the estimations of them in all the control schemes in this thesis are implemented with KF. There are many Kalman observers forms with different system state variables. Most of them require the model of the control plant (e.g., [71] proposes a self-adaption KF to estimate the position and speed with the information of the control plant).

In this section, a KF using the mathematical relationship between position, speed, and acceleration is designed to estimate the position and speed.

The description of a rotating motion system is as follows:

For a continuous second-order KF (KF_2) model in an angular motion system, the relation regarding the position θ, and angular velocity ω can be described by $\dot{\boldsymbol{x}} = \mathbf{A}(t)\,\boldsymbol{x}$, where $\boldsymbol{x} = \left[\begin{array}{cc} \theta & \omega \end{array}\right]^{\top}$,

$$\mathbf{A}(t) = \left[\begin{array}{cc} 0 & 1 \\ 0 & 0 \end{array}\right]. \tag{5.10}$$

For a continuous third-order KF (KF_3) model, the relation regarding the position θ, angular velocity ω, and acceleration a can be described by $\dot{\boldsymbol{x}} = \mathbf{A}(t)\,\boldsymbol{x}$, where $\boldsymbol{x} = \left[\begin{array}{ccc} \theta & \omega & a \end{array}\right]^{\top}$,

$$\mathbf{A}(t) = \left[\begin{array}{ccc} 0 & 1 & 0 \\ 0 & 0 & 1 \\ 0 & 0 & 0 \end{array}\right]. \tag{5.11}$$

It is easy to verify that (3.3) holds. Thus, the transition matrix can be expressed using the form of (3.4).

For a KF_2 model, the position and velocity act as the state variables for $\boldsymbol{x}(k) = [\theta_k\ \omega_k]^{\top}$. The transition matrices of the system model are described as follows:

$$\mathbf{F} = \left[\begin{array}{cc} 1 & T_s \\ 0 & 1 \end{array}\right], \mathbf{H} = \left[\begin{array}{c} 1 \\ 0 \end{array}\right], \mathbf{\Gamma} = \left[\begin{array}{c} \frac{T_s^2}{2} \\ T_s \end{array}\right]. \tag{5.12}$$

For KF_3 model, $\boldsymbol{x}(k) = [\theta_k \ \omega_k \ a_k]^\top$, in which a_k denotes the acceleration state. The corresponding transition matrices can be deduced as

$$\mathbf{F} = \begin{bmatrix} 1 & T_s & \frac{T_s^2}{2} \\ 0 & 1 & T_s \\ 0 & 0 & 1 \end{bmatrix}, \mathbf{H} = \begin{bmatrix} 1 \\ 0 \\ 0 \end{bmatrix}, \mathbf{\Gamma} = \begin{bmatrix} \frac{T_s^2}{2} \\ T_s \\ 1 \end{bmatrix}. \tag{5.13}$$

Note that the input vector of the system is zero, which accounts for the input matrix $\mathbf{G} = \mathbf{0}$ for both of the KF_2 and KF_3. And the observation noise transition matrix is $\mathbf{D} = \mathbf{1}$, which means the grid phase angle is the unique observation state.

Based on these coefficient matrices and some properly set initial values, the states can be estimated using the KF algorithm, which is listed in Algorithm 3.

5.3 Fixed gain filter for angular motion system

It is evident that there are many matrix operations in the Algorithm 3, which is difficult to implement in real time. Although the computational capability of modern processors increased greatly, it is still meaningful to investigate an algorithm that can provide good performance with low computational cost.

In this section, we propose a simple and effective *fixed gain* filter to estimate the *position*, *velocity*, and *acceleration* in angular motion. The novelty lies in that, unlike the conventional KF or extended Kalman filter (EKF), for which an *online tuning* process of the feedback gain matrix is required, the proposed solution employs an *optimal fixed* feedback gain matrix, which is obtained through a simple offline calculation. This significantly reduces the computational burden. Additionally, the proposed filter has only *one* tunable parameter, which greatly eases the required tuning efforts. Meanwhile, the tunable parameter is theoretically calculated and refined to a certain *small* range to further simplify the tuning process. Both the *fixed gain* and the *certain small range* considerably make it easy to put into practice in all the position feedback applications in industries. Compared to the results of the conventional methods, the proposed method has evidently enhanced control performances and advantages, such as faster tracking, easier tuning, error suppressing, and lower program complexity which are confirmed by simulation and experimental data.

5.3.1 Motivation

Position and velocity are the most common feedback signals in angular motion systems, such as the electrical drives. The performances of these systems are decisively influenced by the accuracy/dynamic of the signals of *position* and/or *velocity* [72–74]. For a high-performance motion or drive control, the acceleration signal is required as well, in the feed-forward control, which can be used to ease the adjusting range of the controller so to suppress the disturbance influences and to improve the system control dynamics and

robustness, etc. As a common solution, different sensors (e.g. magnetic devices, resolvers and optical encoders) are mounted on the motor shaft to directly obtain a quantized *position* signal. However, the instantaneous *velocity* and *acceleration* are not obtained directly. Therefore, additional state observers performing the estimation algorithm are required to obtain the velocity and the acceleration, with good accuracy and dynamics [75, 76].

Generally, conventional velocity estimate methods in angular motion fall into three categories: finite-difference (i.e., the so-called *M-method*), *inverse-time* (*T-method*), and the combination of M- and T-methods (*M/T-method*) [77]. The basic concept of *M-method* is to count the number of pulses during a fixed time interval, and the velocity is estimated by dividing the number of pulses by the duration. Due to the limited resolution of the sensors and the existence of the measurement noise, the number of pulses in a fixed time interval may vary abruptly, especially in low-velocity situations, which imposes the requirement of a digital filter to smooth the signal. However, an inevitable delay, caused by the filter, is seen. The *T-method* which measures the time between two consecutive position pulses, is usually adopted to provide more accuracy. The velocity is then calculated by dividing the angle (related to the two successive position pulses) by the time interval. (At least) two consecutive pulses provide a chance to update a valid velocity state. Due to the limited measurement/sampling frequency, the accuracy cannot be ensured in high-velocity cases. To avoid such problems, a combination of M- and T-methods is used in practice. More specifically, *M-method* is used in the *high* velocity range, while *T-method*, in the *low* velocity range. However, determining the switching point is problematic when the two methods change each other to a new operating situation. Furthermore, discontinuous points in the velocity estimation may highly disturb the controller. Another drawback of the *M/T-method* is that the update period is variable. Therefore, using conventional methods is difficult to guarantee a precise velocity estimation. Due to the existence of quantized errors, the estimate of acceleration based on the conventional differential velocity method is even worse.

Many research activities are reported to obtain good estimates of position, angular velocity, and acceleration. E.g., in reference [78], the authors proposed a *double integrator method* to estimate velocity and acceleration based on the assumption that the position signal from the encoder is accurate. However, it only works effectively in low-velocity and low-acceleration regions. In reference [79], a combination of an encoder and an accelerometer were used to improve the estimate of velocity, but at the cost of extra hardware, which increases the cost and system complexity. To the same end, the KF [69] has been extensively explored to estimate the motor position and velocity in both academic and in industrial applications [80–82]. However, the KF usually requires a relatively accurate model of the control plants [71,83] and their parameters (e.g., the inertia and friction factor.). The realization steps involve complex matrix calculations, which impose the very high computational power of the digital controller. The tuning process, which needs the knowledge of process noise w_k and measurement noise v_k, requires much expertise and is quite tedious.

Motivated by the above analysis, in this work, we propose a simple and effective fixed

gain filter (FGF) to solve the afore-mentioned problems. The proposed solution is derived from the conventional KF with an optimal fixed gain matrix, and the optimal fixed gain matrix can be expressed by one parameter ranging from 0 to 1. Thereby, the range of the parameter is further refined through the analysis of stability. The effectiveness and accuracy of the proposed filter are validated by comparing to the conventional methods. The major contributions of this work include: with the proposed FGF,

1. a good solution to overcome the shortcomings in traditional methods (M method, T method, M/T method, and KF) is provided;

2. it realizes a high accuracy tracking of position, angular velocity, and angular acceleration with a short execution time;

3. compared to the KF, the computational burden is greatly reduced, while the advantages of the KF remain;

4. only *one* factor s (the tuning parameter) is required to adjust the performance of the filter and the range of s is refined to $3 - 2\sqrt{2} < s < 1$ through the stability analysis, both of which greatly ease the tuning efforts.

5. the effectiveness and the dynamic performance for tracking position, velocity, and acceleration are either similar to those of the KF or often better due to the optimal fixed gain.

As a result, this practical and effective method is excellent to be utilized in the angular motion.

This work is organized as follows: in Section 5.3.2, the gain of FGF is developed in detail. Section 5.3.4 presents the simulation results of position, velocity, and acceleration with different estimate methods as a proof of concept. In Section 5.3.5, the experiment results are illustrated to confirm the effectiveness of the proposed solution. Finally, conclusions are drawn in Section 5.3.6.

5.3.2 Gain of the FGF

The original FGF was proposed for radar tracing problems with two or three internal states, which are position, velocity and acceleration. For the grid synchronization problem, there are only two internal states, the grid phase angle θ and the grid frequency f. Note that, although the acceleration signal has no practical significance for the grid system, it serves the purpose when grid frequency variation occurs. Thus, the mathematical relationships among the three considered states for both the radar and the grid applications are identical. Consequently, it is possible to apply the insight into the structure of one problem to the other problem based on the system analogy.

In order to quickly determine the feedback gains and reduce the complexity of the algorithm, the filter gains are designed to be constants, and their expressions can be

obtained from the steady state KF algorithm [84]. To achieve the steady state conditions for a KF, the noise signals $\boldsymbol{w}_k$ and $\boldsymbol{v}_k$ must exhibit statistical stationary behavior and the sampling data rate must be a constant; otherwise the proposed filter provides a suboptimal estimate.

The proposed optimal steady-state filter could be expressed as

$$\hat{\boldsymbol{x}}_k = \hat{\boldsymbol{x}}_k^- + \mathbf{K}\left(\boldsymbol{y}_k - \mathbf{H}\hat{\boldsymbol{x}}_k^-\right), \tag{5.14}$$

where $\hat{\boldsymbol{x}}_k^- = \mathbf{F}\hat{\boldsymbol{x}}_{k-1}$, and $\mathbf{K}$ is the constant gain matrix of the filter. $\hat{\boldsymbol{x}}_k$ denotes the estimated state variable from the FGF, and $\hat{\boldsymbol{x}}_k^-$ denotes the predicted state. It is reasonable to regard the error covariances $\mathbf{P}_k^-$ and $\mathbf{P}_{k-1}$ as constants, which is a sufficient condition and can be deduced from the expressions of the $\mathbf{K}$ and $\mathbf{P}_k^-$ in the KF iteration formula. In other words, $\mathbf{P}_k^-$ and $\mathbf{P}_{k-1}$ converge to a steady state,

$$\mathbf{P}_k^- = \mathbf{P}_{k-1}^-, \mathbf{P}_k = \mathbf{P}_{k-1}. \tag{5.15}$$

If we substitute $\mathbf{P}_{k-1}$ into $\mathbf{P}_k^-$ and rearrange the expression of $\mathbf{K}$ in the KF algorithm, the underlying solutions to the new prediction function and correction function are achieved by (5.16) and (5.17):

$$\mathbf{P}_k^- = \mathbf{F}\mathbf{P}_{k-1}\mathbf{F}^\top + \mathbf{\Gamma}\sigma_w^2\mathbf{\Gamma}^\top, \tag{5.16}$$

$$\mathbf{K} = \mathbf{P}_k^-\mathbf{H}^\top\left(\mathbf{H}\mathbf{P}_k^-\mathbf{H}^\top + \mathbf{D}\sigma_v^2\mathbf{D}^\top\right)^{-1}. \tag{5.17}$$

For the second-order FGF (FGF_2) and third-order FGF (FGF_3), the fixed gain matrices can be separately written as

$$\mathbf{K} = \begin{bmatrix} \alpha & \frac{\beta}{T_s} \end{bmatrix}^\top, \tag{5.18}$$

$$\mathbf{K} = \begin{bmatrix} \alpha & \frac{\beta}{T_s} & \frac{2\gamma}{T_s^2} \end{bmatrix}^\top. \tag{5.19}$$

Note that, for the FGF_2, which is a special case of the FGF_3, nothing is different except setting γ as zero. Thus, the FGF_3 is taken as an example in all the following analyses.

If we use the gains that are obtained from the steady state KF algorithm for the models given above, it turns out that α, β, (and γ) can actually be solved in an analytic form, and the solution can be expressed in one parameter. The so-called target maneuvering index, which is the ratio of the motion to the observation uncertainties, is defined as $\lambda = \frac{T_s^2\sigma_w}{\sigma_v}$.

For the above new prediction function and correction functions, α, β, (and γ) are dimensionless constants, and all the parameters in the operator expressions (Equations (5.16) and (5.17)) are now defined. Accordingly, solving (5.16) and (5.17) for the FGF yields the following relations:

$$\lambda = \frac{2\,\gamma}{\sqrt{1-\alpha}}, \tag{5.20}$$

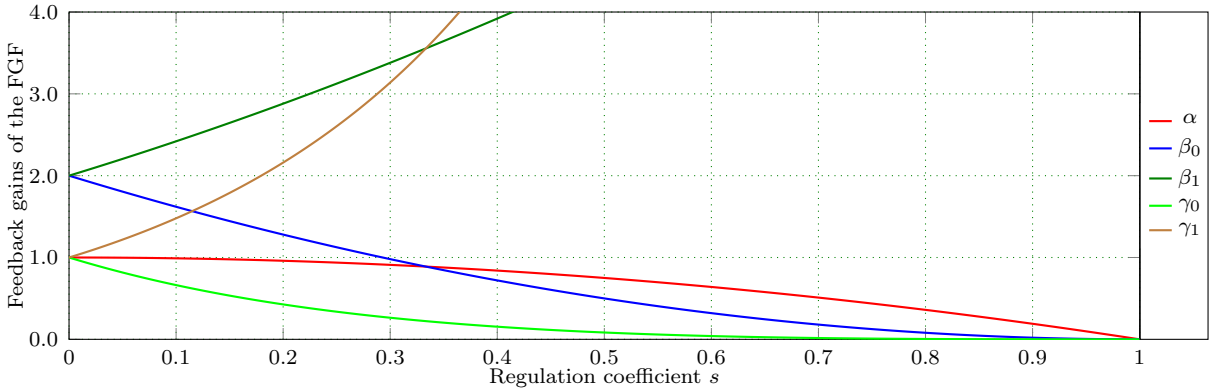

Figure 5.2: The relationship between the feedback gains of the FGF and s.

$$\gamma = \frac{\beta^2}{4\,\alpha}, \tag{5.21}$$

$$\beta = \begin{pmatrix} 4 - 4\sqrt{1-\alpha} - 2\,\alpha \\ 4\sqrt{1-\alpha} - 2\,\alpha + 4 \end{pmatrix}. \tag{5.22}$$

As evident in (5.20)-(5.22), all the feedback gains of the FGF is relative to λ. Once this parameter is evaluated, the optimal steady state gain parameters α, β, (and γ), as well as the resulting performance, are specified in advance.

However, the exact value of λ cannot be determined on account of the complexity of the actual system. Therefore, the feedback gains can be optimized only by the designation of the value of λ that corresponds to the desired system performance.

Since $\lambda > 0$, the range of α can be drawn as $0 \leq \alpha < 1$. In order to further simplify the calculation process, s is defined as $\sqrt{1-\alpha}$, which is called the regulation coefficient. α, β, and γ can be characterized by s, and then the feedback gains can be explicitly expressed in terms of the function of s as

$$\alpha = 1 - s^2, \tag{5.23}$$

$$\beta = \begin{bmatrix} \beta_0 \\ \beta_1 \end{bmatrix} = \begin{bmatrix} 2(s-1)^2 \\ 2(s+1)^2 \end{bmatrix}, \tag{5.24}$$

$$\gamma = \begin{bmatrix} \gamma_0 \\ \gamma_1 \end{bmatrix} = \begin{bmatrix} \frac{(1-s)^3}{s+1} \\ \frac{(s+1)^3}{1-s} \end{bmatrix}. \tag{5.25}$$

The relationship between the feedback gains and s is depicted in Fig. 5.2. As can be seen, α, β_0, and γ_0 have the same monotonicity. Meanwhile, β_1 and γ_1 can also be excluded by the stability analysis, since the conjugate pair of complex roots lies outside the unit circle. Thus, α, β_0, and γ_0 are the real solutions for the FGF_3; whereas, α and β_0 are the real solutions for the FGF_2.

Since λ is characterized by s, the relationship between the two parameters for FGF_2 and FGF_3 can be deduced respectively as (5.26) and (5.27), which is also illustrated in Fig. 5.3.

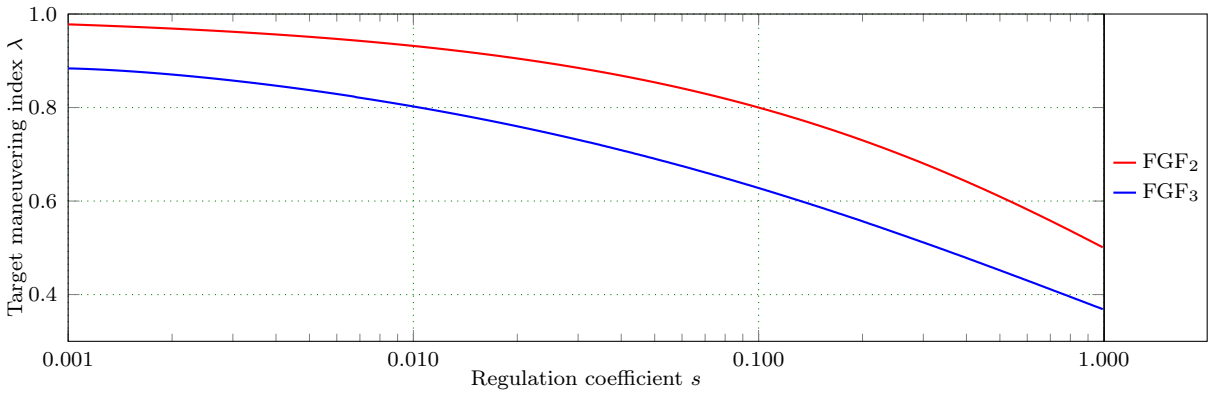

Figure 5.3: The relationship between λ and s for FGF_2 and FGF_3.

Since λ exhibits a drastic change in the vicinity of $s = 0$, the logarithmic relationship is introduced.

$$s = \frac{\lambda}{4} - \frac{\sqrt{\lambda}\sqrt{\frac{\lambda}{4}+2}}{2} + 1, \tag{5.26}$$

$$s = \frac{\sigma}{6} - \frac{\lambda}{6} + \frac{\lambda(\lambda-18)}{6\sigma} + 1, \tag{5.27}$$

where

$$\sigma = \sqrt[3]{27\lambda^2 - 108\lambda - \lambda^3 + 3\sqrt{3}\lambda\sqrt{432-\lambda^2}}. \tag{5.28}$$

In Fig. 5.3, a monotone decreasing relationship can be observed between s and λ within the domain of definition for either the FGF_2 or the FGF_3. Hence, the feedback gains of the FGF can be considered to present a one-to-one mapping with λ. The feedback gains can be optimized by a proper design of s.

The algorithm only requires three equations with multiplication and additions, which greatly simplify the calculation process compared to the traditional KF. Therefore, it is very efficient in terms of computation and application with a DSP controller.

The scheme of the FGF for position, velocity, and acceleration estimation is shown in Figure 5.4.

5.3.3 Stability analysis

The fixed gain with respect to s in Section 5.3.2 gives a solution under which the convergence rate, command tracking, disturbance rejection, and noise immunity achieved in an optimal state due to the characteristic deriving from KF. In this section, the sufficient conditions that make the FGF, described in Section 5.3.2, absolutely stable are determined. Based on the theorem of discrete system control, the asymptotic stability requirement for a discrete system is that all eigenvalues (roots of the characteristic equation) must lie strictly inside the unit circle [85, 86].

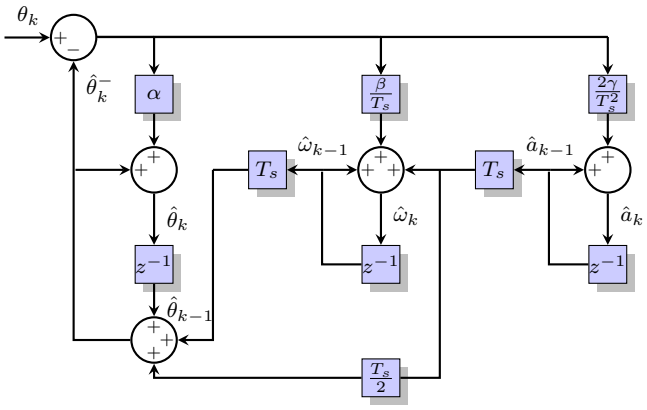

Figure 5.4: The scheme of FGF for position, velocity, and acceleration estimation.

Based on the theorem of discrete system control, the asymptotic stability requirement is that all eigenvalues (roots of the characteristic equation) must lie strictly inside the unit circle [86].

The state difference equation of the FGF can be obtained from (5.14), which can be written as

$$\hat{\boldsymbol{x}}_k = (\mathbf{F} - \mathbf{KHF})\,\hat{\boldsymbol{x}}_{k-1} + \mathbf{KH}\boldsymbol{x}_{k-1}. \tag{5.29}$$

Thus, the state matrix characteristic equation of the FGF is obtained by

$$|z\mathbf{I} - (\mathbf{F} - \mathbf{KHF})| = 0. \tag{5.30}$$

After substituting (5.18) into (5.30), we get the characteristic equation of the FGF_2 as

$$z^2 + \left(s^2 - 4s + 1\right) z + s^2 = 0. \tag{5.31}$$

By substituting (5.19) into (5.30), the characteristic equation of the FGF_3 can be obtained as

$$z^3 - \frac{7s-1}{s+1} z^2 - \frac{s^2\,(s-7)}{s+1} z - s^2 = 0. \tag{5.32}$$

Assuming the roots of the characteristic equation are given by p_0, p_1, and p_2. Then, the homogeneous response of the system is able to be represented in terms of three poles.

$$y\,(k) = C_0 p_0^k + C_1 p_1^k + C_2 p_2^k \tag{5.33}$$

where C_0, C_1, and C_2 are coefficients. The locations of the poles in the z-plane, therefore, determine the homogeneous response as follows:

1. A real pole inside the unit circle ($|p| < 1$) defines an exponentially decaying component (Cp^k) in the homogeneous response. The rate is determined by the pole location. More specifically, the closer the pole to the unit circle, the longer the transient response time is. Conversely, as the distance between the poles and the origin decreases, the transient response becomes faster but noise amplification increases.

Function *Initial ()*
  $\hat{\theta}_0 = 0$;
  $\hat{\omega}_0 = 0$;
  $k = 1$;
Function *Calculation()*
  input : θ_k
  output: $\hat{\theta}_k$, $\hat{\omega}_k$, $\hat{a}_k$
  Get encoder position: θ_k;
  Predict current position:
  $\hat{\theta}_k^- = \hat{\theta}_{k-1} + \hat{\omega}_{k-1}T_s + \hat{a}_{k-1}\frac{T_s^2}{2}$;
  Calculate error:
  $\theta_{err} = \theta_k - \hat{\theta}_k^-$;
  if $\theta_{err} > 0.5$ **then**
    $\theta_{err} = \theta_{err} - 1$;
  else if $\theta_{err} < -0.5$ **then**
    $\theta_{err} = \theta_{err} + 1$;
  else
    $\theta_{err} = \theta_{err}$;
  end
  $\hat{a}_k = \hat{a}_{k-1} + \frac{\gamma}{T_s^2}\theta_{err}$;
  $\hat{\omega}_k = \hat{\omega}_{k-1} + \hat{a}_{k-1}T_s + \frac{\beta}{T_s}\theta_{err}$;
  $\hat{\theta}_k = \hat{\theta}_{k-1} + \hat{\omega}_{k-1}T_s + \hat{a}_{k-1}\frac{T_s^2}{2} + \alpha\theta_{err}$;
  $\hat{\theta}_k$=mod($\hat{\theta}_k$,1);
  $k = k + 1$;

Algorithm 4: Algorithm of position and speed estimator using FGF

2. A complex conjugate pole pair ($p = \rho e^{\pm j\theta}$) inside the unit circle generate a response that is decaying sinusoid in the form of $A\rho^k \sin(k\theta + \varphi)$, where A and φ are determined by initial conditions. The rate of decaying is specified by ρ which satisfies $\rho < 1$. The oscillation frequency is determined by θ.

3. A system with one or more poles lying on the unit circle has non-decaying oscillatory components in the homogeneous response. It is defined to be marginally stable.

4. If any real pole or a pair of conjugate poles are located on the outside of the unit circle, there are divergent response components, causing the system to be unstable.

5. A pole in the unit circle defines a component that is constant in amplitude and defined by the initial conditions.

6. A real pole outside the unit circle ($|p| > 1$) corresponds to an exponentially increasing component Cp^k in the homogeneous response, thus defining the system to be unstable.

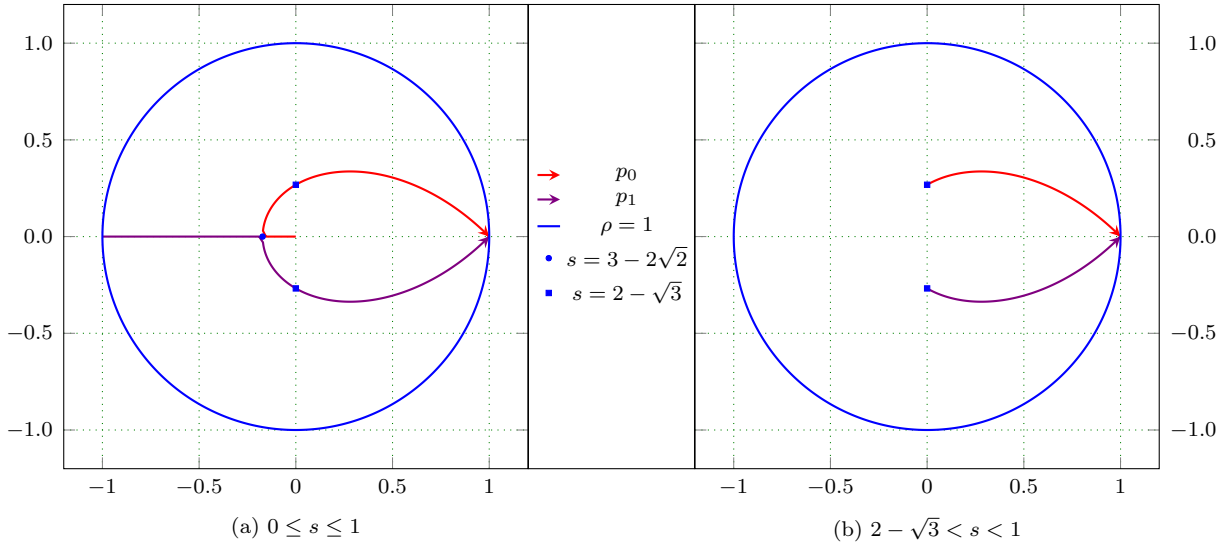

(a) $0 \le s \le 1$ (b) $2 - \sqrt{3} < s < 1$

Figure 5.5: Root locus of discrete FGF_2.

7. A complex conjugate pole pair on the unit circle ($p = e^{\pm j\theta}$) generates an oscillatory component of the form $A\sin(k\theta + \varphi)$. A and φ are determined by initial conditions.

8. A complex pole pair outside the unit circle generates an exponentially increasing oscillatory component.

Fig. 5.5 (a) shows the locus of the roots of (5.31) as s increased from 0 to 1. For $s = 0$, p_0 starts at the origin and p_1 starts at the point $(-1,\, 0\,\mathrm{i})$. With the increasing of s, the two branches of the root locus meet at the negative real axis $\left(s = 3 - 2\sqrt{2}\right)$, move out in the complex plane, cross the imaginary axis $(s = 2 - \sqrt{3})$, and finally end up at the point $(1,\, 0\,\mathrm{i})$ $(s = 1)$.

According to the stability criterion, the range of s can be discussed for the following three aspects.

1) There are two intersections between the root locus and the z-domain unit circle, which indicates a non-decaying oscillatory response of the system, i.e., marginally stable. Therefore, $s = 0$ and $s = 1$, which correspond to the two intersections, are excluded from the stable region. The range of s is now narrowed to $(0,\, 1)$. The root trajectory falls inside the stable region, and in such case, the natural response of the system decays to zero as time increases to infinity.

2) The coordinate of poles at the breakaway point is $(2\sqrt{2} - 3,\, 0\,\mathrm{i})$, corresponding to $s = 3 - 2\sqrt{2}$. When $s \le 3 - 2\sqrt{2}$, the poles are both negative real poles, and when $s > 3 - 2\sqrt{2}$, they are a pair of complex conjugate poles. Since the negative real poles cause the alternate sign of the response components, which will induce an unsatisfactory performance and poor robustness of the system, they are discarded as well. Thus, the range of s is refined to $3 - 2\sqrt{2} < s < 1$.

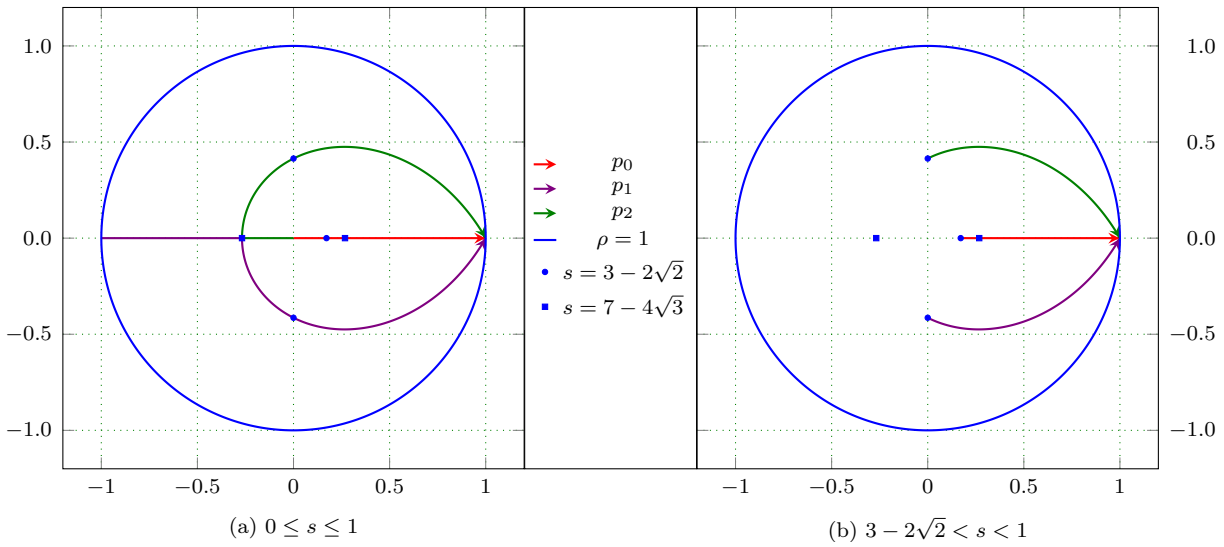

(a) $0 \le s \le 1$ (b) $3 - 2\sqrt{2} < s < 1$

Figure 5.6: Root locus of discrete FGF_3.

3) If the period of the sinusoid response contains 4 discrete steps, the sequence of the sinusoid signal should be [0, 1, 0, -1], which is the worst kind of sinusoid signal. In order to achieve a more precise response, the sinusoid response period should contain more than 4 discrete steps, which implies that $4\theta < 2\pi$. The conjugate poles should be therefore, selected with positive real parts. The coordinate of the critical point between the root trajectory and the imaginary part is $(0, (2-\sqrt{3})\mathrm{i})$, which corresponds to $s = 2 - \sqrt{3}$. Consequently, the range of s is further refined to $2 - \sqrt{3} < s < 1$.

After all the above three points are considered, the locus of the roots with $2-\sqrt{3} < s < 1$ can be depicted as in Fig. 5.5(b). In this case, only a series of conjugate poles are left to consider.

According to the stability criterion of the system, the range of the feedback gains of FGF_3 can be analyzed exactly the same way as that of FGF_2. Therefore, the original root locus shown in Fig. 5.6 (a) is shrunk to Fig. 5.6 (b), and the corresponding range of s is narrowed to be $3 - 2\sqrt{2} < s < 1$. Indeed, the poles of FGF_3 consist of a real positive pole and a pair of conjugate poles.

Actually, for the pole location of the FGF, the closer the pole to the unit circle, the longer is the transient response time. Conversely, the greater distance to the unit circle means a faster transient response yet more severe noise. Therefore, the value of s, as a tradeoff between the noise reduction and maneuver-following capability, can be achieved by the desired system performance design within the stability range.

5.3.4 Simulation Assessment

In the ideal condition, the position input of the estimator is the real position signal which is generated by integrating velocity over time. Such tests are valuable in verifying

Table 5.1: System parameters and configuration for the KF and FGF

Symbols	Parameter	Value
θ_{base}	base value of position	2π rad
ω_{base}	base value of velocity	$100\pi\,\mathrm{rad\,s^{-1}}$
a_{base}	base value of acceleration	$10\,00\pi\,\mathrm{rad\,s^{-2}}$
T_s	sampling time	100 µs
n	encoder bits	12
s	tuning parameter	0.9217
α	filter parameter	0.1505
β	filter parameter	0.0123
γ	filter parameter	2.5e-4
$\mathbf{D}\sigma_v^2\mathbf{D}^\top$	covariance of measurement noise	1
$\mathbf{\Gamma}\sigma_w^2\mathbf{\Gamma}^\top$	covariance of process noise	diag[0.01, 1e5, 2e9]

whether the parameters of the filter are optimal when it is implemented practically.

To simulate the practical case, an encoder simulator is added to convert the real position signal into signal with the quantized error. For a n-bit encoder, the encoder simulator is modeled in such a way:

$$\bar{\theta} = \frac{\mathrm{int}\left(2^n \times \mathrm{mod}\left(\frac{\theta}{2\pi}, 1\right)\right)}{2^n} \tag{5.34}$$

where θ is the real position, $\bar{\theta}$ is the position with quantized error.

A comparison of the new proposed FGF to other methods is necessary to demonstrate its performance. In this section, numerical simulations are performed in matrix laboratory (MATLAB)/Simulink with the proposed algorithm. The parameters used for simulation are listed in Table 5.1. All the positions, velocities, and accelerations acquired by the simulation and the experiment are normalized using the base values.

5.3.4.1 Performance for tracking a step velocity

This section describes the performances of the conventional M method, KF, and FGF for tracking a step velocity, which in comparison to the ramp and parabolic velocities is the worst case. Figure 5.7 shows the step responses under both ideal conditions and with noise. In this work, all the ideal conditions mean that the signal is noise-free and without any quantization error. Since the input position signal has no quantization error under ideal conditions, the position $\hat{\theta}_k^{\mathrm{M}}$ and velocity $\hat{\omega}_k^{\mathrm{M}}$ are the same as the ideal position θ_k and velocity ω_k. For both ideal and noisy conditions, the FGF can track the velocity $\hat{\omega}_k^{\mathrm{FGF}}$ with overshoots slightly larger than $\hat{\omega}_k^{\mathrm{KF}}$ of KF at sharp step edges. Meanwhile, the FGF tracks the acceleration $\hat{a}_k^{\mathrm{FGF}}$ with a faster response than $\hat{a}_k^{\mathrm{KF}}$ of KF, whereas the M method is unable to track the acceleration[1]. Since the ideal infinite acceleration appearing

[1]The acceleration is an impulse.

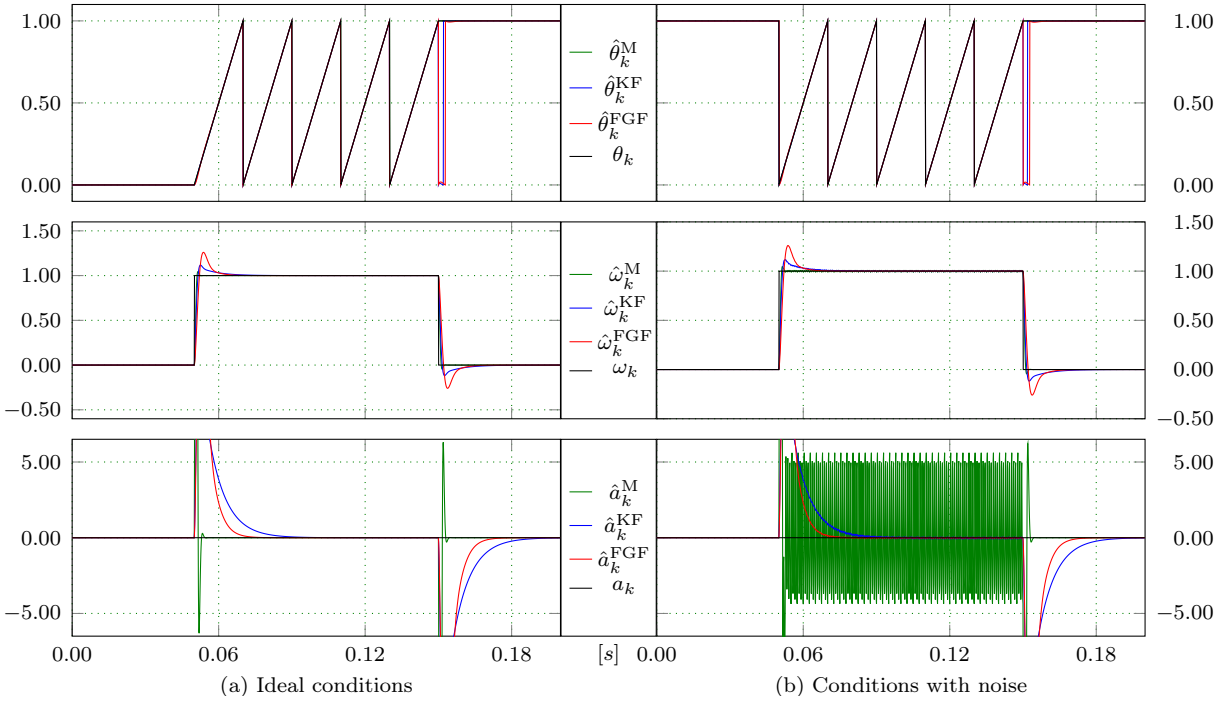

(a) Ideal conditions (b) Conditions with noise

Figure 5.7: The step response of M method, KF, and FGF. θ_k is the real position. $\hat{\theta}_k^{\mathrm{M}}$, $\hat{\theta}_k^{\mathrm{KF}}$, and $\hat{\theta}_k^{\mathrm{FGF}}$ are the estimated positions with the M method, KF, and FGF, respectively. ω_k is the real angular velocity. $\hat{\omega}_k^{\mathrm{M}}$, $\hat{\omega}_k^{\mathrm{KF}}$, and $\hat{\omega}_k^{\mathrm{FGF}}$ are the estimated angular velocities with the M method, KF and FGF, respectively. a_k is the real acceleration. $\hat{a}_k^{\mathrm{M}}$, $\hat{a}_k^{\mathrm{KF}}$, and $\hat{a}_k^{\mathrm{FGF}}$ are the estimated accelerations with the M method, KF, and FGF, respectively.

at the sharp step edge cannot be illustrated, it is set to zero in Figure 5.7. This sharp step edge rarely appears in practice, and the simulation is mere to indicate that the FGF can track sharp step edges similar to the KF.

5.3.4.2 Performances for tracking a ramp velocity and a parabolic velocity under ideal condition

Ramp and parabolic velocities are the common situations in the normal running status of electric drives. Figure 5.8 gives the comparison of the conventional M method, KF, and FGF for tracking ramp and parabolic velocities under ideal condition. Compared to the actual acceleration a_k , $\hat{a}_k^{\mathrm{KF}}$ and $\hat{a}_k^{\mathrm{FGF}}$ have slower responses. And the response rate of $\hat{a}_k^{\mathrm{KF}}$ is higher than the $\hat{a}_k^{\mathrm{FGF}}$. Figure 5.9 shows the error for tracking under ideal conditions the position, velocity, and acceleration for both ramp and parabolic velocities. The errors are calculated by subtracting measured values from real ones. All three methods can precisely estimate the position, velocity, and acceleration for different error levels. The abrupt change of velocity leads to a relatively large error of velocity, position, and acceleration tracking for both FGF and KF, especially for the FGF. Nevertheless, in the whole range of velocity, they have a better velocity estimation than the M method.

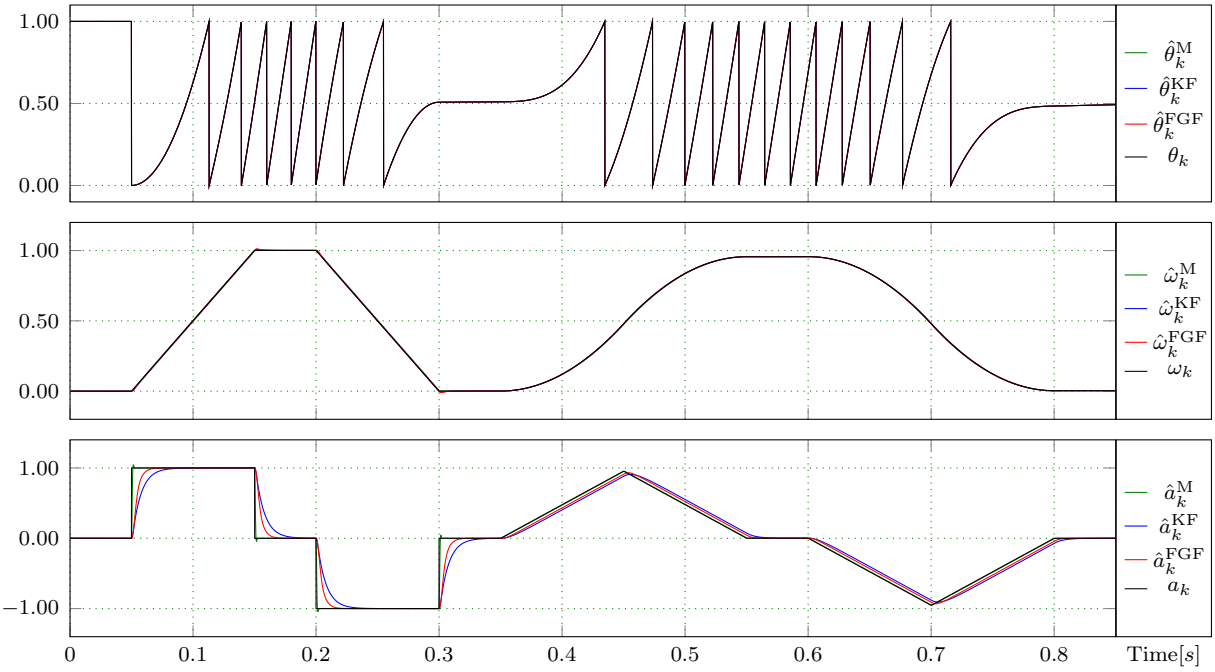

Figure 5.8: Performance for tracking ramp and parabolic velocities under ideal condition.

5.3.4.3 Performances for tracking a ramp velocity and a parabolic velocity with quantized errors

The position signals in electrical drives always have quantized errors that impact the estimate results. The comparison of the conventional M method, KF, and FGF tracking with quantized errors is shown in Figure 5.10. The M method uses a second-order low pass filter (the cut-off frequency is set to 500Hz) to smooth the quantization error. As shown in Figure 5.11, the KF and FGF can successfully calculate the position, velocity, and acceleration, while the M method can only estimate the position $\hat{\theta}_k^{\mathrm{M}}$ and velocity $\hat{\omega}_k^{\mathrm{M}}$, but not the acceleration $\hat{a}_k^{\mathrm{M}}$. Compared to $\hat{\theta}_k^{\mathrm{KF}}$ and $\hat{\theta}_k^{\mathrm{FGF}}$, even with a low pass filter, $\hat{\theta}_k^{\mathrm{M}}$ has the largest deviation for position and velocity estimations. Among them, the FGF has the smallest error and gives the fastest response, since it comprises only one factor, making it easy to acquire the optimum estimate. The KF can also provide the same performance as the FGF when the parameters are optimized. However, as the KF involves several factors, it is very difficult to find the optimal combination. What need reminds is, the parameters of KF are tuned with a lot of effort and the chosen parameters are the ones making the KF have the optimal performance within the entire tuning process.

The simulation numerically demonstrates that the FGF can track step, ramp and parabolic velocities under both ideal and noisy condition. In the case of tracking under ideal condition, the errors of position and acceleration are, $Err^{\mathrm{FGF}} > Err^{\mathrm{KF}} > Err^{\mathrm{M}}$, and the errors of velocity are, $Err^{\mathrm{M}} > Err^{\mathrm{FGF}} > Err^{\mathrm{KF}}$. The tracking responses rates are, $R^{\mathrm{M}} > R^{\mathrm{FGF}} > R^{\mathrm{KF}}$. In the case of tracking with quantized errors, the errors of position, velocity, and acceleration are, $Err^{\mathrm{M}} > Err^{\mathrm{KF}} > Err^{\mathrm{FGF}}$. However, it is difficult

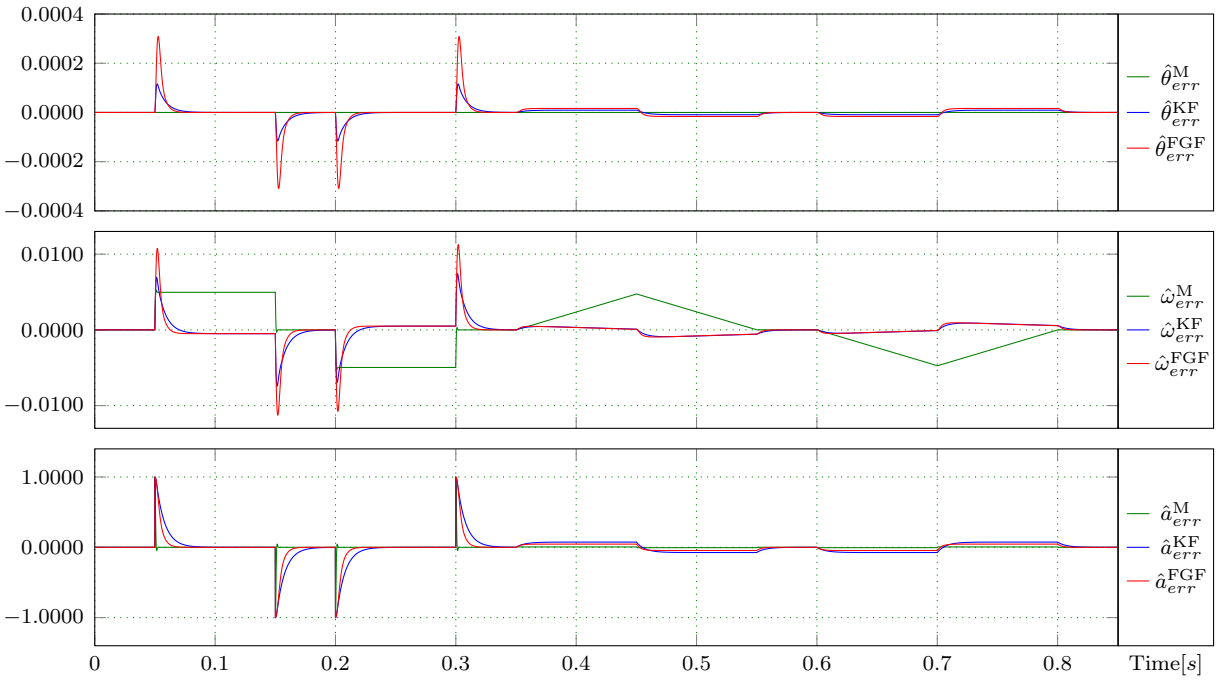

Figure 5.9: Errors for tracking a ramp velocity and a parabolic velocity under ideal condition.$\theta^{\mathrm{M}}_{err}$, $\theta^{\mathrm{KF}}_{err}$, and $\theta^{\mathrm{FGF}}_{err}$ are the estimated errors of positions with M method, KF, and FGF. $\omega^{\mathrm{M}}_{err}$, $\omega^{\mathrm{KF}}_{err}$, and $\omega^{\mathrm{FGF}}_{err}$ are the estimated errors of angular velocities with the M method, KF, and FGF. a^{M}_{err}, a^{KF}_{err}, and a^{FGF}_{err} are the estimated errors of accelerations with the M method, KF, and FGF.

to compare their tracking responses rates.

5.3.5 Experimental Assessment

In this section, a speed control drive system for the induction motor is used to fully evaluate the proposed FGF and the other mentioned methods. The drive is controlled using the vector control. The speed feedback has, therefore, a great influence on the control performance. The parameters of the respective filters used in the experiment are selected as the same way as in the simulation. Thus, only the special information is discussed here. One comment is that the encoder used in the testing is KUBLER T5.2400.1222.1024. It usually provides a resolution of 1024. Because quadrature signals generated by the incremental encoder are combined with an exclusive or (XOR) gate, and the output of the XOR gate is then connected to a counter to record the position, the encoder can provide a resolution of 4096.

5.3.5.1 Programming complexity evaluation

To evaluate the performance of KF and FGF, the first concern is whether they are easy to realize in programming. The algorithms are implemented in C language running

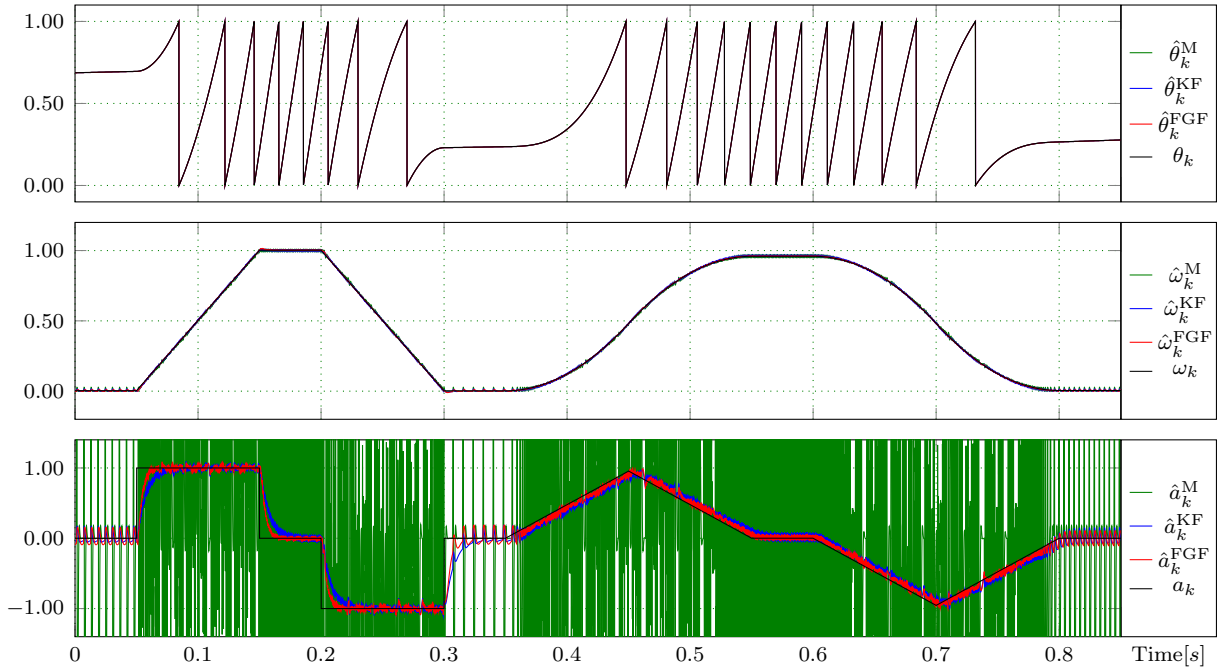

Figure 5.10: Performance for tracking ramp and parabolic velocities with quantized errors.

on STM32F417IGTx, a 168 MHz, advanced reduced instruction set computing machine (ARM) processor. To better evaluate the performance and make it easy to compare to different system setups, all the variables are expressed by normalized values. In the case of using floating-point numbers, both algorithms are easy to implement due to the large dynamic range. In the case of using fixed-point numbers, although the same scale factors for the variables (θ, ω, a) can be selected for both algorithms, they have different complexity. Since the covariance matrix $\mathbf{P}$ of the KF is unknown and has a wide dynamic range, the scale factors for each element of the matrix $\mathbf{P}$, which consists of six different elements[2], should be selected carefully, and all results having operations with $\mathbf{P}$ must be scaled to the respective format based on the scale factors of the operators. Therefore, it is very difficult to design a proper program to satisfy the accuracy requirements of the KF using fixed point (FXP) numbers (KF-FXP). However, the implementation of the FGF using fixed-point numbers (FGF-FXP) is much easier to fulfill, because the parameters (α, β, γ) only depend on one factor s and can be calculated offline. Thus, we do not have to pay much attention to choosing a proper scale factor for the fixed-point numbers. The factor is selected according to its range[3]. This is also one of the motivations why we choose the normalized value to replace the physical value.

Based on the formerly presented description, from the most positive to the most negative degree, the complexity of the implementation is divided into three stages, namely, positive (1), neutral (0) and negative (-1), as shown in Table 5.2. The KF using fixed-point

[2]Since $\mathbf{P}$ is symmetric, the 3×3 matrix has only six unique terms.

[3]In our implementation, the scale factors for α, $\frac{\beta}{T_s}$, and $\frac{2\gamma}{T_s^2}$ are selected as 2^{29}, 2^{19}, and 2^6, respectively.

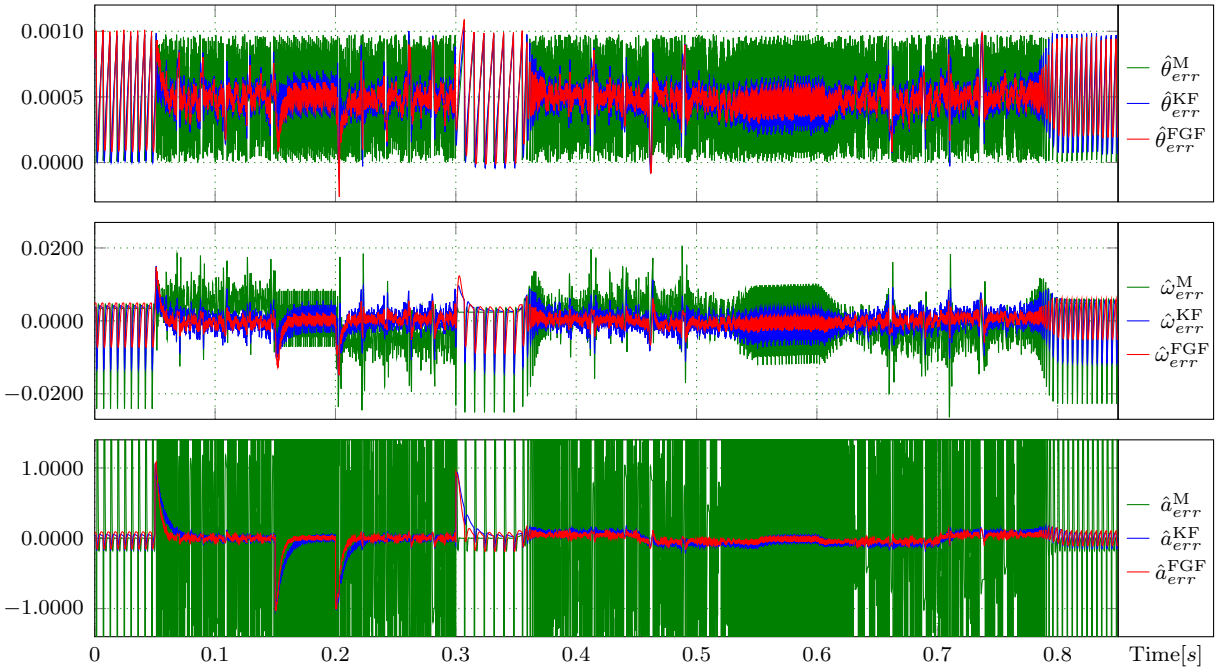

Figure 5.11: Errors for tracking ramp and parabolic velocities with quantized errors.

Table 5.2: Execution time for the KF and FGF

Methods	**CPU ticks**	**Execution time**	**Complexity**
KF-FXP	1105	6.6 μs	-1
KF-FP-FPU	320	1.9 μs	1
KF-FP-FPUE	1631	9.7 μs	1
FGF-FXP	187	1.1 μs	0
FGF-FP-FPU	121	0.7 μs	1
FGF-FP-FPUE	894	5.3 μs	1

numbers is the most complex to program.

The second evaluation is the computational time. Table 5.2 shows the computational time of different KFs and FGFs. The KF using floating point (FP) number (KF-FP) with a floating point unit emulator (FPUE) takes the longest time, 9.7μs, to execute, while the FGF using floating point number (FGF-FP) with a floating point unit (FPU) takes the shortest time, only 0.7μs. Compared to KF-FXP, KF-FP with an FPUE (KF-FP-FPUE), and KF-FP with an FPU (KF-FP-FPU), the execution time of FGF-FP with an FPU (FGF-FP-FPU) is reduced by 89.4%, 92.8%, and 63%, respectively, and for the FGF-FXP the reductions are 83.3%, 88.7%, and 42.1%, respectively.

In summary, considering the complexity of programming and calculation time, the FGF-FP is recommended when the micro-controller has an FPU, and the FGF-FXP is recommended when the micro-controller has no FPU. It should be noted that this conclusion can also be drawn for other processors.

5.3.5.2 Performances evaluation

Since the step velocity cannot be obtained in practice, in the experiment only the ramp and parabolic velocities are tracked. The experiment results with the M method, KF, and FGF tracking ramp and parabolic velocities are shown in Figure 5.12 and Figure 5.14. The three methods successfully track the positions $\hat{\theta}_k^{\mathrm{M}}$, $\hat{\theta}_k^{\mathrm{KF}}$, $\hat{\theta}_k^{\mathrm{FGF}}$ and velocities $\hat{\omega}_k^{\mathrm{M}}$, $\hat{\omega}_k^{\mathrm{KF}}$, $\hat{\omega}_k^{\mathrm{FGF}}$. The accelerations $\hat{a}_k^{\mathrm{KF}}$, $\hat{a}_k^{\mathrm{FGF}}$ and torque current i_q have the same tendency, meaning that the KF and FGF can correctly track the acceleration, while the M method fails to track it. It can be seen that the acceleration tracking performance of the KF and FGF are similar.

Figure 5.13 and 5.15 show the zoomed in positions and velocities from the red frames and blue frames in Figure 5.12 and 5.14. The position $\hat{\theta}_k^{\mathrm{M}}$ acquired with the M method is a step signal with a resolution ratio of $1/(2^{14})$, which is also the maximum error of the estimated position with the M method. As shown at the left side of Figure 5.13 and 5.15, where the velocities are around 0 pu, the KF, and the FGF can decrease the estimated error of position, just as the simulation in Figure 5.11. At the right side of Figure 5.13 and 5.15, the velocities are around 0.36 pu and 0.42 pu, the difference between $\hat{\theta}_k^{\mathrm{KF}}$, $\hat{\theta}_k^{\mathrm{FGF}}$, and $\hat{\theta}_k^{\mathrm{M}}$ is inconspicuous. For both sides of the figures, the velocity $\hat{\omega}_k^{\mathrm{M}}$ has a much more serious ripple and time delay than the velocities $\omega_{err}^{\mathrm{KF}}$ and $\omega_{err}^{\mathrm{FGF}}$. The serious ripple and time delay results in a decreased bandwidth in closed loop systems, which will influence the performance. The velocity $\hat{\omega}_k^{\mathrm{M}}$ is smaller than the velocity $\hat{\omega}_k^{\mathrm{KF}}$ and $\hat{\omega}_k^{\mathrm{FGF}}$, because the M method acquires a smaller velocity when the electrical drive is speeding up, as shown in Figure 5.11. Besides, it can be noticed that the velocity $\omega_{err}^{\mathrm{FGF}}$ has a lower ripple than the velocity $\omega_{err}^{\mathrm{KF}}$. It confirms the former analysis that the FGF is easier to get the optimal Kalman gain because the fixed gain involves only one factor s.

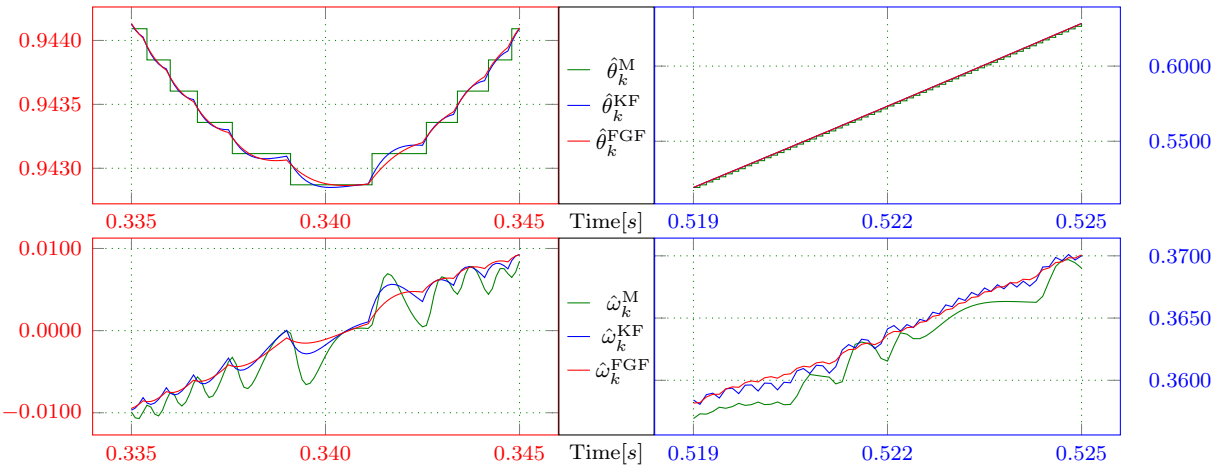

Figure 5.13: Zoomed in experimental comparison for tracking position and velocity from Figure 5.12. The left side and the right side are from the red frame and blue frame of Figure 5.12, respectively.

In general, the experimental results have a good agreement with the simulation results

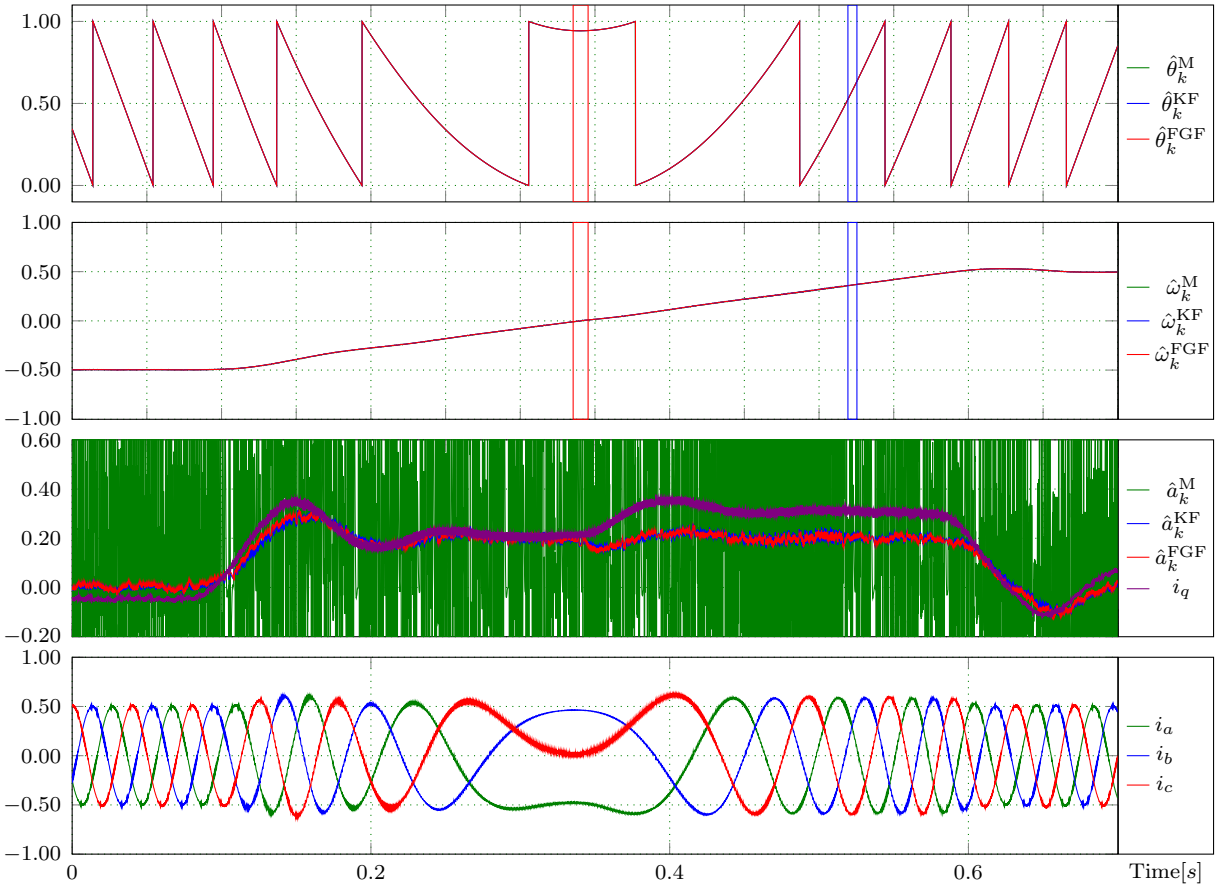

Figure 5.12: Experimental comparison for tracking position, velocity, and acceleration with ramp velocity. i_q is the torque current. i_a, i_b, and i_c are the three-phase current.

with quantized errors (see Figure 5.14). It demonstrates that the simulation model has a high fidelity compared to the real physical hardware. The FGF has a good performance in the entire range of velocity and improves greatly the accuracy of position estimate. Additionally, the FGF decreases the ripple of velocity estimate and can successfully estimate the acceleration, while the M method fails. The performances of FGF for tracking positions, velocities, and accelerations are quite similar as the KF or often better because the FGF is a special form of the KF. The experimental results confirm that the proposed FGF can be utilized to precisely estimate the position, velocity, and acceleration in electrical drives as an alternative of the KF. Meanwhile, as illustrated in Table 5.2, the FGF provides a great saving of calculation time comparing to the KF.

5.3.6 Summary

In this section, an optimal fixed gain filter has been proposed for more precise estimation of position, velocity, and acceleration in angular motion.

As the research has demonstrated and with proven results, it is no wonder that the optimal fixed gain filter is conceptually very simple yet powerful, since it considers the

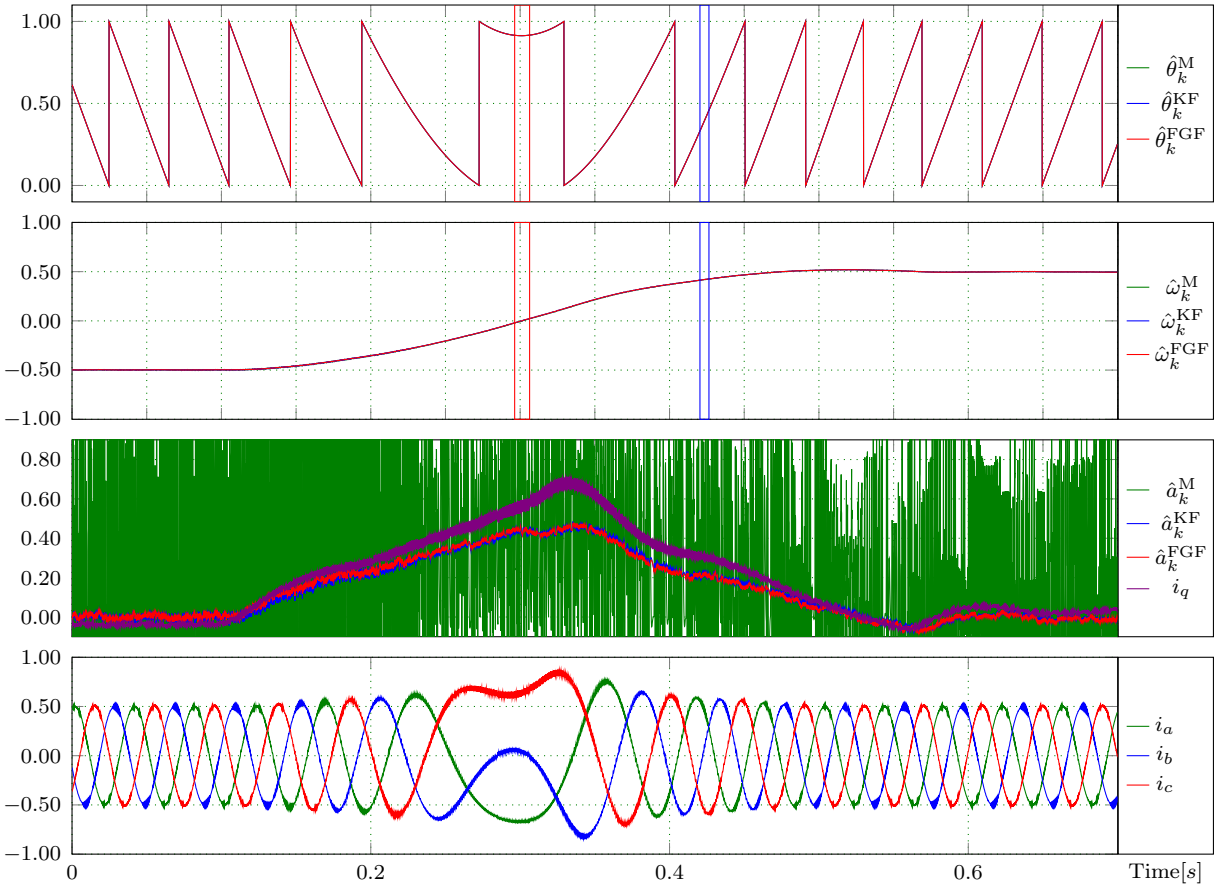

Figure 5.14: Experimental comparison for tracking position, velocity, and acceleration with parabolic velocity.

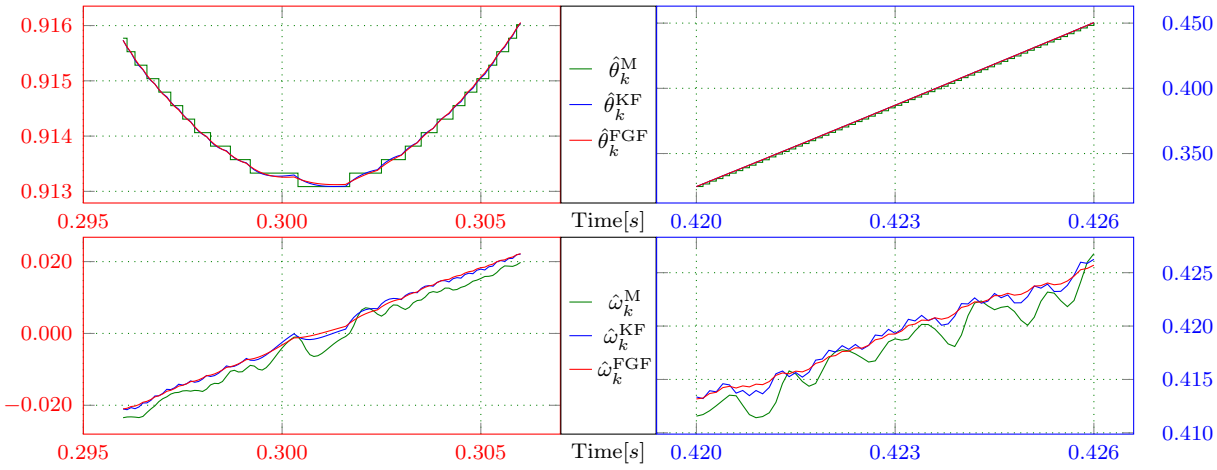

Figure 5.15: Zoomed in experimental comparison for tracking position and velocity from Figure 5.14. The left side and right side are from the red frame and blue frame of Figure 5.14, respectively.

motion nature of the tracking objects. The performances and effectiveness of the proposed optimal fixed gain filter for estimating position, velocity, and acceleration in the angular motion are either similar to those of the Kalman filter or often better because the proposed optimal fixed gain filter is a special form of the Kalman filter and it is much easier to obtain the optimal gain.

Although the fixed gain filter for angular motion estimation was evaluated through the application of encoder in electrical drives, it can be used for all position feedback applications in industries as diverse as sensor-less control, grid synchronous, and motion control, etc. The authors believe that the development of alternating current drives, the changes and evolution of the renewable energy systems, and new more demanding standards will drive the applications of the proposed optimal *fixed gain filter*.

5.4 Relationship of FGF and Luenberger observer

Since the feedback matrices of FGF and LO are all constant, the differences between the use of the FGF and the use of the LO should be clarified.

First, from the name of these two techniques, one is called filter, another is called observer. Thus, the use of the names is different, which determines the interpretation of the two techniques. The FGF is used to smooth the measurable states and estimate the unmeasurable states, which means we know the measurable states at time kT_s ($\boldsymbol{x}_k^m$) and the output of FGF is the estimated measurable states at time kT_s ($\hat{\boldsymbol{x}}_k^m$) and the estimated unmeasurable states at time kT_s ($\hat{\boldsymbol{x}}_k^u$). However, the LO is mainly used to estimate/observe the estimated unmeasurable states at time $(k+1)T_s$ ($\hat{\boldsymbol{x}}_{k+1}^u$) based on $\hat{\boldsymbol{x}}_k^m$.

Second, the definition of the error vector of the states is different. The FGF is derived from KF, and the error vector of the states is defined as $\boldsymbol{x}_k^m$ subtracts the predicted measurable states at time kT_s ($\hat{\boldsymbol{x}}_k^{m-}$) based on the estimated measurable states at time $(k-1)T_s$ ($\hat{\boldsymbol{x}}_{k-1}^m$). Thus, a prediction is required in the implementation of FGF. On the contrary, the prediction is not necessary for the LO due to its definition of the error vector which is defined as the measurable states at time $(k-1)T_s$ ($\boldsymbol{x}_{k-1}^m$) subtracts $\hat{\boldsymbol{x}}_{k-1}^m$. Finally, the stable range is different. From the second analysis and the observer equation (5.3), the characteristic equation of the LO can be written as

$$|z\mathbf{I} - (\mathbf{F} - \mathbf{LC})| = 0. \tag{5.35}$$

If the feedback gain is selected as the same with FGF, then substitute (5.19) into (5.35), the characteristic equation is

$$z^3 - \left(s^2+2\right)z^2 + \frac{3s^3+3s^2-4s+4}{s+1}z - \frac{4s^3-4s^2+s+1}{s+1} = 0. \tag{5.36}$$

Figure 5.16a shows the locus of the roots of (5.36) as s is increased from 0 to 1. Obviously, not all the roots locate in the unit circle. The two intersections between the

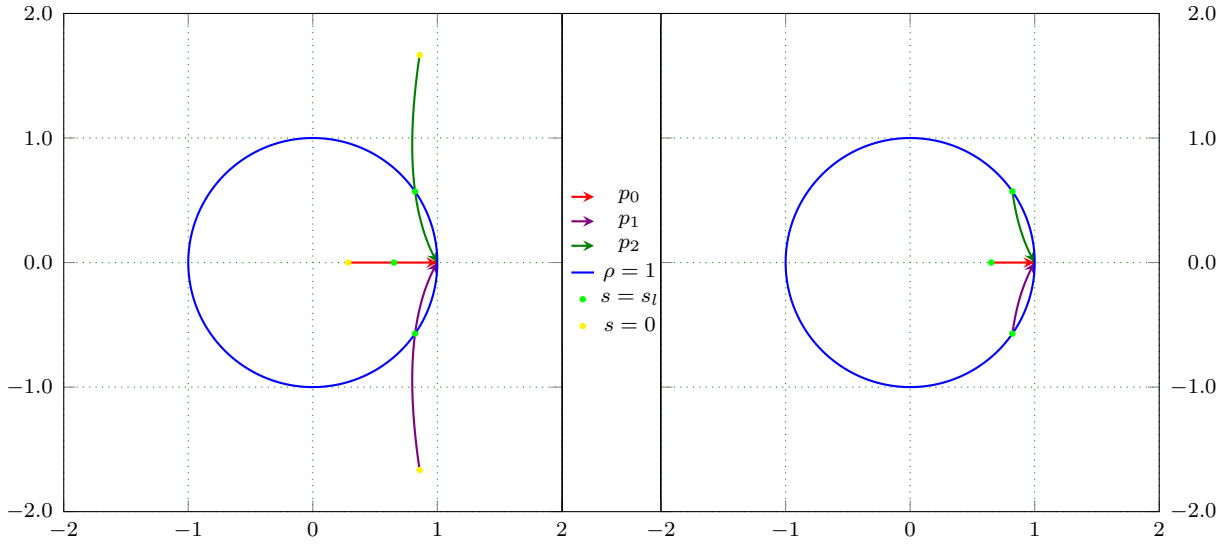

(a) $0 \leq s \leq 1$ (b) $s_l < s < 1$

Figure 5.16: Root locus of discrete Luenberger versus s. The x axis and the y axis are the real part and the imaginary part of the roots.

conjugate root locus and the unit circle locate at $p_2 = p_l$ and $p_3 = \bar{p_1}$ when $s = s_l$ where $p_l = 0.8213 - 0.5705i$, and $s_l = 0.5418685310126252264383277696533 8$.

With this in mind, the stable range is narrowed when the optimal gain is applied in the scheme of LO. This means that LO does not depend on the newest current measurements, which might lead to performance degradation.

Chapter 6

Conclusions and future work

6.1 Summary

This dissertation presents several optimizations for power converters and electrical drives. Two aspects are primary involved to achieve these optimization objectives. One is the theoretical issues. The main theoretical issues in control of power converters and electrical drives seem to be

- The tradeoff between the control performance and the cost to achieve it;
- How to evaluate the control performance.

In practice, this usually leads to the standard linear quadratic regulator (LQR) or model predictive control (MPC). However, this dissertation solves such problem in a unified framework which is optimum control. The other one is the practical issue, which mainly contains the simplification of the control algorithms with comparable or enhanced performance, because the most important requirements for putting control algorithms into an industry are good robustness, low sampling rates, less tuning efforts, and the desire to keep hardware expenses to a minimum. As this work has demonstrated with proven results, both of the two aspects have been demonstrated and were proven. More specifically:

Chapter 3 analyzed the theoretical issues in the conventional LQR and MPC and gave an analytical solution for the control problems.

In Chapter 4, two direct current (DC)-link voltage balance methods were proposed for the three-level neutral point clamped (NPC) converters. The method using the deadbeat control concept is suit for the control algorithm when an space vector pulse width modulation (SVPWM) is employed. In the case of using MPC algorithm, the decoupled method is expected to provide enhanced performance.

In Chapter 5, an optimal fixed gain filter for angular motion estimation has been proposed. It should be noted that this method is an optimal steady state filter, where the

optimal constant feedback gain can be calculated offline. Thus, it minimizes the requirements of resource while meeting the demands of the industry.

6.2 Outlook

There are several possibilities to extend and to modify the work in this thesis. Among the fields touched in this thesis, one may consider the following:

- too much simplification has been done in the proposed optimum control to avoid the discussion of a cubic equation. Future contributions in this area would be getting the exact analytical solution for the optimum control since the exact solution of a cubic equation is solvable.
- the deadbeat control concept for DC-link voltage balance within one pattern of pulse width modulation (PWM) arrangement has been proposed in Chapter 4. Thus, extending this concept to different patterns of PWM arrangement would be important, since different applications demand different PWM patterns.
- the fixed gain filter for angular motion system has been presented in Chapter 5. More importantly, there are many interesting extensions and applications within the subject of fixed gain filter. For instance, one could use this filter in the sensor-less control to replace the phase-locked loop (PLL). This would separate the tuning process of PLL from the tuning process of the whole sensor-less control because the parameter of the fixed gain filter can be optimally obtained offline. Additionally, it would be very beneficial to replace the LO by this kind of filter through the similar derivation. The author expects an universal derivation for the fixed gain filter would be seen in the future.

Appendix A

Nomenclature and Abbreviations

A.1 Abbreviations

AC alternating current

ACIM alternating current induction motor

ADC analog-to-digital converter

ARM advanced reduced instruction set computing machine

CEO chief executive officer

COC continuous optimum control

CPU central processing unit

CSC China scholarship council

DAC digital-to-analog converter

DBC deadbeat control

DC direct current

DFOC direct field oriented control

DFT discrete Fourier transform

DMPC direct model predictive control

DOC discontinuous optimum control

DTC direct torque control

DTFC direct torque flux control

EAL Institute for Electrical Drive Systems and Power Electronics

EKF extended Kalman filter

EMI electromagnetic interference

EUT equipment under test

FCS-MPC finite control set model predictive control

FGF fixed gain filter

FGF$_2$ second-order FGF

FGF$_3$ third-order FGF

FOC field oriented control

FP floating point

FPGA field programmable gate array

FPU floating point unit

FPUE floating point unit emulator

FXP fixed point

HM Hannover Messe

IFOC indirect field oriented control

IGBT insulated gate bipolar transistor

ISO international organization for standardization

ISR interrupt service routine

ITM instrumentation trace macro

KCL Kirchoff's current law

KF Kalman filter

KF$_2$ second-order KF

KF$_3$ third-order KF

LO Luenberger observer

LQR linear quadratic regulator

MATLAB matrix laboratory

MCU micro-controller unit

MHz megahertz

MPC model predictive control

NPC neutral point clamped

PC personal computer

PI proportional-integral

PID proportional–integral–derivative

PLL phase-locked loop

PMSM permanent magnet synchronous motor

PWM pulse width modulation

SI international system of units

SISO single-input and single-output

SMC sliding mode control

SMO sliding mode observer

SPMSM surface mounted permanent magnet synchronous motor

SVM space vector modulation

SVPWM space vector pulse width modulation

THD total harmonic distortion

TUM Technische Universität München

USB universal serial bus

VHDL very high speed integrated circuit (VHSIC) hardware description language

VHSIC very high speed integrated circuit

XOR exclusive or

ZOH Zero-order hold

A.2 Nomenclatures

A.2.1 Variables

$\mathbf{T}_{abc}$ Clark transformation

$\mathbf{T}_{abc}^{-1}$ inverse Clark transformation

$\mathbf{T}_{\alpha\beta}^{-1}$ inverse Park transformation

$\mathbf{T}_{\alpha\beta}$ Park transformation

s_x the switch function of the leg x ($x \in \{a, b, c\}$)

S_x the upper switch of the leg x in two level inverter ($x \in \{a, b, c\}$)

$\bar{S}_x$ the lower switch of the leg x in two level inverter ($x \in \{a, b, c\}$)

S_{xj} the j^{th} switch of the upper leg x in three level inverter

$\bar{S}_{xj}$ the j^{th} switch of the lower leg x in three level inverter

$\boldsymbol{i}_x$ the phase current of the leg x ($x \in \{a, b, c\}$)

$\mathcal{U}^2$ the universal set of the switching state vector $(s_a, s_b, s_c)^\top$ for two level converter

$\mathcal{U}^3$ the universal set of the switching state vector $(s_a, s_b, s_c)^\top$ for three level converter

$\mathcal{U}_z^3$ the set of zero vector for three level converter

$\mathcal{U}_{zp}^3$ the set of zero vector containing P state

$\mathcal{U}_{zo}^3$ the set of zero vector containing O state

$\mathcal{U}_{zn}^3$ the set of zero vector containing N state

$\mathcal{U}_s^3$ the set of small vector for three level converter

$\mathcal{U}_{sp}^3$ the set of small vector containing P state

$\mathcal{U}_{sn}^3$ the set of small vector containing N state

$\mathcal{U}_m^3$ the set of medium vector for three level converter

$\mathcal{U}_b^3$ the set of big vector for three level converter

v_{xo} the pole voltage of phase x ($x \in \{a, b, c\}$)

v_{c0} the voltage between O and N in three-level NPC converter

v_{c1} the voltage between P and O in three-level NPC converter

v_{an} the voltage of phase a to neutral point

v_{bn} the voltage of phase b to neutral point

v_{cn} the voltage of phase c to neutral point

v_{ao} the pole voltage of phase a

v_{bo} the pole voltage of phase b

v_{co} the pole voltage of phase c

i_a the phase current of the leg a

i_b the phase current of the leg b

i_c the phase current of the leg c

$\hat{\boldsymbol{x}}_k^{m-}$ the predicted measurable states at time kT_s

$\hat{\boldsymbol{x}}_{k+1}^{u}$ the estimated unmeasurable states at time $(k+1)T_s$

$\hat{\boldsymbol{x}}_{k-1}^{m}$ the estimated measurable states at time $(k-1)T_s$

$\hat{\boldsymbol{x}}_k^{u}$ the estimated unmeasurable states at time kT_s

$\hat{\boldsymbol{x}}_k^{m}$ the estimated measurable states at time kT_s

$\boldsymbol{x}_k^{m}$ the measurable states at time kT_s

$\boldsymbol{x}_{k-1}^{m}$ the measurable states at time $(k-1)T_s$

A.2.2 Operations with logic variables

$\wedge$	and
$\vee$	or
$\neg$	not
$\Longleftrightarrow$	if and only if
$\equiv$	is defined as

A.2.3 Operations with complex numbers

$\Re(c)$	the real part of c
$\Im(c)$	the imaginary part of c
$\bar{c}$	the complex conjugate of c
$\times$	cross multiply

A.2.4 Set operations and relations

$\cup$ union
$\cap$ intersection
$\in$ element of
$\ni$ contains as an element
$\forall$ for all
$\subseteq$ subset
$\subset$ proper subset
$\supseteq$ superset
$\supset$ proper superset

Appendix B

Testbench

All the control schemes in this work are implemented on the same test bench shown in Figure B.1, where the left side are the electric control unit and power converter; while the right side is the motor under control and the loading machine, which are mechanically coupled together. Besides, the testbench driving the motor under control and the converter driving the loading machine share the same DC-link, which avoids the wasting of energy. If necessary, excessive energy is dissipated in the braking resistor to avoid over-voltage fault in the DC-link.

Note that, the power converter is a three-level NPC converter, which could also be used as two-level converter when the gate signals of the upper insulated gate bipolar transistor (IGBT)s are same.

B.1 Real-time system

The real-time computer system is composed by a micro-controller unit (MCU) and an field programmable gate array (FPGA).

The MCU is STM32F417IGTx which offers the performance of the Cortex™-M4 core (with FPU) running at 168 MHz. The STM32F417IGTx are designed for industrial applications where the high level of integration and performance, embedded memories, and rich peripheral set inside packages are required. Almost all the real-time control algorithms used in this work are implemented in this MCU with C/C++ language, which are triggered by an external interrupt generated by the triangle wave generation unit in the FPGA. One highlight of this system is that it can also send the real-time state (e.g. phase current, encoder angle, encode speed, etc.) to personal computer (PC) and receive the command data (e.g. given speed, start, stop, etc.) from a PC through an universal serial bus (USB) cable.

The FPGA is Cyclone IV-EP4CE10E144 with 10,320 logic elements, 23 Embedded 18×18 multipliers, and 414K bits embedded memory. The crystal frequency for the FPGA is 8 MHz. However, by utilizing the PLL, the main operating frequency is multiplied to

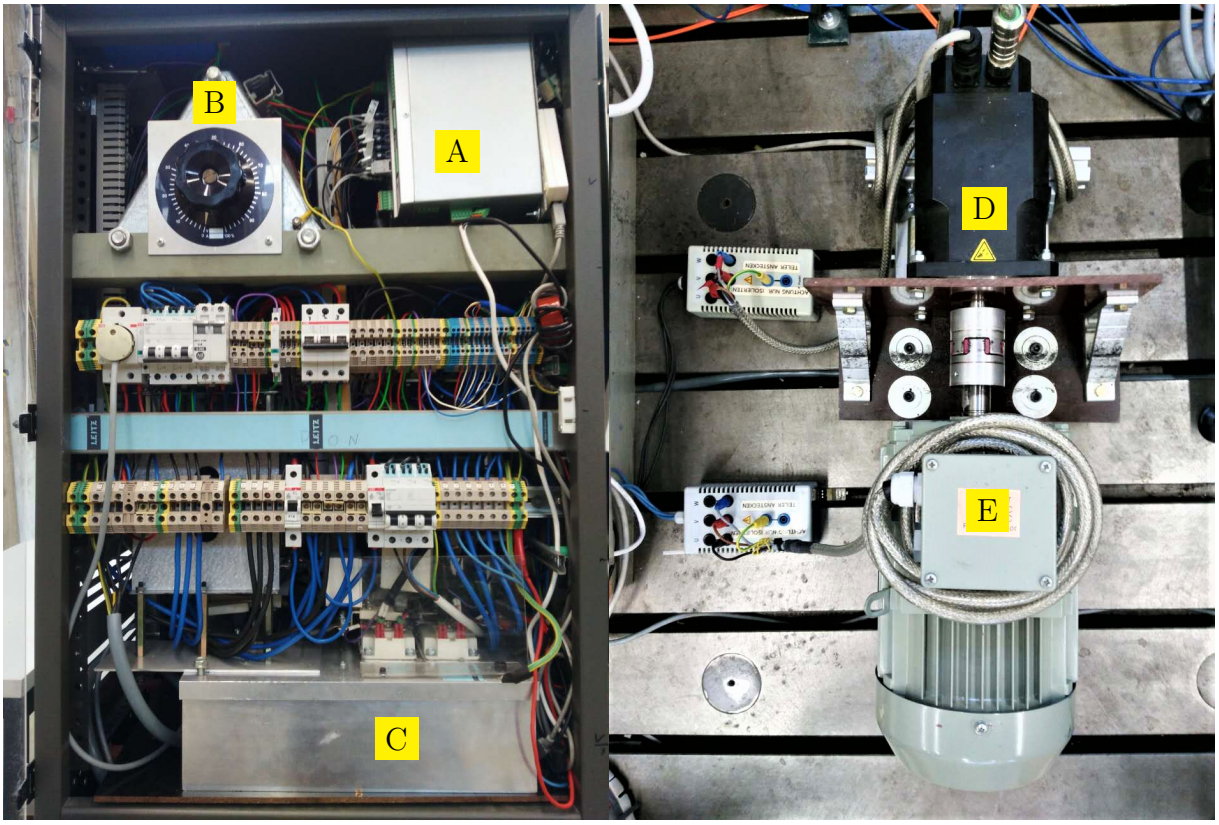

Figure B.1: Setup of the testbench system. *A: real-time system with MCU and FPGA*, B: an autotransformer (used when reducing the DC-link voltage), C: heat/sink and power converter, *D: PMSM*; *E: ACIM*.

96 MHz for a high precision PWM signal generation. In this work, the VHSIC hardware description language (VHDL) codes used for PWM signal generation, state machine, and fiber optical communication were self-written without using the MATLAB code generation technology. By doing so, the performance and the resource usage can achieve an optimal state.

The real-time computer system is isolated with the inverter by optical fiber for the inverter gating signals and information exchange in order to reduce sensitivity of electromagnetic interference (EMI).

B.2 Gate driver board

The main function of the gate driver board consists:

- receive the IGBT gating signals and transmit to the inverter,
- current measurement,

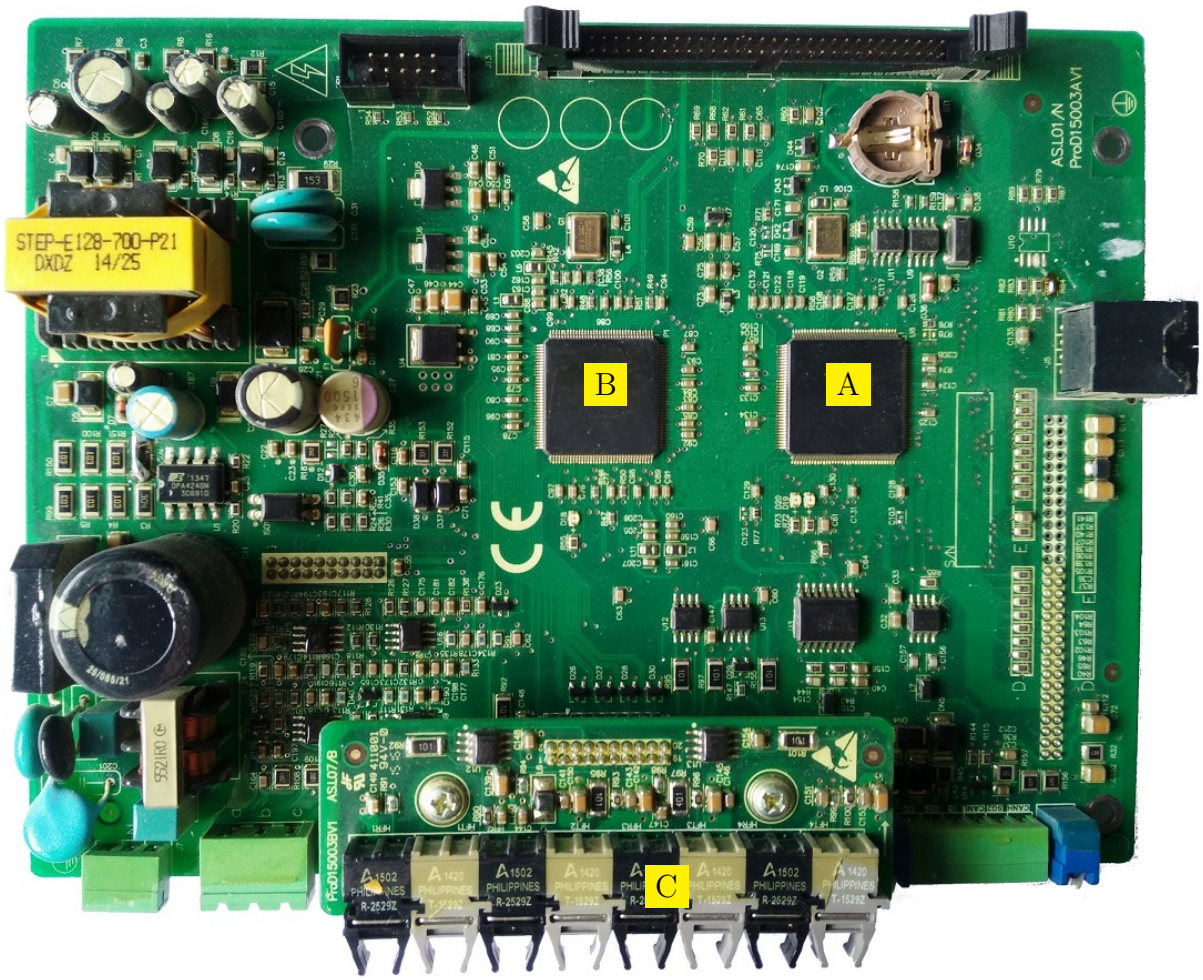

Figure B.2: Real-time system. *A: MCU*, *B: FPGA*, *C: eight pairs of optical interfaces.*

- dead time generation,
- over current protection,
- over voltage protection,
- optical fiber communication.

To achieve this purpose, the gate driver board is designed with an FPGA and an analog-to-digital converter (ADC). The drive board is connected to the real-time computer system through eight pairs of optics fiber which allows to receive the IGBT gating signals and information exchange. The dead time generation unit is handled by an Actel ProASIC3 A3PN250, which ensures the correct timing of gate driving signals, especially in the power-on state.

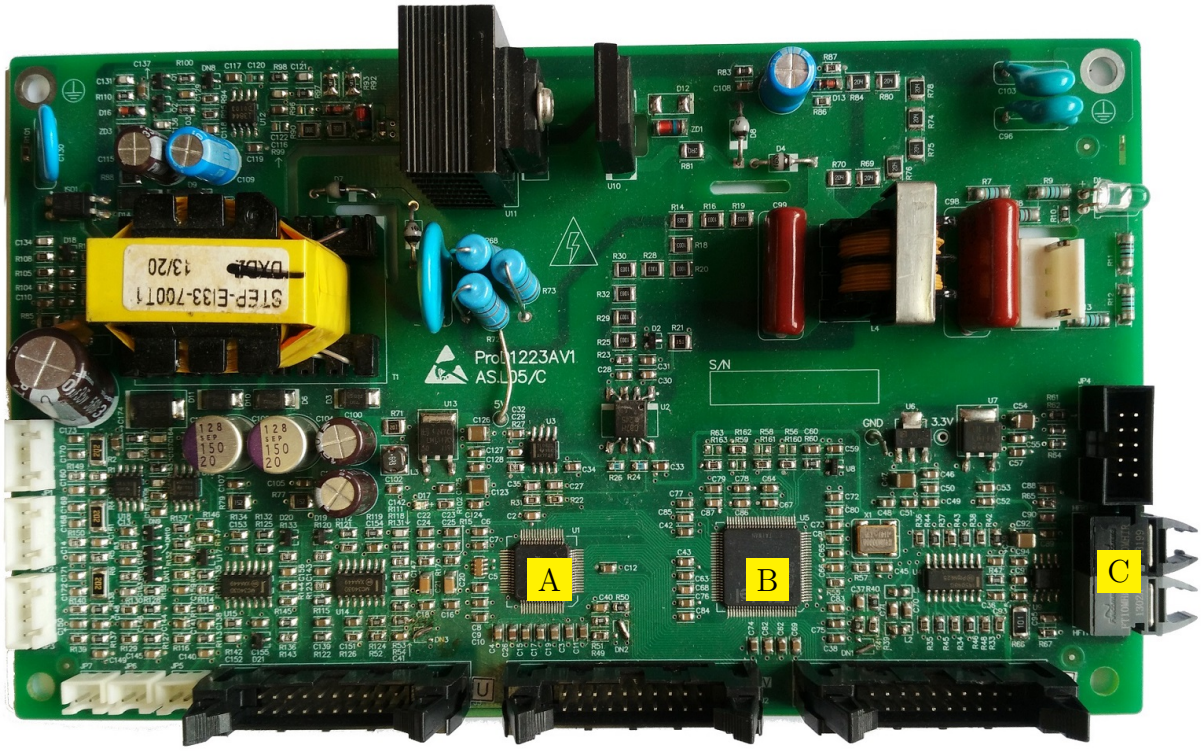

Figure B.3: Gate driver board. *A: ADC*, *B: FPGA*, *C: optical interface*,

B.3 Three-level inverter

The three-level inverter consists of three phase legs. In every leg, two IGBT modules from Infineon and two diodes are used. Both the IGBT modules and the diodes are mounted on the heat sink. The IGBT modules are rated for 100 A, 1700 V. Hence, an output voltage of 1100 V and an output current of 50 A could be generated. The complete DC-link capacitance is 1700 µF.

B.4 DC source

The DC-link is powered by two three phase six-pulse rectifiers connected in series. In this connection, each six-pulse rectifier generates one half of the DC-link voltage. One of the rectifiers is powered by the autotransformer via a 50 Hz isolation phase shifting transformer, the other rectifier is connected to the autotransformer directly. By doing so, the two rectifiers achieve the theoretical reduction in harmonics. The autotransformer is then connected to the 50 Hz grid.

B.5 Induction machine

Technical data of the asynchronous machine used in the experiments is shown in Table B.1.

Table B.1: Parameters for the induction machine.

Symbol	Parameter	Value
R_s	Stator Resistance	1.509 Ω
R_r	Rotor Resistance	1.235 Ω
L_m	Mutual Inductance	232.5 mH
L_s	Stator Inductance	239.5 mH
L_r	Rotor Inductance	239.5 mH
f_{base}	Synchronous frequency	50 Hz
N_e	Nominal speed	2830 rpm
I_e	Nominal current	5.73 A
p	Number of pole pairs	1

B.6 Permanent magnet synchronous motor

Technical data of the PMSM used in the experiments is shown in Table B.2.

Table B.2: Parameters for the PMSM.

Symbol	Parameter	Value
R_s	Stator Resistance	0.95 Ω
L_d	d-axis Inductance	9.6 mH
L_q	q-axis Inductance	9.6 mH
ψ	Flux	0.26 Wb
N_e	Nominal speed	3000 rpm
I_e	Nominal current	6.3 A
V_e	Nominal voltage	380 V
p	Number of pole Pairs	3

Appendix C

Three level NPC SVPWM

C.1 Calculation of triangle 1

C.1.1 Sector I

C.1.1.1 Results of the calculation when $i_a > 0$ and $i_c > 0$

$$m_{a1} = (\gamma - 1)\left(\beta - \sqrt{3}\,\alpha\right) + 2\,\beta\,\gamma - \lambda\left(\beta + \sqrt{3}\,\alpha - 1\right) \tag{C.1}$$

$$m_{a0} = (-\lambda - \mu)\left(\beta + \sqrt{3}\,\alpha - 1\right) + \left(\beta + \sqrt{3}\,\alpha\right) \tag{C.2}$$

$$m_{b1} = 2\,\beta\,\gamma - \lambda\left(\beta + \sqrt{3}\,\alpha - 1\right) \tag{C.3}$$

$$m_{b0} = (-\lambda - \mu)\left(\beta + \sqrt{3}\,\alpha - 1\right) + \gamma\left(\beta - \sqrt{3}\,\alpha\right) + \left(\beta + \sqrt{3}\,\alpha\right) \tag{C.4}$$

$$m_{c1} = -\lambda\left(\beta + \sqrt{3}\,\alpha - 1\right) \tag{C.5}$$

$$m_{c0} = (-\lambda - \mu)\left(\beta + \sqrt{3}\,\alpha - 1\right) + \gamma\left(\beta - \sqrt{3}\,\alpha\right) + \left(\beta + \sqrt{3}\,\alpha + 2\,\beta\,(\gamma - 1)\right) \tag{C.6}$$

C.1.1.2 Results of the calculation when $i_a > 0$ and $i_c < 0$

$$m_{a1} = (\gamma - 1)\left(\beta - \sqrt{3}\,\alpha\right) - 2\,\beta\,(\gamma - 1) - \lambda\left(\beta + \sqrt{3}\,\alpha - 1\right) \tag{C.7}$$

$$m_{a0} = (-\lambda - \mu)\left(\beta + \sqrt{3}\,\alpha - 1\right) + \left(\beta + \sqrt{3}\,\alpha\right) \tag{C.8}$$

$$m_{b1} = -2\,\beta\,(\gamma - 1) - \lambda\left(\beta + \sqrt{3}\,\alpha - 1\right) \tag{C.9}$$

$$m_{b0} = (-\lambda - \mu)\left(\beta + \sqrt{3}\,\alpha - 1\right) + \gamma\left(\beta - \sqrt{3}\,\alpha\right) + \left(\beta + \sqrt{3}\,\alpha\right) \tag{C.10}$$

$$m_{c1} = -\lambda \left(\beta + \sqrt{3}\,\alpha - 1\right) \tag{C.11}$$

$$m_{c0} = (-\lambda - \mu) \left(\beta + \sqrt{3}\,\alpha - 1\right) + \gamma \left(\beta - \sqrt{3}\,\alpha\right) + \left(\beta + \sqrt{3}\,\alpha - 2\,\beta\,\gamma\right) \tag{C.12}$$

C.1.1.3 Results of the calculation when $i_a < 0$ and $i_c < 0$

$$m_{a1} = -2\,\beta\,(\gamma - 1) - \gamma \left(\beta - \sqrt{3}\,\alpha\right) - \lambda \left(\beta + \sqrt{3}\,\alpha - 1\right) \tag{C.13}$$

$$m_{a0} = (-\lambda - \mu) \left(\beta + \sqrt{3}\,\alpha - 1\right) + \left(\beta + \sqrt{3}\,\alpha\right) \tag{C.14}$$

$$m_{b1} = -2\,\beta\,(\gamma - 1) - \lambda \left(\beta + \sqrt{3}\,\alpha - 1\right) \tag{C.15}$$

$$m_{b0} = (-\lambda - \mu) \left(\beta + \sqrt{3}\,\alpha - 1\right) + (1 - \gamma) \left(\beta - \sqrt{3}\,\alpha\right) + \left(\beta + \sqrt{3}\,\alpha\right) \tag{C.16}$$

$$m_{c1} = -\lambda \left(\beta + \sqrt{3}\,\alpha - 1\right) \tag{C.17}$$

$$m_{c0} = 2\,\beta - 3\,\beta\,\gamma - (\lambda + \mu) \left(\beta + \sqrt{3}\,\alpha - 1\right) + \sqrt{3}\,\alpha\,\gamma \tag{C.18}$$

C.1.1.4 Results of the calculation when $i_a < 0$ and $i_c > 0$

$$m_{a1} = \beta\,\gamma - \lambda \left(\beta + \sqrt{3}\,\alpha - 1\right) + \sqrt{3}\,\alpha\,\gamma \tag{C.19}$$

$$m_{a0} = (-\lambda - \mu) \left(\beta + \sqrt{3}\,\alpha - 1\right) + \left(\beta + \sqrt{3}\,\alpha\right) \tag{C.20}$$

$$m_{b1} = 2\,\beta\,\gamma - \lambda \left(\beta + \sqrt{3}\,\alpha - 1\right) \tag{C.21}$$

$$m_{b0} = (-\lambda - \mu) \left(\beta + \sqrt{3}\,\alpha - 1\right) + (1 - \gamma) \left(\beta - \sqrt{3}\,\alpha\right) + \left(\beta + \sqrt{3}\,\alpha\right) \tag{C.22}$$

$$m_{c1} = -\lambda \left(\beta + \sqrt{3}\,\alpha - 1\right) \tag{C.23}$$

$$m_{c0} = \lambda + \mu + \beta\,\gamma - \beta\,\lambda - \beta\,\mu + \sqrt{3}\,\alpha\,\gamma - \sqrt{3}\,\alpha\,\lambda - \sqrt{3}\,\alpha\,\mu \tag{C.24}$$

C.1.2 Sector II

C.1.2.1 Results of the calculation when $i_c > 0$ and $i_b > 0$

$$m_{a1} = \gamma \left(\beta + \sqrt{3}\,\alpha\right) - \lambda\,(2\,\beta - 1) \tag{C.25}$$

$$m_{a0} = 2\,\beta - \gamma \left(\beta - \sqrt{3}\,\alpha\right) + (-\lambda - \mu)\,(2\,\beta - 1) \tag{C.26}$$

$$m_{b1} = \beta + \lambda - \sqrt{3}\,\alpha - 2\,\beta\,\lambda + 2\,\sqrt{3}\,\alpha\,\gamma \tag{C.27}$$

$$m_{b0} = 2\,\beta - (2\,\beta - 1)\,(\lambda + \mu) \tag{C.28}$$
$$m_{c1} = -\lambda\,(2\,\beta - 1) \tag{C.29}$$
$$m_{c0} = \beta + \lambda + \mu - \sqrt{3}\,\alpha - 2\,\beta\,\lambda - 2\,\beta\,\mu + 2\,\sqrt{3}\,\alpha\,\gamma \tag{C.30}$$

C.1.2.2 Results of the calculation when $i_c > 0$ and $i_b < 0$

$$m_{a1} = \gamma\,\left(\beta + \sqrt{3}\,\alpha\right) - \lambda\,(2\,\beta - 1) \tag{C.31}$$
$$m_{a0} = (-\lambda - \mu)\,(2\,\beta - 1) + (\gamma - 1)\,\left(\beta - \sqrt{3}\,\alpha\right) + 2\,\beta \tag{C.32}$$
$$m_{b1} = \lambda + 2\,\beta\,\gamma - 2\,\beta\,\lambda \tag{C.33}$$
$$m_{b0} = 2\,\beta - (2\,\beta - 1)\,(\lambda + \mu) \tag{C.34}$$
$$m_{c1} = -\lambda\,(2\,\beta - 1) \tag{C.35}$$
$$m_{c0} = \lambda + \mu + 2\,\beta\,\gamma - 2\,\beta\,\lambda - 2\,\beta\,\mu \tag{C.36}$$

C.1.2.3 Results of the calculation when $i_c < 0$ and $i_b < 0$

$$m_{a1} = -\,(\gamma - 1)\,\left(\beta + \sqrt{3}\,\alpha\right) - \lambda\,(2\,\beta - 1) \tag{C.37}$$
$$m_{a0} = (-\lambda - \mu)\,(2\,\beta - 1) + (\gamma - 1)\,\left(\beta - \sqrt{3}\,\alpha\right) + 2\,\beta \tag{C.38}$$
$$m_{b1} = \beta + \lambda + \sqrt{3}\,\alpha - 2\,\beta\,\lambda - 2\,\sqrt{3}\,\alpha\,\gamma \tag{C.39}$$
$$m_{b0} = 2\,\beta - (2\,\beta - 1)\,(\lambda + \mu) \tag{C.40}$$
$$m_{c1} = -\lambda\,(2\,\beta - 1) \tag{C.41}$$
$$m_{c0} = \beta + \lambda + \mu + \sqrt{3}\,\alpha - 2\,\beta\,\lambda - 2\,\beta\,\mu - 2\,\sqrt{3}\,\alpha\,\gamma \tag{C.42}$$

C.1.2.4 Results of the calculation when $i_c < 0$ and $i_b > 0$

$$m_{a1} = -\,(\gamma - 1)\,\left(\beta + \sqrt{3}\,\alpha\right) - \lambda\,(2\,\beta - 1) \tag{C.43}$$
$$m_{a0} = 2\,\beta - \gamma\,\left(\beta - \sqrt{3}\,\alpha\right) + (-\lambda - \mu)\,(2\,\beta - 1) \tag{C.44}$$
$$m_{b1} = 2\,\beta + \lambda - 2\,\beta\,\gamma - 2\,\beta\,\lambda \tag{C.45}$$
$$m_{b0} = 2\,\beta - (2\,\beta - 1)\,(\lambda + \mu) \tag{C.46}$$
$$m_{c1} = -\lambda\,(2\,\beta - 1) \tag{C.47}$$
$$m_{c0} = 2\,\beta + \lambda + \mu - 2\,\beta\,\gamma - 2\,\beta\,\lambda - 2\,\beta\,\mu \tag{C.48}$$

C.1.3 Sector III

C.1.3.1 Results of the calculation when $i_b > 0$ and $i_a > 0$

$$m_{a1} = \lambda \left(\sqrt{3}\,\alpha - \beta + 1\right) \tag{C.49}$$
$$m_{a0} = 2\,\beta - 3\,\beta\,\gamma + (\lambda + \mu) \left(\sqrt{3}\,\alpha - \beta + 1\right) - \sqrt{3}\,\alpha\,\gamma \tag{C.50}$$
$$m_{b1} = \lambda \left(\sqrt{3}\,\alpha - \beta + 1\right) - \left(2\,\beta\,(\gamma - 1) + \gamma \left(\beta + \sqrt{3}\,\alpha\right)\right) \tag{C.51}$$
$$m_{b0} = (\lambda + \mu) \left(\sqrt{3}\,\alpha - \beta + 1\right) + \left(\beta - \sqrt{3}\,\alpha\right) \tag{C.52}$$
$$m_{c1} = \lambda \left(\sqrt{3}\,\alpha - \beta + 1\right) - \gamma \left(\beta + \sqrt{3}\,\alpha\right) \tag{C.53}$$
$$m_{c0} = (\lambda + \mu) \left(\sqrt{3}\,\alpha - \beta + 1\right) + \left(\beta - \sqrt{3}\,\alpha - 2\,\beta\,\gamma\right) \tag{C.54}$$

C.1.3.2 Results of the calculation when $i_b > 0$ and $i_a < 0$

$$m_{a1} = \lambda \left(\sqrt{3}\,\alpha - \beta + 1\right) \tag{C.55}$$
$$m_{a0} = (\lambda + \mu) \left(\sqrt{3}\,\alpha - \beta + 1\right) - (\gamma - 1) \left(\beta - \sqrt{3}\,\alpha\right) \tag{C.56}$$
$$m_{b1} = \lambda \left(\sqrt{3}\,\alpha - \beta + 1\right) + \left((\gamma - 1) \left(\beta + \sqrt{3}\,\alpha\right) - 2\,\beta\,(\gamma - 1)\right) \tag{C.57}$$
$$m_{b0} = (\lambda + \mu) \left(\sqrt{3}\,\alpha - \beta + 1\right) + \left(\beta - \sqrt{3}\,\alpha\right) \tag{C.58}$$
$$m_{c1} = (\gamma - 1) \left(\beta + \sqrt{3}\,\alpha\right) + \lambda \left(\sqrt{3}\,\alpha - \beta + 1\right) \tag{C.59}$$
$$m_{c0} = (\lambda + \mu) \left(\sqrt{3}\,\alpha - \beta + 1\right) + \left(\beta - \sqrt{3}\,\alpha - 2\,\beta\,\gamma\right) \tag{C.60}$$

C.1.3.3 Results of the calculation when $i_b < 0$ and $i_a < 0$

$$m_{a1} = \lambda \left(\sqrt{3}\,\alpha - \beta + 1\right) \tag{C.61}$$
$$m_{a0} = (\lambda + \mu) \left(\sqrt{3}\,\alpha - \beta + 1\right) + \left(\beta - \sqrt{3}\,\alpha + 2\,\beta\,(\gamma - 1) + \gamma \left(\beta + \sqrt{3}\,\alpha\right)\right) \tag{C.62}$$
$$m_{b1} = \lambda \left(\sqrt{3}\,\alpha - \beta + 1\right) + \left((\gamma - 1) \left(\beta + \sqrt{3}\,\alpha\right) + 2\,\beta\,\gamma\right) \tag{C.63}$$
$$m_{b0} = (\lambda + \mu) \left(\sqrt{3}\,\alpha - \beta + 1\right) + \left(\beta - \sqrt{3}\,\alpha\right) \tag{C.64}$$
$$m_{c1} = (\gamma - 1) \left(\beta + \sqrt{3}\,\alpha\right) + \lambda \left(\sqrt{3}\,\alpha - \beta + 1\right) \tag{C.65}$$

$$m_{c0} = (\lambda + \mu)\ \left(\sqrt{3}\,\alpha - \beta + 1\right) + \left(\beta - \sqrt{3}\,\alpha + 2\,\beta\ (\gamma - 1)\right) \tag{C.66}$$

C.1.3.4 Results of the calculation when $i_b < 0$ and $i_a > 0$

$$m_{a1} = \lambda\ \left(\sqrt{3}\,\alpha - \beta + 1\right) \tag{C.67}$$
$$m_{a0} = \lambda + \mu + \beta\,\gamma - \beta\,\lambda - \beta\,\mu - \sqrt{3}\,\alpha\,\gamma + \sqrt{3}\,\alpha\,\lambda + \sqrt{3}\,\alpha\,\mu \tag{C.68}$$
$$m_{b1} = \lambda\ \left(\sqrt{3}\,\alpha - \beta + 1\right) + \gamma\ \left(\beta - \sqrt{3}\,\alpha\right) \tag{C.69}$$
$$m_{b0} = (\lambda + \mu)\ \left(\sqrt{3}\,\alpha - \beta + 1\right) + \left(\beta - \sqrt{3}\,\alpha\right) \tag{C.70}$$
$$m_{c1} = \lambda\ \left(\sqrt{3}\,\alpha - \beta + 1\right) - \gamma\ \left(\beta + \sqrt{3}\,\alpha\right) \tag{C.71}$$
$$m_{c0} = (\lambda + \mu)\ \left(\sqrt{3}\,\alpha - \beta + 1\right) + \left(\beta - \sqrt{3}\,\alpha + 2\,\beta\ (\gamma - 1)\right) \tag{C.72}$$

C.1.4 Sector IV

C.1.4.1 Results of the calculation when $i_a > 0$ and $i_c > 0$

$$m_{a1} = \lambda\ \left(\beta + \sqrt{3}\,\alpha + 1\right) \tag{C.73}$$
$$m_{a0} = 3\,\beta\,\gamma - 2\,\beta + (\lambda + \mu)\ \left(\beta + \sqrt{3}\,\alpha + 1\right) - \sqrt{3}\,\alpha\,\gamma \tag{C.74}$$
$$m_{b1} = \gamma\ \left(\beta - \sqrt{3}\,\alpha\right) + \lambda\ \left(\beta + \sqrt{3}\,\alpha + 1\right) \tag{C.75}$$
$$m_{b0} = (\lambda + \mu)\ \left(\beta + \sqrt{3}\,\alpha + 1\right) + \left(2\,\beta\,\gamma - \sqrt{3}\,\alpha - \beta\right) \tag{C.76}$$
$$m_{c1} = \lambda\ \left(\beta + \sqrt{3}\,\alpha + 1\right) + \gamma\ \left(\beta - \sqrt{3}\,\alpha\right) + 2\,\beta\ (\gamma - 1) \tag{C.77}$$
$$m_{c0} = (\lambda + \mu)\ \left(\beta + \sqrt{3}\,\alpha + 1\right) - \left(\beta + \sqrt{3}\,\alpha\right) \tag{C.78}$$

C.1.4.2 Results of the calculation when $i_a > 0$ and $i_c < 0$

$$m_{a1} = \lambda\ \left(\beta + \sqrt{3}\,\alpha + 1\right) \tag{C.79}$$
$$m_{a0} = \lambda + \mu - \beta\,\gamma + \beta\,\lambda + \beta\,\mu - \sqrt{3}\,\alpha\,\gamma + \sqrt{3}\,\alpha\,\lambda + \sqrt{3}\,\alpha\,\mu \tag{C.80}$$
$$m_{b1} = \gamma\ \left(\beta - \sqrt{3}\,\alpha\right) + \lambda\ \left(\beta + \sqrt{3}\,\alpha + 1\right) \tag{C.81}$$
$$m_{b0} = (\lambda + \mu)\ \left(\beta + \sqrt{3}\,\alpha + 1\right) - \left(\beta + \sqrt{3}\,\alpha + 2\,\beta\ (\gamma - 1)\right) \tag{C.82}$$

$$m_{c1} = \lambda \left(\beta + \sqrt{3}\,\alpha + 1\right) - \beta\,\gamma - \sqrt{3}\,\alpha\,\gamma \tag{C.83}$$

$$m_{c0} = (\lambda + \mu) \left(\beta + \sqrt{3}\,\alpha + 1\right) - \left(\beta + \sqrt{3}\,\alpha\right) \tag{C.84}$$

C.1.4.3 Results of the calculation when $i_a < 0$ and $i_c < 0$

$$m_{a1} = \lambda \left(\beta + \sqrt{3}\,\alpha + 1\right) \tag{C.85}$$

$$m_{a0} = (\lambda + \mu) \left(\beta + \sqrt{3}\,\alpha + 1\right) + (-\gamma) \left(\beta - \sqrt{3}\,\alpha\right) - \left(\beta + \sqrt{3}\,\alpha + 2\,\beta\,(\gamma - 1)\right) \tag{C.86}$$

$$m_{b1} = (1 - \gamma) \left(\beta - \sqrt{3}\,\alpha\right) + \lambda \left(\beta + \sqrt{3}\,\alpha + 1\right) \tag{C.87}$$

$$m_{b0} = (\lambda + \mu) \left(\beta + \sqrt{3}\,\alpha + 1\right) - \left(\beta + \sqrt{3}\,\alpha + 2\,\beta\,(\gamma - 1)\right) \tag{C.88}$$

$$m_{c1} = \lambda \left(\beta + \sqrt{3}\,\alpha + 1\right) + (1 - \gamma) \left(\beta - \sqrt{3}\,\alpha\right) - 2\,\beta\,\gamma \tag{C.89}$$

$$m_{c0} = (\lambda + \mu) \left(\beta + \sqrt{3}\,\alpha + 1\right) - \left(\beta + \sqrt{3}\,\alpha\right) \tag{C.90}$$

C.1.4.4 Results of the calculation when $i_a < 0$ and $i_c > 0$

$$m_{a1} = \lambda \left(\beta + \sqrt{3}\,\alpha + 1\right) \tag{C.91}$$

$$m_{a0} = (\lambda + \mu) \left(\beta + \sqrt{3}\,\alpha + 1\right) + (-\gamma) \left(\beta - \sqrt{3}\,\alpha\right) + \left(2\,\beta\,\gamma - \sqrt{3}\,\alpha - \beta\right) \tag{C.92}$$

$$m_{b1} = (1 - \gamma) \left(\beta - \sqrt{3}\,\alpha\right) + \lambda \left(\beta + \sqrt{3}\,\alpha + 1\right) \tag{C.93}$$

$$m_{b0} = (\lambda + \mu) \left(\beta + \sqrt{3}\,\alpha + 1\right) + \left(2\,\beta\,\gamma - \sqrt{3}\,\alpha - \beta\right) \tag{C.94}$$

$$m_{c1} = (1 - \gamma) \left(\beta - \sqrt{3}\,\alpha\right) + 2\,\beta\,(\gamma - 1) + \lambda \left(\beta + \sqrt{3}\,\alpha + 1\right) \tag{C.95}$$

$$m_{c0} = (\lambda + \mu) \left(\beta + \sqrt{3}\,\alpha + 1\right) - \left(\beta + \sqrt{3}\,\alpha\right) \tag{C.96}$$

C.1.5 Sector V

C.1.5.1 Results of the calculation when $i_c > 0$ and $i_b > 0$

$$m_{a1} = \lambda\,(2\,\beta + 1) - \gamma \left(\beta - \sqrt{3}\,\alpha\right) \tag{C.97}$$

$$m_{a0} = -2\,\beta + \gamma \left(\beta + \sqrt{3}\,\alpha\right) + (\lambda + \mu)\,(2\,\beta + 1) \tag{C.98}$$

$$m_{b1} = \lambda\,(2\,\beta + 1) \tag{C.99}$$

$$m_{b0} = \lambda - \beta + \mu - \sqrt{3}\,\alpha + 2\,\beta\,\lambda + 2\,\beta\,\mu + 2\,\sqrt{3}\,\alpha\,\gamma \tag{C.100}$$
$$m_{c1} = \lambda - \beta - \sqrt{3}\,\alpha + 2\,\beta\,\lambda + 2\,\sqrt{3}\,\alpha\,\gamma \tag{C.101}$$
$$m_{c0} = (\lambda + \mu)\,(2\,\beta + 1) - 2\,\beta \tag{C.102}$$

C.1.5.2 Results of the calculation when $i_c > 0$ and $i_b < 0$

$$m_{a1} = (\gamma - 1)\left(\beta - \sqrt{3}\,\alpha\right) + \lambda\,(2\,\beta + 1) \tag{C.103}$$
$$m_{a0} = -2\,\beta + \gamma\left(\beta + \sqrt{3}\,\alpha\right) + (\lambda + \mu)\,(2\,\beta + 1) \tag{C.104}$$
$$m_{b1} = \lambda\,(2\,\beta + 1) \tag{C.105}$$
$$m_{b0} = \lambda - 2\,\beta + \mu + 2\,\beta\,\gamma + 2\,\beta\,\lambda + 2\,\beta\,\mu \tag{C.106}$$
$$m_{c1} = \lambda - 2\,\beta + 2\,\beta\,\gamma + 2\,\beta\,\lambda \tag{C.107}$$
$$m_{c0} = (\lambda + \mu)\,(2\,\beta + 1) - 2\,\beta \tag{C.108}$$

C.1.5.3 Results of the calculation when $i_c < 0$ and $i_b < 0$

$$m_{a1} = (\gamma - 1)\left(\beta - \sqrt{3}\,\alpha\right) + \lambda\,(2\,\beta + 1) \tag{C.109}$$
$$m_{a0} = (\lambda + \mu)\,(2\,\beta + 1) + (1 - \gamma)\left(\beta + \sqrt{3}\,\alpha\right) - 2\,\beta \tag{C.110}$$
$$m_{b1} = \lambda\,(2\,\beta + 1) \tag{C.111}$$
$$m_{b0} = \lambda - \beta + \mu + \sqrt{3}\,\alpha + 2\,\beta\,\lambda + 2\,\beta\,\mu - 2\,\sqrt{3}\,\alpha\,\gamma \tag{C.112}$$
$$m_{c1} = \lambda - \beta + \sqrt{3}\,\alpha + 2\,\beta\,\lambda - 2\,\sqrt{3}\,\alpha\,\gamma \tag{C.113}$$
$$m_{c0} = (\lambda + \mu)\,(2\,\beta + 1) - 2\,\beta \tag{C.114}$$

C.1.5.4 Results of the calculation when $i_c < 0$ and $i_b > 0$

$$m_{a1} = \lambda\,(2\,\beta + 1) - \gamma\left(\beta - \sqrt{3}\,\alpha\right) \tag{C.115}$$
$$m_{a0} = (\lambda + \mu)\,(2\,\beta + 1) + (1 - \gamma)\left(\beta + \sqrt{3}\,\alpha\right) - 2\,\beta \tag{C.116}$$
$$m_{b1} = \lambda\,(2\,\beta + 1) \tag{C.117}$$
$$m_{b0} = \lambda + \mu - 2\,\beta\,\gamma + 2\,\beta\,\lambda + 2\,\beta\,\mu \tag{C.118}$$
$$m_{c1} = \lambda - 2\,\beta\,\gamma + 2\,\beta\,\lambda \tag{C.119}$$
$$m_{c0} = (\lambda + \mu)\,(2\,\beta + 1) - 2\,\beta \tag{C.120}$$

C.1.6 Sector VI

C.1.6.1 Results of the calculation when $i_b > 0$ and $i_a > 0$

$$m_{a1} = (1-\gamma)\left(\beta + \sqrt{3}\,\alpha\right) + \lambda\left(\beta - \sqrt{3}\,\alpha + 1\right) - 2\,\beta\,\gamma \tag{C.121}$$

$$m_{a0} = (\lambda+\mu)\left(\beta - \sqrt{3}\,\alpha + 1\right) + \left(\sqrt{3}\,\alpha - \beta\right) \tag{C.122}$$

$$m_{b1} = \lambda\left(\beta - \sqrt{3}\,\alpha + 1\right) \tag{C.123}$$

$$m_{b0} = (-\gamma)\left(\beta + \sqrt{3}\,\alpha\right) + (\lambda+\mu)\left(\beta - \sqrt{3}\,\alpha + 1\right) + \left(\sqrt{3}\,\alpha - \beta - 2\,\beta\,(\gamma-1)\right) \tag{C.124}$$

$$m_{c1} = \lambda\left(\beta - \sqrt{3}\,\alpha + 1\right) - 2\,\beta\,\gamma \tag{C.125}$$

$$m_{c0} = (-\gamma)\left(\beta + \sqrt{3}\,\alpha\right) + (\lambda+\mu)\left(\beta - \sqrt{3}\,\alpha + 1\right) + \left(\sqrt{3}\,\alpha - \beta\right) \tag{C.126}$$

C.1.6.2 Results of the calculation when $i_b > 0$ and $i_a < 0$

$$m_{a1} = \lambda\left(\beta - \sqrt{3}\,\alpha + 1\right) - \beta\,\gamma + \sqrt{3}\,\alpha\,\gamma \tag{C.127}$$

$$m_{a0} = (\lambda+\mu)\left(\beta - \sqrt{3}\,\alpha + 1\right) + \left(\sqrt{3}\,\alpha - \beta\right) \tag{C.128}$$

$$m_{b1} = \lambda\left(\beta - \sqrt{3}\,\alpha + 1\right) \tag{C.129}$$

$$m_{b0} = \lambda + \mu - \beta\,\gamma + \beta\,\lambda + \beta\,\mu + \sqrt{3}\,\alpha\,\gamma - \sqrt{3}\,\alpha\,\lambda - \sqrt{3}\,\alpha\,\mu \tag{C.130}$$

$$m_{c1} = \lambda\left(\beta - \sqrt{3}\,\alpha + 1\right) - 2\,\beta\,\gamma \tag{C.131}$$

$$m_{c0} = (\gamma-1)\left(\beta + \sqrt{3}\,\alpha\right) + (\lambda+\mu)\left(\beta - \sqrt{3}\,\alpha + 1\right) + \left(\sqrt{3}\,\alpha - \beta\right) \tag{C.132}$$

C.1.6.3 Results of the calculation when $i_b < 0$ and $i_a < 0$

$$m_{a1} = \gamma\left(\beta + \sqrt{3}\,\alpha\right) + \lambda\left(\beta - \sqrt{3}\,\alpha + 1\right) + 2\,\beta\,(\gamma-1) \tag{C.133}$$

$$m_{a0} = (\lambda+\mu)\left(\beta - \sqrt{3}\,\alpha + 1\right) + \left(\sqrt{3}\,\alpha - \beta\right) \tag{C.134}$$

$$m_{b1} = \lambda\left(\beta - \sqrt{3}\,\alpha + 1\right) \tag{C.135}$$

$$m_{b0} = 3\,\beta\,\gamma - 2\,\beta + (\lambda+\mu)\left(\beta - \sqrt{3}\,\alpha + 1\right) + \sqrt{3}\,\alpha\,\gamma \tag{C.136}$$

$$m_{c1} = \lambda\left(\beta - \sqrt{3}\,\alpha + 1\right) + 2\,\beta\,(\gamma-1) \tag{C.137}$$

$$m_{c0} = (\gamma - 1)\left(\beta + \sqrt{3}\,\alpha\right) + (\lambda + \mu)\left(\beta - \sqrt{3}\,\alpha + 1\right) + \left(\sqrt{3}\,\alpha - \beta\right) \tag{C.138}$$

C.1.6.4 Results of the calculation when $i_b < 0$ and $i_a > 0$

$$m_{a1} = (1 - \gamma)\left(\beta + \sqrt{3}\,\alpha\right) + 2\,\beta\,(\gamma - 1) + \lambda\left(\beta - \sqrt{3}\,\alpha + 1\right) \tag{C.139}$$
$$m_{a0} = (\lambda + \mu)\left(\beta - \sqrt{3}\,\alpha + 1\right) + \left(\sqrt{3}\,\alpha - \beta\right) \tag{C.140}$$
$$m_{b1} = \lambda\left(\beta - \sqrt{3}\,\alpha + 1\right) \tag{C.141}$$
$$m_{b0} = (-\gamma)\left(\beta + \sqrt{3}\,\alpha\right) + (\lambda + \mu)\left(\beta - \sqrt{3}\,\alpha + 1\right) + \left(\sqrt{3}\,\alpha - \beta + 2\,\beta\,\gamma\right) \tag{C.142}$$
$$m_{c1} = \lambda\left(\beta - \sqrt{3}\,\alpha + 1\right) + 2\,\beta\,(\gamma - 1) \tag{C.143}$$
$$m_{c0} = (-\gamma)\left(\beta + \sqrt{3}\,\alpha\right) + (\lambda + \mu)\left(\beta - \sqrt{3}\,\alpha + 1\right) + \left(\sqrt{3}\,\alpha - \beta\right) \tag{C.144}$$

C.2 Calculation of triangle 2

C.2.1 Sector I

C.2.1.1 Results of the calculation when $i_a > 0$

$$m_{a1} = \gamma\left(\beta + \sqrt{3}\,\alpha - 2\right) + 1 \tag{C.145}$$
$$m_{a0} = 1 \tag{C.146}$$
$$m_{b1} = 0 \tag{C.147}$$
$$m_{b0} = \beta - \sqrt{3}\,\alpha + \gamma\left(\beta + \sqrt{3}\,\alpha - 2\right) + 2 \tag{C.148}$$
$$m_{c1} = 0 \tag{C.149}$$
$$m_{c0} = (\gamma - 1)\left(\beta + \sqrt{3}\,\alpha - 2\right) \tag{C.150}$$

C.2.1.2 Results of the calculation when $i_a < 0$

$$m_{a1} = 1 - (\gamma - 1)\left(\beta + \sqrt{3}\,\alpha - 2\right) \tag{C.151}$$
$$m_{a0} = 1 \tag{C.152}$$
$$m_{b1} = 0 \tag{C.153}$$

$$m_{b0} = 2\,\beta + 2\,\gamma - \beta\,\gamma - \sqrt{3}\,\alpha\,\gamma \tag{C.154}$$
$$m_{c1} = 0 \tag{C.155}$$
$$m_{c0} = -\gamma\,\left(\beta + \sqrt{3}\,\alpha - 2\right) \tag{C.156}$$

C.2.2 Sector II

C.2.2.1 Results of the calculation when $i_c > 0$

$$m_{a1} = \beta + \sqrt{3}\,\alpha - 2\,\gamma\,(\beta - 1) - 1 \tag{C.157}$$
$$m_{a0} = 1 \tag{C.158}$$
$$m_{b1} = 1 - 2\,(\beta - 1)\,(\gamma - 1) \tag{C.159}$$
$$m_{b0} = 1 \tag{C.160}$$
$$m_{c1} = 0 \tag{C.161}$$
$$m_{c0} = -2\,\gamma\,(\beta - 1) \tag{C.162}$$

C.2.2.2 Results of the calculation when $i_c < 0$

$$m_{a1} = \beta + \sqrt{3}\,\alpha + 2\,(\beta - 1)\,(\gamma - 1) - 1 \tag{C.163}$$
$$m_{a0} = 1 \tag{C.164}$$
$$m_{b1} = 2\,\gamma\,(\beta - 1) + 1 \tag{C.165}$$
$$m_{b0} = 1 \tag{C.166}$$
$$m_{c1} = 0 \tag{C.167}$$
$$m_{c0} = 2\,(\beta - 1)\,(\gamma - 1) \tag{C.168}$$

C.2.3 Sector III

C.2.3.1 Results of the calculation when $i_b > 0$

$$m_{a1} = 0 \tag{C.169}$$
$$m_{a0} = -\,(\gamma - 1)\,\left(\sqrt{3}\,\alpha - \beta + 2\right) \tag{C.170}$$
$$m_{b1} = -\gamma\,\left(\sqrt{3}\,\alpha - \beta + 2\right) + 1 \tag{C.171}$$
$$m_{b0} = 1 \tag{C.172}$$
$$m_{c1} = 0 \tag{C.173}$$

$$m_{c0} = -2\,\beta - \gamma\,\left(\sqrt{3}\,\alpha - \beta + 2\right) + 2 \tag{C.174}$$

C.2.3.2 Results of the calculation when $i_b < 0$

$$m_{a1} = 0 \tag{C.175}$$
$$m_{a0} = \gamma\,\left(\sqrt{3}\,\alpha - \beta + 2\right) \tag{C.176}$$
$$m_{b1} = (\gamma - 1)\,\left(\sqrt{3}\,\alpha - \beta + 2\right) + 1 \tag{C.177}$$
$$m_{b0} = 1 \tag{C.178}$$
$$m_{c1} = 0 \tag{C.179}$$
$$m_{c0} = -2\,\beta + (\gamma - 1)\,\left(\sqrt{3}\,\alpha - \beta + 2\right) + 2 \tag{C.180}$$

C.2.4 Sector IV

C.2.4.1 Results of the calculation when $i_a > 0$

$$m_{a1} = 0 \tag{C.181}$$
$$m_{a0} = \gamma\,\left(\beta + \sqrt{3}\,\alpha + 2\right) \tag{C.182}$$
$$m_{b1} = \beta - \sqrt{3}\,\alpha + \gamma\,\left(\beta + \sqrt{3}\,\alpha + 2\right) - 1 \tag{C.183}$$
$$m_{b0} = 1 \tag{C.184}$$
$$m_{c1} = (\gamma - 1)\,\left(\beta + \sqrt{3}\,\alpha + 2\right) + 1 \tag{C.185}$$
$$m_{c0} = 1 \tag{C.186}$$

C.2.4.2 Results of the calculation when $i_a < 0$

$$m_{a1} = 0 \tag{C.187}$$
$$m_{a0} = -\,(\gamma - 1)\,\left(\beta + \sqrt{3}\,\alpha + 2\right) \tag{C.188}$$
$$m_{b1} = 2\,\beta - \gamma\,\left(\beta + \sqrt{3}\,\alpha + 2\right) + 1 \tag{C.189}$$
$$m_{b0} = 1 \tag{C.190}$$
$$m_{c1} = 1 - \gamma\,\left(\beta + \sqrt{3}\,\alpha + 2\right) \tag{C.191}$$
$$m_{c0} = 1 \tag{C.192}$$

C.2.5 Sector V

C.2.5.1 Results of the calculation when $i_c > 0$

$$m_{a1} = 0 \tag{C.193}$$
$$m_{a0} = \beta + \sqrt{3}\,\alpha - 2\,\gamma\,(\beta + 1) + 2 \tag{C.194}$$
$$m_{b1} = 0 \tag{C.195}$$
$$m_{b0} = -2\,(\beta + 1)\,(\gamma - 1) \tag{C.196}$$
$$m_{c1} = 1 - 2\,\gamma\,(\beta + 1) \tag{C.197}$$
$$m_{c0} = 1 \tag{C.198}$$

C.2.5.2 Results of the calculation when $i_c < 0$

$$m_{a1} = 0 \tag{C.199}$$
$$m_{a0} = \beta + \sqrt{3}\,\alpha + 2\,(\beta + 1)\,(\gamma - 1) + 2 \tag{C.200}$$
$$m_{b1} = 0 \tag{C.201}$$
$$m_{b0} = 2\,\gamma\,(\beta + 1) \tag{C.202}$$
$$m_{c1} = 2\,(\beta + 1)\,(\gamma - 1) + 1 \tag{C.203}$$
$$m_{c0} = 1 \tag{C.204}$$

C.2.6 Sector VI

C.2.6.1 Results of the calculation when $i_b > 0$

$$m_{a1} = (\gamma - 1)\left(\beta - \sqrt{3}\,\alpha + 2\right) + 1 \tag{C.205}$$
$$m_{a0} = 1 \tag{C.206}$$
$$m_{b1} = 0 \tag{C.207}$$
$$m_{b0} = \gamma\left(\beta - \sqrt{3}\,\alpha + 2\right) \tag{C.208}$$
$$m_{c1} = \gamma\left(\beta - \sqrt{3}\,\alpha + 2\right) - 2\,\beta - 1 \tag{C.209}$$
$$m_{c0} = 1 \tag{C.210}$$

C.2.6.2 Results of the calculation when $i_b < 0$

$$m_{a1} = 1 - \gamma \left(\beta - \sqrt{3}\,\alpha + 2\right) \tag{C.211}$$
$$m_{a0} = 1 \tag{C.212}$$
$$m_{b1} = 0 \tag{C.213}$$
$$m_{b0} = -\left(\gamma - 1\right) \left(\beta - \sqrt{3}\,\alpha + 2\right) \tag{C.214}$$
$$m_{c1} = -2\,\beta - \left(\gamma - 1\right) \left(\beta - \sqrt{3}\,\alpha + 2\right) - 1 \tag{C.215}$$
$$m_{c0} = 1 \tag{C.216}$$

C.3 Calculation of triangle 3

C.3.1 Sector I

C.3.1.1 Results of the calculation when $i_a > 0$ and $i_c > 0$

$$m_{a1} = \left(\gamma - 1\right) \left(\beta - \sqrt{3}\,\alpha + 1\right) + \gamma \left(2\,\beta - 1\right) + 1 \tag{C.217}$$
$$m_{a0} = 1 \tag{C.218}$$
$$m_{b1} = \gamma \left(\beta - \sqrt{3}\,\alpha + 1\right) \tag{C.219}$$
$$m_{b0} = \gamma \left(2\,\beta - 1\right) + 1 \tag{C.220}$$
$$m_{c1} = 0 \tag{C.221}$$
$$m_{c0} = \left(2\,\beta - 1\right) \left(\gamma - 1\right) + \gamma \left(\beta - \sqrt{3}\,\alpha + 1\right) \tag{C.222}$$

C.3.1.2 Results of the calculation when $i_a > 0$ and $i_c < 0$

$$m_{a1} = \beta\,\gamma - 2\,\gamma + \sqrt{3}\,\alpha\,\gamma + 1 \tag{C.223}$$
$$m_{a0} = 1 \tag{C.224}$$
$$m_{b1} = -\left(\gamma - 1\right) \left(\beta - \sqrt{3}\,\alpha + 1\right) \tag{C.225}$$
$$m_{b0} = \gamma \left(2\,\beta - 1\right) + 1 \tag{C.226}$$
$$m_{c1} = 0 \tag{C.227}$$
$$m_{c0} = \left(\gamma - 1\right) \left(\beta + \sqrt{3}\,\alpha - 2\right) \tag{C.228}$$

C.3.1.3 Results of the calculation when $i_a < 0$ and $i_c < 0$

$$m_{a1} = 2\,\beta - 3\,\beta\,\gamma + \sqrt{3}\,\alpha\,\gamma \tag{C.229}$$
$$m_{a0} = 1 \tag{C.230}$$
$$m_{b1} = -\left(\gamma - 1\right)\,\left(\beta - \sqrt{3}\,\alpha + 1\right) \tag{C.231}$$
$$m_{b0} = 1 - \left(2\,\beta - 1\right)\,\left(\gamma - 1\right) \tag{C.232}$$
$$m_{c1} = 0 \tag{C.233}$$
$$m_{c0} = -\left(\gamma - 1\right)\,\left(\beta - \sqrt{3}\,\alpha + 1\right) - \gamma\,\left(2\,\beta - 1\right) \tag{C.234}$$

C.3.1.4 Results of the calculation when $i_a < 0$ and $i_c > 0$

$$m_{a1} = \left(\gamma - 1\right)\,\left(\beta - \sqrt{3}\,\alpha + 1\right) - \left(2\,\beta - 1\right)\,\left(\gamma - 1\right) + 1 \tag{C.235}$$
$$m_{a0} = 1 \tag{C.236}$$
$$m_{b1} = \gamma\,\left(\beta - \sqrt{3}\,\alpha + 1\right) \tag{C.237}$$
$$m_{b0} = 1 - \left(2\,\beta - 1\right)\,\left(\gamma - 1\right) \tag{C.238}$$
$$m_{c1} = 0 \tag{C.239}$$
$$m_{c0} = -\gamma\,\left(\beta + \sqrt{3}\,\alpha - 2\right) \tag{C.240}$$

C.3.2 Sector II

C.3.2.1 Results of the calculation when $i_c > 0$ and $i_b > 0$

$$m_{a1} = \gamma\,\left(\sqrt{3}\,\alpha - \beta + 1\right) \tag{C.241}$$
$$m_{a0} = \gamma\,\left(\beta + \sqrt{3}\,\alpha - 1\right) + 1 \tag{C.242}$$
$$m_{b1} = \beta - \sqrt{3}\,\alpha + 2\,\sqrt{3}\,\alpha\,\gamma \tag{C.243}$$
$$m_{b0} = 1 \tag{C.244}$$
$$m_{c1} = 0 \tag{C.245}$$
$$m_{c0} = 2\,\sqrt{3}\,\alpha\,\gamma - \sqrt{3}\,\alpha - \beta + 1 \tag{C.246}$$

C.3.2.2 Results of the calculation when $i_c > 0$ and $i_b < 0$

$$m_{a1} = \gamma \left(\sqrt{3}\,\alpha - \beta + 1\right) \tag{C.247}$$
$$m_{a0} = 1 - (\gamma - 1) \left(\beta + \sqrt{3}\,\alpha - 1\right) \tag{C.248}$$
$$m_{b1} = 2\,\beta + 2\,\gamma - 2\,\beta\,\gamma - 1 \tag{C.249}$$
$$m_{b0} = 1 \tag{C.250}$$
$$m_{c1} = 0 \tag{C.251}$$
$$m_{c0} = -2\,\gamma\,(\beta - 1) \tag{C.252}$$

C.3.2.3 Results of the calculation when $i_c < 0$ and $i_b < 0$

$$m_{a1} = -(\gamma - 1) \left(\sqrt{3}\,\alpha - \beta + 1\right) \tag{C.253}$$
$$m_{a0} = 1 - (\gamma - 1) \left(\beta + \sqrt{3}\,\alpha - 1\right) \tag{C.254}$$
$$m_{b1} = \beta + \sqrt{3}\,\alpha - 2\,\sqrt{3}\,\alpha\,\gamma \tag{C.255}$$
$$m_{b0} = 1 \tag{C.256}$$
$$m_{c1} = 0 \tag{C.257}$$
$$m_{c0} = \sqrt{3}\,\alpha - \beta - 2\,\sqrt{3}\,\alpha\,\gamma + 1 \tag{C.258}$$

C.3.2.4 Results of the calculation when $i_c < 0$ and $i_b > 0$

$$m_{a1} = -(\gamma - 1) \left(\sqrt{3}\,\alpha - \beta + 1\right) \tag{C.259}$$
$$m_{a0} = \gamma \left(\beta + \sqrt{3}\,\alpha - 1\right) + 1 \tag{C.260}$$
$$m_{b1} = 2\,\beta\,\gamma - 2\,\gamma + 1 \tag{C.261}$$
$$m_{b0} = 1 \tag{C.262}$$
$$m_{c1} = 0 \tag{C.263}$$
$$m_{c0} = 2\,(\beta - 1)\,(\gamma - 1) \tag{C.264}$$

C.3.3 Sector III

C.3.3.1 Results of the calculation when $i_b > 0$ and $i_a > 0$

$$m_{a1} = 0 \tag{C.265}$$

$$m_{a0} = -(\gamma - 1)\left(\beta + \sqrt{3}\,\alpha + 1\right) - \gamma\,(2\,\beta - 1) \tag{C.266}$$
$$m_{b1} = 2\,\beta - 3\,\beta\,\gamma - \sqrt{3}\,\alpha\,\gamma \tag{C.267}$$
$$m_{b0} = 1 \tag{C.268}$$
$$m_{c1} = -\gamma\,(2\,\beta - 1) \tag{C.269}$$
$$m_{c0} = 1 - \gamma\left(\beta + \sqrt{3}\,\alpha + 1\right) \tag{C.270}$$

C.3.3.2 Results of the calculation when $i_b > 0$ and $i_a < 0$

$$m_{a1} = 0 \tag{C.271}$$
$$m_{a0} = -(\gamma - 1)\left(\sqrt{3}\,\alpha - \beta + 2\right) \tag{C.272}$$
$$m_{b1} = \beta\,\gamma - 2\,\gamma - \sqrt{3}\,\alpha\,\gamma + 1 \tag{C.273}$$
$$m_{b0} = 1 \tag{C.274}$$
$$m_{c1} = (2\,\beta - 1)\,(\gamma - 1) \tag{C.275}$$
$$m_{c0} = 1 - \gamma\left(\beta + \sqrt{3}\,\alpha + 1\right) \tag{C.276}$$

C.3.3.3 Results of the calculation when $i_b < 0$ and $i_a < 0$

$$m_{a1} = 0 \tag{C.277}$$
$$m_{a0} = (2\,\beta - 1)\,(\gamma - 1) + \gamma\left(\beta + \sqrt{3}\,\alpha + 1\right) \tag{C.278}$$
$$m_{b1} = (\gamma - 1)\left(\beta + \sqrt{3}\,\alpha + 1\right) + \gamma\,(2\,\beta - 1) + 1 \tag{C.279}$$
$$m_{b0} = 1 \tag{C.280}$$
$$m_{c1} = (2\,\beta - 1)\,(\gamma - 1) \tag{C.281}$$
$$m_{c0} = (\gamma - 1)\left(\beta + \sqrt{3}\,\alpha + 1\right) + 1 \tag{C.282}$$

C.3.3.4 Results of the calculation when $i_b < 0$ and $i_a > 0$

$$m_{a1} = 0 \tag{C.283}$$
$$m_{a0} = \gamma\left(\sqrt{3}\,\alpha - \beta + 2\right) \tag{C.284}$$
$$m_{b1} = (\gamma - 1)\left(\beta + \sqrt{3}\,\alpha + 1\right) - (2\,\beta - 1)\,(\gamma - 1) + 1 \tag{C.285}$$
$$m_{b0} = 1 \tag{C.286}$$

$$m_{c1} = -\gamma\ (2\,\beta - 1) \tag{C.287}$$
$$m_{c0} = (\gamma - 1)\ \left(\beta + \sqrt{3}\,\alpha + 1\right) + 1 \tag{C.288}$$

C.3.4 Sector IV

C.3.4.1 Results of the calculation when $i_a > 0$ and $i_c > 0$

$$m_{a1} = 0 \tag{C.289}$$
$$m_{a0} = \gamma\ (2\,\beta + 1) - (\gamma - 1)\ \left(\sqrt{3}\,\alpha - \beta + 1\right) \tag{C.290}$$
$$m_{b1} = \gamma\ (2\,\beta + 1) \tag{C.291}$$
$$m_{b0} = -\gamma\ \left(\sqrt{3}\,\alpha - \beta + 1\right) + 1 \tag{C.292}$$
$$m_{c1} = 3\,\beta\,\gamma - 2\,\beta - \sqrt{3}\,\alpha\,\gamma \tag{C.293}$$
$$m_{c0} = 1 \tag{C.294}$$

C.3.4.2 Results of the calculation when $i_a > 0$ and $i_c < 0$

$$m_{a1} = 0 \tag{C.295}$$
$$m_{a0} = \gamma\ \left(\beta + \sqrt{3}\,\alpha + 2\right) \tag{C.296}$$
$$m_{b1} = \gamma\ (2\,\beta + 1) \tag{C.297}$$
$$m_{b0} = (\gamma - 1)\ \left(\sqrt{3}\,\alpha - \beta + 1\right) + 1 \tag{C.298}$$
$$m_{c1} = (\gamma - 1)\ (2\,\beta + 1) + \left((\gamma - 1)\ \left(\sqrt{3}\,\alpha - \beta + 1\right) + 1\right) \tag{C.299}$$
$$m_{c0} = 1 \tag{C.300}$$

C.3.4.3 Results of the calculation when $i_a < 0$ and $i_c < 0$

$$m_{a1} = 0 \tag{C.301}$$
$$m_{a0} = \gamma\ \left(\sqrt{3}\,\alpha - \beta + 1\right) + (1 - \gamma)\ (2\,\beta + 1) \tag{C.302}$$
$$m_{b1} = (1 - \gamma)\ (2\,\beta + 1) \tag{C.303}$$
$$m_{b0} = (\gamma - 1)\ \left(\sqrt{3}\,\alpha - \beta + 1\right) + 1 \tag{C.304}$$
$$m_{c1} = (-\gamma)\ (2\,\beta + 1) + \left((\gamma - 1)\ \left(\sqrt{3}\,\alpha - \beta + 1\right) + 1\right) \tag{C.305}$$

$$m_{c0} = 1 \tag{C.306}$$

C.3.4.4 Results of the calculation when $i_a < 0$ and $i_c > 0$

$$m_{a1} = 0 \tag{C.307}$$
$$m_{a0} = -(\gamma - 1)\left(\beta + \sqrt{3}\,\alpha + 2\right) \tag{C.308}$$
$$m_{b1} = (1 - \gamma)\,(2\,\beta + 1) \tag{C.309}$$
$$m_{b0} = -\gamma\left(\sqrt{3}\,\alpha - \beta + 1\right) + 1 \tag{C.310}$$
$$m_{c1} = 1 - \beta\,\gamma - \sqrt{3}\,\alpha\,\gamma - 2\,\gamma \tag{C.311}$$
$$m_{c0} = 1 \tag{C.312}$$

C.3.5 Sector V

C.3.5.1 Results of the calculation when $i_c > 0$ and $i_b > 0$

$$m_{a1} = \gamma\left(\beta + \sqrt{3}\,\alpha + 1\right) \tag{C.313}$$
$$m_{a0} = 1 - \gamma\left(\beta - \sqrt{3}\,\alpha + 1\right) \tag{C.314}$$
$$m_{b1} = 0 \tag{C.315}$$
$$m_{b0} = \beta - \sqrt{3}\,\alpha + 2\sqrt{3}\,\alpha\,\gamma + 1 \tag{C.316}$$
$$m_{c1} = 2\sqrt{3}\,\alpha\,\gamma - \sqrt{3}\,\alpha - \beta \tag{C.317}$$
$$m_{c0} = 1 \tag{C.318}$$

C.3.5.2 Results of the calculation when $i_c > 0$ and $i_b < 0$

$$m_{a1} = -(\gamma - 1)\left(\beta + \sqrt{3}\,\alpha + 1\right) \tag{C.319}$$
$$m_{a0} = 1 - \gamma\left(\beta - \sqrt{3}\,\alpha + 1\right) \tag{C.320}$$
$$m_{b1} = 0 \tag{C.321}$$
$$m_{b0} = -2\,(\beta + 1)\,(\gamma - 1) \tag{C.322}$$
$$m_{c1} = 1 - 2\,\beta\,\gamma - 2\,\gamma \tag{C.323}$$
$$m_{c0} = 1 \tag{C.324}$$

C.3.5.3 Results of the calculation when $i_c < 0$ and $i_b < 0$

$$m_{a1} = -(\gamma - 1)\left(\beta + \sqrt{3}\,\alpha + 1\right) \tag{C.325}$$
$$m_{a0} = (\gamma - 1)\left(\beta - \sqrt{3}\,\alpha + 1\right) + 1 \tag{C.326}$$
$$m_{b1} = 0 \tag{C.327}$$
$$m_{b0} = \beta + \sqrt{3}\,\alpha - 2\sqrt{3}\,\alpha\,\gamma + 1 \tag{C.328}$$
$$m_{c1} = \sqrt{3}\,\alpha - \beta - 2\sqrt{3}\,\alpha\,\gamma \tag{C.329}$$
$$m_{c0} = 1 \tag{C.330}$$

C.3.5.4 Results of the calculation when $i_c < 0$ and $i_b > 0$

$$m_{a1} = \gamma\left(\beta + \sqrt{3}\,\alpha + 1\right) \tag{C.331}$$
$$m_{a0} = (\gamma - 1)\left(\beta - \sqrt{3}\,\alpha + 1\right) + 1 \tag{C.332}$$
$$m_{b1} = 0 \tag{C.333}$$
$$m_{b0} = 2\,\gamma\,(\beta + 1) \tag{C.334}$$
$$m_{c1} = 2\,\gamma - 2\,\beta + 2\,\beta\,\gamma - 1 \tag{C.335}$$
$$m_{c0} = 1 \tag{C.336}$$

C.3.6 Sector VI

C.3.6.1 Results of the calculation when $i_b > 0$ and $i_a > 0$

$$m_{a1} = (-\gamma)\,(2\,\beta + 1) + \left(1 - (\gamma - 1)\left(\beta + \sqrt{3}\,\alpha - 1\right)\right) \tag{C.337}$$
$$m_{a0} = 1 \tag{C.338}$$
$$m_{b1} = 0 \tag{C.339}$$
$$m_{b0} = (1 - \gamma)\,(2\,\beta + 1) - \gamma\left(\beta + \sqrt{3}\,\alpha - 1\right) \tag{C.340}$$
$$m_{c1} = -\gamma\left(\beta + \sqrt{3}\,\alpha - 1\right) \tag{C.341}$$
$$m_{c0} = 1 - \gamma\,(2\,\beta + 1) \tag{C.342}$$

C.3.6.2 Results of the calculation when $i_b > 0$ and $i_a < 0$

$$m_{a1} = (\gamma - 1)\ (2\,\beta + 1) + \left(1 - (\gamma - 1)\ \left(\beta + \sqrt{3}\,\alpha - 1\right)\right) \tag{C.343}$$
$$m_{a0} = 1 \tag{C.344}$$
$$m_{b1} = 0 \tag{C.345}$$
$$m_{b0} = \gamma\ \left(\beta - \sqrt{3}\,\alpha + 2\right) \tag{C.346}$$
$$m_{c1} = -\gamma\ \left(\beta + \sqrt{3}\,\alpha - 1\right) \tag{C.347}$$
$$m_{c0} = (2\,\beta + 1)\ (\gamma - 1) + 1 \tag{C.348}$$

C.3.6.3 Results of the calculation when $i_b < 0$ and $i_a < 0$

$$m_{a1} = 3\,\beta\,\gamma - 2\,\beta + \sqrt{3}\,\alpha\,\gamma \tag{C.349}$$
$$m_{a0} = 1 \tag{C.350}$$
$$m_{b1} = 0 \tag{C.351}$$
$$m_{b0} = (\gamma - 1)\ \left(\beta + \sqrt{3}\,\alpha - 1\right) + \gamma\ (2\,\beta + 1) \tag{C.352}$$
$$m_{c1} = (\gamma - 1)\ \left(\beta + \sqrt{3}\,\alpha - 1\right) \tag{C.353}$$
$$m_{c0} = (2\,\beta + 1)\ (\gamma - 1) + 1 \tag{C.354}$$

C.3.6.4 Results of the calculation when $i_b < 0$ and $i_a > 0$

$$m_{a1} = \sqrt{3}\,\alpha\,\gamma - \beta\,\gamma - 2\,\gamma + 1 \tag{C.355}$$
$$m_{a0} = 1 \tag{C.356}$$
$$m_{b1} = 0 \tag{C.357}$$
$$m_{b0} = -\,(\gamma - 1)\ \left(\beta - \sqrt{3}\,\alpha + 2\right) \tag{C.358}$$
$$m_{c1} = (\gamma - 1)\ \left(\beta + \sqrt{3}\,\alpha - 1\right) \tag{C.359}$$
$$m_{c0} = 1 - \gamma\ (2\,\beta + 1) \tag{C.360}$$

C.4 Calculation of triangle 4

C.4.1 Sector I

C.4.1.1 Results of the calculation when $i_c > 0$

$$m_{a1} = 1 - (\gamma - 1)\left(\beta + \sqrt{3}\,\alpha - 2\right) \tag{C.361}$$
$$m_{a0} = 1 \tag{C.362}$$
$$m_{b1} = 2\,\beta - \gamma\left(\beta + \sqrt{3}\,\alpha - 2\right) - 1 \tag{C.363}$$
$$m_{b0} = 1 \tag{C.364}$$
$$m_{c1} = 0 \tag{C.365}$$
$$m_{c0} = -\gamma\left(\beta + \sqrt{3}\,\alpha - 2\right) \tag{C.366}$$

C.4.1.2 Results of the calculation when $i_c < 0$

$$m_{a1} = \gamma\left(\beta + \sqrt{3}\,\alpha - 2\right) + 1 \tag{C.367}$$
$$m_{a0} = 1 \tag{C.368}$$
$$m_{b1} = 2\,\beta + (\gamma - 1)\left(\beta + \sqrt{3}\,\alpha - 2\right) - 1 \tag{C.369}$$
$$m_{b0} = 1 \tag{C.370}$$
$$m_{c1} = 0 \tag{C.371}$$
$$m_{c0} = (\gamma - 1)\left(\beta + \sqrt{3}\,\alpha - 2\right) \tag{C.372}$$

C.4.2 Sector II

C.4.2.1 Results of the calculation when $i_b > 0$

$$m_{a1} = 0 \tag{C.373}$$
$$m_{a0} = \beta + \sqrt{3}\,\alpha + 2\,(\beta - 1)\,(\gamma - 1) \tag{C.374}$$
$$m_{b1} = 2\,\gamma\,(\beta - 1) + 1 \tag{C.375}$$
$$m_{b0} = 1 \tag{C.376}$$
$$m_{c1} = 0 \tag{C.377}$$
$$m_{c0} = 2\,(\beta - 1)\,(\gamma - 1) \tag{C.378}$$

C.4.2.2 Results of the calculation when $i_b < 0$

$$m_{a1} = 0 \tag{C.379}$$
$$m_{a0} = \beta + \sqrt{3}\,\alpha - 2\,\gamma\,(\beta - 1) \tag{C.380}$$
$$m_{b1} = 1 - 2\,(\beta - 1)\,(\gamma - 1) \tag{C.381}$$
$$m_{b0} = 1 \tag{C.382}$$
$$m_{c1} = 0 \tag{C.383}$$
$$m_{c0} = -2\,\gamma\,(\beta - 1) \tag{C.384}$$

C.4.3 Sector III

C.4.3.1 Results of the calculation when $i_a > 0$

$$m_{a1} = 0 \tag{C.385}$$
$$m_{a0} = \gamma\,\left(\sqrt{3}\,\alpha - \beta + 2\right) \tag{C.386}$$
$$m_{b1} = (\gamma - 1)\,\left(\sqrt{3}\,\alpha - \beta + 2\right) + 1 \tag{C.387}$$
$$m_{b0} = 1 \tag{C.388}$$
$$m_{c1} = -\beta + \gamma\,\left(\sqrt{3}\,\alpha - \beta + 2\right) - \sqrt{3}\,\alpha - 1 \tag{C.389}$$
$$m_{c0} = 1 \tag{C.390}$$

C.4.3.2 Results of the calculation when $i_a < 0$

$$m_{a1} = 0 \tag{C.391}$$
$$m_{a0} = -\,(\gamma - 1)\,\left(\sqrt{3}\,\alpha - \beta + 2\right) \tag{C.392}$$
$$m_{b1} = -\gamma\,\left(\sqrt{3}\,\alpha - \beta + 2\right) + 1 \tag{C.393}$$
$$m_{b0} = 1 \tag{C.394}$$
$$m_{c1} = 1 - \gamma\,\left(\sqrt{3}\,\alpha - \beta + 2\right) - 2\,\beta \tag{C.395}$$
$$m_{c0} = 1 \tag{C.396}$$

C.4.4 Sector IV

C.4.4.1 Results of the calculation when $i_c > 0$

$$m_{a1} = 0 \tag{C.397}$$
$$m_{a0} = -(\gamma - 1)\left(\beta + \sqrt{3}\,\alpha + 2\right) \tag{C.398}$$
$$m_{b1} = 0 \tag{C.399}$$
$$m_{b0} = 2\,\beta - \gamma\left(\beta + \sqrt{3}\,\alpha + 2\right) + 2 \tag{C.400}$$
$$m_{c1} = 1 - \gamma\left(\beta + \sqrt{3}\,\alpha + 2\right) \tag{C.401}$$
$$m_{c0} = 1 \tag{C.402}$$

C.4.4.2 Results of the calculation when $i_c < 0$

$$m_{a1} = 0 \tag{C.403}$$
$$m_{a0} = \gamma\left(\beta + \sqrt{3}\,\alpha + 2\right) \tag{C.404}$$
$$m_{b1} = 0 \tag{C.405}$$
$$m_{b0} = \beta - \sqrt{3}\,\alpha + \gamma\left(\beta + \sqrt{3}\,\alpha + 2\right) \tag{C.406}$$
$$m_{c1} = (\gamma - 1)\left(\beta + \sqrt{3}\,\alpha + 2\right) + 1 \tag{C.407}$$
$$m_{c0} = 1 \tag{C.408}$$

C.4.5 Sector V

C.4.5.1 Results of the calculation when $i_b > 0$

$$m_{a1} = \sqrt{3}\,\alpha - \beta + 2\,\gamma\,(\beta + 1) - 1 \tag{C.409}$$
$$m_{a0} = 1 \tag{C.410}$$
$$m_{b1} = 0 \tag{C.411}$$
$$m_{b0} = 2\,\gamma\,(\beta + 1) \tag{C.412}$$
$$m_{c1} = 2\,(\beta + 1)\,(\gamma - 1) + 1 \tag{C.413}$$
$$m_{c0} = 1 \tag{C.414}$$

C.4.5.2 Results of the calculation when $i_b < 0$

$$m_{a1} = \sqrt{3}\,\alpha - \beta - 2\,(\beta+1)\,(\gamma-1) - 1 \tag{C.415}$$
$$m_{a0} = 1 \tag{C.416}$$
$$m_{b1} = 0 \tag{C.417}$$
$$m_{b0} = -2\,(\beta+1)\,(\gamma-1) \tag{C.418}$$
$$m_{c1} = 1 - 2\,\gamma\,(\beta+1) \tag{C.419}$$
$$m_{c0} = 1 \tag{C.420}$$

C.4.6 Sector VI

C.4.6.1 Results of the calculation when $i_a > 0$

$$m_{a1} = 1 - \gamma\,\left(\beta - \sqrt{3}\,\alpha + 2\right) \tag{C.421}$$
$$m_{a0} = 1 \tag{C.422}$$
$$m_{b1} = 0 \tag{C.423}$$
$$m_{b0} = -\,(\gamma-1)\,\left(\beta - \sqrt{3}\,\alpha + 2\right) \tag{C.424}$$
$$m_{c1} = 0 \tag{C.425}$$
$$m_{c0} = -2\,\beta - (\gamma-1)\,\left(\beta - \sqrt{3}\,\alpha + 2\right) \tag{C.426}$$

C.4.6.2 Results of the calculation when $i_a < 0$

$$m_{a1} = (\gamma-1)\,\left(\beta - \sqrt{3}\,\alpha + 2\right) + 1 \tag{C.427}$$
$$m_{a0} = 1 \tag{C.428}$$
$$m_{b1} = 0 \tag{C.429}$$
$$m_{b0} = \gamma\,\left(\beta - \sqrt{3}\,\alpha + 2\right) \tag{C.430}$$
$$m_{c1} = 0 \tag{C.431}$$
$$m_{c0} = \gamma\,\left(\beta - \sqrt{3}\,\alpha + 2\right) - 2\,\beta \tag{C.432}$$

List of Figures

List of Tables

List of Publications

Journal papers

1. X. Cai, C. Wang, and R. Kennel, "A fast and precise grid synchronization method based on fixed gain filter," *IEEE Transactions on Industrial Electronics*, vol. 65, no. 9, pp. 7119–7128, 2018.

2. X. Cai, Z. Zhang, J. Wang, and R. Kennel, "Optimal control solutions for pmsm drives: A comparison study with experimental assessments," *IEEE Journal of Emerging and Selected Topics in Power Electronics*, vol. 6, no. 1, pp. 352–362, March 2018.

Conference papers

1. X. Cai, Z. Zhang, L. Cai, and R. Kennel, "Current balancing control of high power parallel-connected afe with small current ripples," in *2015 9th International Conference on Power Electronics and ECCE Asia (ICPE-ECCE Asia)*, June 2015, pp. 624–630.

2. X. Cai, Z. Zhang, and R. Kennel, "Deadbeat and direct torque-flux control of induction motor: A comparison study," in *2016 IEEE 8th International Power Electronics and Motion Control Conference (IPEMC-ECCE Asia)*, May 2016, pp. 1909–1914.

3. X. Cai, Z. Zhang, Z. Chen, and R. Kennel, "Dc-bus voltage balancing for three-level npc inverter using deadbeat controller," in *2016 IEEE 8th International Power Electronics and Motion Control Conference (IPEMC-ECCE Asia)*, May 2016, pp. 496–501.

4. Z. Chen, X. Cai, R. Kennel, and F. Wang, "Enhanced sensorless control of spmsm based on stationary reference frame high-frequency pulsating signal injection," in *2016 IEEE 8th International Power Electronics and Motion Control Conference (IPEMC-ECCE Asia)*, May 2016, pp. 885–890.

5. Z. Zhang, X. Cai, R. Kennel, and F. Wang, "Model predictive current control of three-level npc back-to-back power converter pmsg wind turbine systems," in *2016 IEEE 8th International Power Electronics and Motion Control Conference (IPEMC-ECCE Asia)*, May 2016, pp. 1462–1467.

6. Z. Zhang, X. Cai, R. Kennel, and F. Wang, "Fully fpga based predictive control of back-to-back power converter pmsg wind turbine systems with space vector modulator," in *2016 IEEE 8th International Power Electronics and Motion Control Conference (IPEMC-ECCE Asia)*, May 2016, pp. 1468–1473.

7. Z. Zhang, F. Wang, M. Acikgoz, X. Cai, and R. Kennel, "Fpga hil simulation of back-to-back converter pmsg wind turbine systems," in *2015 9th International Conference on Power Electronics and ECCE Asia (ICPE-ECCE Asia)*, June 2015, pp. 99–106.

Bibliography

[1] W. C. Duesterhoeft, M. W. Schulz, and E. Clarke, "Determination of instantaneous currents and voltages by means of alpha, beta, and zero components," *Transactions of the American Institute of Electrical Engineers*, vol. 70, no. 2, pp. 1248–1255, July 1951.

[2] R. H. Park, "Two-reaction theory of synchronous machines generalized method of analysis-part i," *Transactions of the American Institute of Electrical Engineers*, vol. 48, no. 3, pp. 716–727, July 1929.

[3] ——, "Two-reaction theory of synchronous machines - part ii," *Electrical Engineering*, vol. 52, no. 1, pp. 44–45, Jan 1933.

[4] J. Holtz, "The dynamic representation of ac drive systems by complex signal flow graphs," in *Industrial Electronics, 1994. Symposium Proceedings, ISIE '94., 1994 IEEE International Symposium on*, May 1994, pp. 1–6.

[5] K. Hasse, "Zum dynamischen verhalten der asynchronmaschine bei betrieb mit variabler ständerfrequenz und ständerspannung," *ETZ-A*, vol. 89, pp. 387–391, 1968.

[6] F. Blaschke, "The principle of field orientation as applied to the new transvector closed-loop control system for rotating-field machines," *ETZ-A*, vol. 34, pp. 217–220, 1972.

[7] M. Barut, S. Bogosyan, and M. Gokasan, "Experimental evaluation of braided ekf for sensorless control of induction motors," *IEEE Transactions on Industrial Electronics*, vol. 55, no. 2, pp. 620–632, Feb 2008.

[8] ——, "Speed-sensorless estimation for induction motors using extended kalman filters," *IEEE Transactions on Industrial Electronics*, vol. 54, no. 1, pp. 272–280, Feb 2007.

[9] Y.-R. Kim, S.-K. Sul, and M.-H. Park, "Speed sensorless vector control of induction motor using extended kalman filter," *IEEE Transactions on Industry Applications*, vol. 30, no. 5, pp. 1225–1233, Sep 1994.

[10] T. Orlowska-Kowalska, "Application of extended luenberger observer for flux and rotor time-constant estimation in induction motor drives," *IEE Proceedings D - Control Theory and Applications*, vol. 136, no. 6, pp. 324–330, Nov 1989.

[11] T.-S. Kwon, M.-H. Shin, and D.-S. Hyun, "Speed sensorless stator flux-oriented control of induction motor in the field weakening region using luenberger observer," *IEEE Transactions on Power Electronics*, vol. 20, no. 4, pp. 864–869, July 2005.

[12] A. Benchaib, A. Rachid, E. Audrezet, and M. Tadjine, "Real-time sliding-mode observer and control of an induction motor," *IEEE Transactions on Industrial Electronics*, vol. 46, no. 1, pp. 128–138, Feb 1999.

[13] C. Lascu, I. Boldea, and F. Blaabjerg, "Direct torque control of sensorless induction motor drives: a sliding-mode approach," *IEEE Transactions on Industry Applications*, vol. 40, no. 2, pp. 582–590, March 2004.

[14] Z. Yan, C. Jin, and V. Utkin, "Sensorless sliding-mode control of induction motors," *IEEE Transactions on Industrial Electronics*, vol. 47, no. 6, pp. 1286–1297, Dec 2000.

[15] H. Kubota, K. Matsuse, and T. Nakano, "Dsp-based speed adaptive flux observer of induction motor," *IEEE Transactions on Industry Applications*, vol. 29, no. 2, pp. 344–348, Mar 1993.

[16] T. Noguchi and I. Takahashi, "Quick torque response control of an induction motor based on a new concept," *IEEJ Tech*, pp. 61–70, Sep 1984.

[17] I. Takahashi and T. Noguchi, "A new quick-response and high-efficiency control strategy of an induction motor," *IEEE Transactions on Industry Applications*, vol. IA-22, no. 5, pp. 820–827, Sept 1986.

[18] M. De Depenbrock, Jul. 14 1988, dE Patent 3,438,504. [Online]. Available: http://google.com/patents/DE3438504C2?cl=ru

[19] M. Depenbrock, "Direct self-control (dsc) of inverter-fed induction machine," *IEEE Transactions on Power Electronics*, vol. 3, no. 4, pp. 420–429, Oct 1988.

[20] T. G. Habetler, F. Profumo, M. Pastorelli, and L. M. Tolbert, "Direct torque control of induction machines using space vector modulation," *IEEE Transactions on Industry Applications*, vol. 28, no. 5, pp. 1045–1053, Sep 1992.

[21] K. B. Lee and F. Blaabjerg, "Sensorless dtc-svm for induction motor driven by a matrix converter using a parameter estimation strategy," *IEEE Transactions on Industrial Electronics*, vol. 55, no. 2, pp. 512–521, Feb 2008.

[22] A. I. Propoi, "Use of linear programming methods for synthesizing sampled-data automatic systems," *Automation and Rempote Control*, vol. 7, no. 24, pp. 837–844, 1963.

[23] S. S. J. Holtz, "A predictive controller or the stator current vector of ac machines fed from a switched voltage source," in *International Power Electronics Conference IPEC*, vol. 2, 1983, pp. 1665–1675.

[24] R. Kennel and D. Schöder, "A predictive control strategy for converters," in *Third IPAC symposium 1983*, 1983, pp. 415–422.

[25] M. A. Stephens, C. Manzie, and M. C. Good, "Model predictive control for reference tracking on an industrial machine tool servo drive," *IEEE Transactions on Industrial Informatics*, vol. 9, no. 2, pp. 808–816, May 2013.

[26] X. Li and P. Shamsi, "Inductance surface learning for model predictive current control of switched reluctance motors," *IEEE Transactions on Transportation Electrification*, vol. 1, no. 3, pp. 287–297, Oct 2015.

[27] M. Vatani, B. Bahrani, M. Saeedifard, and M. Hovd, "Indirect finite control set model predictive control of modular multilevel converters," *IEEE Transactions on Smart Grid*, vol. 6, no. 3, pp. 1520–1529, May 2015.

[28] J. R. Arribas and C. M. V. Gonzalez, "Optimal vector control of pumping and ventilation induction motor drives," *IEEE Transactions on Industrial Electronics*, vol. 49, no. 4, pp. 889–895, Aug 2002.

[29] Z. Zhang, C. Hackl, and R. Kennel, "Fpga based direct model predictive current control of pmsm drives with 3l npc power converter," in *PCIM - 2016, Nurnburg*, May 2016.

[30] Y. Tang, P. C. Loh, P. Wang, F. H. Choo, F. Gao, and F. Blaabjerg, "Generalized design of high performance shunt active power filter with output lcl filter," *IEEE Transactions on Industrial Electronics*, vol. 59, no. 3, pp. 1443–1452, March 2012.

[31] R. J. Wai, S. J. Jhung, J. J. Liaw, and Y. R. Chang, "Intelligent optimal energy management system for hybrid power sources including fuel cell and battery," *IEEE Transactions on Power Electronics*, vol. 28, no. 7, pp. 3231–3244, July 2013.

[32] A. Ajami, H. Ardi, and A. Farakhor, "A novel high step-up dc/dc converter based on integrating coupled inductor and switched-capacitor techniques for renewable energy applications," *IEEE Transactions on Power Electronics*, vol. 30, no. 8, pp. 4255–4263, Aug 2015.

[33] J. Z. Zhang, T. Sun, F. Wang, J. Rodriguez, and R. Kennel, "A computationally-efficient quasi-centralized dmpc for back-to-back converter pmsg windturbine systems without dc-link tracking errors," *IEEE Transactions on Industrial Electronics*, vol. PP, no. 99, pp. 1–1, 2016.

[34] K. I. Hwu and Y. T. Yau, "Performance enhancement of boost converter based on pid controller plus linear-to-nonlinear translator," *IEEE Transactions on Power Electronics*, vol. 25, no. 5, pp. 1351–1361, May 2010.

[35] M. Kazmierkowski, L. Franquelo, J. Rodriguez, M. Perez, and J. Leon, "High-performance motor drives," *Industrial Electronics Magazine, IEEE*, vol. 5, no. 3, pp. 6–26, Sept 2011.

[36] R. D. Lorenz and D. B. Lawson, "Performance of feedforward current regulators for field-oriented induction machine controllers," *IEEE Transactions on Industry Applications*, vol. IA-23, no. 4, pp. 597–602, July 1987.

[37] T. Tarczewski and L. M. Grzesiak, "Constrained state feedback speed control of pmsm based on model predictive approach," *IEEE Transactions on Industrial Electronics*, vol. 63, no. 6, pp. 3867–3875, June 2016.

[38] Z. Zhang, H. Xu, M. Xue, Z. Chen, T. Sun, R. Kennel, and C. Hackl, "Predictive control with novel virtual-flux estimation for back-to-back power converters," *Industrial Electronics, IEEE Transactions on*, vol. 62, no. 5, pp. 2823–2834, May 2015.

[39] J. Rodriguez, J. Pontt, C. A. Silva, P. Correa, P. Lezana, P. Cortes, and U. Ammann, "Predictive current control of a voltage source inverter," *IEEE Transactions on Industrial Electronics*, vol. 54, no. 1, pp. 495–503, Feb 2007.

[40] P. Cortes, M. P. Kazmierkowski, R. M. Kennel, D. E. Quevedo, and J. Rodriguez, "Predictive control in power electronics and drives," *IEEE Transactions on Industrial Electronics*, vol. 55, no. 12, pp. 4312–4324, Dec 2008.

[41] S. Kouro, P. Cortes, R. Vargas, U. Ammann, and J. Rodriguez, "Model predictive control-a simple and powerful method to control power converters," *IEEE Transactions on Industrial Electronics*, vol. 56, no. 6, pp. 1826–1838, June 2009.

[42] S. Kouro, M. A. Perez, J. Rodriguez, A. M. Llor, and H. A. Young, "Model predictive control: Mpc's role in the evolution of power electronics," *IEEE Industrial Electronics Magazine*, vol. 9, no. 4, pp. 8–21, Dec 2015.

[43] L. Pontryagin, V. Boltyanskii, R. Gamkrelize, and E. Mishchenko, *The mathematical theory of optimal processes.* Gordon and Breach Science, 1986, pp. 17–21.

[44] T. Murata, T. Tsuchiya, and I. Takeda, "Vector control for induction machine on the application of optimal control theory," *IEEE Transactions on Industrial Electronics*, vol. 37, no. 4, pp. 283–290, Aug 1990.

[45] B. Leden, "Dead-beat control and the riccati equation," *IEEE Transactions on Automatic Control*, vol. 21, no. 5, pp. 791–792, Oct 1976.

[46] H. Fang, Z. Zhang, X. Feng, and R. Kennel, "Ripple-reduced model predictive direct power control for active front-end power converters with extended switching vectors and time-optimised control," *IET Power Electronics*, vol. 9, no. 9, pp. 1914–1923, 2016.

[47] Z. Zhang, H. Fang, F. Gao, J. Rodriguez, and R. Kennel, "Multiple-vector model predictive power control for grid-tied wind turbine system with enhanced steady state control performances," *IEEE Transactions on Industrial Electronics*, vol. PP, no. 99, pp. 1–1, 2017.

[48] F. Briz, M. W. Degner, and R. D. Lorenz, "Analysis and design of current regulators using complex vectors," *IEEE Transactions on Industry Applications*, vol. 36, no. 3, pp. 817–825, May 2000.

[49] Z. Zhang and R. Kennel, "Fpga based direct model predictive power and current control of 3l npc active front ends," in *PCIM - 2016, Nurnburg*, May 2016.

[50] R. Teichmann and S. Bernet, "A comparison of three-level converters versus two-level converters for low-voltage drives, traction, and utility applications," *Industry Applications, IEEE Transactions on*, vol. 41, no. 3, pp. 855–865, May 2005.

[51] J. Holtz, M. Holtgen, and J. Krah, "A space vector modulator for the high-switching frequency control of three-level sic inverters," *Power Electronics, IEEE Transactions on*, vol. 29, no. 5, pp. 2618–2626, May 2014.

[52] Z. Zhang, X. Cai, and R. Kennel, "Model predictive current control of three-level npc back-to-back power converter pmsg wind turbine systems," in *IPEMC 2016-ECCE Asia. Hefei, China, 2016*, May 2016.

[53] A. Nabae, I. Takahashi, and H. Akagi, "A new neutral-point-clamped pwm inverter," *Industry Applications, IEEE Transactions on*, vol. IA-17, no. 5, pp. 518–523, Sept 1981.

[54] S. Madishetti, B. Singh, and G. Bhuvaneshwari, "Three-level npc inverter based svm-vcimd with feed-forward active pfc rectifier for enhanced ac mains power quality," *Industry Applications, IEEE Transactions on*, vol. PP, no. 99, pp. 1–1, 2015.

[55] B. Schmitt and R. Sommer, "Retrofit of fixed speed induction motors with medium voltage drive converters using npc three-level inverter high-voltage igbt based topology," in *Industrial Electronics, 2001. Proceedings. ISIE 2001. IEEE International Symposium on*, vol. 2, 2001, pp. 746–751 vol.2.

[56] R. Maheshwari, S. Munk-Nielsen, and S. Busquets-Monge, "Design of neutral-point voltage controller of a three-level npc inverter with small dc-link capacitors," *Industrial Electronics, IEEE Transactions on*, vol. 60, no. 5, pp. 1861–1871, May 2013.

[57] H. Zhang, S. Finney, A. Massoud, and B. Williams, "An svm algorithm to balance the capacitor voltages of the three-level npc active power filter," *Power Electronics, IEEE Transactions on*, vol. 23, no. 6, pp. 2694–2702, Nov 2008.

[58] S. Das and G. Narayanan, "Novel switching sequences for a space-vector-modulated three-level inverter," *Industrial Electronics, IEEE Transactions on*, vol. 59, no. 3, pp. 1477–1487, March 2012.

[59] Y. Zhang, H. Yang, and B. Xia, "Model-predictive control of induction motor drives: Torque control versus flux control," *IEEE Transactions on Industry Applications*, vol. 52, no. 5, pp. 4050–4060, Sept 2016.

[60] M. Trabelsi, S. Bayhan, K. A. Ghazi, H. Abu-Rub, and L. Ben-Brahim, "Finite-control-set model predictive control for grid-connected packed-u-cells multilevel inverter," *IEEE Transactions on Industrial Electronics*, vol. 63, no. 11, pp. 7286–7295, Nov 2016.

[61] V. Yaramasu and B. Wu, "Predictive control of a three-level boost converter and an npc inverter for high-power pmsg-based medium voltage wind energy conversion systems," *IEEE Transactions on Power Electronics*, vol. 29, no. 10, pp. 5308–5322, Oct 2014.

[62] T. Geyer and S. Mastellone, "Model predictive direct torque control of a five-level anpc converter drive system," *IEEE Transactions on Industry Applications*, vol. 48, no. 5, pp. 1565–1575, Sept 2012.

[63] S. Vazquez, R. P. Aguilera, P. Acuna, J. Pou, J. I. Leon, L. G. Franquelo, and V. G. Agelidis, "Model predictive control for single-phase npc converters based on optimal switching sequences," *IEEE Transactions on Industrial Electronics*, vol. 63, no. 12, pp. 7533–7541, Dec 2016.

[64] P. Cortes, S. Kouro, B. L. Rocca, R. Vargas, J. Rodriguez, J. I. Leon, S. Vazquez, and L. G. Franquelo, "Guidelines for weighting factors design in model predictive control of power converters and drives," in *2009 IEEE International Conference on Industrial Technology*, Feb 2009, pp. 1–7.

[65] F. Rojas-Lobos, R. Kennel, and R. Cárdenas-Dobson, "Current control and capacitor balancing for 4-leg npc converters using finite set model predictive control," in *IECON 2013 - 39th Annual Conference of the IEEE Industrial Electronics Society*, Nov 2013, pp. 590–595.

[66] D. G. Luenberger, "Observing the state of a linear system," *IEEE Transactions on Military Electronics*, vol. 8, no. 2, pp. 74–80, April 1964.

[67] D. Luenberger, "An introduction to observers," *IEEE Transactions on Automatic Control*, vol. 16, no. 6, pp. 596–602, Dec 1971.

[68] ——, "Observers for multivariable systems," *IEEE Transactions on Automatic Control*, vol. 11, no. 2, pp. 190–197, Apr 1966.

[69] R. E. Kalman, "A new approach to linear filtering and prediction problems," *Transactions of the ASME–Journal of Basic Engineering*, vol. 82, no. Series D, pp. 35–45, 1960.

[70] N. K. Boggarpu and R. C. Kavanagh, "New learning algorithm for high-quality velocity measurement and control when using low-cost optical encoders," *IEEE Transactions on Instrumentation and Measurement*, vol. 59, no. 3, pp. 565–574, March 2010.

[71] T. Shi, Z. Wang, and C. Xia, "Speed measurement error suppression for pmsm control system using self-adaption kalman observer," *IEEE Transactions on Industrial Electronics*, vol. 62, no. 5, pp. 2753–2763, May 2015.

[72] O. Wallmark, L. Harnefors, and O. Carlson, "An improved speed and position estimator for salient permanent-magnet synchronous motors," *IEEE Transactions on Industrial Electronics*, vol. 52, no. 1, pp. 255–262, Feb 2005.

[73] C. K. Lai and K.-K. Shyu, "A novel motor drive design for incremental motion system via sliding-mode control method," *IEEE Transactions on Industrial Electronics*, vol. 52, no. 2, pp. 499–507, April 2005.

[74] Z. Z. Liu, F. L. Luo, and M. A. Rahman, "Robust and precision motion control system of linear-motor direct drive for high-speed x-y table positioning mechanism," *IEEE Transactions on Industrial Electronics*, vol. 52, no. 5, pp. 1357–1363, Oct 2005.

[75] R. D. Lorenz and K. W. V. Patten, "High-resolution velocity estimation for all-digital, ac servo drives," *IEEE Transactions on Industry Applications*, vol. 27, no. 4, pp. 701–705, Jul 1991.

[76] R. Petrella, M. Tursini, L. Peretti, and M. Zigliotto, "Speed measurement algorithms for low-resolution incremental encoder equipped drives: a comparative analysis," in *2007 International Aegean Conference on Electrical Machines and Power Electronics*, Sept 2007, pp. 780–787.

[77] T. Ohmae, T. Matsuda, K. Kamiyama, and M. Tachikawa, "A microprocessor controlled high accuracy wide range speed regulator for motor drives," *IEEE Transactions on Industrial Electronics*, vol. IE-29, no. 3, pp. 207–211, Aug 1982.

[78] S.-H. Lee and J.-B. Song, "Acceleration estimator for low-velocity and low-acceleration regions based on encoder position data," *IEEE/ASME Transactions on Mechatronics*, vol. 6, no. 1, pp. 58–64, Mar 2001.

[79] W. H. Zhu and T. Lamarche, "Velocity estimation by using position and acceleration sensors," *IEEE Transactions on Industrial Electronics*, vol. 54, no. 5, pp. 2706–2715, Oct 2007.

[80] N. Peterfreund, "Robust tracking of position and velocity with kalman snakes," *IEEE Transactions on Pattern Analysis and Machine Intelligence*, vol. 21, no. 6, pp. 564–569, Jun 1999.

[81] P. R. Belanger, "Estimation of angular velocity and acceleration from shaft encoder measurements," in *Proceedings 1992 IEEE International Conference on Robotics and Automation*, May 1992, pp. 585–592 vol.1.

[82] H.-W. Kim and S.-K. Sul, "A new motor speed estimator using kalman filter in low speed range," in *Industrial Electronics, Control and Instrumentation, 1994. IECON '94., 20th International Conference on*, vol. 1, Sep 1994, pp. 503–508 vol.1.

[83] S.-M. Yang and S.-J. Ke, "Performance evaluation of a velocity observer for accurate velocity estimation of servo motor drives," *IEEE Transactions on Industry Applications*, vol. 36, no. 1, pp. 98–104, Jan 2000.

[84] B. Ekstrand, "Poles and zeros of alpha;- beta; and alpha;- beta;- gamma; tracking filters," *IEE Proceedings - Control Theory and Applications*, vol. 148, no. 5, pp. 370–376, Sep 2001.

[85] E.-K. Boukas and F. M. Al-Sunni, *Mechatronic Systems: Analysis, Design and Implementation*. Springer, 2012.

[86] R. Isermann, *Digital Control Systems*, 2nd ed. Springer, 1989, vol. 1.